ABSTRACT

Title of Dissertation: Topology from Quantum Dynamics of Ultracold Atoms

Graham Hair Reid
Doctor of Philosophy, 2023

Dissertation Directed by: Dr. Ian B. Spielman
Joint Quantum Institute,
National Institute of Standards and Technology,
and
Department of Physics, University of Maryland College Park

Ultracold atoms are a versatile platform for studying quantum physics in the lab. Using carefully chosen external fields, these systems can be engineered to obey a wide range of effective Hamiltonians, making them an ideal system for quantum simulation experiments studying exotic forms of matter. In this work, we describe experiments using $^{87}\mathrm{Rb}$ Bose–Einstein condensates (BECs) to study exotic topological matter based on out-of-equilibrium effects. The topological states are prepared through the quantum dynamics of the ultracold atom system subjected to a highly tunable lattice potential described by the bipartite Rice–Mele (RM) model, created by combining dressing from a radiofrequency (RF) magnetic field and laser fields driving Raman transitions. We describe a form of crystal momentum-resolved quantum state tomography, which functions by diabatically changing the lattice parameters, used to reconstruct the full pseudospin quantum state. This allows us to calculate topological invariants characterizing the system.

We apply these techniques to study out-of-equilibrium states of our lattice system, described by various combinations of sublattice, time-reversal and particle-hole symmetry. After quenching between lattice configurations, we observe the resulting time-evolution and follow the Zak phase and winding number. Depending on the symmetry configuration, the Zak phase may evolve continuously. In contrast, the winding number may jump between integer values when sublattice symmetry is transiently present in the time-evolving state. We observe a scenario where the winding number changes by ± 2, yielding values that are not present in the native RM Hamiltonian.

Finally, we describe a modulation protocol in which the configuration of the bipartite lattice is periodically switched, resulting in the Floquet eigenstates of the system having pseudospin-momentum locked linear dispersion, analogous to massless particles described by the Dirac equation. We modulate our lattice configuration to experimentally realize the Floquet system and quantify the drift velocity associated with the bands at zero crystal momentum. The linear dispersion of Floquet bands derives from nontrivial topology defined over the micromotion of the system, which we measure using our pseudospin quantum state tomography, in very good agreement with theory.

Topology from Quantum Dynamics of Ultracold Atoms

by

Graham Hair Reid

Dissertation submitted to the Faculty of the Graduate School of the
University of Maryland, College Park in partial fulfillment
of the requirements for the degree of
Doctor of Philosophy
2023

Advisory Committee:
Professor Steven L. Rolston, Chair
Professor Ian B. Spielman, Advisor, Co-Chair
Professor Alicia J. Kollár
Professor Jay D. Sau
Professor Trey Porto
Professor Edo Waks, Deans Representative

Preface

A Ph.D. thesis serves multiple purposes. It seeks to convey theoretical background, technical details, as well as scientific results. It is a capstone to years of research, putting specialized scientific results into a broader context. This thesis describes the key scientific results of my graduate career, including technical details and nuances that were too long for the papers. It also includes technical and theoretical background which will be familiar to experts, but might prove useful as a reference for future students. If you are searching for technical details of an experiment performed in the RbK lab at NIST between 2018 and 2023, or a reference on the physics of alkali atoms, laser cooling, or topology in condensed matter physics, you are in the right place. I hope this thesis serves you well.

Acknowledgments

The work described in this thesis was possible thanks to contributions from many people. I was lucky to have this help and support throughout my Ph.D., so I wish to thank everyone who contributed in some way. First, the experiments described in this thesis would have been totally impossible without the visionary scientific leadership of my advisor Ian Spielman. I thank Ian for all his scientific insights, as well as support and advice throughout my time in graduate school.

The experiments in the thesis were carried out in the RbK lab at NIST, so I thank all the students and post-docs who contributed to the lab over the years. In particular, I thank Mingwu Lu for developing much of the technical underpinnings of the experiments described in this thesis as well as everything he taught me about atomic physics experiments. I thank Amilson Fritsch for all his contributions to the lab as well as his tireless dedication and unshakable positive attitude. I thank Dina Genkina for welcoming me into the lab and showing me the ropes, and Alina Piñeiro for everything she contributed to my time in RbK. I am glad to have met our newest post doc, Emmanuel Mercdo in my last year and am confident that the lab will be in good hands!

On the scientific side, I benefited greatly from conversations with Bill Phillips about the work described in this thesis. I also thank Nigel Cooper and Max McGinley for their help clarifying the significance of some of our experimental results. The science described in this thesis also benefited from the careful reading and insightful questions of our internal reviewers; for this I thank Charles Clark, Carlos Bracamontes, Nikko Pomata, and Micheal Doris. I also thank

Martin Ritter, Dario D'Amato, and Michael Doris for their help proofreading this document.

I was also lucky to have a an excellent group of colleagues in other labs at NIST. I thank Francisco "Paco" Salces Carcoba for his help and mentorship when I joined the group; Hillary Hurst, Emine Altuntas, and Chris Billington for sharing their post doc wisdom; and Yuchen Yue, Dario D'Amato, and Michael Doris for being there throughout my time at NIST. I also thank my colleagues working at UMD, Mingshu Zhao and Junheng Tao for their camaraderie from afar, and Ana Valdes Curiel for being a welcoming presence in the group during my first years.

Last, but certainly not least, I thank my family for all the support throughout my time in graduate school.

Table of Contents

Preface ii

Acknowledgements iii

Table of Contents v

List of Tables ix

List of Figures x

List of Abbreviations xvi

Chapter 1: Introduction 1
1.1 Thesis Overview . . . 2

Chapter 2: Atomic Physics Background 5
2.1 Alkali Atoms . . . 5
2.1.1 Fine structure . . . 6
2.1.2 Hyperfine Structure . . . 7
2.1.3 External Magnetic Fields . . . 7
2.2 Light Matter Interaction . . . 11
2.2.1 Near-Resonant Excitation and Rabi Flopping . . . 12
2.2.2 Magnetic Transitions . . . 14
2.3 Light Shifts . . . 17
2.3.1 Scattering . . . 20
2.3.2 Optical Dipole Force Traps . . . 21
2.4 Raman Coupling . . . 24
2.5 Measurements . . . 27
2.5.1 Absorption Imaging . . . 27
2.5.2 Time-of-Flight Imaging . . . 30
2.5.3 Stern–Gerlach Imaging . . . 31

Chapter 3: Experimental System 34
3.1 Introduction to Bose–Einstein Condensation . . . 35
3.1.1 Trapped Noninteracting Bose Gas . . . 38
3.1.2 Interacting Bose gas . . . 39
3.2 Laser Cooling . . . 40

3.2.1 Zeeman Slowing . . . 42
3.2.2 Optical Molasses . . . 43
3.2.3 Sub Doppler Cooling . . . 43
3.2.4 Magneto-Optical Traps . . . 44
3.3 BEC Production . . . 45
3.3.1 Optical Dipole Trap . . . 46
3.3.2 Evaporation and State Transfer . . . 47
3.4 Apparatus Overview . . . 47
3.4.1 Control System . . . 50
3.5 Camera Systems . . . 51
3.6 Laser Systems . . . 51
3.7 Magnetic Field Systems . . . 53
3.7.1 Magnetic Field Locking and Monitoring . . . 54
3.7.2 RF Signals . . . 55
3.8 Raman Beams . . . 56
3.9 DMDs . . . 61

Chapter 4: Lattices **63**
4.1 Bloch's Theorem . . . 63
4.2 Single-Band Tight Binding Model . . . 64
4.3 Two-site Lattices . . . 66
4.3.1 Spin Mapping . . . 71

Chapter 5: Topology and Evolution **74**
5.1 Topology of Surfaces . . . 74
5.2 Topology in quantum systems . . . 77
5.2.1 Bulk-boundary Correspondence . . . 77
5.3 Symmetry and Topology . . . 78
5.3.1 Winding Numbers . . . 79
5.4 Berry's Phase . . . 81
5.4.1 Zak Phase . . . 84
5.4.2 Gauge Ambiguity . . . 85
5.4.3 Chern Number . . . 87
5.5 Topological Dynamics . . . 90
5.5.1 Topological Charge Pumps . . . 90
5.5.2 Floquet Winding Numbers . . . 93

Chapter 6: State Dependent Raman Lattice **97**
6.1 Raman Bipartite Lattice . . . 97
6.1.1 Raman Lattice Band Structure . . . 103
6.1.2 Lattice Calibration . . . 106
6.1.3 Measurement . . . 107
6.1.4 Comparison to Bichromatic Method . . . 108
6.2 Pseudospin Rotations . . . 109
6.2.1 Quantum State Tomography on a Subsystem . . . 110

6.2.2 Unit Cells and Secondary Lattices . . . 113
6.2.3 Remaining Phase Ambiguity . . . 114
6.3 Technical Implementation . . . 114
6.4 Measuring the SSH Eigenstates . . . 115
6.4.1 Filled Bands and Parallel Measurements . . . 115
6.4.2 Ground Band Measurements . . . 116
6.5 Measuring Tunneling and Displacement . . . 117

Chapter 7: Measuring Topology out of Equilibrium **122**
7.1 Explicitly and Dynamically Broken Symmetries . . . 123
7.2 Tunneling . . . 124
7.3 Dimerization . . . 128
7.4 TRS Breaking with Tunneling Phase Models . . . 132
7.5 Summary . . . 135

Chapter 8: Topological Dirac Floquet System **137**
8.1 Floquet Theory . . . 137
8.1.1 Floquet Engineering . . . 138
8.1.2 Calculating Floquet Band Structure . . . 138
8.2 Floquet Engineering Dirac Bands . . . 139
8.2.1 Modulation Implementation . . . 142
8.2.2 Floquet Pulsing Experiments . . . 143
8.2.3 Observing Linear Drift in the Floquet System . . . 145
8.2.4 Single-Configuration Modulation . . . 146
8.2.5 Evolution under Different Drive . . . 148
8.3 Measuring Floquet Topology . . . 152
8.4 Dispersion Away from $q = 0$ . . . 155
8.5 Conclusion . . . 156

Chapter 9: Conclusion and Outlook **159**
9.1 Conclusion . . . 159
9.2 Outlook . . . 160

Appendix A: RF Source Design **162**
A.1 Introduction . . . 162
A.2 Operating Principle . . . 164
A.2.1 Performance . . . 165
A.3 Prototype . . . 169
A.4 Testing and Performance . . . 171
A.5 Conclusion . . . 175
A.6 Fourier Coefficients . . . 177

Appendix B: Imaging systems **179**
B.1 Imaging Basics . . . 179
B.1.1 Keplerian telescope . . . 180

B.1.2 Numerical aperture and resolution 182
B.1.3 Performance 183
B.1.4 Coherent and Incoherent Illumination 186
B.1.5 Optical relays 188
B.2 Imaging Objective Design 188
B.2.1 Measuring the vacuum window thickness 191

Appendix C: Creating solitons with controllable and near-zero velocity in Bose–Einstein condensates **196**

Bibliography **206**

List of Tables

5.1 Symmetry classes and topological indices for zero, one, and two dimensional systems. 0 denotes a case where the system lack a symmetry, while + and − correspond to different symmetry operators. 80

7.1 Summary of experiments in this chapter organized by initial state and configuration of evolution Hamiltonian. * indicates that a symmetry is present in the initial state but it is different from that of the evolution Hamiltonian (phase-free SSH model). ** means the evolution Hamiltonian was not fully dimerized for the case studied; the stated dimerization corresponds to the larger tunneling strength. . . . 135

8.1 Calibrated lattice parameters used throughout the chapter. *Calibrated value for configuration I. 158

A.1 Comparison of the two limiting cases of operation where the load is dominated by resistance or inductance, as well as the general expression. 166

List of Figures

2.1 Energy level structure of $^{87}\mathrm{Rb}$. The levels on the left include the fine-structure splitting that gives rise to the D1 and D2 lines, while the right includes hyperfine structure. The energy levels given are in the absence of an external magnetic field. Values for frequency differences and corresponding light wavelengths are from Ref. [1]. 8

2.2 Magnetic sublevels of the electronic ground state of $^{87}\mathrm{Rb}$. The left panel shows the crossover between the low field and high field regimes, while the right shows the details of the low field regime. 11

2.3 Rabi Oscillation starting from $|\psi(0)\rangle = |g\rangle$. (a) Resonant oscillation with $\Omega = 1$, $\delta = 0$ giving $\tilde{\Omega} = \Omega$. (b) Off-resonant oscillation with $\Omega = \delta = 1$ giving $\tilde{\Omega} = \sqrt{2}\Omega$. (c) Eigenvalues of the Rabi Hamiltonian for $\Omega = 1$ with variable δ. At high δ the difference between the coupled eigenenergy (solid curves) and the bare energy (bashed lines) can be understood as light shifts. 15

2.4 Evolution during a resonant RF pulse. (a) Initial state $|m_F = 0\rangle$. (b) Initial state $|m_F = -1\rangle$. 16

2.5 Raman pulsing starting from the $|k = 0, m_F = 0\rangle$ initial state. In this case the $m_F = \pm 1$ states have $k = \pm 2k_R$. Solid lines are theory curves for $\Omega = 10.6E_R$. . 26

2.6 Conceptual sketch of absorption imaging. Atomic absorption attenuates the probe beam. By comparing an image of the attenuated probe to a reference probe image without atoms present, we can determine the OD. The false-color image right shows a cropped region of the sensor for the atoms and probe shots used to form an absorption image, corresponding to the center of Fig. 2.7 (a). 29

2.7 Example absorption images taken after SG ToF. (a) different magnetic states separated along the y direction. (b) States with different momentum and internal state separate along both directions. (c) A distribution with more combinations of internal and momentum state after ToF. (d) A similar distribution after momentum focused ToF. 32

3.1 Bose–Einstein distribution. (a) Occupation number as a function of energy for three different values of z. (b) Ground state occupation as a function of z, which diverges as z approaches 1 corresponding to $\mu = 0$ and Bose–Einstein condensation. (c) Condensate fraction as a function of temperature expressed as T/T_c for an ideal (untrapped) Bose gas. 36

3.2 Overview of the RbK apparatus. The apparatus consists of three levels: the table level, the chamber level, and the upper level. 48

3.3 Sketch of experimental chamber with laser beams. (a) xz cross section view with vertical beams. (b) xy view with horizontal beams. The counterpropagating Raman beams share the $\mathbf{e}_x - \mathbf{e}_y$ axis with the tight dipole trap beam. We switch between the MOT beams and the Raman and ODT beams using flipper mirrors. . 49
3.4 Magnetic field coil arrangement. (a) Perspective. (b) Top view. Not to scale. . . . 54
3.5 Schematic of RF circuits for Raman AOM control. The four mixers receive an analog control signal from our control computer (indicated with solid circles), and the VCA's each receive an analog control signal from a `Newport LB1005-S` servo controller (indicated by solid circles). The output of each branch is controlled by a TTL switch allowing for fast digital control of the AOM signal from the control computer (those channels correspond to solid squares). 59
3.6 Raman AOM setup. The labeled elements are A. Shutter, B. $\lambda/2$ plate used to control the relative power in the A and C branches after polarizing beam splitter, C. AOMs, D. Optical fiber launch. 60
3.7 DMD pattern projection setup. The labeled elements are A. DMD, B. iris, C. $f = 100\mathrm{mm}$ lens, D. iris, E. $f = 50\mathrm{mm}$ lens, F. dichroic mirror. 62

4.1 Band structure for tight-binding models. (a) Cosinusoidal band structure of the single band model. (b) Three cases for the SSH model: $J = 10J'$ (dark green), $J = 2J'$ (teal), and $J = J'$ (light green). The increased imbalance between tunneling strengths is associated with flatter bands and a wider band gap, while with equal tunneling strengths the gap closes. 69

5.1 Normal vector (black), normal sections (dashed), and principal curvatures (blue) for the point $(5/4, 0, 0)$ on a torus with inner radius 1 and outer radius $5/4$. κ_1 and κ_2 have the same sign giving a positive Gaussian curvature $K = 5/16$. 76
5.2 Illustration of crystal momentum dependent gauge transformation. Before the transformation states from $q = -k_R$ to $q = k_R$ trace the equator (left). After the transformation (right), they uniformly point to $\mathbf{e}_x$. Dotted lines indicate the rotation for different q values. 87
5.3 Calculating Chern numbers in a discretely sampled BZ. The Berry curvature $\mathcal{F}(q_x, q_y)$ plays the role of a flux per plaquette in the lattice formed by the discretely sampled BZ. 90
5.4 Charge pumping schematic. (a) Conceptual sketch of Thouless pumping. A periodically modulated lattice potential leads to a nonzero displacement per cycle, here one lattice site. (b) Example of charge pumping in a bipartite lattice. (c) Cyclic pumping trajectory in parameter space for the RM model. Trajectories that encircle the origin result in topological charge pumping. (d) Parameter space for Thouless pumping. The Chern number characterizing a topological charge pump is defined over the periodic q, t space. The quantized charge pumped per cycle is given by integrating the Berry curvature in the cross-hatched region. . . 92
5.5 Example Floquet–Bloch band structure. One band contributes 0 to the sum in Eq. 5.28, while the other contributes 1. Note that the highlighted points at the band edge are connected due to the periodicity of the Floquet–BZ. 95

6.1 Schematic of combined Raman-RF driving. (a) Experimental geometry. Two counter-propagating laser beams each carry two frequency components to drive Raman transitions. (b) Level diagram showing Raman and RF transitions within the $f = 1$ manifold. 98
6.2 Ellipse showing $\mathbf{\Omega}(\hat{x})$ for $\Omega_+ = 12.7$, $\Omega_- = 5.7$ and $\Omega_{\text{RF}} = 4.2$ for $\phi_{\text{RF}} = 0$ (a) and $-\pi/2$ (b). In both cases the ellipse lies in the $x - y$ plane because $\delta = 0$ . . . 100
6.3 Adiabatic potentials for combined Raman-RF lattice for $\Omega_+ = 12.7E_R$, $\Omega_- = 5.7E_R$, $\Omega_{\text{RF}} = 4.2E_R$. The four cases shown have $\phi_{\text{RF}} = -\pi/2,\ \pi/2,\ \pi$, and 0. The central unit cell is shaded in gray. 102
6.4 Band structure of Raman lattice in two configurations. (a) Imbalanced (large Δ) configuration. (b) Balanced (SSH) configuration. (c) Zoom on lowest two bands from (b) and comparison to SHH model with $J = -0.34E_R, J' - 0.0032E_R$ (dashed black curves). 105
6.5 Lattice pulsing experiment for calibration. To simplify the evolution, we sum the population in different k states, showing the internal state summed over k. The theory curves are a fit to ϕ_{RF} with $\Omega_+ = 12.7E_R, \Omega_- = 5.6E_R, \Omega_{\text{RF}} = 4.5E_R$, yielding $\phi_{\text{RF}} = 0.22\pi$. 107
6.6 Bichromatic optical lattice. (a) Optical lattice potential with $V_{\text{s}} = -20E_R$ and $V_{\text{l}} = -5E_R$ in a balanced configuration. (b) Lowest bands. Green solid curves show the numerically calculated band structure for the bichromatic lattice, while black dashed curves show a closely matching SSH model band structure. 109
6.7 Evolution in readout lattices corresponding to pseudospin rotation. (a) y readout lattice. (b) x readout lattice. The left column shows the time evolution under each readout lattice (pictured in the gray inset). Evolution up to the calibrated pulse time is shown with solid symbols and solid lines while evolution past this time is shown with open symbols and dashed lines. The right column shows the corresponding rotations on the Bloch sphere allowing for measurement in the $\hat{\sigma}_x$ and $\hat{\sigma}_y$ bases via native $\hat{\sigma}_z$ measurement. 112
6.8 Measured pseudospin composition of the ground band of our lattice corresponding to SSH configurations I (left) and II (right). (a) Pseudospin state for all q values across the BZ plotted on the Bloch sphere. The raw measurements (open symbols) correspond to mixed states (i.e., they have magnitude < 1); the solid symbols correspond to the the nearest pure states (which lie on the surface of the Bloch sphere). For the eigenstates of configuration I the vectors trace the equator of the Bloch sphere, while for configuration II they are aligned along $\mathbf{e}_x$. (b) Pure-state expectation values of $\hat{\sigma}_x, \hat{\sigma}_y, \hat{\sigma}_z$ shown as a function of q, along with theory predictions from the SSH model (dashed curves). 118
6.9 Observations of tunneling oscillation in a static, balanced lattice configuration. (a) Magnetization associated with changing pseudospin state during tunneling. (b) Average velocity determined from momentum. (c) Displacement calculated by integrating velocity. Solid symbols represent experimental data while dashed curves correspond to numerical simulations. 121

7.1 Pseudospin state during a tunneling oscillation. (a) Full state reconstruction over the oscillation. Color shows $\langle\hat{\sigma}_z(q)\rangle$ while black arrows show $(\langle\hat{\sigma}_x(q)\rangle, \langle\hat{\sigma}_y(q)\rangle)$. Results for the configuration I Hamiltonian are shown on the left with the configuration II case shown on the right. (b) States represented as trajectories on the Bloch sphere for selected evolution times. Solid curves (left) and stars (right) correspond to theory generated from a fit to the fully dimerized SSH model in the appropriate configuration. (c) Corresponding Zak phase and winding numbers for configuration I (teal) and configuration II (magenta). Points correspond to data and solid curves correspond to theory. 126
7.2 Pseudospin state following a dimerization flip. (a) Full state reconstruction over the oscillation. Color shows $\langle\hat{\sigma}_z(q)\rangle$ while black arrows show $(\langle\hat{\sigma}_x(q)\rangle, \langle\hat{\sigma}_y(q)\rangle)$. (b) States represented as trajectories on the Bloch sphere for $t = 0.4T$. Solid curves correspond to theory generated from a fit to the fully dimerized SSH model in the appropriate configuration. (c) Corresponding Zak phase and winding numbers for configuration I (teal) and configuration II (magenta). Points correspond to data and solid curves correspond to theory. 129
7.3 Pseudospin state for tunneling starting from a $\hat{\sigma}_y$ eigenstate in a partially dimerized lattice. (a) Full state reconstruction over the oscillation. Color shows $\langle\hat{\sigma}_z(q)\rangle$ while black arrows show $(\langle\hat{\sigma}_x(q)\rangle, \langle\hat{\sigma}_y(q)\rangle)$. (b) States represented as a trajectory on the Bloch sphere for $t = 400\mu$s. The solid curve corresponds to theory generated from a fit to the SSH model. (c) Corresponding Zak phase over the evolution. Points correspond to data and the solid curve corresponds to theory. The time evolving Zak phase corresponds to dynamically broken SS. 134

8.1 Floquet band structure for switching protocol. (a) Idealized two band (SSH) model with complete dimerization. (b) Full numerical simulation of RF+Raman lattice. The full model matches the idealized version very well (up to an overall offset) except at $q = 0$, where slight deviations from perfect timing cause the spin momentum locked bands to hybridize. 141
8.2 Floquet pulsing experiment. The Hamiltonian is modulated by changing ϕ_{RF} by π every 20 μs (shown with gray boxes). To simplify the evolution, we sum the population in different k states, showing the internal state summed over k. The theory curves are a fit to ϕ_{RF} with $\Omega_+ = 12.7E_R, \Omega_- = 5.7E_R, \Omega_{\text{RF}} = 4.5E_R$, yielding $\phi_{\text{RF}} = -0.01\pi$. 144
8.3 Observation of linear drift velocity under tuned Floquet driving. (a) Lattice parameters during Floquet modulation. (b) Displacement and pseudospin evolution for $|q = 0, \uparrow\rangle$ and $|q = 0, \downarrow\rangle$ initial states. Gray boxes indicate times when the lattice is in SSH configuration I while white corresponds to configuration II. . . . 147
8.4 Observation of periodic motion under single-configuration Floquet driving. (a) Control timing. (b) Observed displacement and magnetization. Gray boxes are shown in analogy with the configuration switching protocol. (c) Calculated Floquet band structure for single-configuration protocol. 149

8.5 Observation of oscillatory motion under mistuned Floquet driving. (a) Oscillating magnetization. The oscillation, corresponding to motion between lattice sites, follows the natural tunneling period T_0 despite the mistimed configuration switching (gray boxes). (b) Oscillating displacement. The displacement oscillates with frequency related to the Floquet band gap. The dashed curves show fits to the displacement with and without a linear offset parameter. 150
8.6 Floquet band gap dependence on drive mistiming. (a) Floquet band structure for the parameters of Fig. 8.5. The quasienergy gap at $q = 0$ is indicated by a dashed line. Note that in this case the band gap crosses the edge of the Floquet BZ. (b) Floquet band gap for a range of mistiming values including theory and data. The highlighted point corresponds to the mistiming case from (a) and Fig. 8.5. 151
8.7 Pseudospin resolved micromotion and Berry curvature used to calculate the topological Floquet winding number. (a) State reconstruction (left: theory, right: filtered and normalized experimental data) for a single period of the ideal switching protocol for the $|\uparrow\rangle$ band. The color plot shows $\hat{\sigma}_z$ while the arrows show $\hat{\sigma}_x$ and $\hat{\sigma}_y$. (b) Berry curvature for three different cases: the switching protocol for the $|\uparrow\rangle$ and $|\downarrow\rangle$ bands, and the single-configuration protocol for a $|\uparrow\rangle$ initial state. . . . 154
8.8 Displacement at finite q over two Floquet periods. 157

A.1 In our design the AC voltage drive for our coils is provided by an H-bridge. During operation, current flows from the input power supply through one of the two 'high-side' switches, through the load, then through the complimentary 'low-side' switch to ground. 163
A.2 The output voltage waveform for our circuit (red) and the resulting load current in three regimes: inductively dominated load (small τ), restively dominated load (large τ), and intermediate. 167
A.3 (a) The magnitude of each component in the Fourier decomposition of the current waveform, normalized in the three cases of operation shown in Fig. A.2. The cases are an inductively dominated load, where the load current is approximately a triangle wave, a resistively dominated load, where the current is approximately a square wave, and an intermediate case where the load has significant resistance and inductance. (b) The amplitude of the fundamental Fourier component as a function of L with fixed $R = 1$ and as a function of R with fixed $L = 1/2\pi$ ($|Z_L| = 1$). 168
A.4 The schematic of our prototype design. In this iteration the power for the board (the digital buffers and gate drivers) is supplied by a separate input from the main coil power. Earlier prototypes had one set of power inputs, with board power provided by the main coil power supply, controlled by a linear regulator. 169
A.5 The prototype GaN FET based H-bridge PCB. The two forward facing banana connectors connect to DC supplies that power the board and the main coils, while the rear banana connectors connect the prototype to the coils. We also worked with smaller prototype boards powered by a single DC supply. 170

A.6 Performance at $f = 1.0$ MHz, $V_{\text{In}} = 15.0$ V, including a series resistance of 0.66 Ω with the coil load. (a) and (b) compare two measurements of the same magnetic field; (a) is based on inductive pickup, while (b) is based on measurements of the voltage drop across a sense resistor. 174
A.7 Performance with negligible load resistance and a single loop coil across a range of frequencies and input voltages. (a) Measured pickup coil voltage and average magnetic field from an inductive measurement at $f = 1.0$ MHz. The blue waveform is the integral of our measured pickup coil voltage, while the red and purple waveforms are Fourier decompositions including only a finite number of terms. (b) Carrier Fourier amplitudes at f = 1.0 MHz through 5.0 MHz at all tested input voltages. (c) Fourier amplitudes at f = 1.0 MHz and 5.0 MHz up to 100 MHz. The values shown are for an input voltage of 14V and reflect the qualitative shape of the Fourier components for lower input voltages. 176

B.1 Schematic of Keplerian telescope operating as a telescope (a) and microscope (b) along with ray labels (c). The telescope configuration corresponds to an object at infinite distance while the microscope corresponds to a finite object distance. In both cases the lenses have a $1/5$ focal length ratio giving a magnification of $m = -5$. 181
B.2 Point spread function and corresponding MTF for an ideal imaging system with NA=0.25. Dotted lines give the lengths and wavevectors associated with the Abbe resolution, the Rayleigh criterion, and the spatial cutoff frequency. 184
B.3 Fourier analysis of imaging or projection of a random pattern. (a) Coordinate space image after propagating through a system with $\text{NA} = 0.25$. (b) 2D Fourier space decomposition of image. (c) 1D cross-section of power spectral density. (d) Radial average of power spectral density. The resulting image/projection includes Fourier components up to $2k_{\text{NA}}$, but the dominant contribution comes from components below k_{NA}. 187
B.4 Prototype acting as a complete imaging system. 190
B.5 Prototype acting as an infinity corrected objective. 191
B.6 Measured PSF for imaging system prototype for design in Fig. B.4. Because of an additional optical relay the total magnification was $M = 22.5$. (a) 2D image. (b) Radially averaged image and fit to the ideal PSF, given by an Airy disk. (c) Cross sections of the 2D Fourier transform, corresponding to the MTF. The "x" marks the location of the cutoff frequency corresponding to the first 0 in the PSF. 192
B.7 Measured PSF for imaging system prototype for the infinity corrected design in Fig. B.5. Because of an additional optical relay the total magnification was $M = 96$. (a) 2D image. (b) Radially averaged image and fit to the ideal PSF, given by an Airy disk. (c) Cross sections of the 2D Fourier transform, corresponding to the MTF. The "x" marks the location of the cutoff frequency corresponding to the first 0 in the PSF. 193
B.8 Window thickness measurement geometry. 194

List of Abbreviations

RF	Radio frequency
RWA	Rotating Wave Approximation
OD	Optical Depth
ToF	Time of Flight
SG	Stern–Gerlach
GPE	Gross–Pitaevskii Equation
MOT	Magneto-Optical Trap
PGC	Polarization Gradient Cooling
ODT	Optical Dipole Trap
AOM	Acousto-optic Modulator
TTL	Transistor-Transistor Logic
AO	Analog Output
VCA	Voltage Controlled Attenuator
PD	Photodiode
DDS	Direct Digital Synthesis
DMD	Digital Micromirror Device
BZ	Brillouin Zone
SSH	Su–Schrieffer–Heeger
RM	Rice–Mele
TRS	Time-reversal Symmetry
PHS	Particle-hole Symmetry
SS	Sublattice Symmetry
QHE	Quantum Hall Effect
GaN	Gallium Nitride
FET	Field Effect Transistor
NMR	Nuclear Magnetic Resonance
TTL	Transistor-Transistor Logic
PCB	Printed Circuit Broad
NA	Numerical Aperture
PSF	Point Spread Function

Chapter 1: Introduction

Quantum simulation is a paradigm of experimental physics first proposed by Feynman [2], in which experimenters use an analog quantum system to study a quantum system of interest, taking advantage of quantum features of the analog system to simulate problems which are computationally difficult using classical computers. Quantum simulators make use of a wide variety of platforms based on disparate physical systems but generally take advantage of many-body quantum effects such as quantum entanglement [3].

Ideal quantum simulation platforms allow the experimenters to precisely control and measure the analog system. Ultracold atoms are a form of quantum-degenerate matter including Bose–Einstein condensates (BECs) and degenerate Fermi gasses, offering superb measurability along with the ability to engineer potentials using external fields. This makes them an excellent platform for quantum simulation of condensed matter systems, allowing the creation of "artificial solids" with desired properties in the lab [4].

Ultracold atom systems build on several major achievements of 20th century physics. Modern atomic physics developed along with quantum mechanics, providing key insights and test cases for the developing theory [5, 6]. Explaining the details of atomic structure and predicting the resulting spectra was a key triumph of the "first quantum revolution," in which physicists used the emerging quantum theory to better understand the natural world. The ability to precisely ma-

nipulate atomic states makes ultracold atoms an excellent platform for technologies engineered to take advantage of quantum mechanics: the "second quantum revolution" [7]. This precise manipulation is enabled by technical innovations including laser cooling [8], making possible the creation of atomic BECs, quantum-degenerate systems where a macroscopic fraction of the atoms occupy the same quantum state, in the lab [9–11].

The experiments presented here use ultracold atoms to study topology in condensed matter physics. Topology provides a paradigm to illuminate phenomena in condensed matter physics including the quantum Hall effect and topological insulators [12–14]. We take advantage of our ability to precisely prepare initial states and observe their evolution to study topology in the context of quantum dynamics, observing changing topology during out-of-equilibrium evolution, and topological dynamics of periodically modulated Floquet systems. Both of these experiments take place in quantum simulated one-dimensional lattice systems. In the first, we observe the changing topology of the time-evolving system, culminating with our observation of a state with higher-order topology in the out-of-equilibrium evolution. In the second, we engineer and characterize a Floquet system mimicking the behavior of massless particles described by the Dirac equation: linear, spin-momentum locked Floquet bands. This experiment culminates with our measurement of the underlying Floquet topological invariant characterizing the system.

1.1 Thesis Overview

This thesis covers three broad topic areas: the first is background, including topics from atomic physics that form the basis for our experimental techniques. The second area is technical details, including some details of our experimental apparatus, as well as how we use it to imple-

ment a tunable bipartite lattice system. The final category is scientific results, including our study of topological states of an out-of-equilibrium lattice system in Ch. 7, and a topological Floquet system with linear, spin-momentum locked (Dirac) dispersion in Ch. 8.

Ch. 2 introduces important tools from atomic physics, including the electronic structure of $^{87}\mathrm{Rb}$ as well as the light matter interactions we harness to produce BECs and manipulate them in quantum simulation experiments.

Ch. 3 introduces the basic theory of BEC as well as the laser and evaporative cooling techniques we apply to produce BEC in the lab. The chapter includes technical details of our experimental apparatus including a thorough review of the Raman system used throughout the experiments described in this thesis.

Ch. 4 describes the basic theory of lattice systems, providing simple models which can be used to understand the key physics of our experiments.

Ch. 5 establishes key ideas from topology in physics, including examples of nontrivial topology in static one and two-dimensional systems, defining the winding number, Zak phase, and Chern number. We also introduce topology for dynamical systems described by Floquet topological invariants (Floquet winding numbers).

Ch. 6 introduces the Raman-RF system used for the bipartite lattice experiments described in this thesis, including the pseudospin measurement techniques we employ to measure the topology of our system. We include a detailed theoretical model of the system at the single-particle level as well as basic experiments to characterize the lattice system in the lab.

Ch. 7 describes an experiment where we measure the topology of the quantum state of atoms in our bipartite lattice as they undergo out-of-equilibrium evolution. We categorize different initial states by symmetry, observing scenarios where topological invariants characterizing the

system can change during the evolution, including a case where the topological winding number takes on a value not possible in our static lattice system.

Ch. 8 describes an experiment in which we realize a Floquet system where the eigenstates are spin-momentum locked linear bands. We observe linear motion predicted for the system, characterize the topological origin of the behavior in terms of a measured Floquet topological invariant, and study how the motion changes with altered modulation.

The appendices describe technical details of an RF signal generator circuit in App. A, some practical aspects of imaging systems along with a description of prototype systems in App. B, and a reproduction of Ref. [15], a study of techniques to create solitonic excitations in our ultracold atom system in App. C.

Chapter 2: Atomic Physics Background

In this chapter we introduce key concepts and results from atomic physics that will be the foundation for understanding our experiments. This includes atomic structure, focusing on alkali atoms, which will provide the state space in which our experiments take place. We also introduce light-matter interactions, providing the key tools we use to manipulate atoms. We discuss the specific ways these concepts can be applied to create optical dipole force traps and drive Raman transitions between the internal states of our atoms. Finally, we introduce how we measure our ultracold atoms systems, using absorption imaging and time-of flight (ToF) techniques. Together, these elements form the toolbox for creating ultracold atoms systems and using them for the quantum simulation experiments we will discuss in later chapters.

2.1 Alkali Atoms

Alkali metals comprise the first column of the periodic table. This gives their neutral electron configuration a filled subshell plus a single valence electron, making their electronic state structure qualitatively similar to hydrogen. For single electron excited states, this means the orbital angular momentum operator $\hat{\mathbf{L}}$ and spin angular momentum operators $\hat{\mathbf{S}}$ simply correspond to the single valence electron, and the electronic state is described by four quantum numbers. The orbital electronic state is characterized by the principal quantum number n, or-

bital angular momentum quantum number l, and magnetic quantum number m_L corresponding to the quantization axis projection of the orbital angular momentum. For alkali atoms there is an additional magnetic quantum number m_S for the electronic spin ($s = 1/2$ owing to the single valence electron). The corresponding quantum numbers are $s = 1/2; m_S = \pm 1/2$ and $l = 0, 1, ...; m_L = 0, \{-1, 0, 1\}, ...$ depending on the orbital angular momentum state, which we denote *S, P, D, ...* using the historical spectroscopic notation [16]. The full spectroscopic notation includes the spin multiplicity $2S + 1$, which is always 2 for our atoms, so we omit it. At this coarse level of electronic structure the ground state of $^{87}\mathrm{Rb}$ is expressed as $5S$ and the first excited state as $5P$.

2.1.1 Fine structure

Fine structure describes lower energy scale features of atomic spectra, which arise due to relativistic effects, including the relativistic kinetic energy and the relative motion of the electrons and the nucleus. The relativistic treatment of the atomic Hamiltonian gives rise to a spin-orbit term, proportional to $\hat{\mathbf{L}} \cdot \hat{\mathbf{S}}$. This is called spin-orbit coupling because it is an interaction between the orbital angular momentum and the spin angular momentum. Diagonalizing the Hamiltonian including this term results in a new electronic angular momentum operator $\hat{\mathbf{J}} = \hat{\mathbf{L}} + \hat{\mathbf{S}}$, so that the eigenstates of the Hamiltonian are described by new quantum numbers j, m_J. Including fine structure, we describe the electronic state in terms of n, l and j denoted nL_j, for example $5S_{1/2}$ for the electronic ground state of $^{87}\mathrm{Rb}$.

The ground state of $^{87}\mathrm{Rb}$, $5S_{1/2}$ has $l = 0$, $j = 1/2$, so there is no fine structure splitting for the ground state. The first excited state has $l = 1$, giving possible values of $j = 1/2$ or

$j = 3/2$, so the fine structure splits the level into separate $5P_{1/2}$ and $5P_{3/2}$ levels. The resulting $5S_{1/2} \rightarrow 5P_{1/2}$ and $5S_{1/2} \rightarrow 5P_{3/2}$ transitions give rise to the D1 and D2 spectral lines. For $^{87}\mathrm{Rb}$ these have wavelengths of $\lambda_{D1} = 794.98\ \mathrm{nm}$[1] and $\lambda_{D2} = 780.24\ \mathrm{nm}$ ($f_{D1} = 377.11\ \mathrm{THz}$, $f_{D2} = 384.23\ \mathrm{THz}$) [1]. This can be expressed in terms of the fine structure splitting $\Delta E_{\mathrm{FS}} = h(f_{D2} - f_{D1})$, $7.12\ \mathrm{THz}$ for $^{87}\mathrm{Rb}$. The state structure at the level of fine structure is shown on the left of Fig. 2.1.

2.1.2 Hyperfine Structure

In addition to the spin-orbit coupling that gives rise to fine structure, the atomic Hamiltonian also includes coupling between the electronic and nuclear spins. For $^{87}\mathrm{Rb}$ we have a nuclear spin $\hat{\mathbf{I}}$ with $i = 3/2$. As before the $\hat{\mathbf{J}} \cdot \hat{\mathbf{I}}$ term can be diagonalized by defining the total angular momentum quantum number $\hat{\mathbf{F}} = \hat{\mathbf{J}} + \hat{\mathbf{I}}$, so that the good quantum number are f and m_F. For $^{87}\mathrm{Rb}$ in the electronic ground state with $j = 1/2$, we have two possible values: $f = 1, 2$. In the absence of external fields, these two state-manifolds are split by a frequency of $6.8347\ \mathrm{GHz}$ [1]. The state structure for $^{87}\mathrm{Rb}$ including hyperfine structure is shown on the right of Fig. 2.1.

2.1.3 External Magnetic Fields

In the presence of a static external magnetic field, all three components of the angular momentum interact with the field B_0 via their individual magnetic moments. The strengths of these interactions all depend on the different magnetic dipole moments associated with each type of angular momentum. It is convenient to write them all in proportion to the Bohr magneton μ_{B}

[1] We have arbitrarily limited number of significant digits for convenience; for the full values with uncertainties, see Ref. [1]

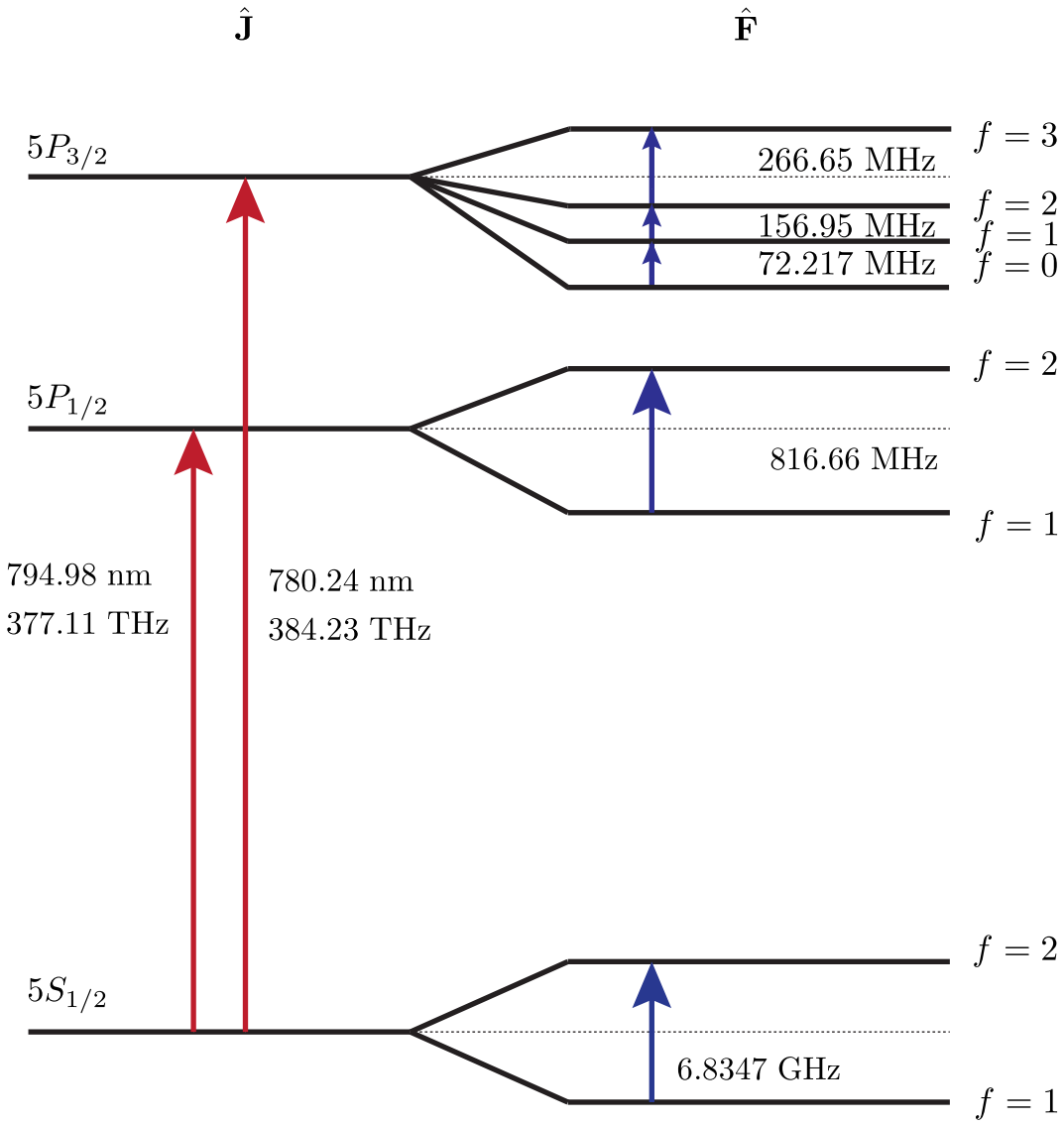

Figure 2.1: Energy level structure of ^{87}Rb. The levels on the left include the fine-structure splitting that gives rise to the D1 and D2 lines, while the right includes hyperfine structure. The energy levels given are in the absence of an external magnetic field. Values for frequency differences and corresponding light wavelengths are from Ref. [1].

with g-factors giving the proportionality. For the electronic spin and orbital angular momentum these are given by $g_S \approx 2$ and $g_L \approx 1$ respectively. The nuclear g_I depends on the details of the nuclear structure, so we rely on experiments rather than calculations. For $^{87}\mathrm{Rb}$ $g_I = -0.0009951$; owing to this small value, we can generally neglect terms including g_I in comparison to terms with g_S or g_L [1, 17].

Since the couplings that gave rise to fine and hyperfine structure are still present, diagonalizing the full Hamiltonian is non-trivial. Despite this, the physics can be understood in two limiting regimes, giving a simple approximate diagonalization of the Hamiltonian: small field, where the couplings between angular momentum components dominate, and large field, where the interactions with the external fields dominate. In the large field case, we consider all the individual dipoles to interact with the external fields and neglect the coupling terms, making $s, m_S; l, m_S;$ and i, m_I good quantum numbers. In the small field case the couplings dominate, so f, m_F are good quantum numbers, so we calculate a Landé g-factor to describe the interaction between the total angular momentum and the external field.

$$g_J \approx 1 + \frac{j(j+1) + s(s+1) - l(l+1)}{2j(j+1)} \tag{2.1}$$

$$g_F = g_J \frac{f(f+1) + j(j+1) - i(i+1)}{2f(f+1)} + g_I \frac{f(f+1) + i(i+1) - j(j+1)}{2f(f+1)}$$

$$g_F \approx \frac{f(f+1) + j(j+1) - i(i+1)}{2f(f+1)} \tag{2.2}$$

For the specific case of alkali atoms with $s = 1/2$, we have the luxury of an analytical

solution for the Hamiltonian eigenvalues at all field strengths: the Breit–Rabi Formula [18, 19].

$$E = \frac{\Delta E_{\mathrm{HFS}}}{2(2I+1)} + g_I \mu_{\mathrm{B}} (m_I \pm m_J) B \pm \frac{\Delta E_{\mathrm{HFS}}}{2} \sqrt{1 + \frac{4(m_I \pm m_J)x}{2I+1} + x^2}; \tag{2.3}$$

$$x = \frac{\mu_{\mathrm{B}} B (g_I - g_J)}{\Delta E_{\mathrm{HFS}}} \tag{2.4}$$

For $^{87}\mathrm{Rb}$ $(m_I \pm m_J)$ takes on the possible values $-2, -1, 0, 1, 2$. The magnetic energy levels for $^{87}\mathrm{Rb}$ are shown in Fig 2.2, including the low-field regime where f, m_F are good quantum numbers and the high-field regime where j, m_J are good quantum numbers. We will primarily work in the low field regime, using states described by f, m_F as our state space.

In the low field regime the energy shift goes as $g_F m_F B$. Although states with $m_F = 0$ do not experience an energy shift proportional to B near $B = 0$, they do experience a quadratic shift (the "clock shift," which is named due to $m_F = 0$ states being of particular use in atomic clocks) [19].

$$e_q = \frac{(g_i - g_j)^2 \mu_{\mathrm{B}}}{2\hbar \Delta E_{\mathrm{HFS}}} B^2 \tag{2.5}$$

This means that the m_F states do not form a perfect ladder system with even energy spacing. Despite this, for the experiments described in this thesis, we worked with $\Delta E = 1\mathrm{MHz}$, corresponding to $e_{\mathrm{q}}/\hbar \approx 150\mathrm{Hz}$, which is negligible for most purposes.

The interaction energy $-\hat{\mu} \cdot \mathbf{B}$ can be used to create external potentials for atoms. This allows for magnetic trapping of atoms in the local minimum of a magnetic field gradient, for atoms in low-field seeking states. For $^{87}\mathrm{Rb}$ in the low-field regime, the trappable states are $|f = 1, m_F = -1\rangle$ and $|f = 2, m_F = \{1, 2\}\rangle$. In regions where the magnetic field goes to 0 it is possible for atoms to transition to non-trappable states, leading to "Majorana" spin-flip

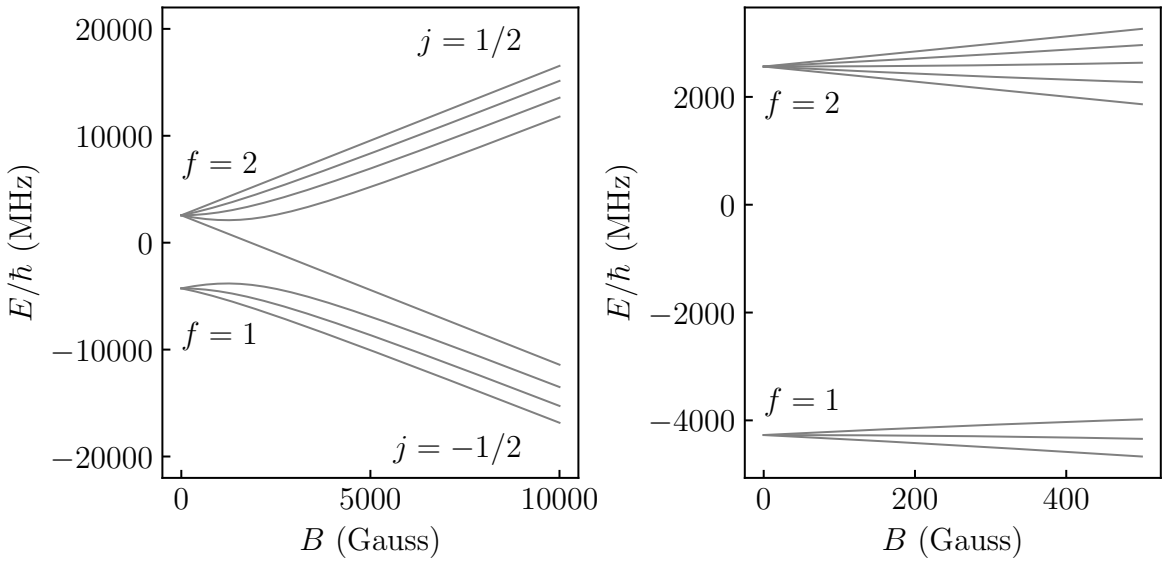

Figure 2.2: Magnetic sublevels of the electronic ground state of $^{87}\mathrm{Rb}$. The left panel shows the crossover between the low field and high field regimes, while the right shows the details of the low field regime.

losses [20].

2.2 Light Matter Interaction

In this section we introduce a model for the interaction of an atom with the electromagnetic field, such as that generated by a (monochromatic) laser or a radiofrequency (RF) antenna with frequency ω. It will be sufficient to consider the external field classically for our purposes. This will provide important tools for coherently manipulating the internal states of our atoms, as well as creating light-dependent forces that allow for cooling and trapping.

2.2.1 Near-Resonant Excitation and Rabi Flopping

First we consider the effect of the atom-light coupling when ω is near resonance. We use a two-level atom as an approximate model. The formalism is applicable to electric dipole transitions between different electronic states or magnetic dipole transition between hyperfine states, although for our experiments the excited state lifetime is too short to observe Rabi flopping between ground and excited electronic states. In both cases we will consider a monochromatic field with time dependence given by $\cos(\omega t)$, neglecting any variation of the field over the atomic length scale (this is justified as long as $\lambda \gg r_{\mathrm{atom}}$). The bare Hamiltonian is

$$\hat{H} = \hbar\omega_0 \left|e\right\rangle\!\left\langle e\right| - \hat{H}_{\mathrm{int}}. \tag{2.6}$$

For our two-level approximation, we write $\hat{H}_{\mathrm{int}}$ is terms of the matrix elements of the electric dipole moment operator $\hat{\mathbf{d}}$ for electric dipole transitions or $\hat{\mu}$ for magnetic dipole transitions: $\mathbf{d}_{eg} = \langle e| \hat{\mathbf{d}} |g\rangle$, and $\mathbf{d}_{eg} = \langle g| \hat{\mathbf{d}} |e\rangle = \mathbf{d}_{eg}^{*}$ and likewise for $\hat{\mu}_{eg}$. It is convenient to write these in terms of the quantity Ω. For the electric dipole case we have

$$\hbar\Omega = \mathbf{d}_{eg} \cdot \hat{\epsilon} E_0(\mathbf{r}). \tag{2.7}$$

And for the magnetic dipole case we have

$$\hbar\Omega = \hat{\mu}_{eg} \cdot \hat{\beta} B_0(\mathbf{r}). \tag{2.8}$$

This gives an interaction Hamiltonian

$$\hat{H}_{\text{int}} = -\hbar(\Omega \left|e\right\rangle\!\left\langle g\right| \cos(\omega t) + \Omega^* \left|g\right\rangle\!\left\langle e\right| \cos(\omega t)). \tag{2.9}$$

We transform into a rotating frame at ω by applying $\hat{U} = \left|g\right\rangle\!\left\langle g\right| + \left|e\right\rangle\!\left\langle e\right| e^{i\omega t}$ via $H_{\text{int}} \rightarrow \hat{U} H_{\text{int}} \hat{U}^\dagger$. In the rotating frame, the Hamiltonian is

$$\begin{aligned} \hat{H}_{\text{int}} &= -\hbar(\Omega \left|e\right\rangle\!\left\langle g\right| e^{-i\omega t} \cos(\omega t) + \Omega^* \left|g\right\rangle\!\left\langle e\right| e^{i\omega t} \cos(\omega t)) && (2.10) \\ &= -\hbar/2 \left(\Omega \left|e\right\rangle\!\left\langle g\right| (1 + e^{-i2\omega t}) + \Omega^* \left|g\right\rangle\!\left\langle e\right| (1 + e^{i2\omega t})\right) && (2.11) \end{aligned}$$

The rotating frame transformation also changes the bare Hamiltonian to

$$\hbar(\omega - \omega_0) \left|e\right\rangle\!\left\langle e\right|. \tag{2.12}$$

Following this we can neglect "fast rotating" terms with frequency $\omega + \omega_0$ by taking the rotating wave approximation (RWA). This can be thought of as ignoring time dependence on the scale defined by ω, which is femtosecond scale for light oscillations and microsecond scale for RF. We define $\delta = \omega - \omega_0$ to write the RWA version of the full Hamiltonian in simplified form

$$\hat{H} = \hbar \left(-\delta \left|e\right\rangle\!\left\langle e\right| + \frac{\Omega}{2} \big(\left|e\right\rangle\!\left\langle g\right| + \left|g\right\rangle\!\left\langle e\right| \big) \right), \tag{2.13}$$

assuming $\Omega = \Omega^*$. Time evolution under Eq. 2.13 $\hat{U}_{\text{Rabi}}(t) = e^{-i\hat{H}t/\hbar}$ generates Rabi oscillations [21]. Fig. 2.3 shows the sinusoidal populations in the $|g\rangle$ and $|e\rangle$ states over this time evolution starting from $|g\rangle$ for different values of δ. For $\delta = 0$ the population oscillates with full

contrast with angular frequency Ω, which is called the Rabi frequency. For finite δ, the contrast decreases and the oscillation frequency increases, to the generalized Rabi frequency

$$\tilde{\Omega} = \sqrt{\Omega^2 + \delta^2}. \tag{2.14}$$

In addition to considering the effects of the pulsed Rabi Hamiltonian (Rabi flopping) we can gain understanding from the eigenstates of the Rabi Hamiltonian. The eigenvalues of Eq. 2.13 are shown in Fig. 2.3 (c) for $\Omega = 1$ as a function of δ, showing an avoided crossing at $\delta = 0$. The energy shift, negative for $\delta < 0$ (red detuning) and positive for $\delta > 0$ (blue detuning), shows the basic physics of light shifts, which we will discuss in detail in Sec. 2.3. For high δ the eigenstates are essentially bare states with shifted energy due to the coupling.

2.2.2 Magnetic Transitions

One common application for Rabi oscillations in our experiments is driving transition between the hyperfine sublevels of the $^{87}\mathrm{Rb}$ electronic ground state, either between hyperfine manifolds ($f = 1 \leftrightarrow f = 2$), or between sublevels within a hyperfine manifold. The magnetic dipole moment can be determined from the angular momentum, the Landé g-factor (Eq. 2.2), and the Bohr magneton, determining the Rabi frequency via Eq. 2.8. We will be working in the low-field limit introduced in Sec. 2.1.3, so f will be a good quantum number and $\hat{\mathbf{F}}$ will be the relevant angular momentum operator.

When driving transitions between sublevels of a hyperfine manifold, there are often more than two relevant states to consider. In these cases the field may drive transitions between more than two states, such as the three states of the $f = 1$ hyperfine manifold of $^{87}\mathrm{Rb}$. The three state

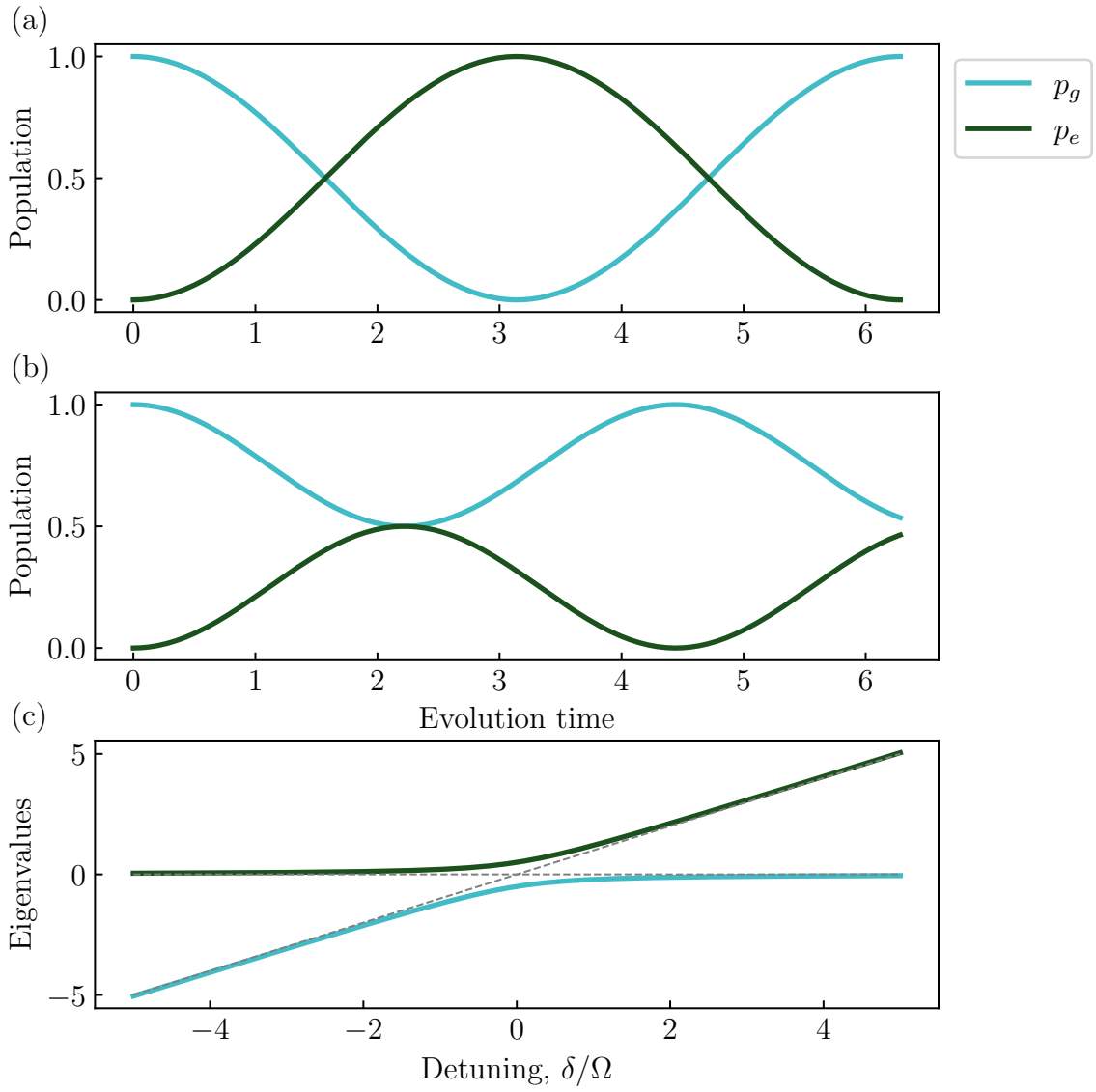

Figure 2.3: Rabi Oscillation starting from $|\psi(0)\rangle = |g\rangle$. (a) Resonant oscillation with $\Omega = 1$, $\delta = 0$ giving $\tilde{\Omega} = \Omega$. (b) Off-resonant oscillation with $\Omega = \delta = 1$ giving $\tilde{\Omega} = \sqrt{2}\Omega$. (c) Eigenvalues of the Rabi Hamiltonian for $\Omega = 1$ with variable δ. At high δ the difference between the coupled eigenenergy (solid curves) and the bare energy (bashed lines) can be understood as light shifts.

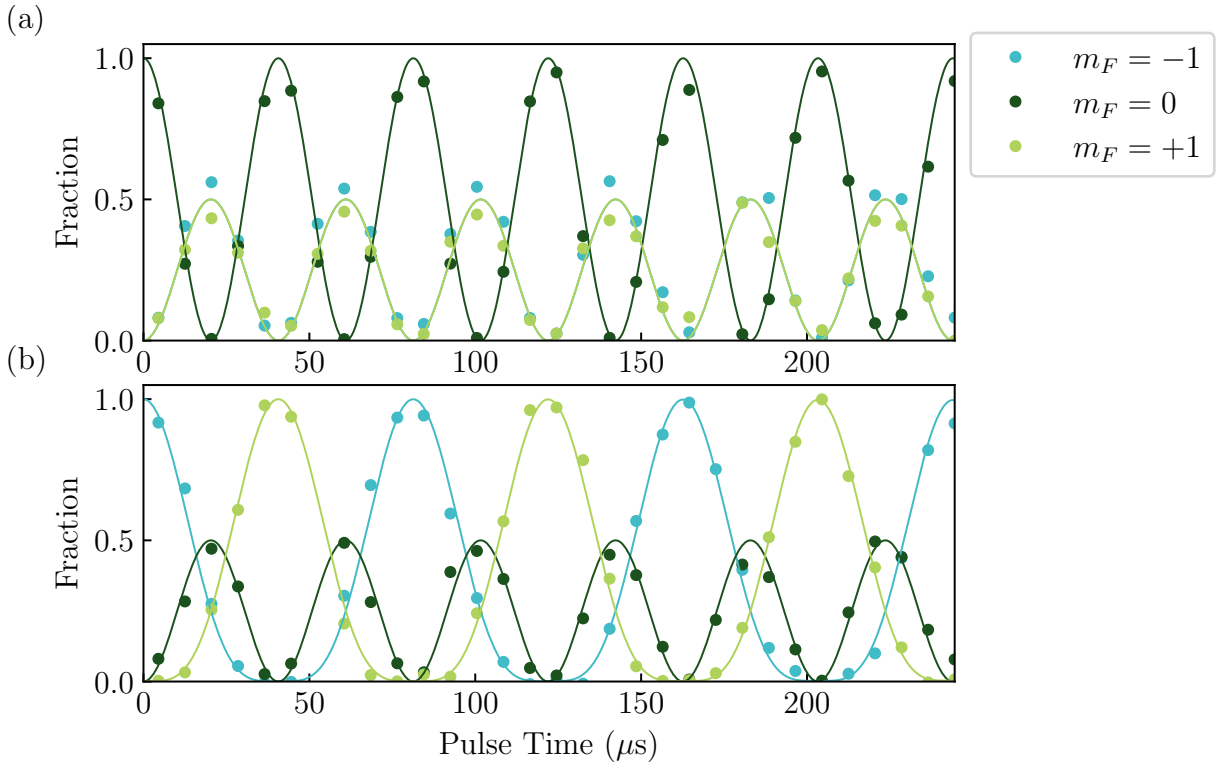

Figure 2.4: Evolution during a resonant RF pulse. (a) Initial state $|m_F = 0\rangle$. (b) Initial state $|m_F = -1\rangle$.

Rabi Hamiltonian is analogous to Eq. 2.13, including terms proportional to Ω between each rung of the ladder (terms coupling states separated by $2\omega_0$ are neglected after taking the RWA). As we introduced in Sec. 2.1.3, our hyperfine sublevels are not a perfect ladder because of the presence of the quadratic Zeeman shift, which enters as a diagonal term $e_q |m_F = 0\rangle\langle m_F = 0|$.

Fig. 2.4 shows experimental data for RF Rabi driving for two different initial states: $|m_F = 0\rangle$ and $|m_F = -1\rangle$, with $\omega_{\mathrm{RF}}/2\pi = 1\mathrm{MHz}$ and $\delta \approx 0$. At the selected Zeeman energy, the quadratic Zeeman shift can be safely neglected for strong driving.

2.3 Light Shifts

In addition to driving transitions between states, external light fields can shift the energy levels of the internal atomic states. In this section we will focus on the effects of the interaction with the electric field of the light wave, since the interaction with the magnetic component will be much weaker. As before, we consider a monochromatic external field.

$$\begin{aligned}\mathbf{E}(t) &= \mathbf{E}_0(\mathbf{r})\cos(\omega t) \\ &= \mathbf{E}^+(\mathbf{r})e^{-i\omega t} + \mathbf{E}^-(\mathbf{r})e^{i\omega t} \\ &= \hat{\epsilon}E^+(\mathbf{r})e^{-i\omega t} + \hat{\epsilon}E^-(\mathbf{r})e^{i\omega t}\end{aligned} \tag{2.15}$$

$\mathbf{E}_0(\mathbf{r})$ is a spatial envelope function and $\hat{\epsilon}$ accounts for the polarization. It is useful to define a basis for the polarization based on the quantization axis for the atoms $\mathbf{e}_z$ in terms of σ^+ (right-circularly polarized), σ^- (left-circularly polarized), and π (linearly polarized along $\mathbf{e}_z$) states. As a guide, we can think of the response of a classical oscillator coupled to the electric field with polarization (electric dipole moment per unit volume)

$$\mathbf{p}(t) = \alpha\mathbf{E}(t). \tag{2.16}$$

The interaction energy in this model is proportional to $\mathbf{p}(t)\cdot\mathbf{E}(t)$, corresponding to the electric dipole moment interacting with the external field. The polarizability α will have real and imaginary parts corresponding to oscillations in phase and out of phase with the external field; these oscillations give rise to (conservative) dipole forces and (dissipative) scattering forces [22].

As we develop a model for the interaction between our quantum mechanical atoms and the external field, we will determine the quantum model for α and corresponding dipole and scattering forces. We begin by considering the Hamiltonian describing interactions between an atom and the external field. The dominant term in the multipole expansion for the light-matter interaction is the electric dipole term.

$$\hat{H}_{\mathrm{d}} = \hat{\mathbf{d}} \cdot \mathbf{E}(t); \tag{2.17}$$

$$\hat{\mathbf{d}} = -e \sum_{n} \mathbf{r}_n, \tag{2.18}$$

where n sum over the electrons of the atom and $-e\mathbf{r}_n$ is the electric dipole moment operator for the n^{th} electron, with e being the fundamental charge.

Next we consider how interaction with off-resonant light effects the energy levels of an atom. Using second order perturbation theory in $\hat{H}_{\mathrm{d}}$, we can write the energy shift of the ground state. The interaction energy is the dipole interaction from Eq. 2.17 and can be expressed in terms of the atomic polarizability, quantifying the atomic response to the external field.

We first consider a two-level atom with excited state $|e\rangle$ and ground state $|g\rangle$. In this case the energy level of the $|e\rangle$ state is shifted by [19]

$$\Delta E_g = -\frac{2\omega_{eg} |\langle g| \mathbf{E}(\mathbf{r})^{+} \cdot \hat{\mathbf{d}} |e\rangle|^2}{\hbar(\omega_0^2 - \omega^2)}. \tag{2.19}$$

This provides a simple model to understand the scalar light shift from far detuned laser beams. When $\omega < \omega_0$ (lower than resonant frequency or red detuned) the energy shift is negative. As a result atoms are attracted to regions of high laser intensity. By contrast, for $\omega > \omega_0$ (higher than

resonant frequency or blue detuned) the shift is positive, leading to repulsive forces in regions of high intensity. This ground state scalar light shift forms the basis for red detuned dipole trapping (Sec. 2.3.2).

The form of Eq. 2.19 motivates us to define the dynamic (AC) polarizability

$$\alpha(\omega) = -\frac{\omega_0 |\langle g| \hat{\epsilon} \cdot \hat{\mathbf{d}} |k\rangle|^2}{\hbar(\omega_0^2 - \omega^2)} \tag{2.20}$$

defined so that

$$\Delta E_g = -\alpha(\omega)|\mathbf{E}|^2. \tag{2.21}$$

To describe light shifts in multilevel atoms, we use a sum to include terms from all the atomic states. We will also need to account for the different angular momentum states of our system. To capture the interaction between different polarizations and angular momentum states, we introduce a frequency-dependent polarizability tensor [19, 23] for state $|i\rangle$,

$$\alpha_{\mu\nu}(i;\omega) = \sum_j \frac{2\omega_{ij} \langle i| d_\mu |j\rangle \langle j| d_\nu |i\rangle}{\hbar(\omega_{ij}^2 - \omega^2)}, \tag{2.22}$$

where j sums over the excited states. $\alpha_{\mu\nu}(i;\omega)$ is defined so that

$$\Delta E_i(\omega) = -\alpha_{\mu\nu}(i;\omega) E_\mu^+ E_\nu^-, \tag{2.23}$$

where the repeated indices μ, ν are summed over.

When we write an expression for $\alpha_{\mu\nu}$ it is helpful to decompose it into different parts, depending on how they transform under rotation. This leads to scalar, vector, and tensor contri-

butions to the polarizability.

$$\alpha^{(0)} = \alpha_{\nu\nu} \tag{2.24}$$

$$\alpha^{(1)}_{\eta} = \epsilon_{\eta\mu\nu}(\alpha_{\mu\nu} - \alpha_{\nu\mu}) \tag{2.25}$$

$$\alpha^{(2)}_{\mu\nu} = \alpha_{\mu\nu} - \frac{1}{3}\alpha_{\eta\eta}\delta_{\eta,\eta}, \tag{2.26}$$

where $\epsilon_{\eta\mu\nu}$ is the rank-3 antisymmetric tensor (Levi–Civita symbol), $\delta_{\eta,\eta}$ is the Kronecker delta, and summation over repeated indices is implied.

We are interested in the polarizability of atomic hyperfine states in the linear Zeeman regime, where f, m_F are good quantum numbers, so we will specify by exchanging $i \to f, m_F$ and $j \to f', m'_F$. In this case, after converting to spherical tensors, only one independent component remains for the scalar, vector and tensor polarizabilities, $\alpha^{(0)}, \alpha^{(1)}, \alpha^{(2)}$. See Ref. [19] for a full derivation. The interaction Hamiltonian can be written in terms of these components and the angular momentum operator $\mathbf{F}$.

$$\hat{H}_d = -\alpha^{(0)}|E^+|^2 - \alpha^{(1)} i(E^+ \times E^-) \cdot \mathbf{F} - \alpha^{(2)}(...). \tag{2.27}$$

Our experiments work in a regime where only the first two contributions are important, so we will neglect terms including $\alpha^{(2)}$.

2.3.1 Scattering

Our treatment of Rabi oscillation neglected spontaneous emission from the excited state. In many cases, when the lifetime τ of the excited state is shorter than or comparable to the Rabi

frequency, spontaneous emission cannot be neglected. Instead, an atomic ensemble will come to a steady state, where the rate of excitation from the external field equals the rate of spontaneous emission, or scattering. The scattering rate depends on the decay rate $\Gamma = 1/\tau$, detuning from resonance δ, and saturation intensity I_{sat} [24]

$$\Gamma_{\text{sc}} = \frac{I}{I_{\text{sat}}} \frac{\Gamma/2}{1 + I/I_{\text{sat}} + 4(\delta/\Gamma)^2}. \tag{2.28}$$

The saturation intensity

$$I_{\text{sat}} = \frac{2\pi^2 \Gamma \hbar c}{3\lambda^3}, \tag{2.29}$$

quantifies when saturation effects become significant. Note that these expressions do not account for a Doppler shift between the atom and the excitation light.

2.3.2 Optical Dipole Force Traps

A key consequence of the scalar polarizability and resulting dipole force is the ability to create attractive potentials with red detuned light and repulsive potentials with blue detuned light. The scalar polarizability for state i is

$$\alpha^{(0)} = \sum_j \frac{2\omega_{ij} |\langle i| \mathbf{d} \cdot \hat{\epsilon} |\mathbf{j}\rangle|^{\mathbf{2}}}{\hbar(\omega_{ij}^2 - \omega^2)}. \tag{2.30}$$

The polarizability can be neatly expressed in terms of the Fermi golden rule [25] transition rate [22]

$$\Gamma_{ij} = \frac{\omega_{ij}^3}{3\pi\epsilon_0 \hbar c^3} |\langle i| |\mathbf{d} \cdot \hat{\epsilon}| |j\rangle|^2. \tag{2.31}$$

For a two-level atom with only $i = g, j = e$ we simplify the notation $\omega_{ij} \to \omega_0, \Gamma_{ij} \to \Gamma$. The scalar polarizability results in a dipole potential expressed [22]

$$U(\mathbf{r}) = \frac{3\pi c^2}{2\omega_0^2}\left(\frac{\Gamma}{\omega_0 - \omega} + \frac{\Gamma}{\omega_0 + \omega}\right) I(\mathbf{r}), \tag{2.32}$$

in terms of the intensity $I = 2\epsilon_0 c|E|^2$. The off-resonant scattering rate for this scenario is

$$\Gamma_{\text{sc}} = \frac{3\pi c^2}{2\hbar\omega_0^2}\left(\frac{\omega}{\omega_0}\right)^3\left(\frac{\Gamma}{\omega - \omega_0} + \frac{\Gamma}{\omega + \omega_0}\right)^2 I(\mathbf{r}). \tag{2.33}$$

In the RWA where the detuning $\delta = \omega - \omega_0$ is relatively small, $|\delta| \ll \omega_0$, we can neglect the counter-rotating $(\omega + \omega_0)$ terms, giving

$$U(\mathbf{r}) = \frac{3\pi c^2}{2\omega_0^2}\frac{-\Gamma}{\delta} I(\mathbf{r}), \tag{2.34}$$

and

$$\Gamma_{\text{sc}} = \frac{3\pi c^2}{2\hbar\omega_0^2}\left(\frac{\Gamma}{\delta}\right)^2 I(\mathbf{r}). \tag{2.35}$$

This potential forms the basis for optical dipole trapping, in which a spatial intensity pattern, typically a tightly focused Gaussian laser beam or a pair of crossed beams creates a region of high intensity, resulting in a locally harmonic trap. Our implementation of optical dipole trapping is discussed in Sec. 3.3.1.

In general the two-level atom approximation and RWA should be thought of at approximately the same level; this is because when the counter rotating term cannot be neglected, the contribution from other excited states is generally also non-negligible [19]. Note that the ra-

tio of potential depth to off-resonant scattering is $\hbar\delta/\Gamma$, meaning that we can reduce unwanted scattering by increasing the detuning, with the resulting loss in potential depth compensated by increasing the intensity.

A more rigorous treatment must take into account the multi-level internal state structure of real atoms. For alkali atoms such as $^{87}\mathrm{Rb}$ this means including separate contributions from the D1 and D2 lines as well as the particular hyperfine ground state [22] (as before we consider the linear Zeeman regime where f, m_F are good quantum numbers).

$$U(\mathbf{r}) = \frac{\pi c^2 \Gamma}{2\omega_0^2}\left(\frac{2 + P g_F m_F}{\delta D2} + \frac{1 - P g_F m_F}{\delta D1}\right) I(\mathbf{r}), \tag{2.36}$$

where $P = 0, \pm 1$ for light with $\pi, \sigma^{\pm}$ polarization. For far detuned light such that $\delta \gg \Delta E_{\mathrm{FS}}$, it makes sense to define the average detuning δ defined relative to the center of the D-line doublet. In this case we can approximate the potential as

$$U(\mathbf{r}) = \frac{\pi c^2 \Gamma}{2\omega_0^2 \delta}\left(1 + \frac{1 P g_F m_F \Delta E_{\mathrm{FS}}}{\delta}\right) I(\mathbf{r}). \tag{2.37}$$

As we introduced in Sec. 2.1.1 ΔE_{FS} is the $5P$ fine structure splitting. This shows the diminishing role of fine structure as we detune further from resonance. For example, our optical dipole trap operates at 1064 nm so that the two-level approximation is highly accurate and fine structure can be neglected. For closer detuned potentials, such as the phase imprinting potentials we used for the experiment described in App. C with 777.6 nm ($\omega/2\pi = 685.5\mathrm{THz}$), the dominant contribution comes from the 0^{th} order term with a correction due to the internal structure. For light with frequency very close to the D1 and D2 transitions, the approximation is not valid.

2.4 Raman Coupling

The vector polarizability allows light to create state dependent potentials and drive Raman transitions between different internal states. In a Raman transition there are two or more light fields with frequency components ω_+ and ω_-, which a drive transition between different internal states accompanied by a change in momentum. This can be thought of as a two-photon transition via a virtual excited state.

We will focus on the vector light shift for the state structure of alkali atoms in the linear Zeeman regime. Recall that the vector polarizability part of Eq. 2.27 was a term of the form $\mathbf{E} \times \mathbf{E} \cdot \hat{\mathbf{F}}$. Because of this, the vector light shift part of the Hamiltonian can be expressed in terms of an effective magnetic field $\mathbf{\Omega}$.

$$\hat{H}_{\mathrm{v}} = \frac{\mu_{\mathrm{B}} g_F}{\hbar} (\mathbf{\Omega} \cdot \hat{\mathbf{F}}) \tag{2.38}$$

The effective field is proportional to the vector polarizability [23],

$$\alpha^{(1)} = \frac{2\alpha^{(0)} \Delta E_{\mathrm{FS}}}{3\delta}. \tag{2.39}$$

For a combination of laser fields $E_{\omega+}$ and $E_{\omega-}$ with frequency components ω_+ and ω_-

differing by $\omega_{\mathrm{RF}} = \omega_{\mathrm{Z}} + \delta_{\mathrm{RF}}$, the effective magnetic field takes the form [23]

$$\begin{aligned}\mathbf{\Omega} = \frac{\alpha^{(1)} g_f}{\hbar g_j}[&- \mathrm{Im}[(\mathbf{E}^*_{\omega-} \times \mathbf{E}_{\omega+}) \cdot (\mathbf{e}_x - i\mathbf{e}_y)], \\ &- \mathrm{Re}[(\mathbf{E}^*_{\omega-} \times \mathbf{E}_{\omega+}) \cdot (\mathbf{e}_x - i\mathbf{e}_y)], \\ &\delta_{\mathrm{RF}} \frac{\hbar g_j}{\alpha^{(1)} g_f} + i(\mathbf{E}^*_{\omega-} \times \mathbf{E}_{\omega-} + \mathbf{E}^*_{\omega+} \times \mathbf{E}_{\omega+}) \cdot \mathbf{e}_z].\end{aligned} \tag{2.40}$$

The $\Omega_\pm = 1/2(\Omega_x \pm \Omega_y)$ components drive transitions between different m_F sublevels, while the Ω_z component acts as an effective bias field. Note that δ_{RF}, which defines resonance for coupling the m_F internal states, should not be confused with the single photon detuning, δ which is often large when driving Raman transitions.

For the specific case of two equal intensity beams counter propagating along $\mathbf{e}_x$, with the ω_- beam linearly polarized along $\mathbf{e}_y$ and the ω_+ beam linearly polarized along $\mathbf{e}_z$, we have $\mathbf{E}_{\omega-} = Ee^{ik_R x}\mathbf{e}_y$ and $\mathbf{E}_{\omega+} = Ee^{-ik_R x}\mathbf{e}_z$. The configuration results in a spatially rotating effective Zeeman field

$$\mathbf{\Omega} = [\Omega_{\mathrm{R}} \sin(2k_R x), \Omega_{\mathrm{R}} - \cos(2k_R x), \delta_{\mathrm{RF}}], \tag{2.41}$$

The Raman Rabi frequency $\Omega_{\mathrm{R}} = E^2 \alpha^{(1)} g_f / g_j \hbar$ corresponds to the proportionality in Eq. 2.40. If we are free to define the origin for x we can effectively change the phase of the $\sin$ and $\cos$ terms in the position dependent magnetic field.

Fig. 2.5 shows the time evolution under the influence of a Raman Hamiltonian of this type starting from $|k = 0, m_F = 0\rangle$. Configurations other than counterpropagating beams are equally possible, with the recoil direction defined by the intersection angle θ between the beams and the length and energy scales changing as $\cos(\pi - \theta)/2$ [23].

More complicated arrangements of fields can yield additional structure. For example if

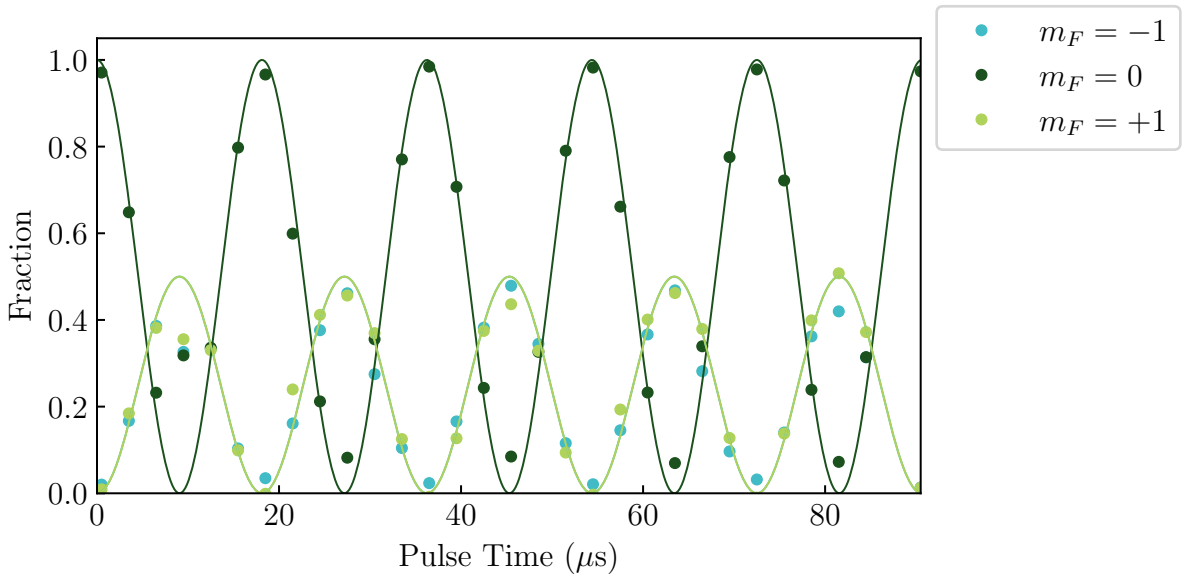

Figure 2.5: Raman pulsing starting from the $|k = 0, m_F = 0\rangle$ initial state. In this case the $m_F = \pm 1$ states have $k = \pm 2k_R$. Solid lines are theory curves for $\Omega = 10.6E_R$.

each beam carries both frequency tones ω_-, ω_+, the field components are $\mathbf{E}_{\omega-} = E_A e^{ik_R x}\mathbf{e}_y + E_B e^{-ik_R x}\mathbf{e}_z$ and $\mathbf{E}_{\omega+} = E_A e^{-ik_R x}\mathbf{e}_y + E_B e^{ik_R x}\mathbf{e}_z$. For this arrangement Eq. 2.40 yields

$$\mathbf{\Omega} = [(\Omega_\mathrm{A} + \Omega_\mathrm{B})\sin(2k_R x), (\Omega_\mathrm{A} - \Omega_\mathrm{B})\cos(2k_R x), \delta_\mathrm{RF}], \tag{2.42}$$

where the Raman Rabi frequencies are defined for individual field pairs: $\Omega_{A,B} = E_{A,B}^2 \alpha^{(1)} g_f / g_j \hbar$. The addition of a magnetic field oscillating at ω_RF adds a position independent component to the effective field: $\Omega_\mathrm{RF}\cos(\phi_\mathrm{RF})\mathbf{e}_x - \Omega_\mathrm{RF}\sin(\phi_\mathrm{RF})\mathbf{e}_y$, where ϕ_RF is the relative phase between the RF and Raman fields. This arrangement forms the basis for the lattice system we will introduce in Ch. 6.

2.5 Measurements

One of the key advantages of ultracold atoms as a platform for studying diverse physics is their high degree of measurability. This includes absorption imaging, quantifying light removed from a probe beam by resonant absorption by the atoms; phase contrast imaging, quantifying the phase shift acquired by the beam through dispersive interaction with the atoms; and fluorescence imaging, quantifying light re-emitted by the atoms after resonant absorption. We focus on absorption imaging, which allows us to image the column density of an atomic cloud either in-situ, or after a time-of-flight (ToF) expansion.

2.5.1 Absorption Imaging

We can quantify absorption and dispersion with a density-dependent complex index of refraction. In the two-level approximation this gives [26]

$$n = 1 + \frac{\sigma_0 \rho \lambda}{4\pi} \left(\frac{i}{1 + (2\delta/\Gamma)^2 I/I_{\text{sat}}} - \frac{\delta}{1 + (2\delta/\Gamma)^2 I/I_{\text{sat}}} \right), \tag{2.43}$$

with resonant cross section $\sigma_0 = 6\pi\bar{\lambda}^2$, atomic density ρ, detuning $\delta = \omega - \omega_0$ and saturation intensity I_{sat} (defined in Eq. 2.29). For simplicity we factor out the density dependence, defining $n_0 - 1 = (n-1)/\rho$.

As light passes through the 3D atomic density distribution, it will be attenuated by the imaginary part of n. This leads to an optical depth related to the atomic column density.

$$\frac{d}{dz} I(x,y,z) = -\text{Im}[n(x,y,z)] I(x,y,z) \tag{2.44}$$

Integrating along z from the initial condition of $I(x, y, 0)$ yields the solution

$$I(x, y, z) = I(x, y, 0)e^{-\tilde{\rho}(x,y,z)\mathrm{Im}[n_0]}, \tag{2.45}$$

where $\tilde{\rho}(x, y, z) = \int_0^{z'} \rho(x, y, z')$ is the integrated atomic column density up to z.

The optical depth of the medium is the quantity $\tilde{\rho}(x, y, z)\mathrm{Im}[n_0] = \mathrm{OD(x, y)}$ for $z \to \infty$ (i.e. after the beam has passed through the region containing atoms). We can extract the OD by comparing an image of the probe beam attenuated by atoms to a bare image of the probe beam.

$$\frac{I_\mathrm{a}(x, y)}{I_\mathrm{p}(x, y)} = e^{-\mathrm{OD}(x,y)} \tag{2.46}$$

In practice we also subtract a "dark" image taken with no probe light to reduce the contribution from technical noise such as stuck pixels. Fig. 2.6 shows how we use absorption to generate an image of the atomic distribution. This may be the in-situ distribution of trapped atoms, or the distribution after the atoms are released using ToF imaging as we will explore in the next section.

The number of atoms can be calculated from the OD on a per-pixel basis. In the limit of probe intensity much less than I_sat this gives

$$n_\mathrm{p} = \frac{A_\mathrm{p}\mathrm{OD}}{\sigma_0}, \tag{2.47}$$

where A_p is the in-situ pixel area, taking into account any magnification of the imaging system. As a rule we treat the absolute atom number from the measured OD as an estimate rather than a quantitative measurement, as accurate atom number counting from OD requires careful calibration and elimination of systematic error.

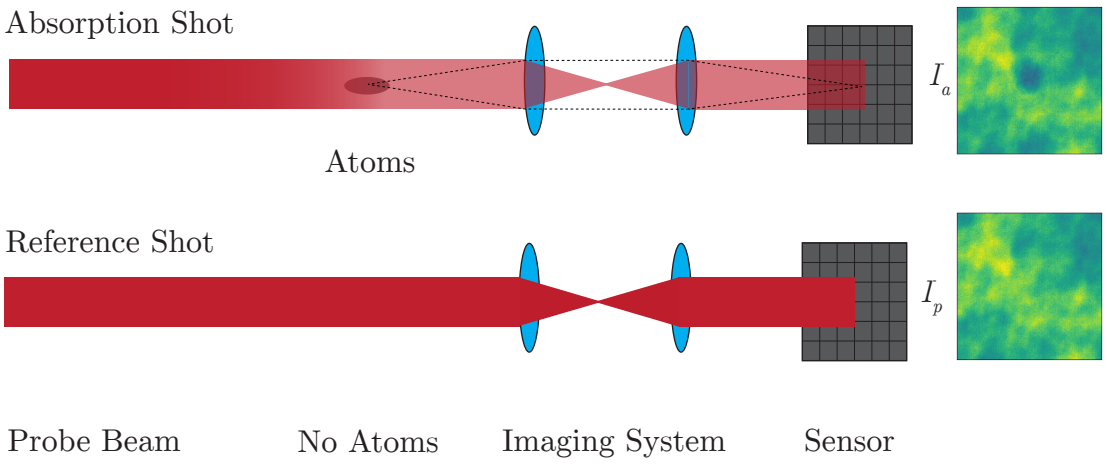

Figure 2.6: Conceptual sketch of absorption imaging. Atomic absorption attenuates the probe beam. By comparing an image of the attenuated probe to a reference probe image without atoms present, we can determine the OD. The false-color image right shows a cropped region of the sensor for the atoms and probe shots used to form an absorption image, corresponding to the center of Fig. 2.7 (a).

Our absorption imaging uses the $f = 2, f' = 3$ transition of the $D2$ line, meaning that the probe light must be accompanied by a "repumper" beam (discussed in Sec. 3.2.1) so that atoms may undergo multiple absorption-emission cycles and any atoms in $f = 1$ are pumped into a state addressable by the cycling transition. Alternately we can use a microwave pulse to transfer some or all of the atoms from $f = 1$ to $f = 2$ before imaging. This is the basis for partial transfer absorption imaging [27] which is useful when the OD is high or to perform a measurement without fully destroying the cold atom system. We do not use partial transfer imaging for any of the scientific data reported in this thesis, but we use it for a magnetic field monitoring technique described in Sec. 3.7.1.

2.5.2 Time-of-Flight Imaging

We are often interested in the momentum distribution of our ultracold atoms. To probe this, we use time-of-flight (ToF) imaging, in which we release our atoms from their trap, allowing for a period of mean-field driven expansion, followed by free expansion (the atomic density quickly reduces to the point where interactions are negligible and the expansion can be considered free). If the expansion time is long compared to the initial spatial distribution of atoms, the ToF distribution will reflect the initial momentum of the atoms at the start of the expansion. This approach has the added benefit of allowing the atoms to spread out, so their OD is lower, allowing for more faithful imaging. Atoms experience radiation pressure from the resonant probe light during absorption imaging as well as momentum changes due to spontaneous emission. To avoid complications due to this, we used a probe pulse time of 30μs for the experiments described in this thesis, which is fast compared to the timescale for atomic motion. Fig. 2.7 (a-c) shows ToF images of condensates with different momentum components separated along the horizontal direction (separation along the vertical direction will be discussed in the next section).

The spatial ToF distribution can be qualitatively thought of as the in-situ momentum distribution. This equivalence is only quantitative in the limit of very long ToF, which can be especially hard to reach in anisotropic traps with weak longitudinal confinement, in which case the initial size is large in the longitudinal direction. To compensate for this we can use momentum focusing [28–30]. In this technique we briefly deepen the harmonic trap in the longitudinal direction, providing a restoring force to the atoms related to their displacement from the trap center, for a quarter period of the deepened trap, followed by free propagation. This is analogous to the action of a lens in optics followed by a region of free space for the light to come to a focus. This trans-

lates the initial momentum information into position information removing any contributions to the ToF distribution from the in-situ condensate size. Fig. 2.7 (c) and (d) compare ToF images with and without momentum focusing along the $\mathbf{e}_x$ direction, corresponding to the horizontal direction in the images.

When working with systems with narrow peaks in their momentum distributions, this method presents a drawback because the final distribution will be more tightly focused compared to a conventional ToF distribution, making the peak OD higher and atom number counting correspondingly harder.

2.5.3 Stern–Gerlach Imaging

In addition to the momentum distribution of atoms, we also often desire to measure their internal state. We can measure the internal angular momentum of atoms using the Stern–Gerlach (SG) effect in combination with ToF imaging. The principle of SG imaging, borrowed from the famous 1922 experiment [6, 31], uses an inhomogeneous magnetic field to spatially separate atoms by their magnetic moment. In the classic realization an atomic beam passes through an inhomogeneous magnetic field; in our case the movement comes from the atoms falling due to gravity during the ToF. For our experiments, the magnetic field is approximately a quadruple configuration, produced by a pair of coils in an anti-Helmholtz configuration (see Sec. 3.4). As we saw in Sec. 2.1.3 the different internal m_F states have different magnetic moments, meaning the spatial distribution after SG ToF gives us the distribution of m_F internal states.

SG imaging is compatible with momentum resolved imaging when we measure momentum along only one direction of the system, perpendicular to the SG separation direction. As

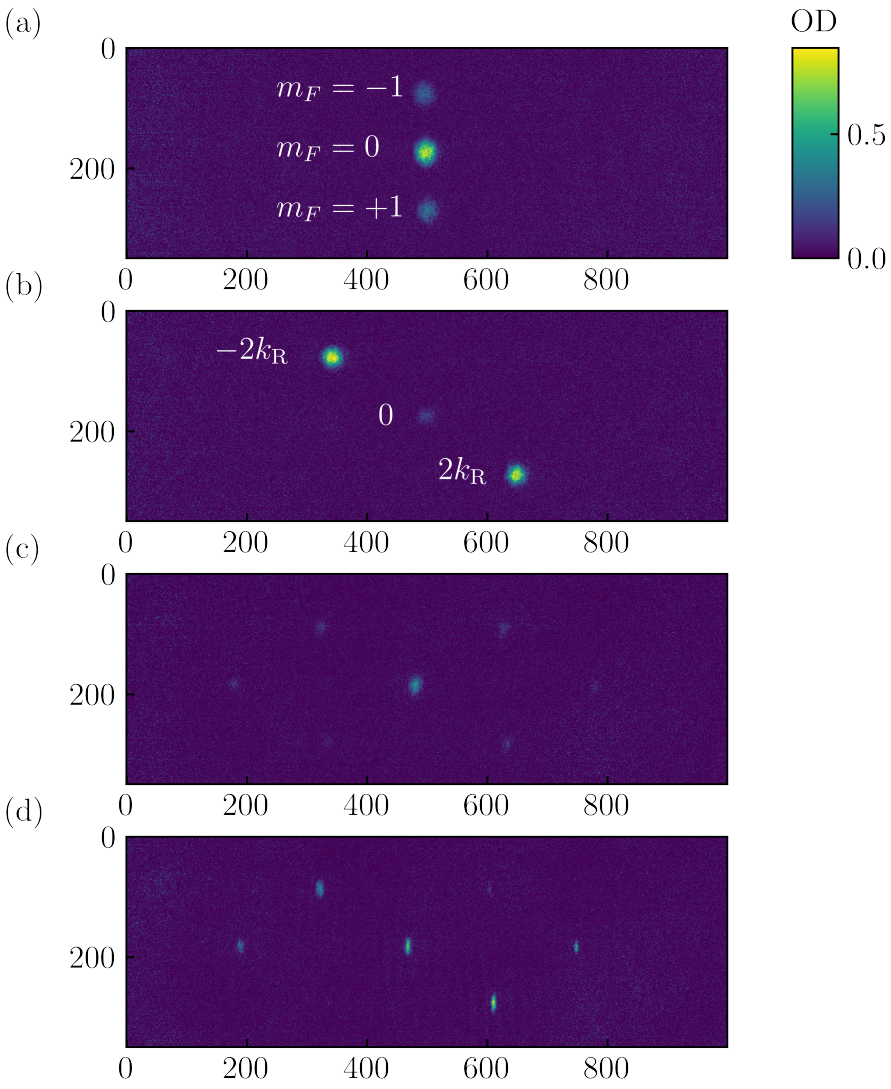

Figure 2.7: Example absorption images taken after SG ToF. (a) different magnetic states separated along the y direction. (b) States with different momentum and internal state separate along both directions. (c) A distribution with more combinations of internal and momentum state after ToF. (d) A similar distribution after momentum focused ToF.

demonstrated in Fig. 2.7 this allows us to measure in the basis of $|k, m_F\rangle$ states. The relative population in each state can be found by counting the OD in each region where there is a density peak, and dividing each by the total OD. This provides something analogous to the probability associated with each basis state in a single particle measurement.

Chapter 3: Experimental System

Bose–Einstein condensation (BEC) is a striking manifestation of quantum mechanical effects, in which a macroscopic number of particles occupy the same quantum state. Creating and manipulating BECs in the lab allows us to directly see quantum effects, such as matter-wave interference [32] and perform quantum simulation experiments. Laser cooling [8] is a set of techniques that exploit the intricacies of atomic physics and light-matter interactions to cool atomic ensembles to extremely low temperatures providing key technical steps to achieving BEC in the lab.

In this chapter, we review the basic principles of Bose–Einstein condensation and laser cooling, applying the atomic physics principles from the last chapter. We then describe relevant details of our experimental apparatus, including the system we use to drive Raman transitions that we make use of in our topological lattice experiments. Most of the details of our apparatus have been covered in past theses [33–35], so this chapter provides an overview and reports changes and updates to the apparatus in more detail. Secs. 3.8 and 3.9 report on changes to the Raman beam setup and the addition of a digital micromirror device, respectively.

3.1 Introduction to Bose–Einstein Condensation

The statistical mechanics of a system of quantum particles must take into account their indistinguishably. In 3D systems, indistinguishable quantum particles are either fermions with half-integer spin or bosons, with integer spin [36]. Fermions must have a many-body wavefunction that is antisymmetric under particle exchange, leading to the Pauli exclusion principle, which restricts the occupation number for quantum states to be zero or one. In contrast bosons, whose many-body wavefunction must be symmetric under exchange, can have occupation numbers of any integer.

The Bose–Einstein distribution describes the thermal average occupation number of states in a system of bosons at temperature T [37].

$$n_T(i) = \frac{1}{e^{(E_i-\mu)/k_\mathrm{B}T} - 1}, \tag{3.1}$$

where E_i is the energy of state i, k_B is Boltzmann's constant, and μ is the chemical potential. It is convenient to rewrite the distribution in terms of the fugacity $z = e^{\mu/(k_\mathrm{B}T)}$

$$n_z(i) = \frac{z}{e^{(E_i)/k_\mathrm{B}T} - z}. \tag{3.2}$$

The occupation as function of E is shown in Fig. 3.1 (a) for a range of z values.

For an ideal Bose gas, the Bose–Einstein distribution reduces to the classical Maxwell–Boltzmann distribution for an ideal gas in the limit where $z \ll 1$ corresponding to the limit where all the average particle occupation numbers are small. In contrast, quantum effects become important as the inter-particle spacing d, which scales like the cube root of the real-space number

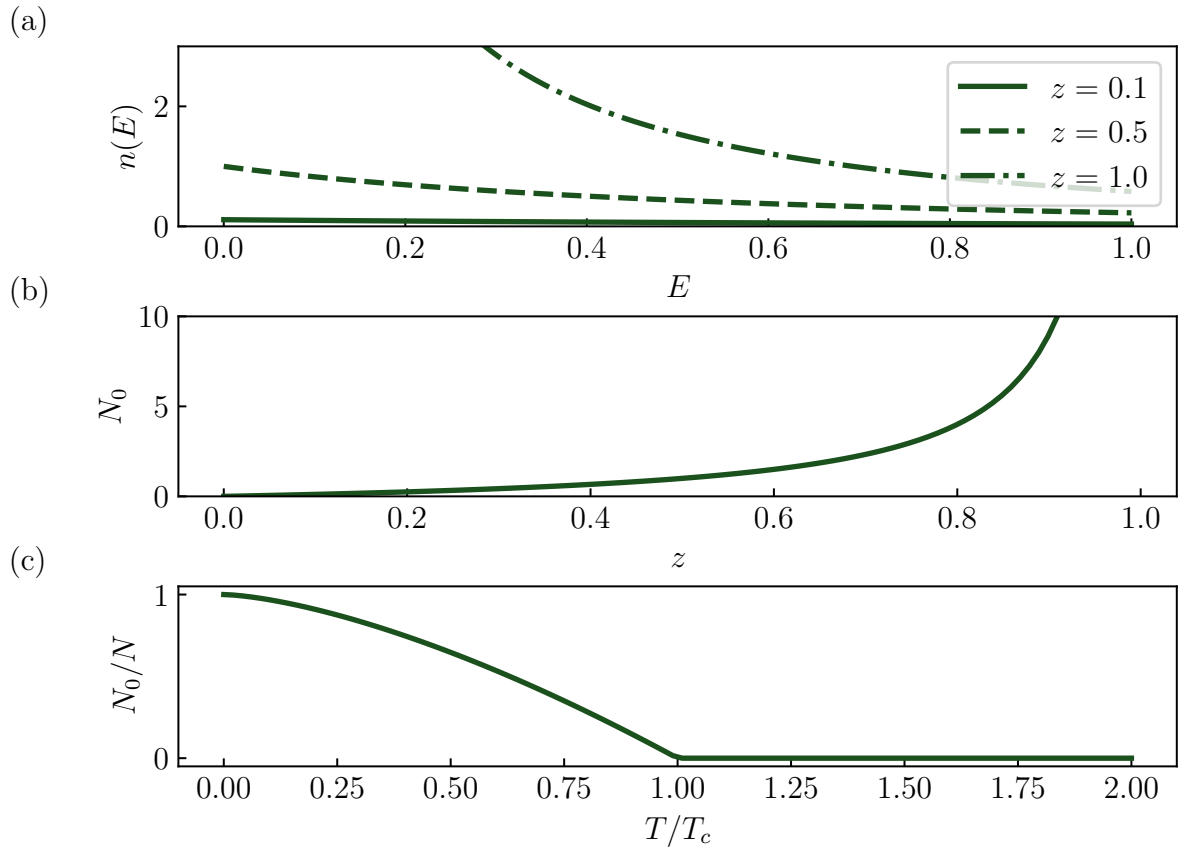

Figure 3.1: Bose–Einstein distribution. (a) Occupation number as a function of energy for three different values of z. (b) Ground state occupation as a function of z, which diverges as z approaches 1 corresponding to $\mu = 0$ and Bose–Einstein condensation. (c) Condensate fraction as a function of temperature expressed as T/T_c for an ideal (untrapped) Bose gas.

density n, decreases.

We can gain some insight into Bose–Einstein condensation by considering an ideal Bose gas at low temperature. For this toy model, there are no interactions and there is no external potential. The model consists of N bosons in a space with periodic boundary conditions, and the Hamiltonian eigenstates are plane waves with energy given by the kinetic energy $(\hbar k)^2/2m$.

Bose–Einstein condensation occurs when a the ground state has macroscopic occupation number $N_0/N \not\approx 0$. Remarkably, this is possible for temperatures above absolute zero, and happens when d is comparable to the thermal de Broglie wavelength $\lambda_{dB} = \hbar\sqrt{\frac{2\pi}{mk_{\mathrm{B}}T}}$. The conditions for Bose–Einstein condensation depend on the temperature and the density (as well as the dimensionality of the system); at fixed density n the critical temperature is [38]

$$T_C = 0.527 n^{2/3} \frac{2\pi\hbar^2}{mk_{\mathrm{B}}}. \tag{3.3}$$

The the total occupation of the ground state as a function of T is [38]

$$\frac{N_0}{N} = 1 - \left(\frac{T}{T_C}\right)^{3/2}, \tag{3.4}$$

as shown in Fig. 3.1 (c).

3.1.1 Trapped Noninteracting Bose Gas

We can make the scenario more realistic by adding a harmonic trap to our model. The potential for a harmonic trap in 3D is

$$V(\mathbf{r}) = \frac{m}{2}\sum_i \omega_i^2 x_i^2, \tag{3.5}$$

where the index i ranges over x, y, z, and $\omega_{x,y,z}$ are the frequencies of the trap in each direction.

Unlike for the ideal Bose gas, the single-particle ground state for the trapped gas is localized at the center of the trap. This means a condensed trapped gas has a localized real space and momentum space density [39]. The geometric mean harmonic oscillator frequency $\tilde{\omega} = (\prod_i \omega_i)^{1/3}$ defines length and energy scales $a_{\text{ho}} = \sqrt{\hbar/(m\tilde{\omega})}$ and $\hbar\tilde{\omega}$.

For the trapped gas, the critical temperature for condensation is

$$T_C = 0.94\hbar\tilde{\omega}N^{1/3}. \tag{3.6}$$

And the condensate fraction is [39]

$$\frac{N_0}{N} = 1 - \left(\frac{T}{T_C}\right)^3. \tag{3.7}$$

Finite system size effects are beyond our discussion here but result in a smoothing of the transition and a correction to the transition temperature that scales as $N^{-1/3}$ [39].

3.1.2 Interacting Bose gas

In this section we will explore how interactions between bosons modify their low-temperature behavior. In the dilute limit, the interactions between atoms can be approximated as a contact interaction

$$V_{\text{int}}(\mathbf{r_1}, \mathbf{r_2}) = V_0 \delta(\mathbf{r_1}, \mathbf{r_2}). \tag{3.8}$$

Atoms repel each other (or attract each other for $V_0 < 0$) when they overlap, but do not interact when they are separated by finite distance. The strength of the contact interaction is related to the s-wave ($l = 0$) term in the partial wave expansion for scattering, with scattering length a_s:

$$V_0 = \frac{4\pi\hbar^2 a_s}{m} \tag{3.9}$$

In the spirit of the Bogoliubov treatment of a Bose gas, we can describe the system by a single complex wavefunction (order parameter) evolving according to a wave equation including the interaction potential as an effective nonlinearity [39]

$$i\hbar\partial_t \psi(\mathbf{r}, \mathbf{t}) = \left(\frac{\hbar^2}{2m}\nabla^2 + V_{\text{ext}}(r) + V_0 |\psi(\mathbf{r}, \mathbf{t})|^2 \right) \psi(\mathbf{r}, \mathbf{t}). \tag{3.10}$$

Eq. 3.10 is called the Gross–Pitaevskii equation (GPE). The GPE neglects contributions from the uncondensed (thermal) component of the system but is nonetheless a very good approximation to the behavior of condensates well below T_C.

When the number of atoms is large, the interaction term dominates over the kinetic energy

term, leading to an approximate solution to the GPE with density profile given by

$$|\psi(\mathbf{r})| = \sqrt{\frac{\mu - V_{\text{ext}}(\mathbf{r})}{V_0}}. \tag{3.11}$$

Qualitatively, this means the BEC fills the potential to the point where the mean field interaction cancels with the external potential. This is called the Thomas–Fermi approximation and means that for a harmonic trap, the condensate size can be characterized by the Thomas–Fermi radius [39].

3.2 Laser Cooling

In the previous section we introduced a basic description of low temperature bosonic systems. We now turn to the practical challenge of producing low temperature bosons. Laser cooling provides a key set of tools for cooling bosonic atoms. Our experiments make use of many of these tools to achieve a low temperature cloud, with quantum degeneracy and Bose–Einstein condensation coming after evaporative cooling in a conservative trap.

The main idea of laser cooling is to remove kinetic energy from atoms using a combination of stimulated and spontaneous light scattering, resulting in cooling. The essential physics of laser cooling comes from the momentum transferred between atoms and the electromagnetic field when an atom absorbs or emits light. Absorbing a photon results in a change in atomic velocity given by the recoil velocity $v_r = \hbar k_0/m$, where $k_0 = 2\pi/\lambda$ is the wavevector of the light. We will consider light from spectrally narrow lasers with a well defined frequency ω and wavelength λ. It is possible to slow and cool a beam of atoms in one direction using a single beam, as we will see in Sec. 3.2.1. Cooling in multiple directions can be achieved with an arrangement of

beams producing velocity dependent forces, so that the net force due to absorbing and scatting light must be velocity dependent, resulting in damping of fast moving atoms.

Moving atoms experience a Doppler shift of the laser field $\omega_{\mathrm{D}} = -\mathbf{k} \cdot \mathbf{v}$, where $\mathbf{v}$ is the atomic velocity and $\mathbf{k}$ is the light wavevector. This frequency shift, combined with the linewidth of typical cycling transitions, as well as the spectral width of typical lasers, means that the laser field will only be resonant with atoms within a relatively narrow range of velocities (specifically the velocity component in the laser propagation direction). This velocity selectivity can be leveraged to give the desired damping force resulting in laser cooling [24].

The recoil velocity for real atoms—$5.9\mathrm{mm/s}$ for the D2 line of $^{87}\mathrm{Rb}$—is tiny compared to typical thermal velocities at realistic temperatures—$v_{\mathrm{RMS}} = 360\mathrm{m/s}$ for $^{87}\mathrm{Rb}$ at 450 K, a typical temperature for our atom source oven, based on the classical Maxwell–Boltzmann distribution [37]. Despite this, an individual atom can absorb and emit many photon on a "cycling" transition, allowing a large change in the average velocity. A transition will work well as a cyclic transition if the atom is very likely to return to its original ground state after spontaneous emission. We use the $f = 2 \rightarrow f' = 3$ transition of the D2 line, because atoms are more likely to decay from $f = 3$ to back to $f = 2$ compared to $f = 1$ due to selection rules.

Because each absorption on the cycling transition must be accompanied by an emission, the atoms will experience random momentum kicks. These fluctuations act as a form of heating; when balanced with the disruptive force this results in a steady state thermal distribution. The lowest achievable temperature in this configuration is the Doppler limit [40].

$$T_{\mathrm{D}} = \frac{\hbar \Gamma_{\mathrm{sc}}}{2 k_{\mathrm{B}}}, \tag{3.12}$$

where Γ_{sc} is the scattering rate, which is limited by the lifetime of the excited state $\Gamma_{\mathrm{max}} = 1/\tau$.

3.2.1 Zeeman Slowing

One application of laser cooling is to slow an atomic beam using a single laser beam, propagating antiparallel to the atoms. Because the cycling transition linewidth and laser linewidth are narrow compared to the Doppler shift of light experience by the thermal atoms, the resonance condition will change as atoms are slowed. This means that as atoms are cooled, they will come out of resonance with fixed-frequency cooling light. This effect can be countered by changing the frequency of the cooling light (chirp cooling), by using a spectrally wide source (broadband cooling), or by changing the resonance condition for the atoms to absorb light (Zeeman cooling). In the latter approach, an inhomogeneous magnetic field can be engineered around the atomic beam, to form a Zeeman slower in which the detuning from resonance changes as atoms progress to the end of the beam, allowing atoms to be continually slowed by absorbing light from the fixed-frequency laser as they move through the beam, losing velocity as the travel forward [8].

As is clear from our discussion in the previous chapter, real atoms have an internal state structure beyond a single ground state and a single excited state. This includes hyperfine ground states not coupled by the cycling transition. As atoms undergo many cycles of absorption and emission, they may decay into other sublevels of the atomic ground state, a form of optical pumping. If these ground state sublevels are not coupled to the laser cooling light, the optically pumped atoms can no longer be cooled using the cycling transition. This undesired optical pumping can be compensated with additional optical pumping, using a seconder "repumper" laser beam to pump atoms out of the undesired sublevels, back to states coupled to the cycling transition.

3.2.2 Optical Molasses

In addition to slowing atoms in a beam, it is possible to use lasers to cool atoms in a particular region of space. In the simplest case, a pair of counter-propagating laser beams can be used to cool atoms in 1D in the area where the beams intersect. The detuning of the beams can be set so that left-moving atoms resonantly absorb light from the right-going laser and are slowed, and vice-versa for right-moving atoms. The resulting average force on the atoms is a velocity dependent damping force analogous to movement in a viscous fluid. As a result, this technique is called optical molasses. This simple model allows atoms to be cooled to T_{D} in the direction of the counter propagating beams [8, 40]. Naively, one might expect this to generalize to the 3D case. In 3D, polarization effects of the overlapping beams become important, allowing for new cooling mechanisms we will explore in the next section.

3.2.3 Sub Doppler Cooling

Perhaps shockingly, the internal state structure of atoms, combined with the polarization properties of the cooling light, make it possible to cool below T_{D}. This is possible through the interplay between light shifts driven by polarization gradients, and optical pumping rates related to the atomic state structure [24]. This gives rise to a class of techniques call polarization gradient cooling (PGC).

Two common configurations for PGC involve linearly polarized beams with perpendicular polarization (lin $\perp$ lin PGC), or circularly polarized beams with opposite circular polarization ($\sigma^+\sigma^-$ PGC) [24]. In the lin $\perp$ lin configuration, atoms experience a spatially dependent light shift depending on their internal state. The laser fields optically pump atoms into the state for

which they are at a potential minimum, meaning they lose energy as the move away from the minimum. As the atoms move toward the maximum of their state dependent potential, they are more likely to be optically pumped into a different internal state, for which the state-dependent potential is reversed, so that the cycle can repeat. This is known as Sisyphus cooling owing to the atoms repeatedly climbing potential hills to lose energy. In the $\sigma^+\sigma^-$ configuration atoms are optically pumped into different magnetic sublevels depending on their motion making them more likely to absorb light from the beam propagating opposite their motion direction. We make use of $\sigma^+\sigma^-$ PGC in our experiments because we have circularly polarized beams can be readily used for to created a $\sigma^+\sigma^-$ configuration.

3.2.4 Magneto-Optical Traps

In addition to cooling using manipulation of atomic detuning from resonance, it is possible to create a system where atoms feel a restoring force due to spatially varying absorption of laser light. A magneto-optical trap (MOT) uses a magnetic field gradient to change resonance conditions so that atoms resonantly absorb more trapping light as they travel away from the trap center.

We create MOTs where the magnetic field gradient is a quadrupole configuration field supplied by our anti-Helmholtz coils. Each axis of the trap has a pair of counter-propagating beams with σ^+ and σ^- polarization. The gradients and polarizations combine so that atoms resonantly absorb light preferentially when they move away from the trap center; the preferentially absorbed light is from a beam propagating from the resonance position toward the trap center, resulting in the restoring force toward the trap center [40].

3.3 BEC Production

Our system uses several stages of laser and evaporative cooling to achieve an ultracold Bose gas. The system start with an atom source: gaseous Rubidium from an oven is collimated by a heated nozzle and chilled cold-cup, feeding hot atoms into a Zeeman slower [41]. Slower and repumper laser beams cool and slow the atoms in the longitudinal direction, providing a flux of atoms in our main vacuum chamber.

In the main chamber, atoms from the slower beam are captured in a MOT formed by three pairs of counter propagating beams and a quadrupole magnetic field generated by a pair of anti-Helmholtz configured coils (Sec. 3.4). We load atoms into our MOT for $1 - 3$ s depending on the desired atom number[1]. Following this, we perform additional cooling and optical pumping stages before transferring to a magnetic trap. We then cool the atoms using optical molasses and $\sigma^+\sigma^-$ PGC. Following this, we optically pump atoms into the $f = 1$ hyperfine state, our desired final state.

Next, the atoms are captured in a magnetic trap formed from the same quadrupole coils used for the MOT. After capturing low-field seeking atoms in our quadrupole trap, we increase the current to compress the trap. This process increases the temperature, but increases the phase space density in preparation for evaporative cooling. Evaporative cooling, in which atoms with higher kinetic energy are allowed to leave the trap, resulting in a smaller lower temperature cloud [42], is a key step along our path to Bose–Einstein condensation.

The first stage of evaporation in our magnetic trap uses an RF magnetic field to transfer

[1] We sometimes increase the loading time to compensate for slight misalignment of the MOT beams. We characterize the MOT by the fluorescence it produces. The final fluorescence and the time to rise to $2/3$ of the final value characterize the MOT.

atoms from trappable to non-trappable states. This results in a loss of atoms from the trap at locations where the RF field is resonant with the transition between internal atomic magnetic sublevels. We start the RF at a relatively high frequency (approximately 15 MHz)[2], so that it is resonant with atoms near the edge of the trap, which on average have higher kinetic energy than atoms closer to the trap center. As the atoms are evaporatively cooled and the cloud shrinks, we lower the RF frequency, to be resonant with atoms closer to the trap center. The moving RF frequency is sometimes called a "knife edge" because it acts to remove atoms a certain distance away from the trap center. We end at an RF frequency around 5 MHz.

Following RF evaporation, we relax the magnetic trap and transfer atoms to an optical dipole trap (ODT) formed from the intersection of two approximately Gaussian 1064 nm laser beams. This is based on the hybrid technique described in Ref. [43]. Following this transfer, we reduce the ODT trap depth, allowing atoms near the edge of the trap to more easily escape, so that the ensemble continues to undergo evaporative cooling until we reach our final trap depth. Because the technique uses a magnetic trap the resulting condensate has an internal state with $m_F = -1$ in the conventional form of this procedure.

3.3.1 Optical Dipole Trap

Compared to earlier experiments using the RbK apparatus (see Refs. [33–35]), we use a different optical dipole trap (ODT) configuration (see Fig. 3.3). In the past, our lab used a configuration where the beam from an `IPG Fiber Laser` passed through a "split" acousto-optic modulator (AOM) providing two orders, which we used to form a crossed ODT. Instead, we

[2]The starting frequency was 14.5 MHz at time of writing, but this is periodically changed when we optimize the BEC production sequence. A higher initial frequency will provide better evaporative cooling for a larger initial cloud.

use one order from this laser AOM configuration along with an independent laser beam from a separate 1064nm `IPG Fiber Amplifier`. This second beam, which propagates with our Raman beams, provides the transverse confinement allowing us to achieve an anisotropic cigar shaped trap with frequencies $(\omega_x, \omega_y, \omega_z)/2\pi \approx (15, 150, 100)$ Hz at the final trap depth. The dither beam from the split AOM provides the relatively weak longitudinal condiment with frequencies ranging from $\approx 15 - 25$ Hz depending on the dithering control.

3.3.2 Evaporation and State Transfer

In many of our experiments, we desire to start with a BEC in the $m_F = 0$ internal state. To provide this efficiently, we optionally employed a combination of a short resonant RF pulse and magnetic field gradients during the final stage of evaporation. The magnetic field gradients tilt the trap seen by $m_F = -1$ atoms, gradually releasing them from the trap as the depth decreases. Ideally this means that the magnetic component of the atomic cloud can act as a sympathetic coolant for the desired nonmagnetic component. By tuning the duration of the RF pulse and the strength of the magnetic field gradients, we can control the size of the final $m_F = 0$ BEC.

3.4 Apparatus Overview

The RbK apparatus, shown in Fig. 3.2, consists of several subsystems that perform multiple key functions, which together allow us to create ultracold atomic gases and use them for quantum simulation experiments. These subsystems include, vacuum systems, atom source systems, lasers and optics for beam forming and alignment, imaging systems and cameras, near DC magnetic field systems, and coils/antennas for oscillating magnetic fields and a digital micromirror device

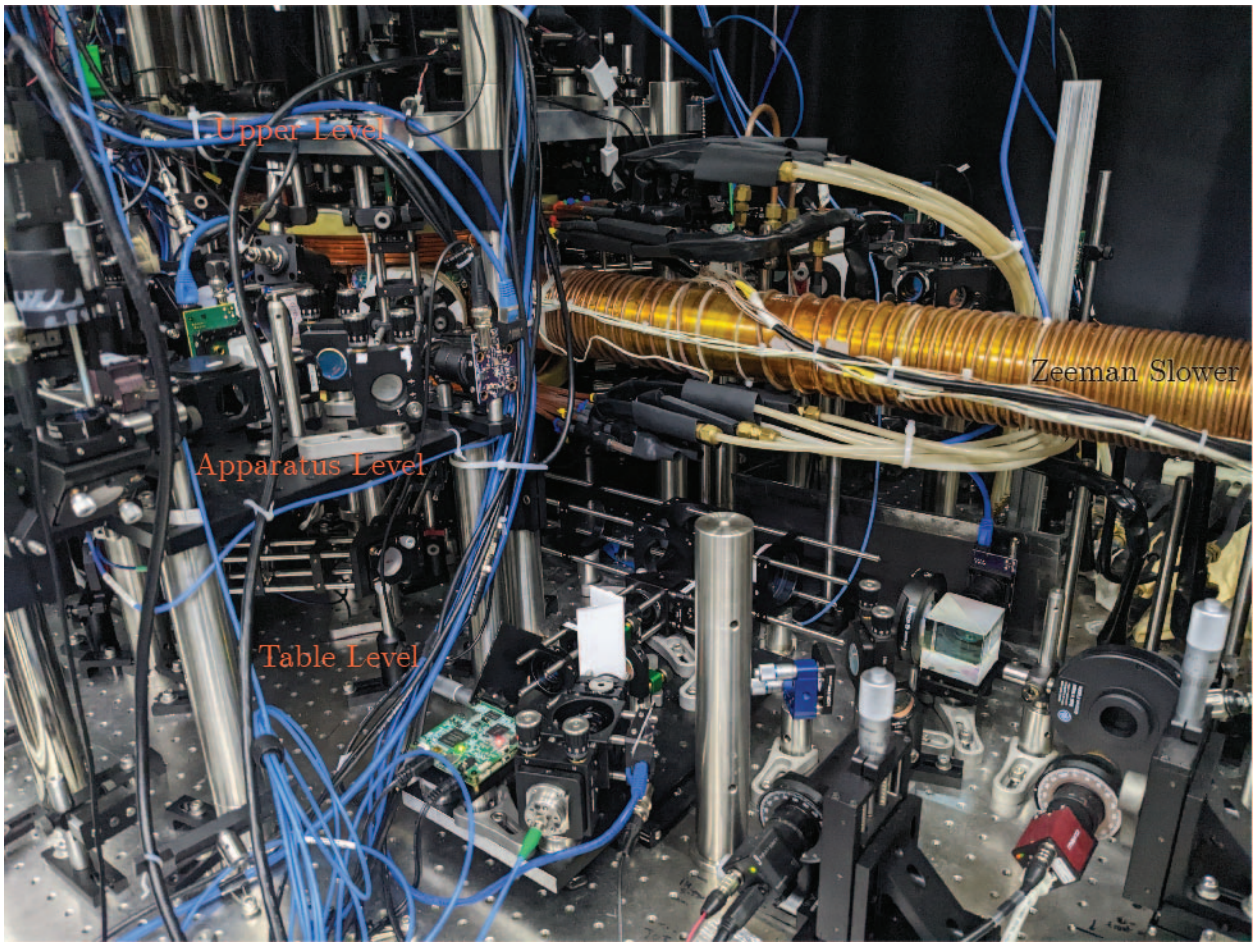

Figure 3.2: Overview of the RbK apparatus. The apparatus consists of three levels: the table level, the chamber level, and the upper level.

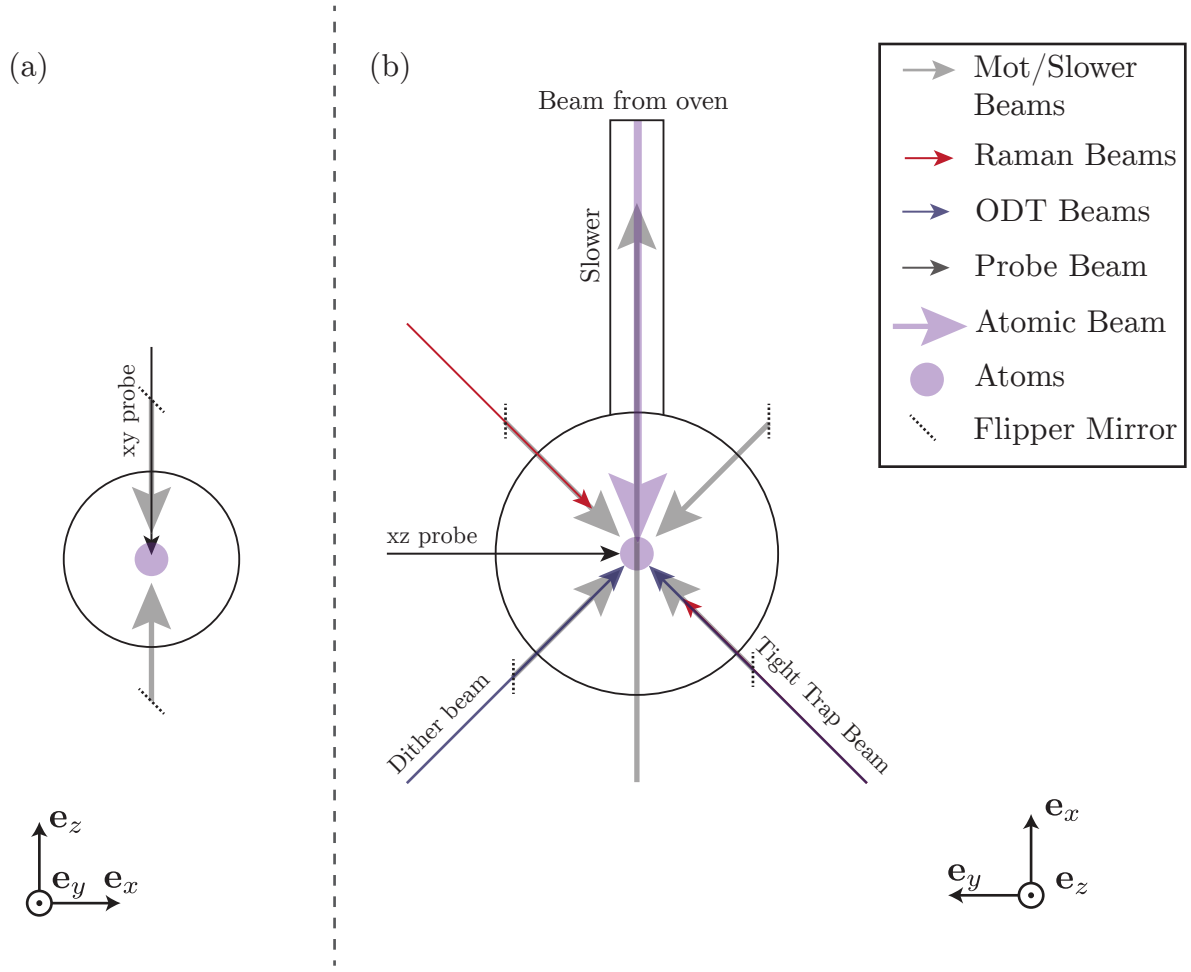

Figure 3.3: Sketch of experimental chamber with laser beams. (a) xz cross section view with vertical beams. (b) xy view with horizontal beams. The counterpropagating Raman beams share the $\mathbf{e}_x - \mathbf{e}_y$ axis with the tight dipole trap beam. We switch between the MOT beams and the Raman and ODT beams using flipper mirrors.

for spatially patterning laser beams.

The laser systems include a slowing beam and repumper beam aligned along the Zeeman slower axis, six beams to form our MOT along with repumper beams, probe beams for our imaging system in the xy and xz planes, beams for our optical dipole trap, and beams to drive Raman transitions. The arrangement of beams propagating through the experimental chamber is shown in Fig. 3.3.

The near DC magnetic field system include three sets of coils in a Helmholtz configura-

tion to control the three components of the bias (quantization) magnetic field, a pair coils in an anti-Helmholtz configuration to produce gradients along the z axis, and a two sets of gradient cancellation coils. The oscillatory magnetic field systems consist of a pair of coils above the chamber used for RF evaporation and driving RF transitions, as well as a microwave horn for driving transition between state in the $f = 1$ and $f = 2$ hyperfine manifolds. The details of the magnetic field system are reported in Sec. 3.7.

3.4.1 Control System

The control and analysis system for our apparatus is organized around the labscript suite [44]. Labscript uses a modular architectures allowing many devices potentially controlled by multiple computers to contribute to the control and analysis of each experimental shot. The operation of the devices is synchronized by pseudoclock lines, which tell devices when to update based on preprogrammed instructions, from the channels of a pulse generator. The command instructions for each shot are generated from user created python scripts defining the sequence and parameters and global variables that set the specific parameter values for each shot. Each shot corresponds to a `HDF5` file containing the instruction for all the programmed devices; as the shot is run data gathered during the shot (such as images) are added to the file.

Our control system centers on a `SpinCore PulseBlaster USB` digital pulse generator whose channels act as pseudoclock lines to control other devices. We use three `NI 6733` PCI analog output (AO) devices, two `NI 6229` USB multi function output devices, and one `NI 6343` USB multi function output device to provide analog and additional digital channels used to control the experiment.

3.5 Camera Systems

The apparatus includes several cameras for use with absorption imaging. The xy ToF camera is a `Mako G-504B` (CMOS sensor). We control the ToF camera position using a `Zaber T-LSR 300B` translation stage. This allows us to change the camera position automatically if we wish to change the ToF duration.

The xy in-situ camera is a `Point Grey Flea FL3-FW-031M` (CCD sensor). It is advantageous to have an independent second camera for in situ imaging, so that we can independently take in-situ and ToF images in the same shot. We use the capability to monitor magnetic field drift (see Sec. 3.7.1). Both the xy ToF and xy in-situ cameras use the same imaging system, consisting of a two-lens compound objective with effective focal length $f = 83\mathrm{mm}$ coupled with an $f = 500\mathrm{mm}$ achromatic doublet giving a magnification of 6.

The xz camera is a `Point Grey Flea FL3-FW-031M` (CCD sensor). This is generally only used for diagnostics because our scientific imaging uses the xy camera.

3.6 Laser Systems

The RbK apparatus includes multiple laser systems used to cool, trap, manipulate, and measure our atomic systems. The details of their implementation are reported in Refs. [33–35]. We summarize them here for completeness.

The system includes three tunable-wavelength diode lasers operating near $780\mathrm{nm}$ close to the $^{87}\mathrm{Rb}$ D2 transition. The master laser is a `Toptica DL Pro` diode laser. It uses saturated absorption spectroscopy [45] to lock to the $f = 2 \rightarrow f' = 2$ $f' = 3$ crossover peak. It serves

as a frequency reference for the other lasers only. The repumper laser is a Toptica DL 100 diode laser. The repumper generates beams to optically pump atoms out of $f = 1$ ($f = 1 \rightarrow f' = 2$) used for the slower, MOT and imaging stages. In 2021 we switched the frequency servo from the integrated Toptica servo to an external Newport LB1005-S servo controller. The cycling/cooling laser is a Toptica TA Pro tapered amplifier system operating close to the $f = 2 \rightarrow f' = 3$ transition. This laser generates beams for our Slower, MOT, PCG, and imaging stages.

Our optical dipole trap lasers are an IPG YDL-10-LP Fiber Laser (conventionally called the ODT laser) and an IPG YAR-10K-1064-LP-SF Fiber Amplifier (conventionally called the lattice laser), both operating at $1064\mathrm{nm}$.

Our Raman beam laser is a titanium doped sapphire laser (Ti:Sapph) Coherent MBR 110 pumped by a Verdi V10, itself a diode-pumped solid-state Nd:YAG laser (the pump laser produces a 532 nm beam derived using a nonlinear crystal for frequency doubling the usual 1064 nm Nd:YAG emission line.) The Ti:Sapph is widely tunable in wavelength; for the experiments reported here we operated it near $790\mathrm{nm}$.

At the time of writing, the lab also includes an additional Verdi V10, slated for use with an under development sheet trap system for additional confinement in the z direction, as well as an extra Toptica TA 100, originally purchased for use near $780\mathrm{nm}$, available for miscellaneous uses.

3.7 Magnetic Field Systems

Our experimental magnetic field system consists of a set of three pairs of Helmholtz-configuration bias coils, used to produce approximately homogeneous fields along $\mathbf{e}_x+\mathbf{e}_y$, $\mathbf{e}_x-\mathbf{e}_y$ and $\mathbf{e}_z$. The apparatus also includes coils surrounding the Zeeman slower to generate the necessary magnetic field profile as a well as a set of "reverse" coils to cancel the slower field in the experimental chamber. The apparatus is also equipped with a set of quadrupole gradient coils in an anti-Helmholtz configuration for use in our MOT and magnetic trapping stages as well as Stern–Gerlach ToF imaging. The relative placement of the coils is shown in Fig. 3.4.

Each of the three sets of bias coils are controlled by a separate `Kepco BOP20-20M` 20 A bipolar power supply, controlled by a home-built current servo. Current in the quadrupole coils is driven by an `Agilent 6690A` 440 A unipolar power supply. The coil current is controlled by a home-built transistor bank and servo. The slower and reverse coil currents are each driven by a `Kepco ATE6-100M` 100 A unipolar power supply.

In addition to these main coils, we also have two sets of gradient cancellation coils, primarily used to remove residual gradients in the system (these may arise because the bias coil pairs are not separated by the ideal distance for a Helmholtz configuration, for example). These sets are designed to control gradients of the form $\partial B_z/\partial z$ and $\partial B_{xy}/\partial z$. These coils are not designed to have their current ramped during the experiment, and are thus controlled by smaller `Agilent` power supplies driving a constant current throughout the experimental sequence.

For RF evaporation as well as coherent manipulation, we drive RF signals through a pair of coils above the chamber. These coils have two loops, arranged to produce a field in the $\mathbf{e}_x$ direction. In 2021 we upgraded the RF amplifier used for RF evaporation as well as our lattice

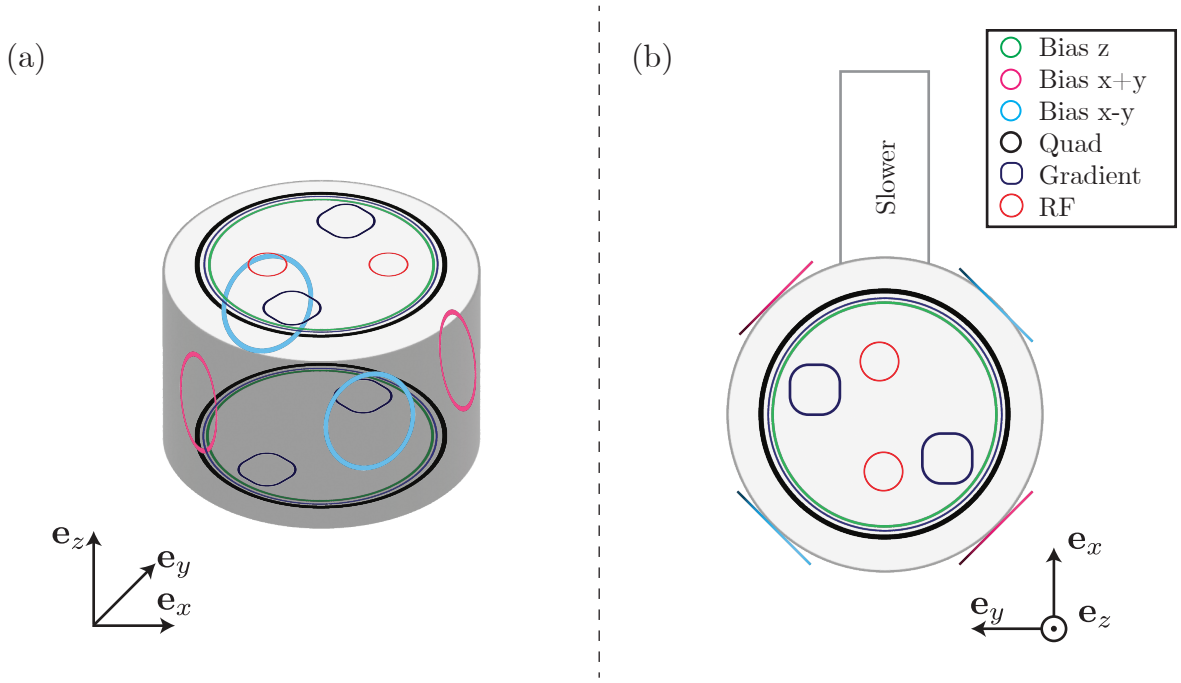

Figure 3.4: Magnetic field coil arrangement. (a) Perspective. (b) Top view. Not to scale.

experiments to a `Mini-Circuits LZY-22+`. This upgrade resolved issues where the previous amplifier produced a small residual current after its input signal was abruptly changed.

3.7.1 Magnetic Field Locking and Monitoring

For many of our experiments it is important to keep the bias magnetic field constant in order to keep the detuning for RF and/or Raman transitions at the desired level (usually on resonance). This is a challenge due to drifts in the external magnetic field caused by activity in neighboring labs. To address this, we use a system of partial transfer imaging to evaluate the resonance condition of our bias field before each experimental shot. In this scheme we use two microwave pulses from $|f = 1, m_F = -1\rangle$ to $|f = 2, m_F = -2\rangle$, deliberately detuned, one with $\delta > 0$ and the other with $\delta < 0$. This is a "stretched" transition, especially sensitive to changes in the external field, since the two states experience opposite energy shits with changes in $\mathbf{B}$. We

take an image without rempump light to only measure the atoms transferred by the pulse. We compare the number of atoms in each image; when the number is equal, the bias field is calibrated, otherwise we must make an adjustment to the bias coil current for subsequent shots.

In principle this process could be used to generate an error signal which could be used for automated feedback to stabilize the magnetic field. Because our workflow involves creating large sequences of experimental shots (≈ 100), we did not implement any automated feedback for the experiments described in this thesis. In general the external field was sufficiently stable on the timescale of our sequences that our experiments did not require active feedback. We monitored the detuning signal and discarded any data where the imbalance was too large, then made adjustments between sequences throughout the day.

3.7.2 RF Signals

Several application in the lab require controllable RF signals. These include the dynamic RF coils, the Raman signal generation (Sec. 3.8), and controls for the laser frequency servos. We generate these signals using `Novatech` direct digital synthesis (DDS) synthesizers.

Because the Raman and RF drive channels are used simultaneously, it is important we have control over the relative phase between these signals. For reasons that will be made clear in Sec. 6.1.3 it is advantageous for us have two independent DDS channels for the RF field with a different phases (both well defined relative to the Raman phases).

At the time when the experiments in this thesis were conducted, we used two `Novatech 409-B` signal generators. In our configuration each `Novatech` signal generator has two channels that can be dynamically updated during the experiment and two static channels. Static channels

have limited application, and are unsuitable for uses like RF evaporation where the frequency is ramped, or control experiments where the RF phase is changed during the experiment. The two `Novatech` devices were unsynchronized for the experiments described in this thesis, meaning the relative phase between channels controlled by the same `Novatech` devices was well defined and controllable, but the phase between channels on separate devices was not. After completion of the experiments described here, we replaced our `Novatech` signal generators with models that support an external $10\mathrm{MHz}$ clock for phase synchronization across devices.

3.8 Raman Beams

Our Raman laser system consists of two counterpropagating beams (Raman-A and Raman-C) of wavelength $\approx 790\mathrm{nm}$ with frequency difference ω_{RF}. In a single-tone Raman configuration, one beam has frequency ω and the other $\omega+\omega_{\mathrm{RF}}$. In the two-tone configuration employed in many of our experiments, each beam contains ω and $\omega + \omega_{\mathrm{RF}}$ components. For the experiments in this thesis $\omega_{\mathrm{RF}} = 1\mathrm{MHz}$. Both beams derive from a Coherent `MBR 110` Ti:Sapphire laser pumped by a Coherent `Verdi-V10`.

To achieve the desired frequency components in each beam, we pass each beam through its respective AOM, with the first diffraction order aligned with an optical fiber to be sent to the experiment. This arrangement is shown in Fig 3.6. Instead of working with frequency components 0 and 1 MHz, we add an offset of 80 MHz, so both tones fit within the AOM's performance window, and the desired frequency component is found in the first order diffraction peak for both beams.

For the single-tone configuration, we require an 80 MHz shift for Raman-A and 81 MHz

for Raman-C. In the two-tone configuration both beams require an 80 MHz shift and an 81 MHz shift. While the 80 MHz and 81 MHz tones result in slightly different diffraction patterns, in practice, the fiber alignment can be tuned so that both components are coupled to the fiber.

We implement a network of RF hardware to create the desired frequency components, shown in Fig. 3.5. A pair of `Novatech` DDS synthesizer channels produce 80 MHz and 81 MHz signals (hereafter f_1 and f_2). Each signal is passed through an RF power splitter, model `Mini-Circuits ZSC-2-4+`, and each of the resulting four signals is sent to an RF mixer, model `Mini-Circuits ZAD-3+`, allowing independent control of each amplitude by an AO channel from our control computer. Following the mixers, one pair of frequencies f_1 and f_2 are combined using a power splitter to form the RF signal for Raman A and the other pair are combined to give Raman C. These signals could be sent directly to independent RF amplifiers to generate the AOM drive signal for each beam. In order to lock the beam power, we implement an additional step.

The total power in each beam is controlled by a voltage controlled attenuator (VCA), model `Mini-Circuits ZX73-2500-S+`. The output signal of each variable attenuator is sent through a preamplifier and a fixed attenuator (the latter is only used to match the final amplifier's desired input power; in principle we could have used a preamplifier with a smaller gain, were one available). The RF signal for each beam is then passed through an RF switch, model `Mini-Circuits ZYSWA-2-50 DR`, allowing for fast digital control, before amplification by a `Mini-Circuits ZHL-1-2W+` RF amplifier. The final RF signal is sent to the AOM for the A and C beams, each containing f_1 and f_2 components with relative amplitude controlled by the mixers.

We label the frequency components as A1, A2, C1, and C2, with A1 and A2 both being sent to the Raman A AOM and likewise for the C components and C AOM. The frequency components A1 and C1 form a Raman pair and thus must be have frequency difference ω_{RF}, as with A2 and

C2. To optimize Raman coupling at fixed optical power, we use the same mixer voltage for the A1/C1 pair (controlling the Raman Rabi frequency Ω_1 for the corresponding transition) and a different voltage for the A2/C2 pair (determining the Raman Rabi frequency Ω_2).

To lock the power in each beam we use a `Newport LB1005-S` analog servo controller to generate an error signal. The signal is generated by comparing the voltage from a photodiode (PD) on the experiment side of the optical fiber for each Raman beam to a setpoint voltage generated by an AO our control computer. Because the PD signal contains a 1 MHz oscillation when operating in the two-tone configuration, we low-pass filter the PD signal. This allows us to lock the total optical power in each Raman beam, though not the relative power in each frequency component, compensating for drifts in the fiber coupling. In practice this means the stability of a single-tone configuration is higher than the stability of the two-tone configuration, owing to possible fluctuations in the relative strength of each frequency component at fixed optical power.

When using the servo, the total optical power is controlled by the servo set point, so only the relative values of the mixer control voltages matter for the signal, not their absolute values. We can bypass the optical power servo to operate the setup in a "manual mode" by disengaging the servo lock function and turning the output offset to maximum. In this configuration the value of each mixer control voltage sets the strength of the corresponding frequency component in each beam, in practice determining Ω_1 and Ω_2.

On the experiment side, the beams are collimated out of fiber (the estimated $1/e^2$ beam diameter based on the `Thorlabs` specification is 1.5 mm). Each beam is focused to the atoms by a 300 mm singlet lens. Based on the nominal beam divergence of the collimator (0.03 deg at 790 nm), we can estimate the Rayleigh range to be 60 mm and the $1/e^2$ beam waist to be 300 um [46].

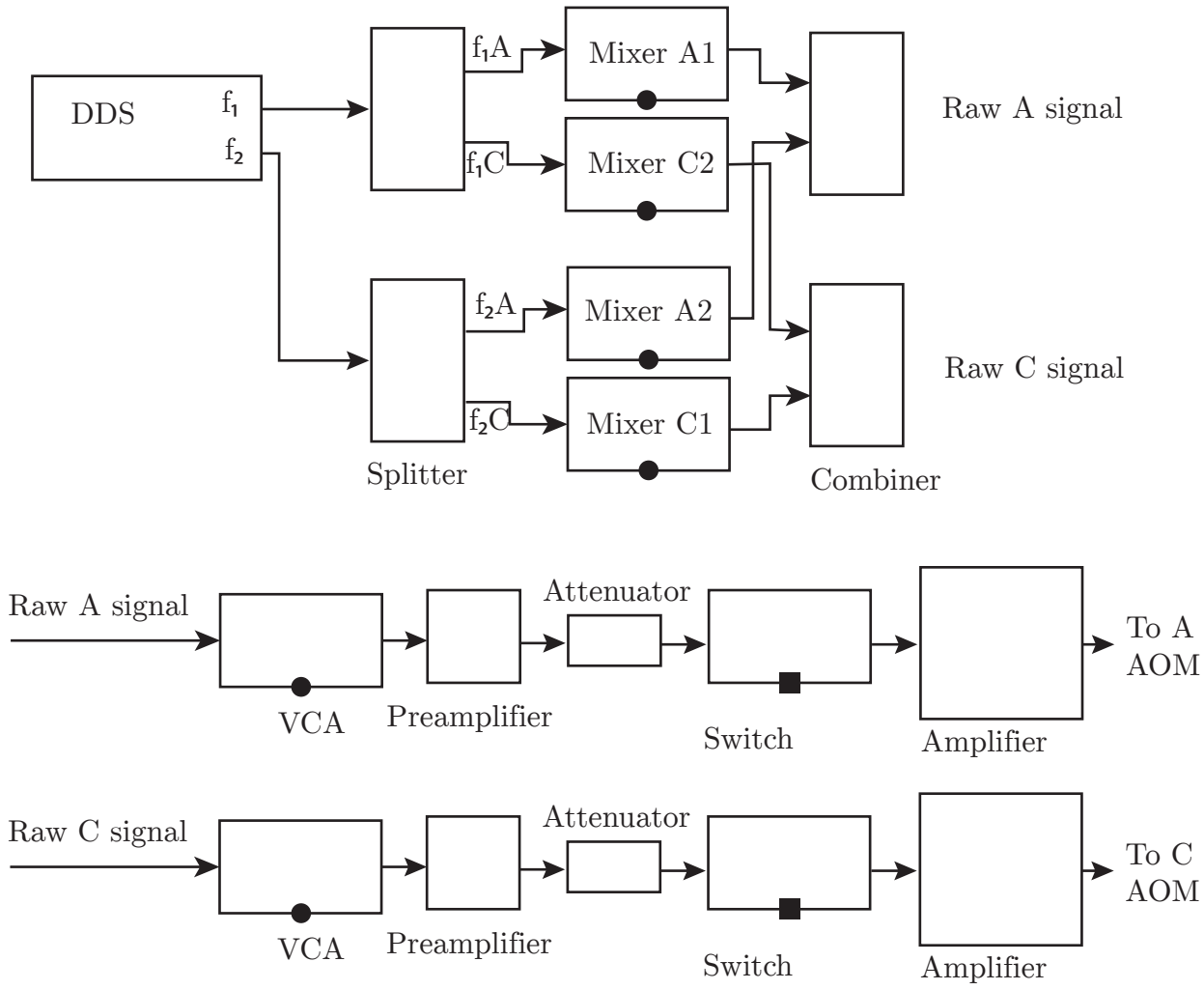

Figure 3.5: Schematic of RF circuits for Raman AOM control. The four mixers receive an analog control signal from our control computer (indicated with solid circles), and the VCA's each receive an analog control signal from a `Newport LB1005-S` servo controller (indicated by solid circles). The output of each branch is controlled by a TTL switch allowing for fast digital control of the AOM signal from the control computer (those channels correspond to solid squares).

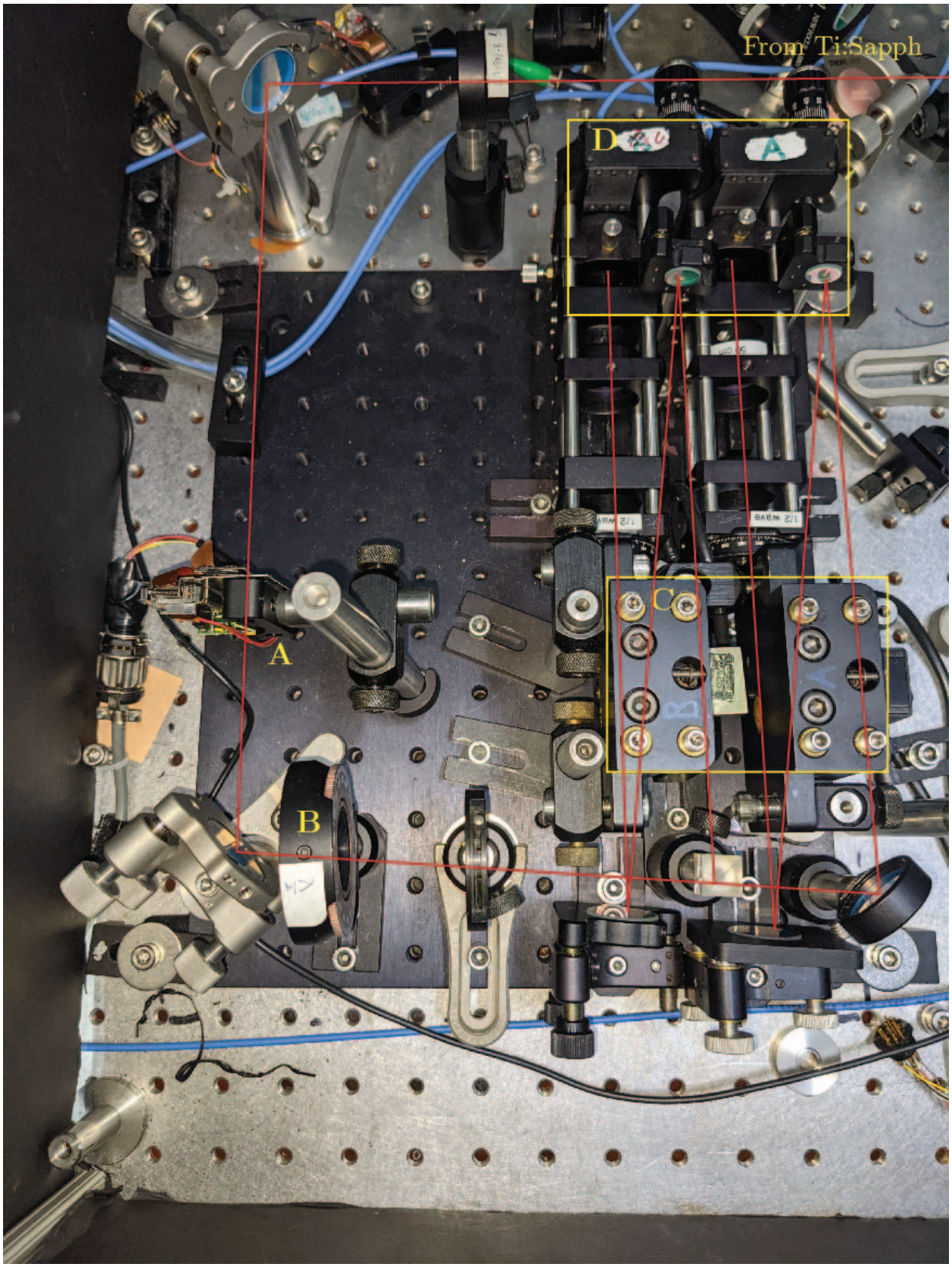

Figure 3.6: Raman AOM setup. The labeled elements are A. Shutter, B. $\lambda/2$ plate used to control the relative power in the A and C branches after polarizing beam splitter, C. AOMs, D. Optical fiber launch.

We also implement `Flea3` cameras to image each beam after passing through the chamber, in order to identify potential drifts. In principle images from these cameras could be used when post-selecting data to reject any shots where the one or both of the beams deviated from their optimal position. In practice we did not find this useful for the experiments described in this thesis.

3.9 DMDs

At time of writing the RbK apparatus includes one digital micromirror device (DMD) in a direct imaging configuration [47] to project potentials using off-resonant light. The DMD is a `TI DLP 3000` integrated into a `TI LightCrafter` evaluation board. The optical setup, shown in Fig. 3.7, begins with a fiber collimator, an angled half-wave plate acting as a pick off for a photodiode and an $f = 50\mathrm{mm}$ lens directing the incoming beam to the DMD surface. After the DMD surface, the patterned light is directed through a Keplerian telescope demagnifying the pattern with $m = -1/2$, consisting of $f = 100\mathrm{mm}$ and $f = 50\mathrm{mm}$ singlet lenses. We have determined that the singlet lenses are a significant source of spherical aberration degrading the projection performance As of the writing of the thesis, we plan to replace the spherical signets with achromatic doublets as soon as is reasonably practical. The system also include two irises: one before the telescope to block unwanted diffraction orders from the DMD and the other between the lenses of the telescope, acting to control its numerical aperture (see App. B). After the telescope, the patterned light is directed into the imaging system path where it is combined using a dichroic mirror.

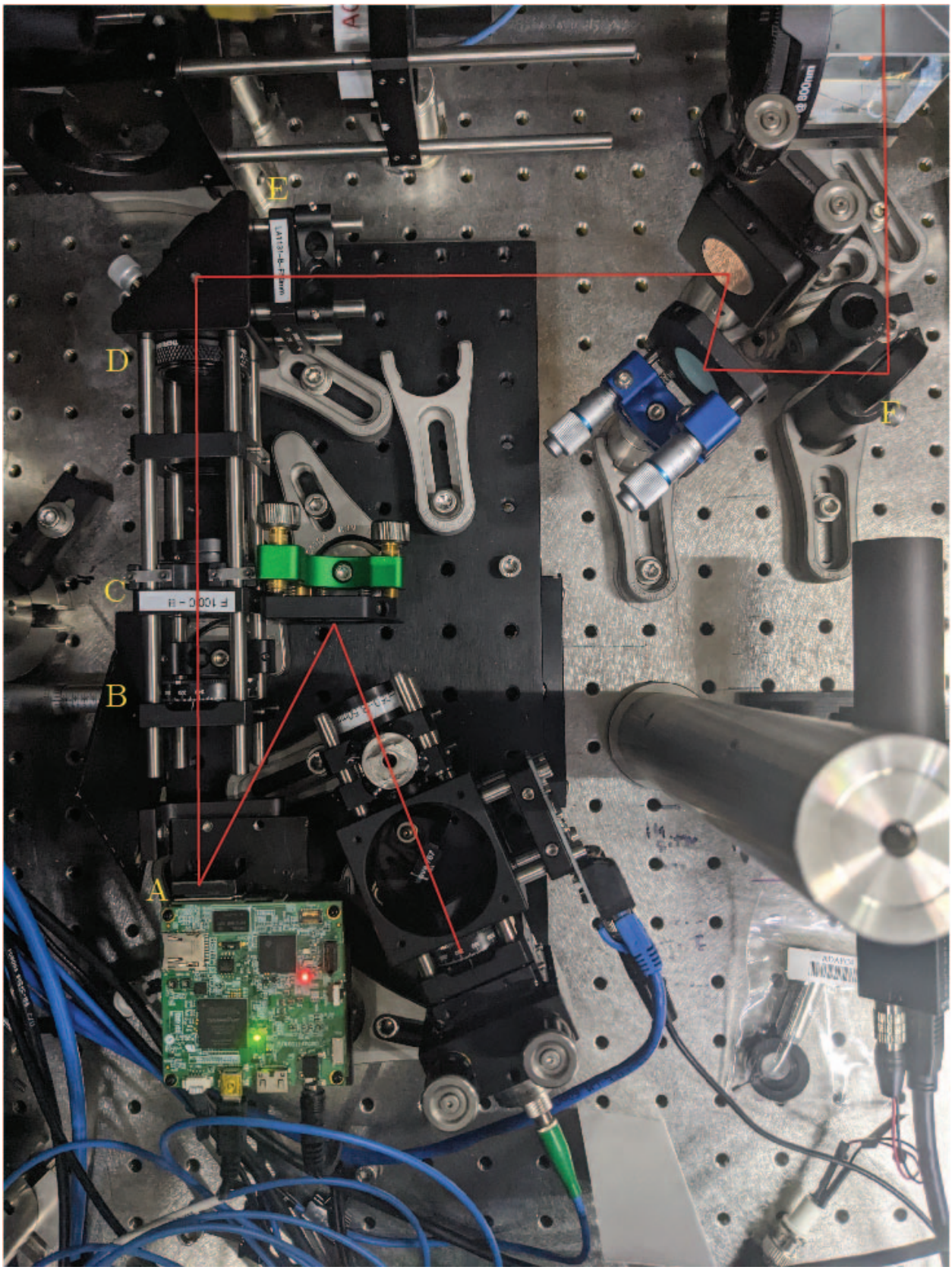

Figure 3.7: DMD pattern projection setup. The labeled elements are A. DMD, B. iris, C. $f = 100\text{mm}$ lens, D. iris, E. $f = 50\text{mm}$ lens, F. dichroic mirror.

Chapter 4: Lattices

This chapter introduces the essential physics of one-dimensional (1D) lattice systems. We describe simple models that capture the qualitative physics of atoms confined to a one-dimensional lattice with two subsites per unit cell. We also describe how multi-subsite lattices map to lattice models of particles with spin. These models provide a starting point to understand the experimental lattice system discussed in Ch. 6.

4.1 Bloch's Theorem

Lattice systems have a discrete translational symmetry: the system is invariant under displacements of multiples of the lattice constant a. The presentation here will assume a 1D lattice, but the ideas generalize to higher dimensions. The Hamiltonian of a particle experiencing a lattice potential is thus invariant under lattice constant a displacements: $\hat{\mathcal{D}}\hat{H} = \hat{H}$. This symmetry means that eigenstates of the Hamiltonian can be labeled by crystal momentum q. Crystal momentum is defined in the reciprocal space of the lattice, the Brillouin zone (BZ). In our convention the reciprocal space has periodicity $2k_R$ and the real space lattice has periodicity $\lambda_{\mathrm{R}}/2 = \pi/k_R$. This convention is chosen to match the atomic physics implementation we will introduce in Ch. 6.

According to Bloch's theorem [48], lattice eigenstates can be written

$$|\psi_q\rangle = e^{iq\cdot r}\,|u_q\rangle\,. \tag{4.1}$$

This leads to real space wavefunctions

$$\psi_q(r) = e^{iq\cdot r}u_q(r). \tag{4.2}$$

$|u_q\rangle$, called the Bloch state, is a unit cell periodic wavefunction. In general, $|u_q\rangle$ will also have a band index n. The Bloch states are eigenvectors of the Bloch Hamiltonian

$$\hat{H}_q = e^{iq\cdot r}\hat{H}e^{-iq\cdot r}. \tag{4.3}$$

4.2 Single-Band Tight Binding Model

We first consider a simple model of a 1D lattice consisting of a single state per unit cell. This toy model will provide a starting point from which to study richer models as well as some useful insights about lattice systems.

The single-band tight binding model consists of a set of lattice sites with corresponding basis states $|j\rangle$ localized to the lattice site, with tunneling matrix elements J between nearest neighbors. We will consider a finite system size of N lattice sites. In real space the Hamiltonian is

$$\hat{H} = \sum_j \big(-J\,|j\rangle\langle j+1|\,\big) + \text{H.c.}. \tag{4.4}$$

As we have seen in the previous section, the discrete translational symmetry of the lattice means the eigenstates will be labeled by crystal momentum q, defined within the BZ so that $-k_R \leq q \leq k_R$. Eigenstates of q have a Fourier series relationship with position eigenstates labeled by j.[1]

$$|q\rangle = \frac{1}{\sqrt{N}} \sum_j e^{ix_j \pi q/k_R} |j\rangle \tag{4.5}$$

$$|j\rangle = \frac{1}{\sqrt{N}} \sum_q e^{-ix_j \pi q/k_R} |q\rangle \tag{4.6}$$

The model is a single-band model because there is only one state at each q value, a direct consequence of limiting the model to one state per lattice site. Rewriting the Hamiltonian in terms of eigenstates of q, we find

$$\hat{H} = \frac{1}{\sqrt{N}} \frac{1}{\sqrt{N}} \sum_{j,q,q'} -e^{-ix_j \pi q/k_R} |q\rangle\langle q'| e^{ix_{j+1} \pi q'/k_R} + \text{H.c.} \tag{4.7}$$

$$= \frac{1}{N} \sum_{j,q,q'} -(e^{-i(q-q')x_j \pi/k_R} e^{-i\pi q'/k_R} |q\rangle\langle q'| + \text{H.c.}) \tag{4.8}$$

$$= \sum_{q,q'} -\delta_{q,q'} (e^{i\pi q'/k_R} |q\rangle\langle q'| + \text{H.c.}), \tag{4.9}$$

where we have used the Kronecker delta sum identity

$$\frac{1}{N} \sum_j e^{i(q-q')j/N} = \delta_{q,q'}$$

with $x_j = aj/N$, where a is the lattice constant and $q_n = 2n\pi/a$, to evaluate the sum over j.

[1] In our case this is a discrete Fourier series due to the finite lattice size.

This gives us an expression for $\hat{H}_q$, which can be thought of as the diagonalized form of the Hamiltonian.

$$\hat{H}_q = -(e^{i\pi q/k_R} + e^{-i\pi q/k_R}) = -2J\cos(\pi q/k_R) \tag{4.10}$$

The spectrum of our tight binding model is a single band with cosinusoidal dispersion with bandwidth set by the tunneling strength J. Weaker tunneling strength—corresponding to a deeper lattice potential—results in a flatter band. The band structure is shown in Fig. 4.1 (a) for $J = 1$. Real lattice systems can approximate the behavior of the tight binding model when their potential is sufficiently deep so that only nearest-neighbor tunneling is present and excitations above the lowest band are not present.

4.3 Two-site Lattices

Next we consider lattices with two subsites per unit cell. The minimal model to understand the physics of two-site 1D lattices is the tight-binding Rice–Mele (RM) model [49].

$$\hat{H}_{\text{RM}} = \sum_j \Big[-\left(J' \left|j\uparrow\right\rangle\!\left\langle j\downarrow\right| + J \left|j+1\uparrow\right\rangle\!\left\langle j\downarrow\right|\right) + \text{H.c.} + \Delta(\left|j\uparrow\right\rangle\!\left\langle j\uparrow\right| - \left|j\downarrow\right\rangle\!\left\langle j\downarrow\right|)\Big] \tag{4.11}$$

This can be viewed as a generalization of Eq. 4.4 to include two sites per unit cell with separate intercell and intracell tunneling strengths (J and J'), as well as a relative energy offset between the subsites given by Δ. Because the RM model only allows tunneling between nearest neighbor subsites, it represents a bipartite lattice consisting of $\uparrow$ and $\downarrow$ sublattices, where sites in the $\uparrow$ sublattice are only coupled to sites in the $\downarrow$ sublattice and vice-versa. Because the bipartite RM model is a common theoretical tool to understand the physics of two-subsite lattices, the term

bipartite lattice is sometimes used to refer to two-subsite lattices without direct reference to the sublattice definition [50].

For the special case of $\Delta = 0$ the RM model reduces to the Su–Schrieffer–Heeger (SSH) model, originally developed to study electrons in polyethylene molecules [51].

$$\hat{H}_{\text{SSH}} = \sum_{j} -\left(J' \left|j \uparrow\right\rangle\!\left\langle j \downarrow\right| + J \left|j+1 \uparrow\right\rangle\!\left\langle j \downarrow\right|\right) + \text{H.c.} \tag{4.12}$$

Which tunneling strength J or J' is larger defines the dimerization of the lattice. We denote models with $J > J'$ as configuration I and $J' > J$ as configuration II. Note that the configuration definitions depend on the choice of unit cell.

Eqs. 4.11 and 4.12 express the non-interacting Hamiltonian in first-quantized form and express the site degree of freedom within each unit cell as a pseudospin-1/2 with the left subsite labeled by $\uparrow$ and the right subsite $\downarrow$. This can be thought of as mapping the spatial subsite degree of freedom to an internal degree of freedom possessed by each unit cell. Under this interpretation, we can describe intercell tunneling as a site jump accompanied by a pseudospin flip and intracell tunneling as a pseudospin flip. Tunneling between $\uparrow$ and $\downarrow$ subsites within the same unit cell flips the pseudospin leaving j unchanged, while tunneling to an adjacent unit cell flips the pseudospin and changes j by ± 1. We will elaborate on this mapping in Sec. 4.3.1.

Just as in the single band case, the discrete translational symmetry of this model leads to eigenstates labeled by crystal momentum, q, with each q value having two basis states to account

for the pseudospin degree of freedom, indexed by $\sigma = \uparrow, \downarrow$.

$$|q, \sigma\rangle = \frac{1}{\sqrt{N}} \sum_j e^{i x_j \pi q / k_R} |j, \sigma\rangle \tag{4.13}$$

$$|j, \sigma\rangle = \frac{1}{\sqrt{N}} \sum_q e^{-i x_j \pi q / k_R} |q, \sigma\rangle \,, \tag{4.14}$$

where j sums over unit cells. As before, we simply substitute these definitions to find the Hamiltonian's momentum space representation:

$$\begin{aligned} \hat{H} =& \Bigg[\frac{1}{N} \sum_{j,q,q'} J' e^{-ij(q-q')\pi/k_R} |\uparrow\rangle\langle\downarrow| + J e^{-i(j+1)(q-q')\pi/k_R} |\uparrow\rangle\langle\downarrow| + \text{H.c.} \\ & + \Delta(|q,\uparrow\rangle\langle q',\uparrow| - |q,\downarrow\rangle\langle q',\downarrow|) \Bigg] \end{aligned} \tag{4.15}$$

$$\hat{H}_q = -J'\hat{\sigma}_x - J\left(\cos(\pi q/k_R)\hat{\sigma}_x + \sin(\pi q/k_R)\hat{\sigma}_y\right) + \Delta\hat{\sigma}_z. \tag{4.16}$$

As before we used the Kronecker δ function identity to evaluate the sums over j and q'. Because the model includes a subsite degree of freedom, we are left with a 2×2 matrix for each q value. The Hamiltonian has eigenvalues within each q block given by

$$\epsilon_\pm(q) = \pm\sqrt{J^2 + J'^2 + 2JJ'\cos q + \Delta^2}. \tag{4.17}$$

Fig. 4.1 (b) shows the band structure for $\Delta = 0$ and different relative values of J and J'. When one tunneling strength dominates (either $J \gg J'$ or $J' \gg J$), the energies become essentially q-independent, meaning the bands are flat. In this case we say the lattice is fully dimerized because the system essentially consists of pairs of subsites coupled to each other but

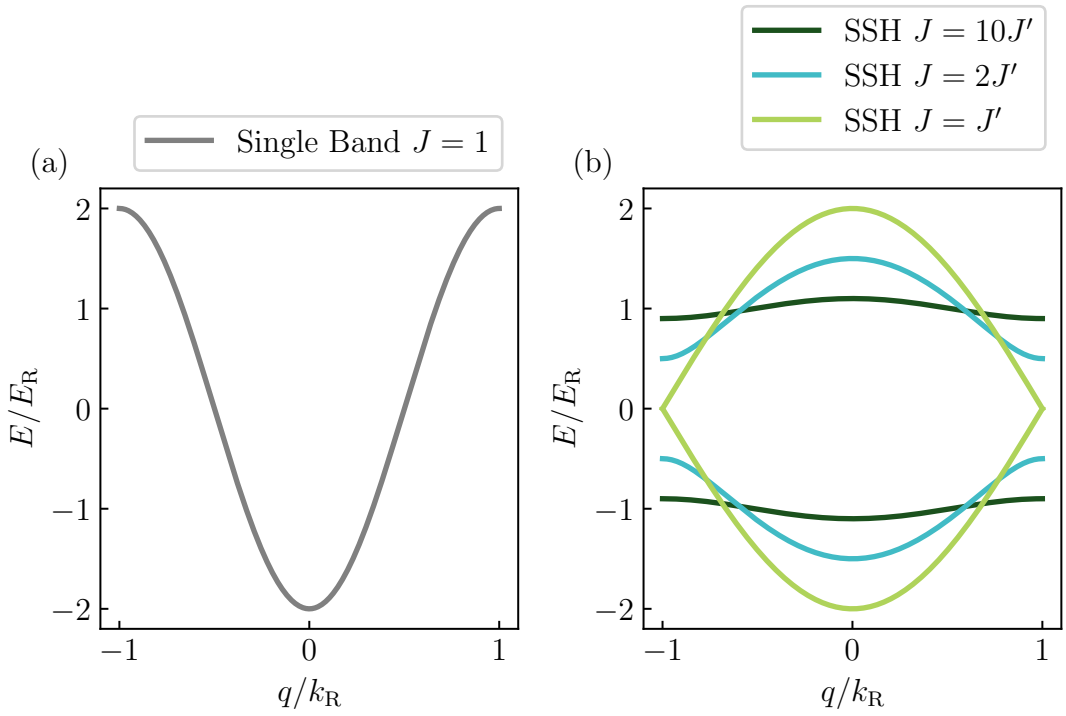

Figure 4.1: Band structure for tight-binding models. (a) Cosinusoidal band structure of the single band model. (b) Three cases for the SSH model: $J = 10J'$ (dark green), $J = 2J'$ (teal), and $J = J'$ (light green). The increased imbalance between tunneling strengths is associated with flatter bands and a wider band gap, while with equal tunneling strengths the gap closes.

uncoupled form the rest of the lattice.

In addition to the eigenvalues, we can study the form of the eigenstates for each q value. Since we have expressed $\hat{H}_q$ in terms of Pauli operators, we can interpret its eigenstates as being aligned along a vector $\mathbf{h}$ on the pseudospin Bloch sphere.

$$\mathbf{h} = (J' + J\cos q, J\sin q, \Delta)/|\epsilon| \tag{4.18}$$

$$\mathbf{h} = (\sin\theta\cos\phi, \sin\theta\sin\phi, \cos\theta), \tag{4.19}$$

where ϕ and θ are the azimuthal and polar angles on the Bloch sphere respectively, given by

$$|\epsilon|e^{-i\phi(q)} = Je^{iqa} + J', \tag{4.20}$$

and

$$\theta = \arctan\left(\frac{\sqrt{J^2 + J'^2 + 2JJ'\cos q}}{\Delta}\right). \tag{4.21}$$

Later, we will leverage this interpretation to describe pseudospin evolution under $\hat{H}$ as rotations about the $\mathbf{h}$ axis. The eigenstates of $\hat{H}$ are aligned along the $\mathbf{h}$ axis on the Bloch sphere, allowing us to use the familiar form [52] to write them.

$$u_{\pm}(q) = \begin{pmatrix} \cos(\theta(q)/2) \\ \pm\sin(\theta(q)/2)e^{-i\phi(q)} \end{pmatrix} \tag{4.22}$$

In the degenerate subsite ($\Delta \to 0$) limit the RM model reduces to the SSH model; for larger values of Δ the gap between the two bands increases. For the SSH case the eigenstates lie on the

equator of the Bloch sphere:

$$u_{\pm}(q) = \frac{1}{\sqrt{2}} \begin{pmatrix} 1 \\ \\ \pm e^{-i\phi(q)} \end{pmatrix}. \tag{4.23}$$

The band structure is unaffected by exchanging the role of J and J' as captured by Eq. 4.17. Despite this, the form of the eigenstates depends of the values of J and J' as determined by $\phi(q)$ in Eq. 4.23, not only the degree of dimerization. In the fully dimerized limit, this means the configuration I eigenstates wrap around the Bloch sphere with q, while the configuration II eigenstates are q-independent, pointing along $\mathbf{e}_x$ for all q. We will explore the topological implications of this fact in Ch. 5.

4.3.1 Spin Mapping

For completeness, we will review how we can interpret the tight binding RM Hamiltonian as a system with particles possessing spin, as well as the second quantized form of the Hamiltonian commonly used in the condensed matter literature. This section contains no new ideas; it only clarifies the relationship between different mathematical formations of equivalent models.

First, we note that the RM model from Eq. 4.11 can be equivalently expressed in second quantized notation:

$$\hat{H}_{\text{RM}} = -\sum_j \left[\left(J' \hat{b}_j^\dagger \hat{a}_j + J \hat{a}_{j+1}^\dagger \hat{b}_j + \text{h.c.} \right) + \Delta(\hat{a}_j^\dagger \hat{a}_j - \hat{b}_j^\dagger \hat{b}_j) \right], \tag{4.24}$$

where the $\hat{a}_j$ and $\hat{b}_j$ operators annihilate a particle on subsite $\uparrow$ or $\downarrow$ in the j^{th} unit cell.

Formally, it is always possible to factorize the Hilbert space for a particle in this tight binding model into a lattice site degree of freedom and a subsite degree of freedom, which can

be thought of as an internal pseudospin. The creation and annihilation operators can written as a spinor $\hat{\psi}_j = (\hat{\psi}_{j\uparrow}, \hat{\psi}_{j\downarrow})$ in the $|\uparrow\rangle, |\downarrow\rangle$ basis, with

$$\hat{a}_j \equiv \hat{\psi}_{j\uparrow} \tag{4.25}$$

$$\hat{b}_j \equiv \hat{\psi}_{j\downarrow}. \tag{4.26}$$

Terms from the second quantized RM Hamiltonian can thus be written

$$\hat{b}_j^\dagger \hat{a}_j + \text{H.c.} = \hat{\psi}_{j\uparrow}^\dagger \hat{\psi}_{j\downarrow} + \hat{\psi}_{j\downarrow}^\dagger \hat{\psi}_{j\uparrow} \tag{4.27}$$

$$= \hat{\psi}_j^\dagger \sigma^+ \hat{\psi}_j + \hat{\psi}_j^\dagger \sigma^- \hat{\psi}_j \tag{4.28}$$

$$= \hat{\psi}_j^\dagger \sigma_x \hat{\psi}_j \tag{4.29}$$

$$\hat{a}_{j+1}^\dagger \hat{b}_j + \text{H.c.} = \hat{\psi}_{j+1\downarrow}^\dagger \hat{\psi}_{j\uparrow} + \text{H.c.} \tag{4.30}$$

$$= \hat{\psi}_{j+1}^\dagger \sigma^+ \hat{\psi}_j + \text{H.c.} \tag{4.31}$$

$$\hat{a}_j^\dagger \hat{a}_j - \hat{b}_j^\dagger \hat{b}_j = \hat{\psi}_{j\uparrow}^\dagger \hat{\psi}_{j\uparrow} - \hat{\psi}_{j\downarrow}^\dagger \hat{\psi}_{j\downarrow} \tag{4.32}$$

$$= \hat{\psi}_j^\dagger \sigma_z \hat{\psi}_j. \tag{4.33}$$

Under this mapping, we can interpret multi-subsite lattices as spinful lattice systems. In the pseudospin language we can write the RM Hamiltonian as

$$\hat{H}_{\text{RM}} = \sum_j \left(J' \hat{\psi}_j^\dagger \sigma_x \hat{\psi}_j + J(\hat{\psi}_{j+1}^\dagger \sigma^+ \hat{\psi}_j + \text{H.c.}) + \Delta \hat{\psi}_j^\dagger \sigma_z \hat{\psi}_j \right), \tag{4.34}$$

and the SSH Hamiltonian as

$$\hat{H}_{\text{SSH}} = \sum_j \left(J' \hat{\psi}_j^\dagger \sigma_x \hat{\psi}_j + J(\hat{\psi}_{j+1}^\dagger \sigma^+ \hat{\psi}_j + \text{H.c.}) \right). \tag{4.35}$$

This explicitly shows how the RM model is equivalent to systems where spin plays a key role, such as the Floquet system with a spin-momentum locked linear (Dirac) dispersion system described in Ref. [53]. We will study this system experimentally using a bipartite lattice in Ch. 8.

Chapter 5: Topology and Evolution

In this chapter, we discuss the topology of quantum systems including static systems and dynamically evolving systems. Topology is of particular interest in condensed matter physics, because topological order [12,54] presents a paradigm to classify phases of matter distinct from and complimentary to the conventional approach based on spontaneously broken symmetries [55].

In mathematics, topology is the study of the global properties of spaces. The topology of a space is insensitive continuous changes to the local geometric properties of the space. Thus, topology quantifies the connectedness of a space but not the details like the distance between specific points. The local details can be changed by continuous deformation, but the topology cannot. Spaces or surfaces can be classified as topologically equivalent based on quantities called topological invariants [56]. In this chapter, we explore how these invariants arise, first in the mathematics of surfaces, then in the structure of quantum states, and finally in the dynamics of time-evolving Floquet systems.

5.1 Topology of Surfaces

We can gain some intuition for topology by thinking about the topology of 2D surfaces embedded in 3D space. The local geometry of a surface is quantified by its curvature, which can be changed by continuous deformations. The connectedness of a surface is quantified by the

genus g, which counts the number of holes in the surface.

The local curvature of a surface $\mathcal{M}$ is quantified by the Gaussian curvature K, defined as follows for a point $\mathbf{r}$ on $\mathcal{M}$. The normal vector $\mathbf{n}$ for the point $\mathbf{r}$ defines an infinite set of planes $p_{\mathbf{n}}$ containing $\mathbf{n}$. Each $p_{\mathbf{n}}$ corresponds to a normal section by its intersection with $\mathcal{M}$. The curvature κ_p for each plane is defined by the second derivative of the normal section at $\mathbf{r}$. The maximum and minimum values of κ_p are the principal curvatures at $\mathbf{r}$: κ_1, κ_2. The product of the principal curvatures gives the Gaussian curvature: $K = \kappa_1\kappa_2$.

An example for a point on a torus with inner radius 1 and outer radius $5/4$ is shown in Fig. 5.1, along with the planes corresponding to the principal curvatures, the principal normal sections (dashed lines), and the quadratic approximations to the normal sections (solid blue lines). In this case the normal sections of the torus are circles, so the quadratic approximation shown only approximately follows normal sections of the torus for points close to $\mathbf{r} = (5/4, 0, 0)$. For the point shown the Gaussian curvature is $K = 5/16$.

We note that K can also be defined in terms of the Ricci curvature scalar: $K = R/2$, which is itself defined as a contraction of the Riemann curvature tensor, defined in terms of derivatives of the metric tensor describing $\mathcal{M}$ [57].

Remarkably, the local curvature, quantified by K, is connected to the global topology, quantified by the genus, when we integrate contributions from the entire surface. This connection is given by the Gauss–Bonnet theorem [56], which we state for the case where the surface has no boundary:

$$\frac{1}{2\pi}\int_{\mathcal{M}} K dA = 2 - 2g. \tag{5.1}$$

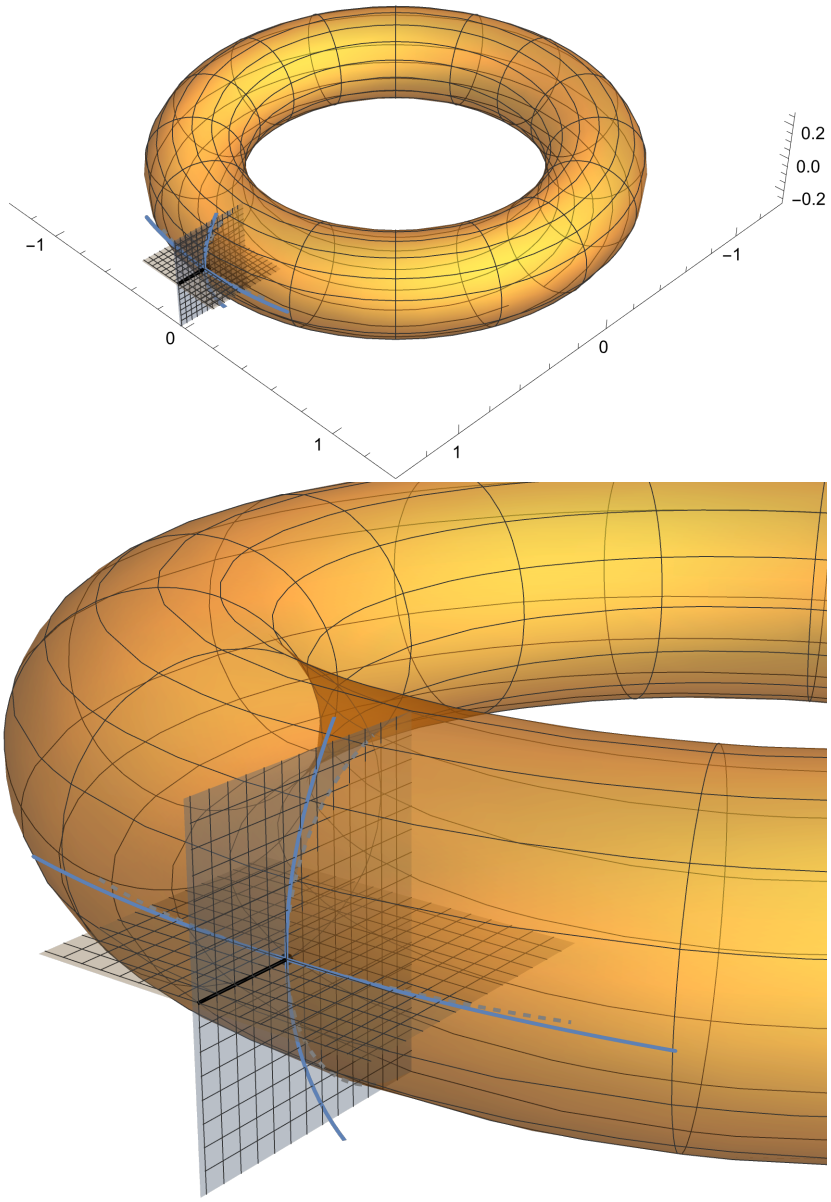

Figure 5.1: Normal vector (black), normal sections (dashed), and principal curvatures (blue) for the point $(5/4, 0, 0)$ on a torus with inner radius 1 and outer radius $5/4$. κ_1 and κ_2 have the same sign giving a positive Gaussian curvature $K = 5/16$.

5.2 Topology in quantum systems

In this section we describe how to quantify the topology of a set of quantum states, such as the states in the band of a lattice. We introduce how the presence of nontrivial topology ushers in edge states with interesting properties through the bulk-boundary correspondence. We define topological invariants for quantum systems, which classify equilibrium systems and are robust under continuous changes to the system Hamiltonian as long as no gaps close and no symmetries are added or removed. Finally, we extend these ideas, developed to topologically classify Hamiltonians based on their equilibrium eigenstates, by applying them to time-evolving systems.

5.2.1 Bulk-boundary Correspondence

One of the most striking consequences of topological physics is the bulk-boundary correspondence, which connects the bulk topology to the presence of dispersing states located on the boundary (or surface) of a system [13, 14, 58]. In fermionic systems, when these features exist in the band gap and intersect the Fermi energy, they acquire quantized, disorder resistant conduction properties. These features include edge states associated with the integer quantum Hall effect (QHE) and topological insulators [12, 13], which provide applications in metrology [59] and spintronics [60] respectively. This means that wherever we can find nontrivial topology, there is a possibility of finding edge states at the boundary between different regions (such as the boundary between a system with nontrivial topology and the vacuum).

For example, in the integer QHE, a large magnetic field induces a quantized Hall conductance (i.e. the ratio between the current and the perpendicular Hall voltage) [61], due to chiral

edge states connected to the bulk-boundary correspondence [62]. In this case the edge states can be thought of as 1D conducting channels whose origin lies with the topology of the 2D insulating bulk (we will introduce a description of the bulk topology in Sec. 5.4.3). Similarly 2D $\mathbb{Z}_2$ topological insulators (TIs) feature a pair of counter propagating edge states whose origin lies in the topology of the insulating 2D bulk [13]. The symmetry properties of these case are different, leading to different topological classifications, as we will explore in Sec. 5.3. The topological Floquet system we will describe in Ch. 8 has properties closely related to the conducting edge states of a $\mathbb{Z}_2$ TI, although the topological character of that system derives from the time resolved micromotion, rather than the bulk as in the TI case. The correspondence also is behind the existence of edge states in the 1D SSH model [51]. Since the boundaries of a 1D system are points, the edge states localized and can be thought of as zero dimensional.

5.3 Symmetry and Topology

The topological invariants that characterize equilibrium gapped quantum systems depend on the dimensionality of the system and what symmetries the system possesses [63–65].

"Ordinary" symmetries, described by unitary operators, can be used to decompose a Hamiltonian into decoupled sectors labeled by quantum numbers corresponding to eigenvalues of the symmetry operator. For example the discrete translational symmetry of lattice models allows us to write the Hamiltonian in terms of $\hat{H}_q$, giving a decoupled Hamiltonian for each crystal momentum value. With "nonunitary" symmetries this is not possible. The three "nonunitary" symmetries of particular interest are time-reversal symmetry (TRS) corresponding to $\mathcal{T}$, particle-hole symmetry corresponding to $\mathcal{P}$, and sublattice symmetry corresponding to $\mathcal{S}$. $\mathcal{T}$ is an antiunitary

operator that commutes with $\hat{H}$; $\mathcal{P}$ is an antiunitary operator that anticommutes with $\hat{H}$; and $\mathcal{S}$ is a unitary operator that anticommutes with $\hat{H}$. An antiunitary operator can be factorized into a unitary operator composed with complex conjugation, so we can write our three symmetries in terms of unitary operators. The symmetries are expressed in terms of unitary operators T, C, and S as $\hat{T}\hat{H}^*T^\dagger = \hat{H}$ for TRS, $\hat{C}\hat{H}^*\hat{C}^\dagger = -\hat{H}$ for PHS, and $\hat{S}\hat{H}\hat{S}^\dagger = -\hat{H}$ for SS. Note that it is possible to have $\hat{T}\hat{T}^* = \pm 1$ and $\hat{C}\hat{C}^* = \pm 1$, with $+$ and $-$ corresponding to different cases (in the case of TRS, systems with Kramer's degeneracy [25] have $-$).

These three symmetries are what determines the possible set of topological invariants for a system. Once the system has factorized into irreducible blocks, there are 10 possible ways the irreducible blocks can transform under combinations of $\mathcal{T}$, $\mathcal{P}$, and $\mathcal{S}$. This leads to the "ten-fold way," a classification of topological superconductors and topological insulators. Following Ref. [65], these classes are tabulated in Tab. 5.1, along with the topological indices for zero, one, and two dimensional systems. Here we assume the absence of defects, which modify the effective dimensionality of the system [65]. A value of 0 indicates that nontrivial topology is not possible in the given configuration. $\mathbb{Z}$ indicates the applicable topological invariant takes integer values, $2\mathbb{Z}$ corresponds to even integers, and $\mathbb{Z}_2$ corresponds to integers modulo 2. Tab. 5.1 merely states the existence of topological invariants. In the following sections we will explore how these invariants can be defined and calculated for specific cases.

5.3.1 Winding Numbers

The 1D SSH model possesses all three symmetries, with operators $\hat{S} = \hat{\sigma}_z$ for SS, $\hat{C} = \hat{\sigma}_z$ for PHS, and $\hat{T} = \hat{I}$ for TRS, putting it in class BDI. This means we expect an integer ($\mathbb{Z}$)

Symmetry class	TRS	PHS	SS	d=0	d=1	d=2
A	0	0	0	$\mathbb{Z}$	0	$\mathbb{Z}$
AIII	0	0	1	0	$\mathbb{Z}$	0
AI	+	0	0	$\mathbb{Z}$	0	0
BDI	+	+	1	$\mathbb{Z}_2$	$\mathbb{Z}$	0
D	0	+	0	$\mathbb{Z}_2$	$\mathbb{Z}_2$	$\mathbb{Z}$
DIII	-	+	1	0	$\mathbb{Z}_2$	$\mathbb{Z}_2$
AII	-	0	0	$2\mathbb{Z}$	0	$\mathbb{Z}_2$
CII	-	-	1	0	$2\mathbb{Z}$	0
C	0	-	0	0	0	$2\mathbb{Z}$
CI	+	-	1	0	0	0

Table 5.1: Symmetry classes and topological indices for zero, one, and two dimensional systems. 0 denotes a case where the system lack a symmetry, while $+$ and $-$ correspond to different symmetry operators.

topological invariant. For the SSH Hamiltonian this corresponds to a topological winding number ν. Recall from Eq. 4.18 that $\hat{H}_q$ can be defined in terms of the vector $\mathbf{h}(q)$. The winding number is defined as the number of times $\mathbf{h}(q)$ encircles the $\mathbf{e}_z$ axis as q ranges across the BZ [14]. Configurations with $J < J'$ have $\nu = 0$ while $J > J'$ gives $\nu = 1$, corresponding to the configurations I and II we introduced in Ch. 4.

In order to deform an SSH Hamiltonian with $\nu = 1$ to one with $\nu = 0$, we would need to pass through a point in parameter space with $J = J'$. Recall from Fig. 4.1 that for $J = J'$ the gap between the bands of the SSH model closes. Since the two configurations cannot be deformed into each other without closing the band gap, the configurations are topologically distinct, underscoring the role of ν as a topological invariant for the SSH model. Adding a finite Δ to generalize from the SSH model to the RM model breaks SS. (In general the RM model only possesses TRS.) When finite Δ is allowed, it becomes possible to adiabatically transform the $\nu = 0$ SSH configuration to $\nu = 1$ without closing the gap. Thus the winding number is not a topological invariant in the absence of SS. In contrast, adding perturbations that break TRS and

PHS while respecting SS moves the SSH model to class AIII, for which ν is still well defined. Thus the SS specifically can be said to protect ν.

As required by Tab. 5.1, ν can take on any integer value, although the simple SSH model only allows 0 and 1. Higher winding numbers are possible in models where matrix elements couple longer range states (although these couplings must preserve SS). The winding number can be used to quantify the topology of any state that includes all q in the BZ, including the out-of-equilibrium states we study in Ch. 7.

5.4 Berry's Phase

Another route to constructing topological invariants for quantum systems starts with the Berry's or geometric phase. To define the Berry's phase, we consider a quantum state evolving under the Hamiltonian $\hat{H}(\mathbf{n})$ where $\mathbf{n}$ is a general set of parameters for the Hamiltonian. In this framework we want to quantify how the state space defined by the eigenbasis of $\hat{H}(\mathbf{n})$ changes with changes in $\mathbf{n}$. Our introduction will closely follow Ref. [66]. We consider evolution starting from the j^{th} eigenstate of $\hat{H}(\mathbf{n}_0)$, with all changes made adiabatically. The state evolves under the time dependent Hamiltonian as

$$i\hbar\partial_t \left|\psi(t)\right\rangle = \hat{H}(\mathbf{n}(t)) \left|\psi(t)\right\rangle . \tag{5.2}$$

Because the evolution is adiabatic, the state will always be the j^{th} eigenstate of the instantaneous Hamiltonian $\hat{H}(\mathbf{n}(t))$. We will consider a cycle c in parameter space where $\mathbf{n}(T) = \mathbf{n}(0)$ at the

end of the cycle. At time t the state can be written

$$|\psi(t)\rangle = \exp(i\phi_d)\exp(i\phi_g)\,|j(\mathbf{n}(t))\rangle\,. \tag{5.3}$$

The evolution produces two phase factors: a dynamical phase ϕ_d and a geometric phase ϕ_g. The dynamical phase is the phase winding we expect from quantum mechanical evolution

$$\phi_d = -\frac{1}{\hbar}\int_0^T E_j(\mathbf{n}(t'))dt'. \tag{5.4}$$

This phase depends on the details of the evolution time and trajectory in parameter space and is not useful for topological classification. In contrast, the geometric phase can be viewed as a characterization of the Hamiltonian as function of its parameter space and the local geometry of its eigenbasis. The geometric phase is written

$$\phi_g = i\oint_c \langle j(\mathbf{n})|\,\nabla_{\mathbf{n}}\,|j(\mathbf{n})\rangle\cdot d\mathbf{n}, \tag{5.5}$$

where c is the cyclic path in parameter space. Each eigenvector $|j\rangle$ has its own Berry phase, with corresponding index j, which we will omit for simplicity. While the Berry's phase is often studied in quantum systems, it is also applicable to many areas in classical physics, from pendulums [67] to optical systems [68, 69].

Following Ref. [58], in analogy to the phase factor associated with gauge transformations of the electromagnetic field in quantum mechanics, and assuming three parameters, we define the Berry connection

$$\mathbf{A} = -i\,\langle j(\mathbf{n})|\,\nabla_n\,|j(\mathbf{n})\rangle\,, \tag{5.6}$$

and curvature

$$\mathbf{F} = \nabla_{\mathbf{n}} \times \mathbf{A}. \tag{5.7}$$

The connection and curvature are defined so that the Berry's phase can be calculated as a line integral of $\mathbf{A}$ or a surface integral of $\mathbf{F}$ in parameter space:

$$\phi_g(c) = \oint_c \mathbf{A} \cdot d\mathbf{l} \tag{5.8}$$

$$\phi_g(c) = \int_{\mathbf{S}} \mathbf{F} \cdot d\mathbf{S} \tag{5.9}$$

where $\mathbf{S}$ is the region of parameter space bounded by the curve c. The connection between line integrals of $\mathbf{A}$ and surface integrals of $\mathbf{F}$ is given by Stokes theorem, in direct analogy with the vector potential and magnetic field from electromagnetism. The Berry's phase is connected to the global phase freedom of the wavefunction. Under a gauge transformation, the Bloch states transform as

$$|u(q)\rangle \rightarrow e^{i\varphi(q)} |u(q)\rangle . \tag{5.10}$$

Likewise the Berry connection transforms as

$$\mathbf{A} \rightarrow \mathbf{A} + \nabla_q \varphi(q). \tag{5.11}$$

In contrast, the Berry curvature is gauge invariant.

For a spin- (or pseudospin-)1/2 particle, where the state space corresponds to the Bloch sphere, the Berry's phase is proportional to the area on the Bloch sphere (or solid angle) traced by a cyclic trajectory in parameter space [66].

Just as the local geometry (curvature) of a surface can be integrated to quantify its topology, the Berry's phase can be used to define topological invariants for quantum systems. The Berry's phase concept underlies the Zak phase in 1D lattice systems and the Chern number in 2D lattice systems.

5.4.1 Zak Phase

The state space of particles in a lattice in reciprocal space is the Brillouin Zone (BZ) as introduced in Ch. 4. In 1D, the BZ is a circle from $-k_R$ to k_R, so we can use the Berry phase acquired along a cyclic trajectory across the BZ as a topological classification:

$$\phi_{\mathrm{Z}} = i \int_{\mathrm{BZ}} dq \, \langle \psi(q) | \, \partial_q \, | \psi(q) \rangle \, . \tag{5.12}$$

This concept was first developed by Zak [70] and is connected to the average particle position within the unit cell (i.e. the polarization when the particles are charged) and is useful for studying ferroelectricity [58, 71].

In the presence of sublattice symmetry, as in the case of the SSH model, the Zak phase is equivalent to the winding number, and they are related by

$$\nu = \frac{\phi_{\mathrm{Z}}}{\pi}. \tag{5.13}$$

As with the winding number, SS is required for the Zak phase to be a topological invariant.

5.4.2 Gauge Ambiguity

As we noted when introducing the SSH model (Sec. 4.3), the role of J and J' depends on the choice of unit cell. Thus which models correspond to configurations I and II, with $\nu = 1$ and $\nu = 0$, depends on the labeling of unit cells. Unit cell dependence of nontrivial topology is a commonly accepted feature in topological models, though it is not always present (see for example Ref. [72]). This ambiguity is connected to the gauge freedom of the Berry's phase from the previous section, which extends to the Zak phase. A change in the unit cell can be viewed as a reciprocal-space gauge transformations that results in a change in the Zak phase and winding number [73].

Consider changing the unit cell to reverse the roles of J and J'. This change essentially flips the dimerization, causing states with a Zak phase of π to have a new phase of 0 and vice-versa. These two cases are related by a crystal momentum dependant unitary transformation

$$\hat{U}_q = \begin{pmatrix} 1 & 0 \\ 0 & e^{-iq\pi/k_R} \end{pmatrix}. \tag{5.14}$$

We can see how this operator changes the dimerization by applying it to the momentum space Hamiltonian, which in matrix form is

$$\hat{H}_q = \begin{pmatrix} 0 & -(e^{-iq\pi/k_R}J' + J) \\ -(e^{iq\pi/k_R}J' + J) & 0 \end{pmatrix}. \tag{5.15}$$

The transformed Hamiltonian is

$$\hat{U}_q \hat{H}_q \hat{U}_q^\dagger = \begin{pmatrix} 0 & -e^{iq\pi/k_R}\left(J' + Je^{-iq\pi/k_R}\right) \\ -e^{-iq\pi/k_R}\left(J' + Je^{iq\pi/k_R}\right) & 0 \end{pmatrix} \tag{5.16}$$

$$= \begin{pmatrix} 0 & -(e^{iq\pi/k_R}J' + J) \\ -(e^{-iq\pi/k_R}J' + J) & 0 \end{pmatrix}. \tag{5.17}$$

Moving the unit cell by half the lattice constant also flips the role of $\uparrow$ and $\downarrow$, exchanging the off diagonal matrix elements to give the original momentum space Hamiltonian with J and J' switched.

The Bloch sphere based on the new unit cell is different the one for the original model. $\hat{U}_q$ rotates the Bloch sphere about the $\mathbf{e}_z$ axis by a different amount for each q, so that a set of states that previously wrapped around the equator with q (giving $\phi_{\mathrm{Z}} = \pi$) have a fixed position on the new Bloch sphere (giving $\phi_{\mathrm{Z}} = 0$), thus changing the winding number of the trajectory given by the set of states. This example is illustrated in Fig. 5.2, where the untransformed states wrap around the equator, giving $\phi_{\mathrm{Z}} = \pi$, while the transformed states uniformly point to $\mathbf{e}_x$, giving $\phi_{\mathrm{Z}} = 0$.

More generally, it is possible to redefine the position of the $\uparrow$ and $\downarrow$ lattice sites within the unit cell to $ja + \delta_\uparrow$ and $ja + \delta_\downarrow$ via a gauge transformation [73]. This choice is related to our usual picture by the unitary

$$\hat{U}_q = \begin{pmatrix} e^{iq\delta_\uparrow} & 0 \\ 0 & e^{iq\delta_\downarrow} \end{pmatrix}. \tag{5.18}$$

Correspondingly, the eigenstates of $\hat{H}_q$ are modified with the azimuthal Bloch sphere angle

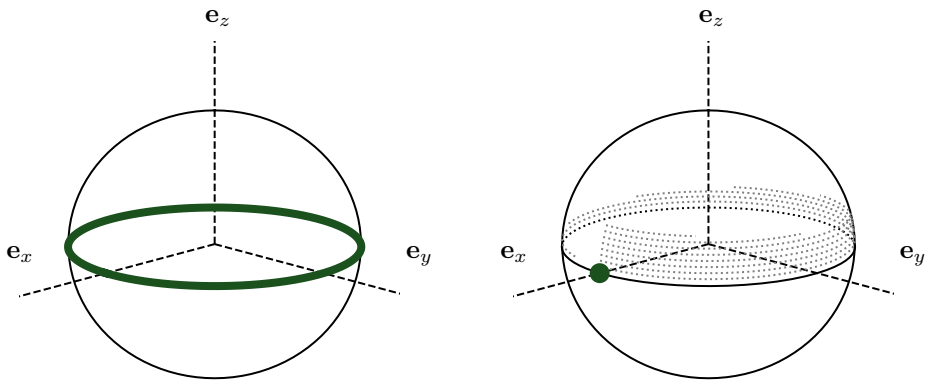

Figure 5.2: Illustration of crystal momentum dependent gauge transformation. Before the transformation states from $q = -k_R$ to $q = k_R$ trace the equator (left). After the transformation (right), they uniformly point to $\mathbf{e}_x$. Dotted lines indicate the rotation for different q values.

changing as $\phi(q) \to \phi(q) + q(\delta_\uparrow - \delta_\downarrow)$ and the Zak phase is changed by $\pi(\delta_\uparrow - \delta_\downarrow)/a$. This is related to the approach of Ref. [74], which ascribes a displacement of $a/2$ to inter- and intra-cell tunneling processes rather than treating the pseudospin as an internal degree of freedom, resulting in the Zak phase for the SSH bands being $\pm\pi/2$ for configurations with opposite dimerization.

Due to the gauge dependence of ϕ_{Z}, its absolute value generally does not have physical consequences. Differences in ϕ_{Z} do have physical consequences and will have the same value regardless of gauge or unit cell choice. In Sec. 6.2 we will introduce a technique that allows us to measure the full pseudospin state, and thus calculate ϕ_{Z}, by introducing a secondary lattice. This will allow us to avoid the unit cell ambiguity, essential giving measured quantities relative to the unit cell defined by the secondary lattice.

5.4.3 Chern Number

Chern numbers provide a topological classification of 2D insulators, capturing the topology of the integer quantum Hall effect. In a pioneering work, Thouless, Kohomoto, Nightingale, and

den Nijs first explained the quantized conductance in the integer QHE in terms of a topological invariant [12]. The TKNN invariant was later shown by Simon to be connected to the Berry's phase and the Chern class, a topological invariant from the mathematics of fiber bundles [75].

The Chern number does not rely on the presence of symmetry and corresponds to the $\mathbb{Z}$ invariant for Class A, $d = 2$ in Tab. 5.1. As suggested by its connection to the QHE, where a large magnetic field breaks TRS, an overall nonzero Chern number requires TRS to be broken.

The Chern number is defined in terms of the Berry curvature integrated over reciprocal space. The reciprocal space of a 2D lattice forms a torus, with q_x and q_y defining the 2D parameter space. We can interpret the Berry curvature as a flux going through the area elements of this reciprocal space.

$$\mathcal{F}(q_x, q_y) = \mathbf{F}(q_x, q_y) \cdot d\mathbf{S}_{(q_x,q_y)} = \frac{\partial A_x}{\partial q_y} - \frac{\partial A_y}{\partial q_x} \tag{5.19}$$

The Chern number is defined by integrating the flux of the Berry curvature.

$$c_n = \frac{1}{2\pi} \iint_{\mathrm{BZ}} \mathcal{F}(q_x, q_y) dq_x dq_y \tag{5.20}$$

For discretely sampled systems Ref. [76] provides a robust approach to calculating Chern numbers that enforces the integer requirement. Thus noise or experimental imperfections will not result in a noninteger Chern number, even when a naive calculation with Eq. 5.20 would. In this framework we define a set of link variables describing how the q-space wavefunction changes between points on the discretely sampled BZ, which acts as a q-space lattice. For simplicity, we will assume the 2D BZ discretely sampled at intervals of Δ, although this constraint can be

relaxed. The link variables are defined

$$U_x(q_x, q_y) = \langle j(q_x, q_y)|j(q_x + \Delta, q_y)\rangle \,/|\, \langle j(q_x, q_y)|j(q_x + \Delta, q_y)\rangle \,|. \tag{5.21}$$

The $U_x(q_x, q_y)$ link variable is the normalized overlap between the state at (q_x, q_y) and the state on the next lattice site in the x direction. $U_y(q_x, q_y)$ is similarly defined for the state at the next site in the y direction.

The link variables define the discretely sampled Berry connection and curvature.

$$A_x(q_x, q_y) = \frac{1}{i} \ln U_x(q_x, q_y), \tag{5.22}$$

and

$$\mathcal{F}(q_x, q_y) = \frac{1}{i} \ln U_x(q_x, q_y) U_y(q_x + \Delta, q_y) U_x(q_x, q_y + \Delta)^{-1} U_y(q_x, q_y)^{-1}, \tag{5.23}$$

where both quantities are defined on the branch of the logarithm giving $A_x(q_x, q_y)$, $\mathcal{F}(q_x, q_y)$ within $[-\pi, \pi)$. Formally, $\mathcal{F}$ is defined at each discrete BZ point, but it should be thought of as corresponding to a plaquette, as shown in Fig. 5.3

The Chern number can be calculated by summing the Berry curvature over the BZ:

$$c_n = \frac{1}{2\pi} \sum_{\text{BZ}} \mathcal{F}(q_x, q_y). \tag{5.24}$$

This method produces equivalent results to the continuum definition (Eq. 5.20), but always yields an integer, meaning errors and noise will not alter the result unless they are large enough to overwhelm the signal [76]. This property relies on the periodicity of wavefunctions in the BZ.

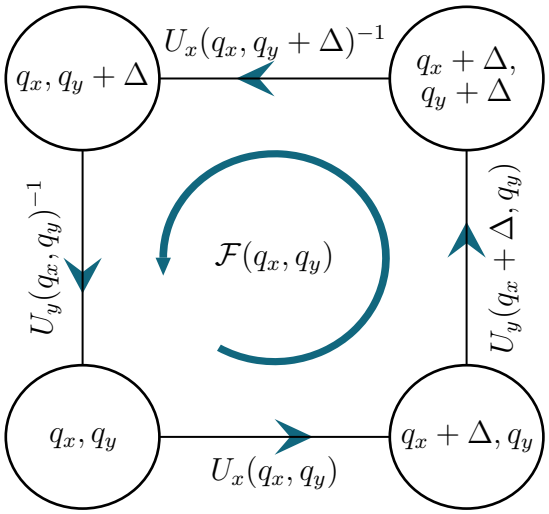

Figure 5.3: Calculating Chern numbers in a discretely sampled BZ. The Berry curvature $\mathcal{F}(q_x, q_y)$ plays the role of a flux per plaquette in the lattice formed by the discretely sampled BZ.

5.5 Topological Dynamics

We introduced topology describing the properties of a set of quantum states, particularly the (equilibrium) eigenstates of a Hamiltonian. This is just the beginning for us; next we explore how we can use topology to understand the dynamics of a time-evolving quantum system. This includes scenarios when the static topological invariants, such as the Zak phase and winding number, change under quantum evolution, explored experimentally in Ch. 7. Additionally we study scenarios where a topological invariant can be defined over the dynamics themselves, explored experimentally in Ch. 8.

5.5.1 Topological Charge Pumps

In addition to the Quantum Hall effect, Thouless provided an paradigmatic example of topological physics with a description of adiabatic charge pumping in a 1D driven system [12].

This system consists of a time modulated 1D lattice with a filled lower band. Fig. 5.4 (a) shows a cartoon of how periodic lattice modulation can lead to a displacement of one unit cell per period. Bipartite lattices are a common choice for studying charge pumping. Fig. 5.4 (b) shows schematically how the bipartite lattice potential can be cyclically changed to give a net displacement per cycle. We can understand this type of charge pumping with a time dependent RM model (Eq. 4.11) with periodically modulated $J(t) = J(t+T)$, $J'(t) = J'(t+T)$, and $\Delta(t) = \Delta(t+T)$. In parameter space, in terms of Δ and $J-J'$ (Fig. 5.4 (c)) the number of times the cyclic trajectory encircles the origin gives the net charge pumped per cycle [77, 78].

We can calculate the charge moved by the system by using the connection between the Zak phase and the instantaneous polarization, with the flow of charge given by the change in polarization over the cycle.

$$\Delta p = \frac{1}{2\pi}\left(\oint_{\mathrm{BZ}} dq\, \langle\psi(t=0,q)|\, \partial_q\, |\psi(t=0,q)\rangle - \oint_{\mathrm{BZ}} dq\, \langle\psi(t=T,q)|\, \partial_q\, |\psi(t=T,q)\rangle\right), \tag{5.25}$$

where p is the dimensionless polarization, proportional to the electrostatic polarization by the charge e when the pumped particles are electrons. The line integrals are taken in opposite direction along the BZ as shown in Fig 5.4 (d). We can apply Stokes theorem to turn the line integral into an integral of the Berry curvature, making the pumped charge equal to the Chern number for the space spanned by q and t [12, 58].

$$\Delta p = c_n = \frac{1}{2\pi}\int_{BZ}\int_0^T \mathcal{F}(t,q)\, dq dt \tag{5.26}$$

This nicely shows the topological origin of the charge pump as well as the quantization of

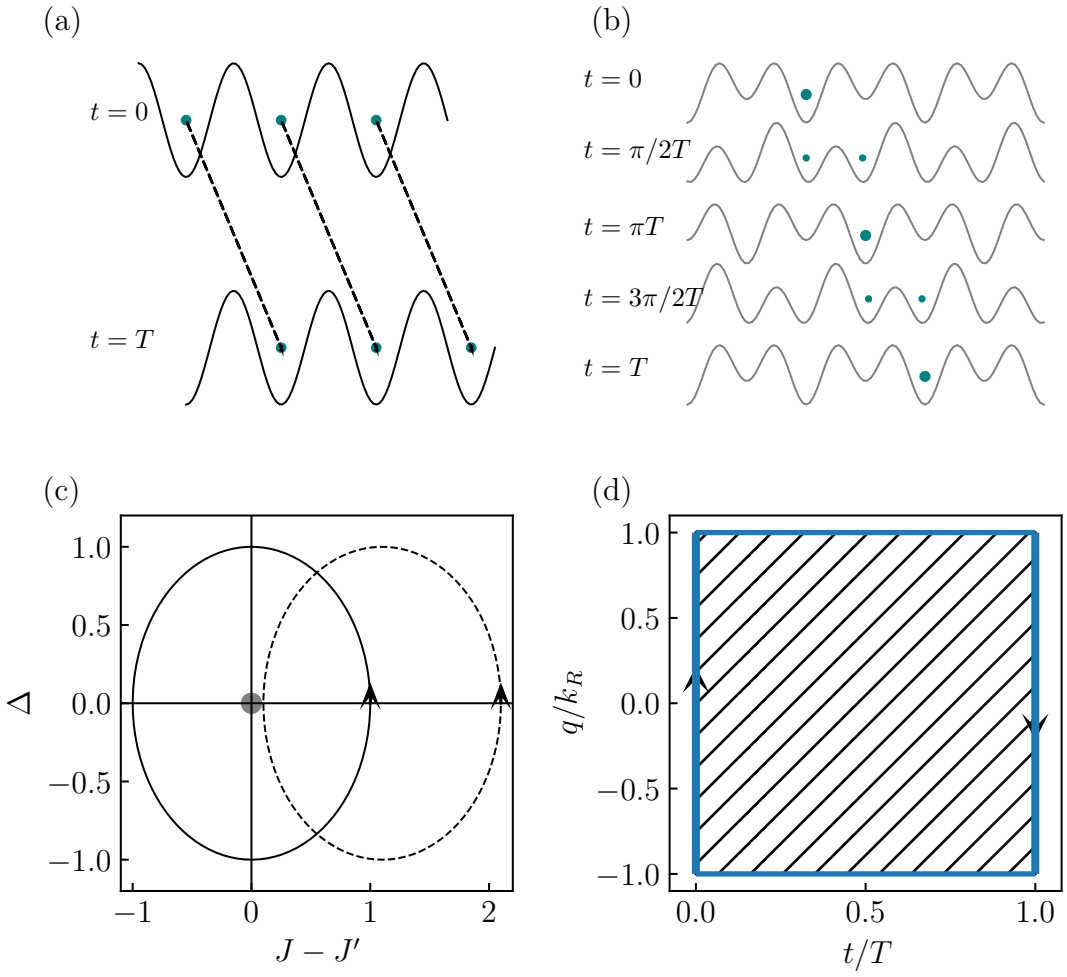

Figure 5.4: Charge pumping schematic. (a) Conceptual sketch of Thouless pumping. A periodically modulated lattice potential leads to a nonzero displacement per cycle, here one lattice site. (b) Example of charge pumping in a bipartite lattice. (c) Cyclic pumping trajectory in parameter space for the RM model. Trajectories that encircle the origin result in topological charge pumping. (d) Parameter space for Thouless pumping. The Chern number characterizing a topological charge pump is defined over the periodic q, t space. The quantized charge pumped per cycle is given by integrating the Berry curvature in the cross-hatched region.

the charge pumped per cycle, given by c_n. This is a special case of the much broader topological classification of Floquet systems we will explore in Sec. 5.5.2.

These ideas have been brought into the lab in several ultracold atom experiments [50, 78–80], using both fermions and bosons. Since the topological charge pump requires a filled band, in the bosonic case if the BEC wavefunction is localized around a single q value, the pumping can be thought of as "geometrical" charge pumping, with the particle transport depending on the local geometry of the band structure, rather than its global topology. Recently theorist have sought to generalize the usual adiabatic pumping to high frequency topological pumps [81, 82].

5.5.2 Floquet Winding Numbers

The insight that dynamics themselves can have topology was greatly extended by Kitagawa et. al. in Ref. [83] to classify the topology of Floquet quantum systems, creating a general topological classification based on the dynamics of the system. To understand this classification, we must introduce the preliminaries of Floquet theory.

Particles experiencing a periodically time varying Hamiltonian, with $\hat{H}(t) = \hat{H}(t+T)$, can be described in terms of Floquet modes $|\psi_\nu(t)\rangle = \exp\{(-i\epsilon_\nu t/\hbar)\}|\upsilon_\nu(t)\rangle$, where $|\upsilon_\nu(t)\rangle = |\upsilon_\nu(t+T)\rangle$ has the time periodicity of the Hamiltonian and ϵ_ν is the quasienergy of the Floquet mode, defined modulo $2\pi\hbar/T$. The mathematics of Floquet theory are directly analogous to Bloch's theorem, applicable when the potential is periodic in space as introduced in Sec. 4.1. The stroboscopic dynamics (observed periodically at intervals of T) of a Floquet system can be described by a time independent Hamiltonian $\hat{H}^{\mathrm{F}}$ whose eigenvalues are the quasienergies ϵ_ν. The stroboscopic evolution of a lattice Floquet system is thus described by Bloch–Floquet

eigenstates defined in the Floquet–Brillouin zone.

The evolution over a Floquet period is given by a time ordered exponential

$$\hat{U}(t_0, t_0 + T) = \mathcal{T} \exp\left[\int_{t_0}^{t_0+T} -\frac{i}{\hbar}\hat{H}(t')dt'\right]. \tag{5.27}$$

Note that the specific form of the operator depends on the choice of initial time t_0. Physically this means that the stroboscopic behavior depends on the choice of time when the stroboscopic observations are made. For simplicity we will take $t_0 = 0$. Numerically the time evolution can be calculated by treating $\hat{H}(t)$ as constant over the interval δt, to give the unitary evolution operator from t to $t + \delta t$, then taking the matrix product of the corresponding unitaries.

The Floquet topological invariants (winding numbers) classify the Floquet time evolution operator $\hat{U}(T)$. Static topological systems have trivial Floquet topology, and Floquet systems can have nontrivial Floquet topology even in the absence of static/conventional topology. This clarifies the distinction between systems where Floquet engineering is used to achieve nontrivial static topology, such as the first proposed Floquet topological insulators [84] and cases like charge pumping where the nontrivial topology derives from the evolution itself. This topological classification is not specific to lattice (Floquet–Bloch) systems, but as we are focused on lattices, we will specify our discussion to Floquet–Bloch systems.

The winding number is related to the quasienergy spectrum, and to the micromotion within each Floquet period [83,85]. For a Floquet–Bloch system the first winding number can be written

$$\nu = \frac{1}{2\pi}\sum_{\alpha}\int_{\mathrm{BZ}} \frac{d\varepsilon_\alpha(q)}{dq} T dq \tag{5.28}$$

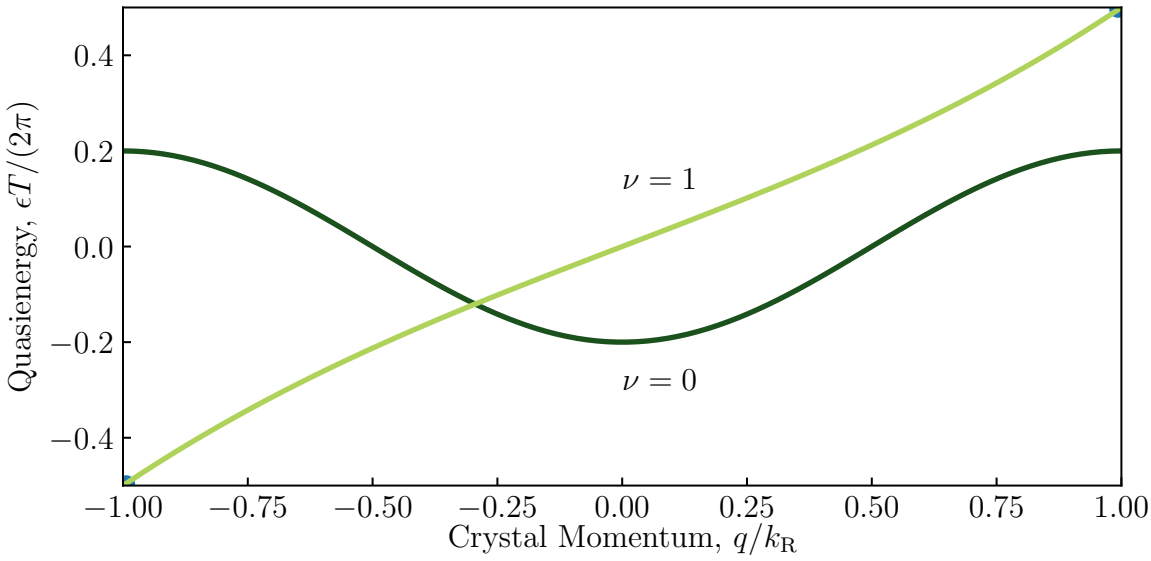

Figure 5.5: Example Floquet–Bloch band structure. One band contributes 0 to the sum in Eq. 5.28, while the other contributes 1. Note that the highlighted points at the band edge are connected due to the periodicity of the Floquet–BZ.

where α indexes the quasienergy bands. Fig. 5.5 show two example bands contributing 0 and 1 to the sum defining the Floquet winding number. The periodicity of the Floquet–BZ allows continuous bands to span the quasienergy coordinate, making $\nu > 0$ possible for a continuous band. This is not possible in static systems with well behaved lattice potentials, where bands are continuous across the edge of the BZ.

When symmetry allows us to separate the state space into decoupled sectors (as will be the case in Sec. 8.3) we can define individual winding numbers for the sectors.

$$\nu_\sigma = \frac{1}{2\pi} \int_{\mathrm{BZ}} \frac{d\varepsilon_\sigma(q)}{dq} T dq \tag{5.29}$$

where σ labels the sector. In Ch. 8 we will introduce a Floquet system where nontrivial topology, characterized by Floquet winding numbers gives rise to linear dispersion across the BZ.

Ref. [83] generalizes this understanding to higher order winding numbers for higher di-

mensional system, but we will focus on ν. ν can be applied to topological charge pumps with the modification that the sum in Eq. 5.28 only ranges over the filled bands [83]. In this case the quasienergy winding number is equivalent to the q, t Chern number defined over the micromotion in Eq. 5.26, discussed in Sec. 5.5.1.

Floquet topology underlies the idea of "anomalous" Floquet topological insulators which have nontrivial topology described by the winding number only in contrast to the first proposed Floquet topological insulators [84], which use Floquet modulation to achieve conventional (static) topology. These are systems inspired by a proposal from Kitagawa et. al. [83] for a 2D system in a modulated hexagonal lattice with chiral edge modes characterized by ν. These ideas have been realized in photonic systems [86, 87] as well as ultracold atoms [88]. The latter experiment measured the underlying winding number using a clever simplification [89] rather than a full characterization of the micromotion or quasienergy spectrum.

Chapter 6: State Dependent Raman Lattice

In this chapter we introduce the experimental details of our state dependent lattice systems, describing the tools we use in the lab to realize the theory models we introduced in Ch. 4. Our implementation uses a combination of RF and Raman dressing fields to produce a highly tunable and measurable two-subsite lattice, which closely matches the bipartite Rice–Mele (RM) lattice model for appropriate parameters. We introduce a measurement technique that allows us to measure the population in each sublattice, which we extend using quantum state tomography to fully characterize the quantum state of the sublattice pseudospin degree of freedom. We describe the theory of our system, including its band structure, then present experimental data showing the pseudospin makeup of the ground bands in different configurations as well as the displacement over a tunneling oscillation between subsites. This chapter includes results published in Refs. [90] and [91] in Secs. 6.4.2 and 6.5 respectively.

6.1 Raman Bipartite Lattice

Our experimental two-site lattice system consists of two optical Raman fields and one RF magnetic field all driving transitions between the internal states $|f = 1, m_F = 0, \pm 1\rangle$ of our BECs, as shown in Fig. 6.1. This builds on work described in Ref. [50] as well as a related case with single-tone Raman fields from Refs. [33, 92]. The three hyperfine states are separated by

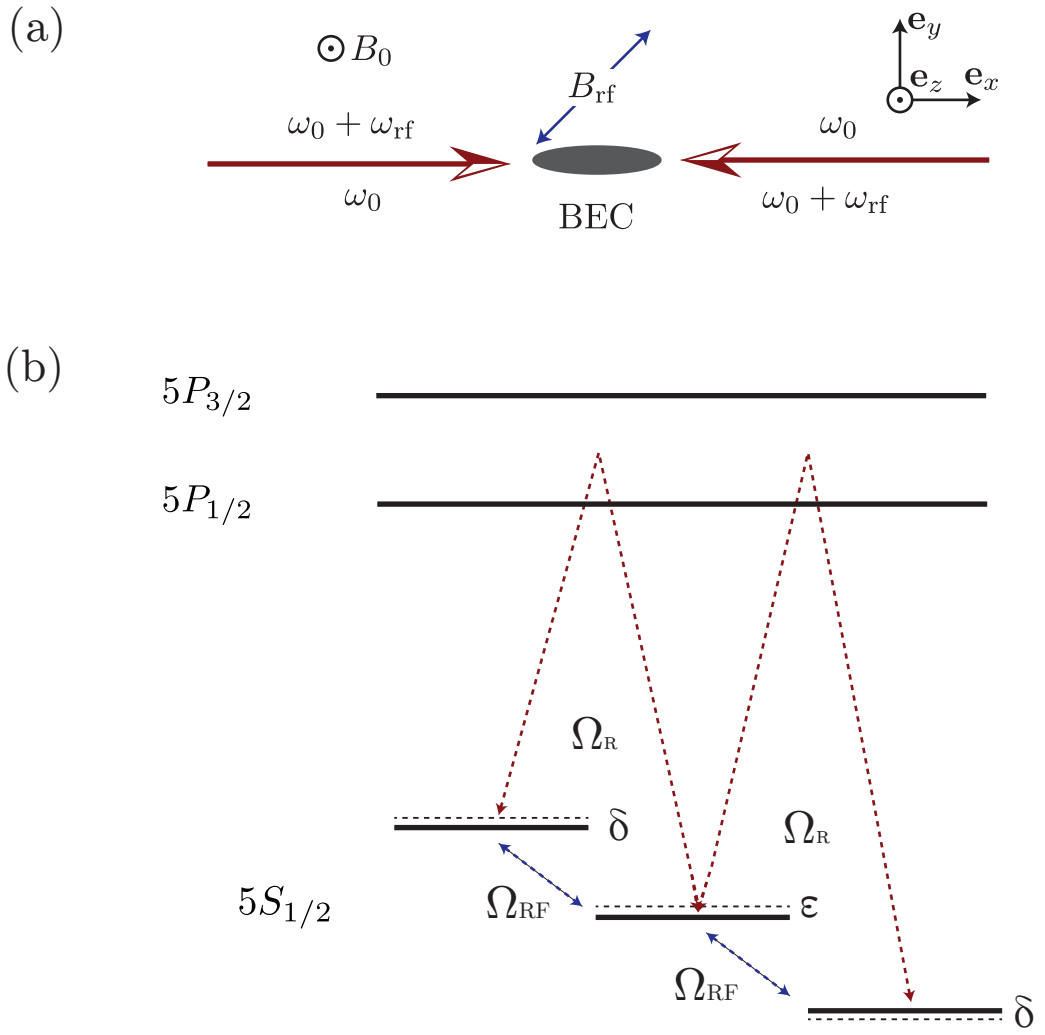

Figure 6.1: Schematic of combined Raman-RF driving. (a) Experimental geometry. Two counter-propagating laser beams each carry two frequency components to drive Raman transitions. (b) Level diagram showing Raman and RF transitions within the $f = 1$ manifold.

Zeeman frequency $\omega_{\mathrm{Z}} \approx 1\ \mathrm{MHz}$, induced by an external magnetic field of $\approx 0.1\mathrm{mT}$ along z. Our control fields consist of an RF magnetic field with frequency ω_{RF} and two pairs of cross-polarized laser fields each with frequency components ω_0 and ω_{RF} in order to drive Raman transitions. The RF field couples hyperfine states with the same momentum ($|k, m_F\rangle \leftrightarrow |k, m_F \pm 1\rangle$), with strength Ω_{RF}. The two pairs of Raman fields couple hyperfine states with different momentum ($|k, m_F\rangle \leftrightarrow |k \pm 2k_R, m_F \pm 1\rangle$) with strengths Ω_+ and Ω_-. We used $790.03(2)\mathrm{nm}$ (close to the "magic" or tune-out wavelength [93]) for the Raman laser beams in order to cancel the state independent scalar light shift from the D1 and D2 transitions; this choice also gives close to the minimum spontaneous emission rate for a given Raman coupling.

Following our discussion in Sec. 2.4 the interaction between the atoms and the fields can be expressed as a fictitious magnetic field [23, 94] interacting with the total atomic angular momentum operator $\hat{\mathbf{F}}$:

$$H_{\mathrm{int}} = \mathbf{\Omega}(\hat{x}) \cdot \hat{\mathbf{F}}. \tag{6.1}$$

The fictitious magnetic field

$$\mathbf{\Omega}(\hat{x}) = [\Omega_{\mathrm{RF}} \cos(\phi_{\mathrm{RF}}) + \bar{\Omega} \cos(2k_R\hat{x}), -\Omega_{\mathrm{RF}} \sin(\phi_{\mathrm{RF}}) - \delta\Omega \sin(2k_R\hat{x}), \sqrt{2}\delta]/\sqrt{2} \tag{6.2}$$

includes terms originating from the detuning $\delta = \omega_{\mathrm{Z}} - \omega_{\mathrm{rf}}$; the RF Rabi frequency Ω_{RF}; the relative phase ϕ_{RF} between the RF and Raman fields; and Raman parameters $\bar{\Omega} = \Omega_+ + \Omega_-$ and $\delta\Omega = \Omega_+ - \Omega_-$, which derive from $\Omega_\pm$ [50, 91]. This follows from Eqs. 2.40 and 2.42 for the specific form of our two-tone laser fields with the addition of an RF magnetic field.

The spatial components of the field $\mathbf{\Omega}(\hat{x})$ trace an ellipse as x ranges from 0 to $\lambda_{\mathrm{R}}/2$, which

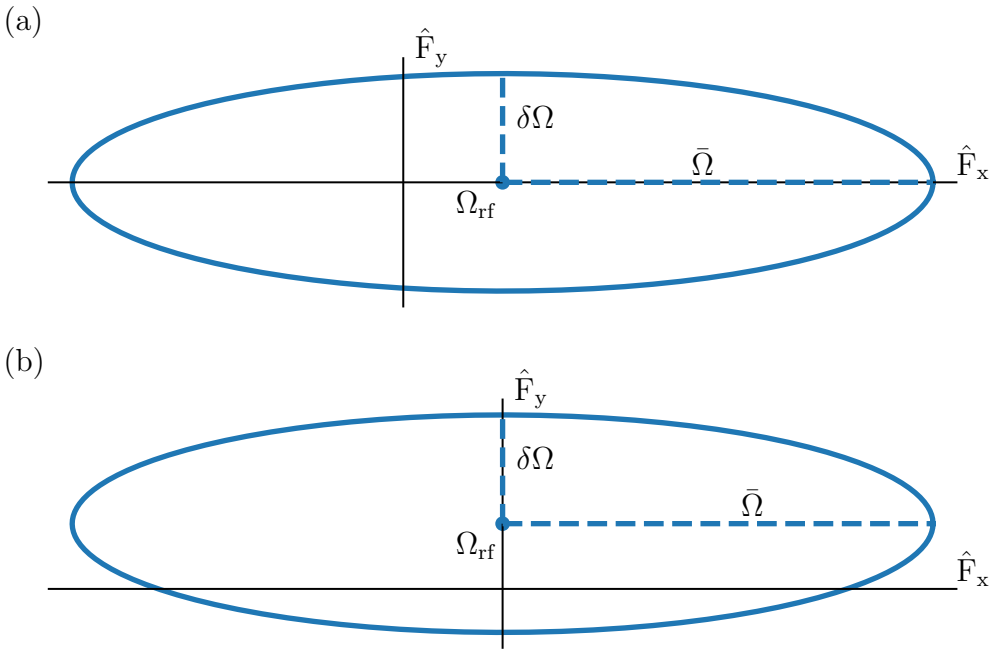

Figure 6.2: Ellipse showing $\mathbf{\Omega}(\hat{x})$ for $\Omega_+ = 12.7$, $\Omega_- = 5.7$ and $\Omega_{\mathrm{RF}} = 4.2$ for $\phi_{\mathrm{RF}} = 0$ (a) and $-\pi/2$ (b). In both cases the ellipse lies in the $x-y$ plane because $\delta = 0$

.

defines our unit cell. The $\mathbf{e}_z$ component is entirely controlled by δ, which we will take to be small compared to the other terms. The major and minor axes of the ellipse are set by $\bar{\Omega}$ and $\delta\Omega$, while the center is set by Ω_{RF}. This ellipse is plotted in Fig. 6.2 for two representative configurations with different values of ϕ_{RF}. Conceptually, the vertices correspond to the potential minima of the lattice, so the major axis length, set by $\bar{\Omega}$, along with the $\mathbf{e}_x$ components of Ω_{RF} determines the depth of the potential minima. The covertices approximately correspond to the potential maxima, so the barrier height is set by $\bar{\Omega}$ and the $\mathbf{e}_y$ components of Ω_{RF}. This picture gives some intuition for the tunability of the resulting lattice system. By selecting ϕ_{RF}, we can select between a lattice with a large energy offset between its subsites as in (a), or a lattice with an imbalance between the two barrier heights as in (b).

Adiabatic (Born–Oppenheimer) potentials for the setup are shown in Fig. 6.3 for represen-

tative parameter values and different values of ϕ_{RF}. As we can see from the adiabatic potentials, the system produces a two-site lattice whose barrier heights and sublattice energy splitting can be controlled by the RF and Raman parameters. Additionally the internal state depends on the position in the lattice, with $\langle \hat{F}_x \rangle = \pm 1$ corresponding to the two subsite minima within each unit cell. This system can be well approximated by the Rice–Mele (RM) model, characterized by nearest-neighbor tunneling strengths J, J', and energy offset Δ, as long as the lattice is deep enough that we can neglect next-nearest-neighbor tunneling. This condition effectively makes our system a bipartite lattice.

The Raman lattice also has a full spectrum of higher bands, included unbound bands, which are not present in the RM model. In our experiments, we tried to limit any population in higher bands, and used temporal filtering on our data to reduce the contribution from any higher band population, which is associated with higher frequency components.

We tune the parameters of the lattice using ϕ_{RF}, controlling both the energy splitting Δ and the imbalance between J and J'. In practice we are most interested in the limiting cases of a balanced lattice with $J \gg J'$ (configuration I) or $J' \gg J$ (configuration II); or a tilted lattice with large Δ and $J \approx J'$. A relatively strong RF coupling makes each case possible for the appropriate value of ϕ_{RF}. We use intermediate cases for our pseudospin readout protocol (described in Sec. 6.2). The coupling strength Ω_{RF} controlls the magnitude of Δ or the imbalance between J and J', depending on the value of ϕ_{RF}. We select the values of Ω_+ and Ω_- to produce a deep lattice with negligible next-nearest-neighbor tunneling and a value of Ω_{RF} large enough to produce a highly dimerized system when desired.

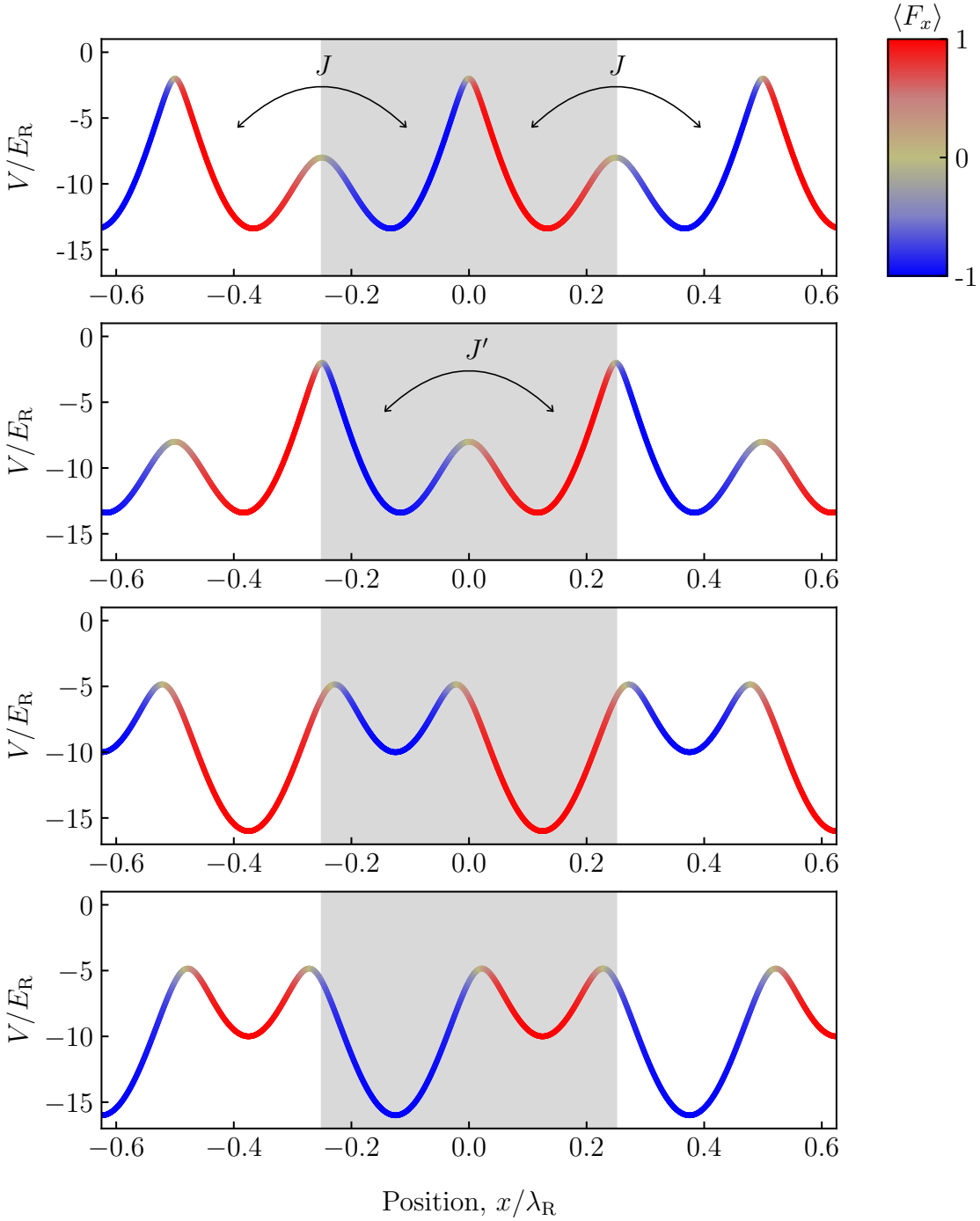

Figure 6.3: Adiabatic potentials for combined Raman-RF lattice for $\Omega_+ = 12.7E_R$, $\Omega_- = 5.7E_R$, $\Omega_{\mathrm{RF}} = 4.2E_R$. The four cases shown have $\phi_{\mathrm{RF}} = -\pi/2,\ \pi/2,\ \pi$, and 0. The central unit cell is shaded in gray.

6.1.1 Raman Lattice Band Structure

To calculate the band structure of the lattice, we write the Hamiltonian for the system in momentum space, using a basis of

$$\{|q + 2Nk_R, m_F = 1\rangle, |q + 2Nk_R, m_F = 0\rangle, |q + 2Nk_R, m_F = -1\rangle\},$$

where N formally ranges from $-\infty$ to $+\infty$; for calculations, we truncate the basis at $\pm N_{\max}$, restricting our model to the lowest $3(2N_{\max}+1)$ bands. The RF field appears as a matrix element between hyperfine states with the same momentum ($|q + 2Nk_R, m_F\rangle \leftrightarrow |q + 2Nk_R, m_F \pm 1\rangle$), proportional to Ω_{RF}. The two pairs of Raman fields provide matrix element coupling between hyperfine states with momentum differing by $2k_R$ ($|q + 2Nk_R, m_F\rangle \leftrightarrow |q + 2Nk_R \pm 2k_R, m_F \pm 1\rangle$) proportional to Ω_+ and Ω_-. We combine these terms, along with the kinetic energy and quadratic Zeeman energy to write the momentum space Hamiltonian in matrix form.

$$\hat{H} = \begin{pmatrix} \ddots & \mathbf{RA} & & & \\ \mathbf{RA}^\dagger & (\mathbf{KE}(-1) + \mathbf{RF}) & \mathbf{RA} & & \\ & \mathbf{RA}^\dagger & (\mathbf{KE}(0) + \mathbf{RF}) & \mathbf{RA} & \\ & & \mathbf{RA}^\dagger & (\mathbf{KE}(+1) + \mathbf{RF}) & \mathbf{RA} \\ & & & \mathbf{RA}^\dagger & \ddots \end{pmatrix} \tag{6.3}$$

Where the three submatrices are

$$\mathbf{KE}(N) = \hbar^2(q - 2Nk_R)^2/2m \otimes \mathbf{1}, \tag{6.4}$$

corresponding to the kinetic energy with $\mathbf{1}$ being the identify matrix on the internal angular momentum subspace;

$$\mathbf{RF} = \begin{pmatrix} \delta & \Omega_{\text{RF}}\exp(-i\phi_{\text{RF}})/2 & 0 \\ \Omega_{\text{RF}}\exp(i\phi_{\text{RF}})/2 & -e_{\text{q}} & \Omega_{\text{RF}}\exp(-i\phi_{\text{RF}})/2 \\ 0 & \Omega_{\text{RF}}\exp(i\phi_{\text{RF}})/2 & -\delta \end{pmatrix}, \tag{6.5}$$

corresponding to the RF coupling along with the detuning from RF/Raman resonance δ and the quadratic Zeeman shift (given by $-e_{\text{q}}$); and

$$\mathbf{RA} = \begin{pmatrix} 0 & \Omega_+/2 & 0 \\ \Omega_-/2 & 0 & \Omega_+/2 \\ 0 & \Omega_-/2 & 0 \end{pmatrix}, \tag{6.6}$$

corresponding to the two-tone Raman coupling.

Fig. 6.4 shows the band structure (calculated from the eigenvalues of Eq. 6.3) for the full model for two configurations, one with a large subsite energy offset and one with equal subsite energies. For the configuration in (a) the large sublattice energy offset results in the two lowest bands being composed of states localized to different sublattice sites, giving them significantly different magnetization. The lowest band is almost entirely composed of the $|\downarrow\rangle$ states with $\langle \hat{F}_x \rangle = -1$, while the next band consists almost entirely the $|\uparrow\rangle$ states with $\langle \hat{F}_x \rangle = +1$, giving them nearly pure magnetization. In contrast, the case shown in (b) has balanced sublattice sites, resulting in equal sublattice populations for the band states (as predicted in Eq. 4.23), giving $\langle \hat{F}_x \rangle = 0$. The flatness of the bands indicates that our system will work well to approximate

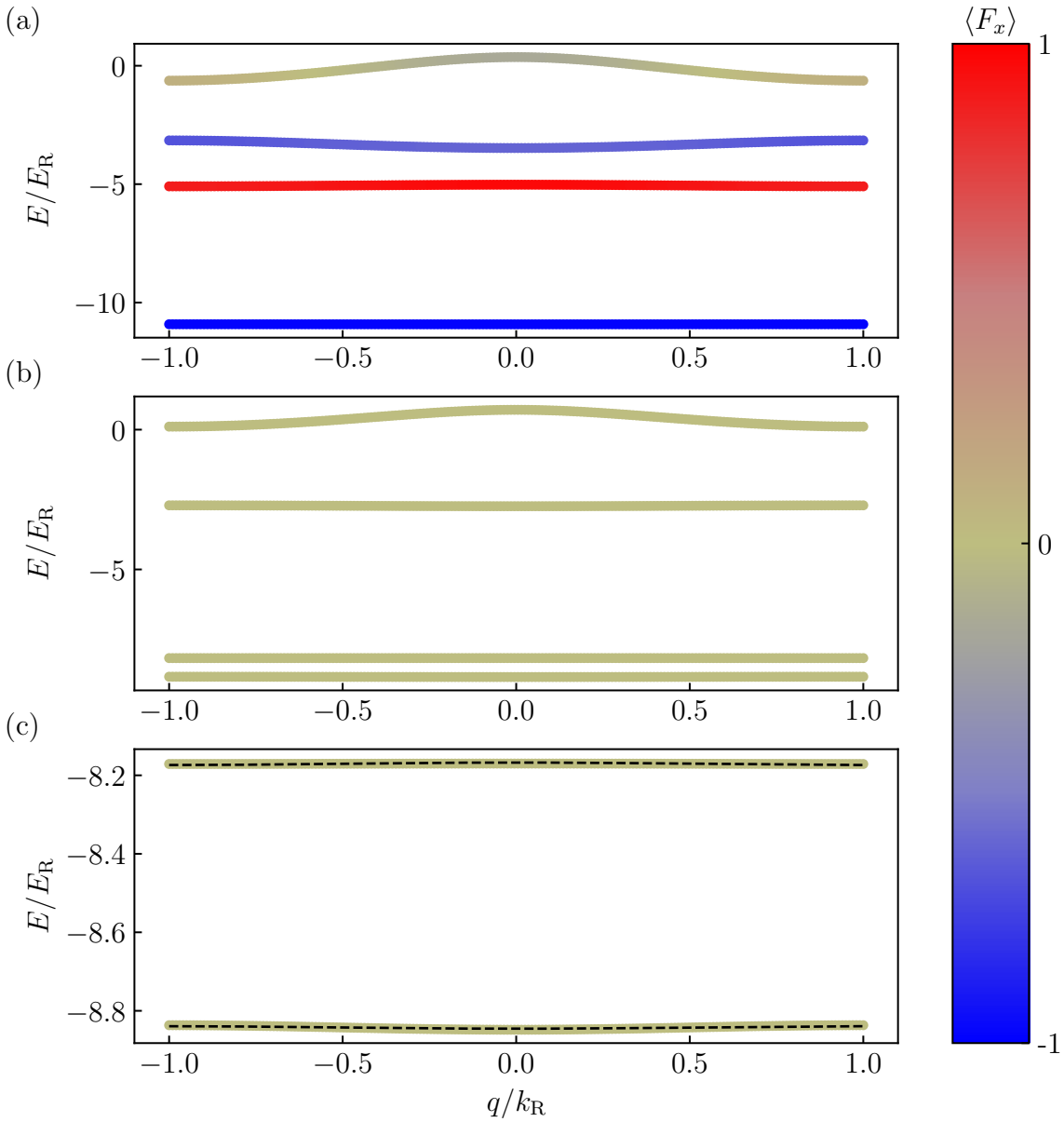

Figure 6.4: Band structure of Raman lattice in two configurations. (a) Imbalanced (large Δ) configuration. (b) Balanced (SSH) configuration. (c) Zoom on lowest two bands from (b) and comparison to SHH model with $J = -0.34E_R, J' - 0.0032E_R$ (dashed black curves).

a highly dimerized RM model, as shown by the fit to the RM band structure in (c). The large separation between the lowest band (in the case of (a)) or doublet of bands (in the case of (b)) indicates that higher bands in our system will not inhibit our system from approximating the RM model (in large Δ cases the separation will only be valid for states occupying the lowest band).

6.1.2 Lattice Calibration

In order to determine the parameters of our lattice, we employ pulsing experiments starting from a well defined initial state: a BEC at rest corresponding to $|k = 0\rangle$ with initial internal state $|f = 1, m_F = 0\rangle$ (other internal states could be used, but we selected $|f = 1, m_F = 0\rangle$ for reasons of symmetry). By abruptly turning on the lattice, we observe transitions into higher momentum states along with changes to the internal state. This evolution is described by the momentum space Hamiltonian in Eq. 6.3.

The RF signals used to generate the frequency shifted Raman laser fields as well as the RF magnetic field are generated by phase coherent channels from the same `Novatech` DDS synthesizer, equipped with four phase-synchronous outputs (see Sec. 3.7.2). The relative phase of the fields experienced by the atoms depends on the path each signal takes as it is amplified and, in the case of the Raman signals, imprinted on the laser beams. Thus the relative phase at the atoms must be calibrated, so that the control phase can be set to yield the desired value of ϕ_{RF}.

The pulsed lattice time evolution could be used to fit to a model for all the RF and Raman parameters, including ϕ_{RF}. In practice it is best to calibrate the RF and Raman components separately, using the combined evolution to calibrate ϕ_{RF} only. An example of pulse data with a fit is shown in Fig. 6.5, where we simplify the data by summing over k states, only showing the

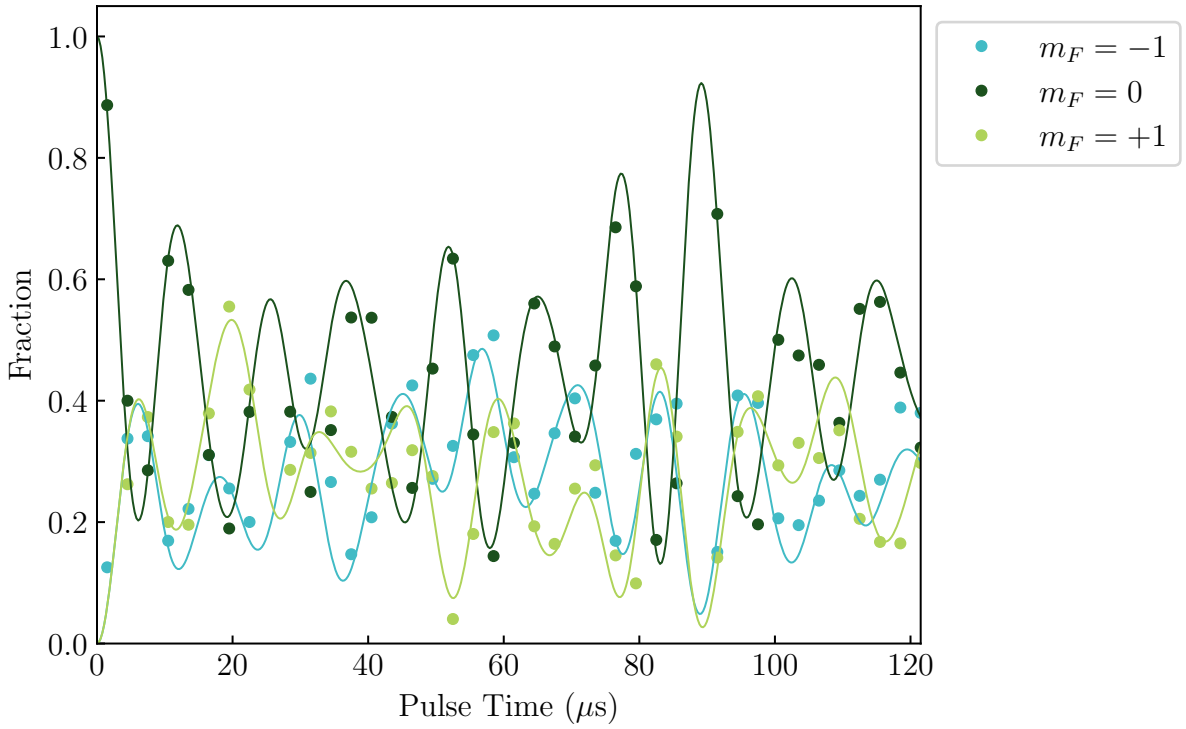

Figure 6.5: Lattice pulsing experiment for calibration. To simplify the evolution, we sum the population in different k states, showing the internal state summed over k. The theory curves are a fit to ϕ_{RF} with $\Omega_+ = 12.7E_R, \Omega_- = 5.6E_R, \Omega_{\text{RF}} = 4.5E_R$, yielding $\phi_{\text{RF}} = 0.22\pi$.

internal state.

6.1.3 Measurement

Measurement of the pseudospin degree of freedom requires measuring the relative population within the $\uparrow$ and $\downarrow$ sublattices. This could in principle be achieved with sublattice site resolution imaging [95], but we take a less direct approach leveraging the state dependence of our lattice. The subsite populations are highly correlated with the internal atomic state, specifically the angular momentum, which we can measure using Stern–Gerlach time-of-flight (SG ToF) imaging as introduced in Sec. 2.5.2.

As shown in Fig. 6.3, $\uparrow$ and $\downarrow$ sites are highly polarized, with $\langle \hat{F}_x \rangle \approx \pm 1$, corresponding

to atomic states $|m_x = \pm 1\rangle$. Our default readout sequence begins by abruptly removing the coupling fields and applying an RF pulse to map eigenstates of $\hat{F}_x$ to the standard $\hat{F}_z$ measurement basis. During the following ToF the SG effect separates the hyperfine states, ultimately yielding the momentum distribution of the $|\uparrow, \downarrow\rangle$ pseudospin states. Summing the populations separated by $2k_R$ yields the pseudospin resolved crystal momentum distribution, from which we can obtain $\langle \hat{\sigma}_z(q) \rangle$ for the pseudospin. We discuss how to extend this protocol to other pseudospin bases in Sec. 6.2.

6.1.4 Comparison to Bichromatic Method

Another natural approach to producing two-site lattices uses the scalar light shift from two phase-coherent laser beams of wavelength λ and $\lambda/2$ [73, 74]. As with garden variety single component optical lattices, the optical field results from the interference between forward-going and retro-reflected beams giving a standing wave intensity pattern $\propto \cos^2$. Both the λ and $\lambda/2$ lattices can be considered far detuned (although one may be blue detuned with the other red detuned) and produce a state independent potential via the scalar light shift. The combined lattice potential for the bichromatic configuration is

$$V(x) = V_\mathrm{s} \cos^2(k_R x/2) + V_\mathrm{l} \cos^2(k_R x + \phi_\mathrm{l}), \tag{6.7}$$

where $k_R = 2\pi/\lambda$ is defined in terms of the long period lattice. For a deep lattice the lowest bands of the bichromatic configuration can closely match the properties of the SSH model, as show in Fig. 6.6.

Like our Raman-RF lattice, this approach allows the relative barrier heights and tunneling

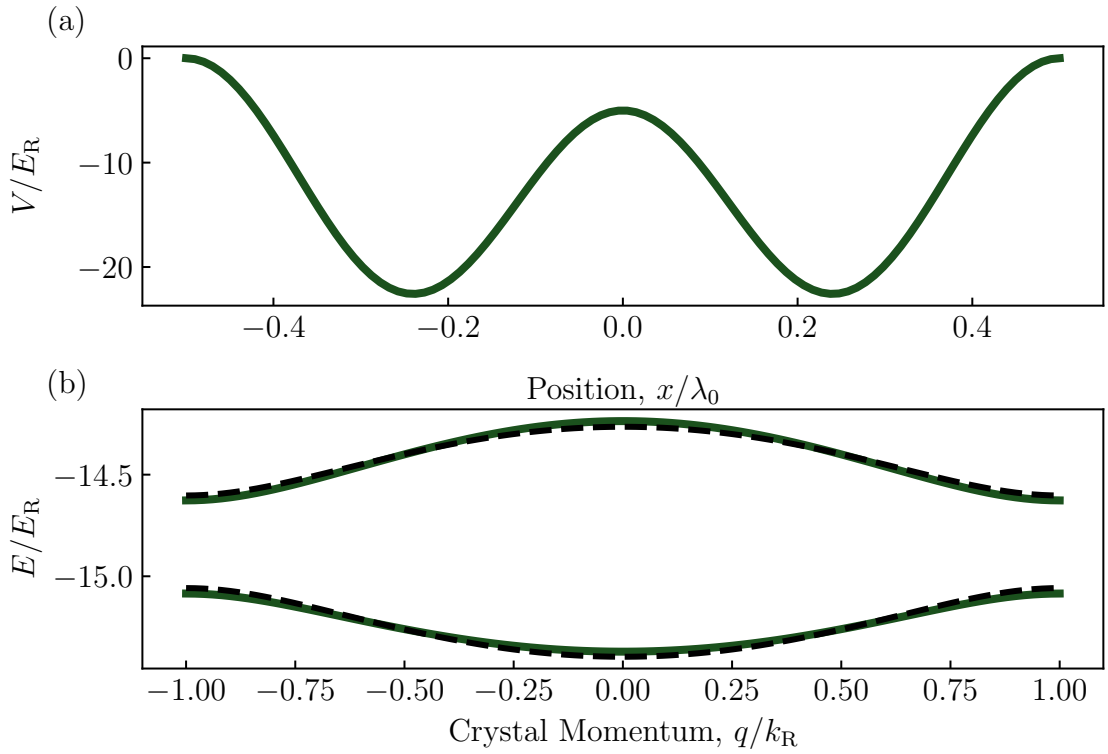

Figure 6.6: Bichromatic optical lattice. (a) Optical lattice potential with $V_{\mathrm{s}} = -20E_R$ and $V_{\mathrm{l}} = -5E_R$ in a balanced configuration. (b) Lowest bands. Green solid curves show the numerically calculated band structure for the bichromatic lattice, while black dashed curves show a closely matching SSH model band structure.

strengths to be tuned, in this case with the relative phase between the two optical standing waves. Because this approach involves different wavelengths an additional phase shift can be introduced by changes in air pressure due to the differential index of refraction between the two wavelengths.

This approach lacks the versatile measurability of our system, but techniques have been developed to measure the sublattice populations in general two-site lattices [96, 97].

6.2 Pseudospin Rotations

We use the tunability of our bipartite optical lattice to implement a form of quantum state tomography, allowing us to characterize the full quantum state of the pseudospin degree of free-

dom for each q value. Our standard readout protocol to measure the $\langle \hat{F}_x \rangle$ component of atomic angular momentum is a measurement of subsite pseudospin degree of freedom in the $|\uparrow\rangle, |\downarrow\rangle$ basis (yielding $\langle \hat{\sigma}_z \rangle$). To measure other components of the pseudospin, $\langle \hat{\sigma}_x \rangle$ and $\langle \hat{\sigma}_y \rangle$, we must apply evolution equivalent to a rotation on the pseudospin Bloch sphere, from the $\mathbf{e}_x$ or $\mathbf{e}_y$ axis to the $\mathbf{e}_z$ axis.

By allowing our system to evolve under a set of carefully chosen secondary lattices, we apply a q-independent pseudospin rotation, allowing us to measure the subsite degree of freedom in three linearly independent bases ($\langle \hat{\boldsymbol{\sigma}}(q) \rangle$). Together, these three measurements allow us to reconstruct full the quantum state via quantum state tomography.

6.2.1 Quantum State Tomography on a Subsystem

Quantum state tomography is a method of reconstructing the full quantum state of a system from multiple measurements on similarly prepared systems. In the simplest case of a two-state system, tomography can be achieved by measurements in the eigenbases of the familiar $(\hat{\sigma}_x, \hat{\sigma}_y, \hat{\sigma}_z)$ Pauli operators, with each expectation value specifying a component of the Bloch vector $\mathbf{b} = (\langle \hat{\sigma}_x \rangle, \langle \hat{\sigma}_y \rangle, \langle \hat{\sigma}_z \rangle)$, although expectations values of any set of three linearly independent operators can be used to reconstruct $\mathbf{b}$ [98]. In this simple case, the state can be reconstructed as

$$\hat{\rho} = \frac{1}{2} \left(I + \langle \hat{\sigma}_x \rangle \hat{\sigma}_x + \langle \hat{\sigma}_y \rangle \hat{\sigma}_y + \langle \hat{\sigma}_z \rangle \hat{\sigma}_z \right). \tag{6.8}$$

These measurements can be constructed by performing a unitary transformation then measuring in a fixed basis (normally $\hat{\sigma}_z$ by convention). The effective measurement basis after applying the

unitary $\hat{U}$ and measuring in the $\hat{\sigma}_z$ basis corresponds to the operator $\hat{U}^\dagger \hat{\sigma}_z \hat{U}$:

$$\langle \hat{\sigma}_z \rangle_{\hat{U}\hat{\rho}_0\hat{U}^\dagger} = \mathrm{Tr}\left(\hat{U}\hat{\rho}_0\hat{U}^\dagger\hat{\sigma}_z\right) \tag{6.9}$$

$$= \mathrm{Tr}\left(\hat{\rho}_0\hat{U}^\dagger\hat{\sigma}_z\hat{U}\right) \tag{6.10}$$

$$= \left\langle \hat{U}^\dagger\hat{\sigma}_z\hat{U} \right\rangle_{\hat{\rho}_0} \tag{6.11}$$

where we used the cyclic property of the trace in the second equality.

In our lattice systems we perform tomography on a single degree of freedom—the pseudospin. This is possible if our pre-measurement unitary transformations are q-independent, meaning they rotate the pseudospin state equivalently for all q and leave q unchanged. Because we combine the pseudospin measurements with momentum-resolved time-of-flight imaging, our measurements independently give the pseudospin state for all q values present in the system.

Unitary evolution under our lattice Hamiltonian corresponds to a pseudospin rotation about an axis determined by J, J', and Δ, as discussed in the context of Eq. 4.18. In general this axis is q-dependent, except when $J = 0$. Using configurations with $J' \gg J$, allows us to approximate q-independent evolution. By setting $\Delta = 0$ and allowing evolution for a calibrated time we can achieve a rotation about the $\mathbf{e}_x$ axis, allowing us to rotate $\hat{\sigma}_y$ eigenstates to $\hat{\sigma}_z$ eigenstates via a $\pi/2$ rotation. Unfortunately, our system does not allow for $\mathbf{e}_y$ axis rotations; however, we can circumvent this limitation with a different lattice configuration. We use a $J' = \Delta$ configuration to generate rotation about an axis between $\mathbf{e}_x$ and $\mathbf{e}_z$. Rotating about this axis by π transforms $\hat{\sigma}_x$ eigenstates to $\hat{\sigma}_z$ eigenstates. Data from our experimental realizations of the readout evolution are shown in Fig. 6.7 along with the corresponding trajectory on the pseudospin Bloch sphere. In principle we could also achieve the desired rotation by first rotating by $\pi/2$ around $\mathbf{e}_z$ then by

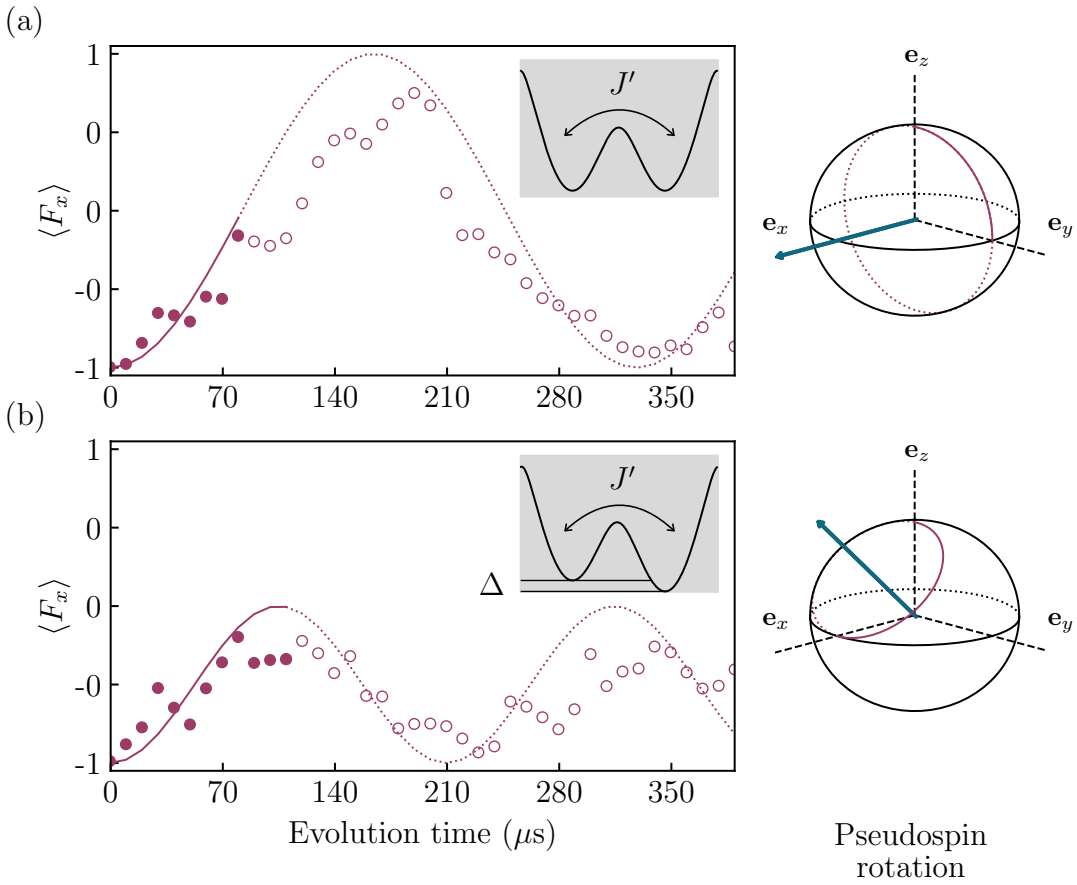

Figure 6.7: Evolution in readout lattices corresponding to pseudospin rotation. (a) y readout lattice. (b) x readout lattice. The left column shows the time evolution under each readout lattice (pictured in the gray inset). Evolution up to the calibrated pulse time is shown with solid symbols and solid lines while evolution past this time is shown with open symbols and dashed lines. The right column shows the corresponding rotations on the Bloch sphere allowing for measurement in the $\hat{\sigma}_x$ and $\hat{\sigma}_y$ bases via native $\hat{\sigma}_z$ measurement.

$\pi/2$ around $\mathbf{e}_x$. In practice each switch between secondary lattices adds experimental complexity and requires additional calibration, so we opt for the single-rotation approach.

Hauke et. al. proposed a related approach to pseudospin measurement in a bipartite lattice in which the system is quenched to a Hamiltonian with flat, energy offset bands (analogous to $\Delta \gg J' \gg J$ for our system) for a variable time, allowing the pseudospin Bloch vector for each q value to be determined from the amplitude and phase of resulting oscillation [99]. This form of Bloch state tomography has been applied experimentally in bipartite 2D lattices in and out of equilibrium [100–102].

6.2.2 Unit Cells and Secondary Lattices

As can be seen in Fig. 6.3, which tunneling strengths correspond to J and J' depends on the definition of the unit cell. Since the unit cell definition is arbitrary, one would expect the key physics to be agnostic to this choice. However, our pseudospin mapping treats intercell and intracell tunneling differently, making the unit cell definition important. In order to measure pseudospin quantities that depend on the unit cell (i.e. $\langle\hat{\sigma}_x\rangle$ and $\langle\hat{\sigma}_y\rangle$ but not $\langle\hat{\sigma}_z\rangle$) we must use a secondary lattice, which effectively fixes our unit cell. The secondary lattice is highly dimerized with one dominant tunneling strength J'; to treat secondary lattice evolution as q-independent we must define our unit cell as the unit cell where the secondary lattice allows intracell tunneling. Our unit cell- or basis-dependent pseudospin measurements are thus defined relative to the secondary lattice.

6.2.3 Remaining Phase Ambiguity

Quantum states are only defined up to an overall phase. For a two-state system, we can parameterize all possible states by the probability amplitude associated with each basis vector and a relative phase. When reconstructing a state vector from the density operator, the result has an arbitrary overall phase. For an individual two-state system this phase has no physical meaning and can be chosen to fit the a desired convention.

Our crystal momentum-resolved pseudospin state reconstruction suffers from a potential ambiguity since the overall phase of reconstructed state for each q becomes a relative phase between the different $|\psi(q)\rangle$. This choice can be viewed as a momentum space gauge transformation and thus affects no observables but in some cases introduces an offset to the calculated Zak phase.

6.3 Technical Implementation

To implement the lattice, we use two pairs of counterpropagating Raman beams, using the setup introduced in Sec. 3.8 and an RF magnetic field, using the setup introduced in Sec. 3.7.2. Our lattice system requires phase coherence between all the RF tones in the system. To achieve this, we generate all the tones for our lattice experiments using a single `Novatech` DDS synthesizer. As discussed in Sec. 6.1.3 we use an RF magnetic field for the readout process as well as the lattice portions of our experiment. To provide full flexibility for the phase of the readout field, we implement a separate readout channel connected to the RF amplifier and coils.

Our pseudospin measurement process requires another, nominally independent phase. Ideally this would be implemented with a fifth phase synchronized DDS channel. Due to the tech-

nical limitations of our setup we instead reuse the RF readout channel for this purpose. This is possible because the phase required for the $\hat{F}_x \rightarrow \hat{F}_z$ RF pulse has the same phase required for a balanced lattice in configuration II, naturally providing the lattice secondary configuration for measuring $\langle\hat{\sigma}_y\rangle$. The secondary lattice required for measuring $\langle\hat{\sigma}_x\rangle$ requires a phase different by $\approx 0.04\pi$; this is not the perfect phase for the RF readout pulse, but in practice it only introduces an error that scales as $1 - \cos 0.04\pi \approx 0.01$. Other sources of error in our experiment are larger than 1%, so this non-ideal scheme is hardly noticeable. We compared the RF readout scheme to using the primary RF branch for the secondary lattice (in limited situations where possible) and found comparable results.

6.4 Measuring the SSH Eigenstates

Next, we look at using our techniques to measure the pseudospin makeup of the ground band of our lattice in a balanced configuration. By comparing our result to the prediction of the SSH model, we can see how well our system matches the idealized theory.

6.4.1 Filled Bands and Parallel Measurements

Our bosonic system will normally populate one q value in the lattice.[1] Since we are interested in measuring the pseudospin state for the whole band, we fill the lowest band of the lattice before performing our measurements. This can be thought of as simulating the momentum distribution of a fermionic system, where Pauli exclusion results in filled bands up to the Fermi level. Note that in our case the band is not necessarily uniformly filled, so the simulation is not perfect.

[1] Due to the finite system size the crystal momentum distribution will have a finite width even in the BEC case, but this is small enough to be ignored for our purposes.

Nonetheless, non-uniformly filled bands suffice for our purposes, since our measurements rely on the relative population at each q value rather than the absolute population.

Our experiments begin by adiabatically ramping the coupling fields to their final values over 2.5 ms, loading our BEC into the ground band of our initialization lattice at $q = 0$. Following loading, we dephase the BEC to populate states across the BZ. We achieve this by applying a force along the x direction to drive many repeated Bloch oscillation, a method used in Ref. [103]. We apply the force for $35\ \mathrm{ms}$ by displacing one of our dipole trap beams. Over this time, dephasing processes and crystal momentum changing collisions result in population, initially localized at $q = 0$, spreading across the BZ. Because the experimental Hamiltonian conserves crystal momentum (dephasing, interactions, and collisional effects can be neglected over our short experimental timescales), the evolution for each q value is effectively independent, allowing us to study all q values in parallel during each experimental realization.

6.4.2 Ground Band Measurements

Our results for the pseudospin components in each SSH configuration are shown in Fig. 6.8. The three expectations values $\langle \hat{\boldsymbol{\sigma}}(q) \rangle$ are measured independently via the pseudospin rotation described in Sec. 6.2. Each of the three expectation values corresponds to the average of about 30 repetitions, with each repetition including every q value. Fig. 6.8 (a) Combines the three measurements to show the state at each q value on the Bloch sphere. Fig. 6.8 (b) shows the results for each measurement independently. Because our measurements do not have perfect contrast, the reconstructed states (open symbols in (a)) are not pure. In order to compare directly to theory, we construct the closest agreeing pure state by taking the principal eigenvector of $\hat{\rho}$,

equivalent to normalizing the Bloch vector. This is in the spirit of Ref. [104], as will become clear when we use the reconstructed states to calculate topological invariants in Ch. 7. In configuration I the pseudospin rotates around the $\mathbf{e}_z$ axis with q, while in configuration II the states uniformly point to $\mathbf{e}_x$, independently of q. In both cases the sublattice symmetry restricts the state to the equator.

Our data closely agree with the predicted states of Eq. 4.23 for a highly dimerized SSH lattice, indicating that the lowest band of our lattice closely matches the highly dimerized SSH model, as well as validating our pseudospin measurement and state reconstruction procedure.

Our data can be readily used to calculated the Zak phase from Eq. 5.12. This gives $\phi_{\mathrm{Z}} = 0.99(3)\pi$ and $\phi_{\mathrm{Z}} = -0.0005(1)\pi$ for configurations I and II, respectively, closely agreeing with theory. [2] Any deviation from integer multiples of π likely results from small breaking of sublattice symmetry.

6.5 Measuring Tunneling and Displacement

To measure motion of atoms in our system we can time-integrate the drift velocity, obtained from the momentum distribution via our time-of-flight images [105, 106]. We perform these displacement measurements starting with a BEC with a particular crystal momentum (here $q = 0$). The instantaneous drift velocity is determined from the momentum distribution

$$\langle p \rangle = \sum_n 2n\hbar k_R |\langle k = 2nk_R | \psi \rangle|^2; \tag{6.12}$$

$$v_{\mathrm{d}} = \langle p \rangle / m_{87}, \tag{6.13}$$

[2] The uncertainties are calculated as the sample standard deviation of the individually calculated Zak phase for the ≈ 30 separate measurements.

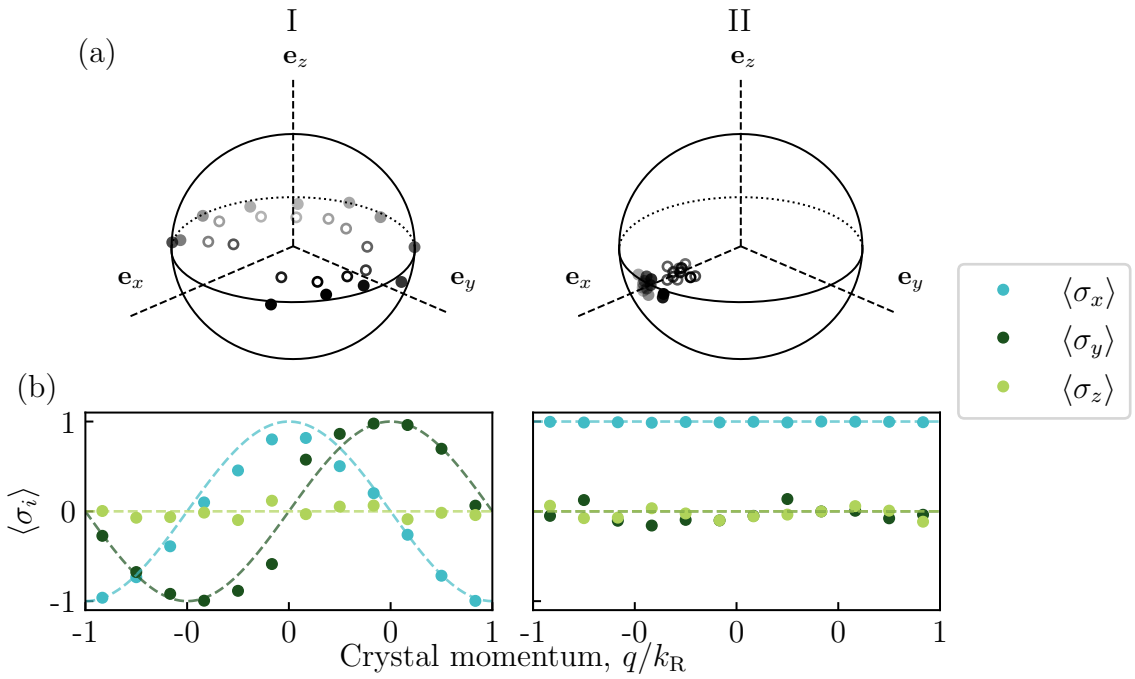

Figure 6.8: Measured pseudospin composition of the ground band of our lattice corresponding to SSH configurations I (left) and II (right). (a) Pseudospin state for all q values across the BZ plotted on the Bloch sphere. The raw measurements (open symbols) correspond to mixed states (i.e., they have magnitude < 1); the solid symbols correspond to the the nearest pure states (which lie on the surface of the Bloch sphere). For the eigenstates of configuration I the vectors trace the equator of the Bloch sphere, while for configuration II they are aligned along $\mathbf{e}_x$. (b) Pure-state expectation values of $\hat{\sigma}_x, \hat{\sigma}_y, \hat{\sigma}_z$ shown as a function of q, along with theory predictions from the SSH model (dashed curves).

where n ranges over the momentum orders present in our ToF image, typically from -2 to $+2$. The displacement at time t, $x(t)$, is obtained by integrating the drift velocity:

$$x(t) = \int_0^t dt' v_{\mathrm{d}}(t'). \tag{6.14}$$

We use this technique to measure the displacement during a tunneling oscillation starting from $|q = 0, \downarrow\rangle$, shown in Fig. 6.9. Because we can measure the magnetization as well as the momentum distribution of our system, we can use both quantities to understand the oscillation. Panel (a) shows the magnetization $\langle \hat{F}_x \rangle$ coherently oscillating with a period of $366(3)$ μs, providing a clear signal of motion between neighboring sites, with small wiggles coming from higher band population. The higher band populations is taken into account by our numerical model (dotted lines), and the theory prediction is qualitatively consistent with our observations. Panel (b) plots the instantaneous drift velocity obtained from the momentum distribution. As before the high frequency oscillations correspond to population in higher bands; they are more prominent in this measurement because the higher band states include more overlap with high k states in the bare momentum basis and thus contribute more to the drift velocity. These high frequency oscillations are repeatable between experimental shots. Their amplitude is consistent with a ≈ 7 % occupation of higher bands, as predicted by our numerical model. Panel (c) shows the integrated group velocity, corresponding to $x(t)$. This confirms our understanding of the process as a tunneling oscillation between adjacent lattice sites, which are separated by nearly $1/2$ of a unit cell, ≈ 200 nm. The high frequency components are much less prominent in the measured atomic displacement at the tunneling timescale, because time integration acts as a low-pass filter. Physically, we can understand this as as the displacement from faster motion associated with the higher

band population averaging to 0 over the tunneling timescale.

Although our model for the lattice predicts symmetric behavior for the two SSH configuration with $\phi_{\text{RF}} = \pm\pi/2$, we empirically found a $6(2)\%$ difference in their tunneling periods. Similarly the difference in commanded RF phase between the two configurations was $\approx 1.03\pi$ instead of π. These observations correspond to physics beyond our model, and thus indicate small distortions of the lattice potentials. One possible explanation for this deviation is a weak optical lattice. Conceivably this could be due to our retro-reflected fields from our Raman lasers, although this would be unlikely if our experiment truly operated at the magic wavelength as we indented.

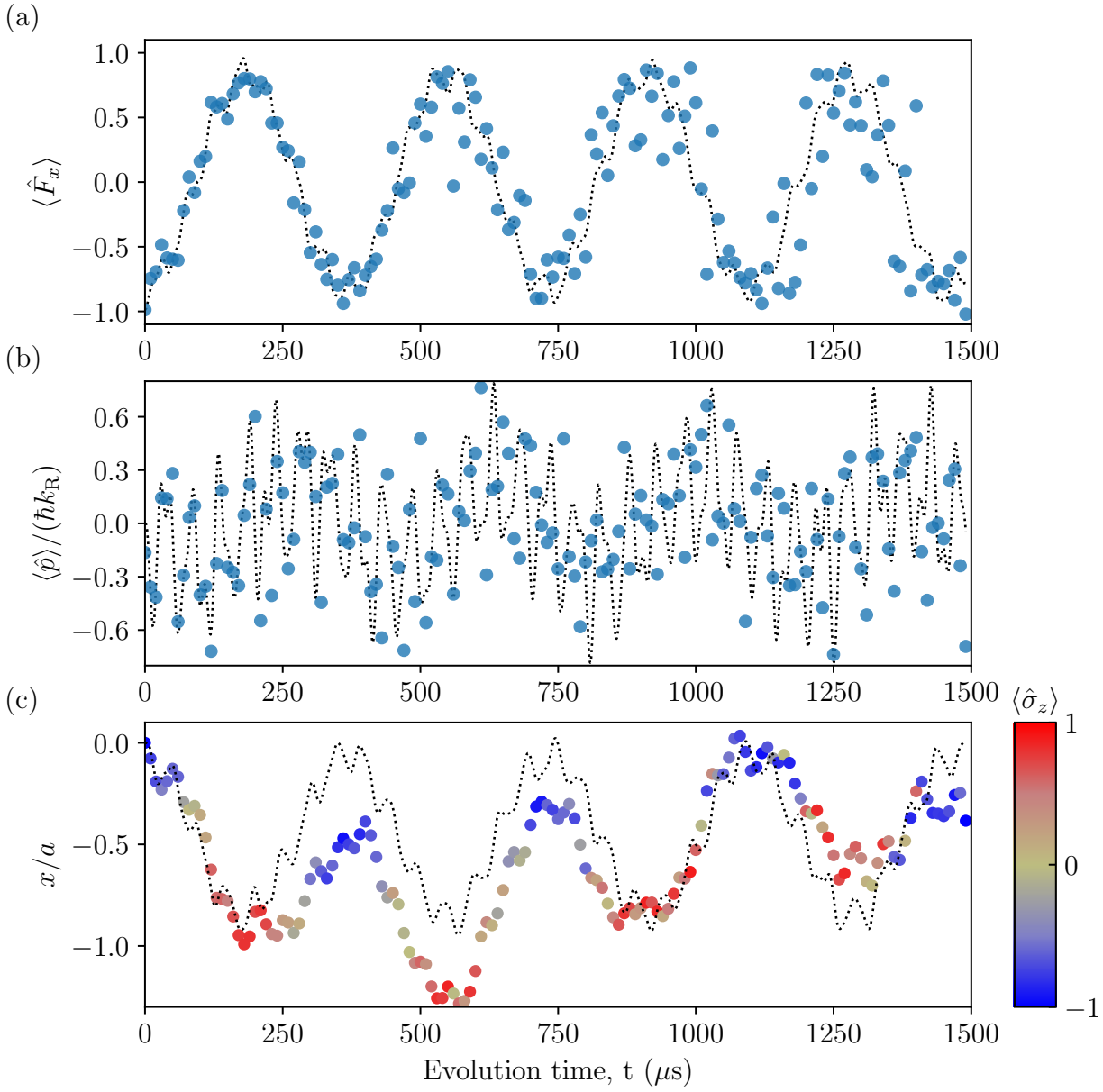

Figure 6.9: Observations of tunneling oscillation in a static, balanced lattice configuration. (a) Magnetization associated with changing pseudospin state during tunneling. (b) Average velocity determined from momentum. (c) Displacement calculated by integrating velocity. Solid symbols represent experimental data while dashed curves correspond to numerical simulations.

Chapter 7: Measuring Topology out of Equilibrium

In this chapter we describe experiments measuring the topology of a filled band of a bipartite lattice as the system evolves out-of-equilibrium under different Hamiltonians. We make use of the bipartite lattice system as well as the crystal momentum resolved pseudospin measurement technique introduced in the previous chapter. We categorize the out-of-equilibrium evolution by the symmetry of the initial state and evolution Hamiltonian and follow the time evolution of the Zak phase and winding number. Cases where a symmetry is absent from the initial state or evolution Hamiltonian are categorized as explicit symmetry breaking, resulting in the symmetry being absent from the time-evolving state. In contrast it is also possible for a symmetry to be broken in the time-evolving state, despite its presence in the initial state and evolution Hamiltonian; this case is called dynamically induced symmetry breaking [107].

When sublattice symmetry (SS) is broken, the Zak phase in general evolves continuously, while the winding number may jump between integer values when SS is transiently present in the out-of-equilibrium state, making the winding number well defined. We describe an example of explicit symmetry breaking, observing large Zak phase oscillations. We also demonstrate a subtle example of dynamically induced symmetry breaking in a system where the initial state and evolution Hamiltonian both respect SS, where the winding number jumps by ± 2 despite the Zak phase ideally being constant. Finally we describe a case where the SS is dynamically

broken, allowing for a time dependent Zak phase, despite SS being present in the initial state and evolution Hamiltonian. We describe our results at the level of the RM model, which is sufficient to capture the qualitative physics of our real system. The results presented in this chapter are published in Ref. [90].

7.1 Explicitly and Dynamically Broken Symmetries

In Ch. 5 we introduced topological invariants for static (equilibrium) systems and Floquet systems, with symmetry playing a central role in the possible invariants. Ref. [107] extends this understanding to out-of-equilibrium systems, detailing the conditions in which topological invariants can change in 1D systems. A time-evolving invariant can be due to explicit symmetry breaking, for example when the evolution Hamiltonian breaks SS, the Zak phase may vary in time. Likewise if the initial state breaks SS, the Zak phase may change in time, also due to explicit symmetry breaking. In contrast, the symmetry breaking is dynamically induced when the time-evolving state lacks a symmetry despite it being present in the initial state and evolution Hamiltonian.

In the case of explicit symmetry breaking, it comes as little surprise that the time-evolving state will in general lose its original symmetry, and hence topological indices may change for the time-evolving state. The dynamically induced case is particularly interesting and counter-intuitive, because it describes changes in topological quantities even when the symmetries that protect them in equilibrium are present in the evolution Hamiltonian.

7.2 Tunneling

Our first out-of-equilibrium scenario is a tunneling oscillation, analogous to what we studied in Sec. 6.5, but here for a filled band. We employ a q-independent initial state $|\psi(q)\rangle = |\downarrow\rangle$, which is the ground state of the RM model with $\Delta \gg (J, J')$. As with all finite Δ RM models this state lacks SS and particle-hole symmetry (PHS), only retaining time-reversal symmetry (TRS). We prepare the state by adiabatically loading into a maximally imbalanced initialization lattice with $\Delta \approx 5E_R$ and $J = J' \approx 0.1\ E_R$. The evolution begins when we abruptly switch the Hamiltonian to a maximally dimerized SSH lattice with $\Delta = 0$ in either configuration I or II.

The pseudospin evolution can naturally be understood as rotations on the Bloch sphere around the Hamiltonian axis $\mathbf{h}(q)$ we introduced in Sec. 4.3. In both configurations, the evolution Hamiltonian obeys SS, restricting $\mathbf{h}(q)$ to lie in the $\mathbf{e}_x$-$\mathbf{e}_y$ plane. Because our system is highly dimerized, with nearly flat bands, $|\mathbf{h}(q)|$ is approximately constant with q. Fig. 7.1(a) shows the evolving state for both configurations. Fig. 7.1(b) shows the state represented on the Bloch sphere for selected evolution times. In both configurations, the high degree of dimerization results in $\langle\hat{\sigma}_z\rangle$ oscillating between $\downarrow$ and $\uparrow$ poles nearly independently of q. The oscillation has full contrast because the subsites are degenerate for the evolution lattice ($\Delta = 0$). The $\langle\hat{\sigma}_{x,y}\rangle$ components (black arrows in (a)) evolve in a q-dependent way in configuration I but are approximately q-independent in configuration II. Because our raw data include unwanted contributions from higher band excitations, we use a temporal low-pass filter to produce the final data. We also apply a filter in the spatial direction to reduce the effects of measurement noise. This is especially important when calculating the Zak phase, which involves differentiating and thus amplifies noise with high spatial frequency components. The filter has root mean square Gaussian widths $k_R/8$

and 10μs in crystal momentum and time, respectively.

The evolution in configuration I corresponds to a rotation about a different axis in $\mathbf{e}_x$-$\mathbf{e}_y$ plane for each q value, determined by $\mathbf{h}(q) = [J\cos q, J\sin q, 0]$. This evolution causes $\langle\hat{\boldsymbol{\sigma}}(q)\rangle$ to wrap around the Bloch sphere as its $\hat{\sigma}_z$ component increases until reaching the $\uparrow$ pole. This evolution goes along with the changing Zak phase shown in Fig. 7.1(c) (teal points). The Zak phase starts at $2\pi = 0 \pmod{2\pi}$, reaches π when $\langle\hat{\boldsymbol{\sigma}}(q)\rangle$ reaches at the equator, and reaches its extremal value of 0, corresponding to a full covering of the Bloch sphere, when $\langle\hat{\boldsymbol{\sigma}}(q)\rangle = \mathbf{e}_z$. Following this, the state reverses this evolution, returning to the initial $|\downarrow\rangle$ state at $T \approx 360$ μs. Because the Zak phase is defined modulo 2π, we used a phase unwrapper to produce a smooth function between 0 and 2π for our experimental data.

In contrast, for configuration II, the Hamiltonian is q-independent with $\mathbf{h}(q) = [J', 0, 0]$. This results in $\langle\hat{\boldsymbol{\sigma}}(q)\rangle$ orbiting $\mathbf{e}_x$, for all values of q. The state starts from the $-\mathbf{e}_z$ pole and reaches the $+\mathbf{e}_z$ pole via $\mathbf{e}_y$ and returns to $-\mathbf{e}_z$ after one period T. As implied by the derivative in the Zak phase formula (Eq. (5.12)) any state that is constant with q has $\phi_{\mathrm{Z}} = 0$. Equivalently, the Bloch sphere trajectory of a state that is constant with q will not cover any surface area. This agrees with our observations throughout the evolution shown in Fig. 7.1(c) (magenta points). The Zak phase includes sub-percent level oscillations at timescales faster than T, corresponding to the small spread in the state as a function of q seen in Fig. 7.1 (b)-right. This is likely due to the small contribution from higher band population that escaped our filtering process.

As we noted in Ch. 5, a changing Zak phase is associated with changing polarization and particle current. In the configuration I case, the change of 2π between the initial state and the state at $T = \frac{1}{2}$ corresponds to a net particle movement of one unit cell. The atoms undergo similar motion in the configuration II case, but their motion is within the unit cell, so it does not

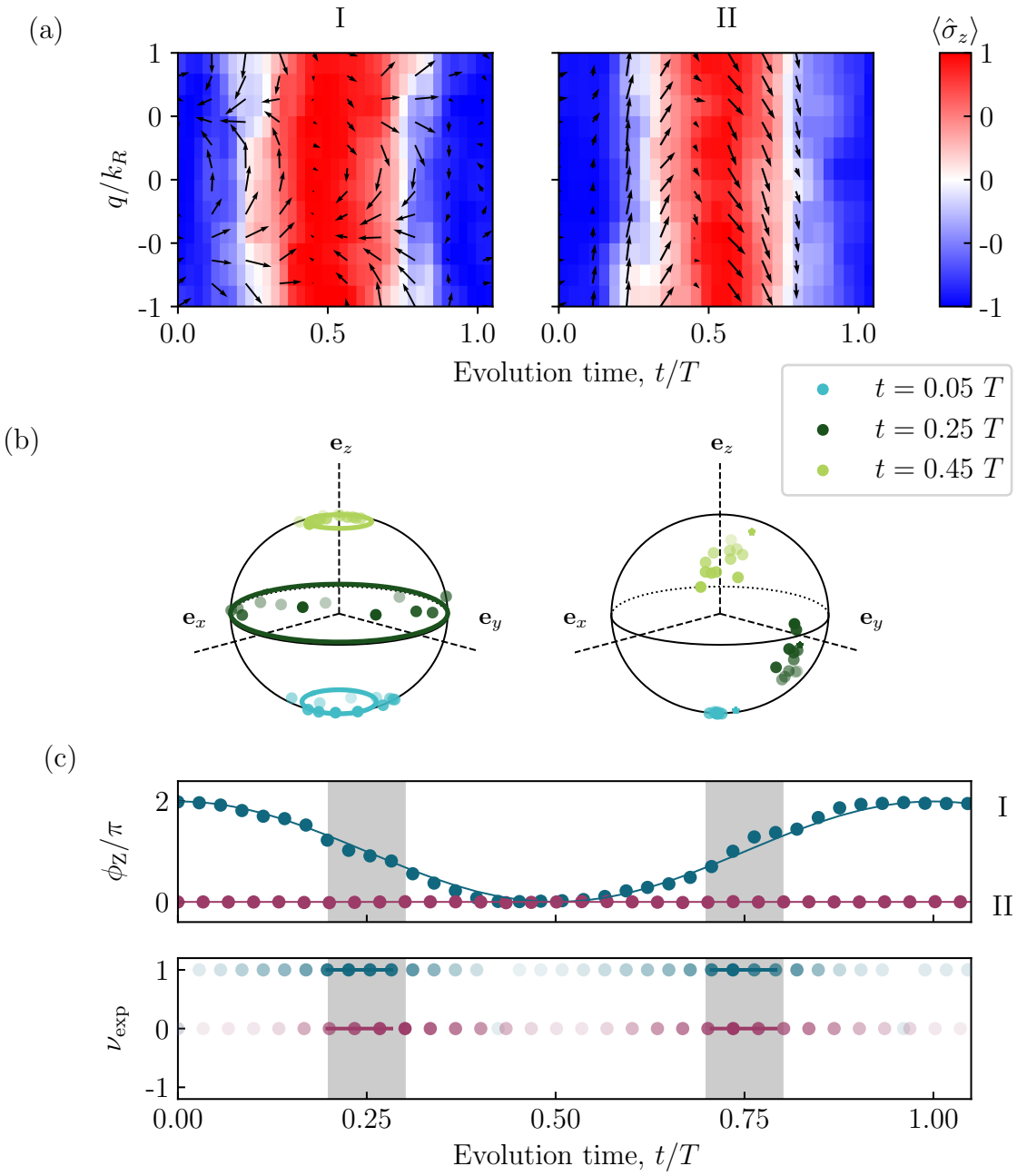

Figure 7.1: Pseudospin state during a tunneling oscillation. (a) Full state reconstruction over the oscillation. Color shows $\langle\hat{\sigma}_z(q)\rangle$ while black arrows show $(\langle\hat{\sigma}_x(q)\rangle, \langle\hat{\sigma}_y(q)\rangle)$. Results for the configuration I Hamiltonian are shown on the left with the configuration II case shown on the right. (b) States represented as trajectories on the Bloch sphere for selected evolution times. Solid curves (left) and stars (right) correspond to theory generated from a fit to the fully dimerized SSH model in the appropriate configuration. (c) Corresponding Zak phase and winding numbers for configuration I (teal) and configuration II (magenta). Points correspond to data and solid curves correspond to theory.

correspond to a changing Zak phase or a current between unit cells. This difference can be seen as arising from our treating the sublattice pseudospin degree of freedom as an internal degree of freedom, as we introduced in Ch. 4.

In general, the SSH Hamiltonian (with $J, J' \neq 0$) will generate q-dependent evolution for this initial state, resulting in the Zak phase being time dependent, except when $J = 0$. In both examples, throughout the evolution, the state is an eigenstate of an RM Hamiltonian in the initial configuration, with time-dependent Δ and complex tunneling matrix elements, as are present in lattice systems with an external magnetic vector potential [92].

All experimental data has some contribution along $\mathbf{e}_z$, and thus breaks SS to some degree. To address this, we projected our measurements onto the $\mathbf{e}_x$-$\mathbf{e}_y$ plane, enforcing SS, then renormalized the data to compute an integer valued winding number ν_{exp}, calculated via the Zak phase for the renormalized, equatorial state. For this state the Zak phase must be an integer multiple of π, yielding integer values for ν_{exp}. Our results, along with the predicted winding numbers of 1 and 0 for the two cases, are shown in Fig. 7.1 (c)-lower. The opacity of each symbol marks the projection of the reconstructed state onto the $\mathbf{e}_x$-$\mathbf{e}_y$ plane, with bold symbols corresponding to states with little violation of SS. We estimate the degree of SS breaking by the root mean square of $\langle \hat{\sigma}_z \rangle$:

$$\sqrt{\int_{\text{BZ}} dq \, \langle \hat{\sigma}_z(q) \rangle^2}, \tag{7.1}$$

which gives 1 for states that maximally break SS and 0 for states where SS is obeyed exactly for every q.

The vertical gray bands mark the regions within 10% of $T/4 + nT/2$, when our theory model predicts SS should be recovered. ν_{exp} is defined throughout but should only be compared

to ν when SS is recovered. Within the gray bands SS is maximally restored, and we confirm $\nu_{\text{exp}} = \nu$ for these times. Interestingly, ν_{exp} remains constant when CS is violated, except for three points in configuration I when $\langle \hat{\boldsymbol{\sigma}}(q) \rangle$ is nearly aligned along $\mathbf{e}_z$, and measurement noise dominates the $\mathbf{e}_x$-$\mathbf{e}_y$ projection.

We fit the observed pseudospin evolution to the evolution predicted by the SSH Hamiltonian to find the model parameters for each case. For configuration I the model parameters are $J = 0.395(2)E_R$, $J' = 0.012(2)E_R$. For configuration II we have $J = 0.038(3)E_R$, $J' = 0.379(2)E_R$. Ideally we would expect the values for the smaller and larger tunneling strengths to be very close in the two configurations (i.e. J in configuration I should nearly equal J' in configuration II and vice-versa); deviations from this result suggest small miscalibrations (i.e. ϕ_{RF} was slightly closer to the correct value for configuration I than configuration II or vice-versa) or that something is present in our experimental system beyond the lattice model. Fitting to only the $\langle \hat{\sigma}_z(q) \rangle$ distribution yields qualitatively similar results to fitting to the full $\langle \hat{\boldsymbol{\sigma}}(q) \rangle$.

7.3 Dimerization

Next, we study a case where the initial state and evolution Hamiltonian both respect all three symmetries—TRS, PHS, and SS. For this case, our initial states are eigenstates of the highly dimerized SSH Hamiltonian and the evolution Hamiltonian is the highly dimerized SSH Hamiltonian of the opposite configuration. In this case, the Zak phase is predicted to be constant; however, SS is not present during much of the evolution, and when it is recovered ν changes its value. Remarkably, in this case ν can take on values that are not present in the equilibrium SSH Hamiltonian, confirming a counterintuitive prediction of Ref. [107].

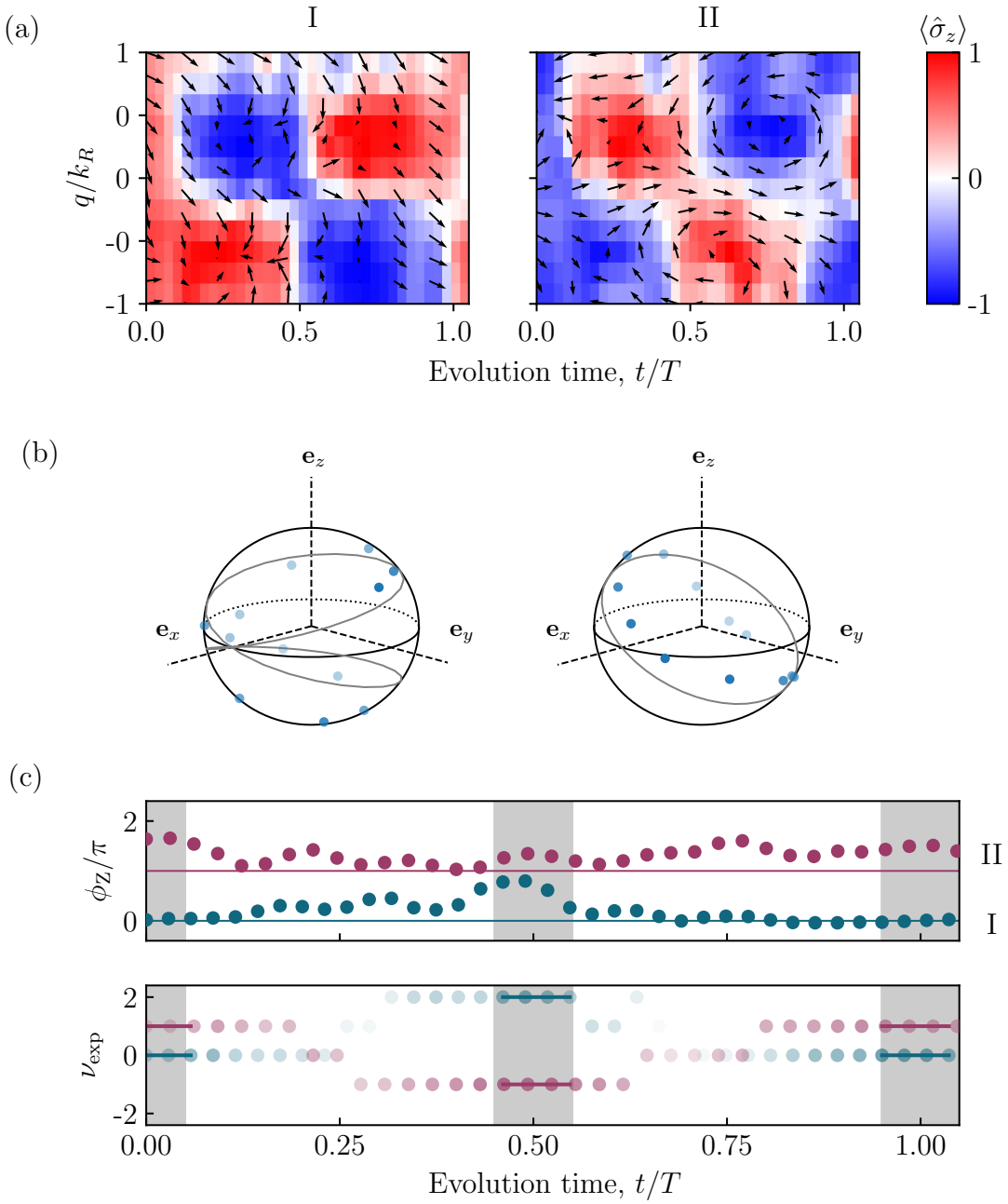

Figure 7.2: Pseudospin state following a dimerization flip. (a) Full state reconstruction over the oscillation. Color shows $\langle\hat{\sigma}_z(q)\rangle$ while black arrows show $(\langle\hat{\sigma}_x(q)\rangle, \langle\hat{\sigma}_y(q)\rangle)$. (b) States represented as trajectories on the Bloch sphere for $t = 0.4T$. Solid curves correspond to theory generated from a fit to the fully dimerized SSH model in the appropriate configuration. (c) Corresponding Zak phase and winding numbers for configuration I (teal) and configuration II (magenta). Points correspond to data and solid curves correspond to theory.

As in Sec. 7.2, when the system evolves in configuration I, the state for each q value orbits a different axis in $\mathbf{e}_x$-$\mathbf{e}_y$ plane, while in configuration II, the evolution corresponds to a rotation about the $\mathbf{e}_x$ axis for all q. For the first case, shown in Fig. 7.2 (a)-left, the initial state, a configuration II eigenstate, has $\langle\hat{\boldsymbol{\sigma}}(q)\rangle$ aligned along $\mathbf{e}_x$ for all q. As the state evolves under the configuration I Hamiltonian, $\langle\hat{\boldsymbol{\sigma}}(q)\rangle$ traces out a figure-8 shape on the Bloch sphere as shown in Fig. 7.2 (b)-left. Ideally this trace is symmetric, with the loops in the upper and lower hemispheres of the Bloch sphere having equal area; our data agree with this prediction qualitatively but not quantitatively.

In the second case, shown in Fig. 7.2 (a)-right, the initial state is a configuration I eigenstate for which $\langle\hat{\boldsymbol{\sigma}}(q)\rangle$ encircles the equator of the Bloch sphere. As the state evolves under the configuration II Hamiltonian, the circle traced by $\langle\hat{\boldsymbol{\sigma}}(q)\rangle$ rotates about $\mathbf{e}_x$ by an angle $2J't$, as shown in Fig. 7.2 (b)-right. As with configuration I, our experimental data show the expected qualitative pattern but show quantitative deviation, meaning they do not precisely trace a great circle on the Bloch sphere.

As before, we use a fit to determine the model parameters for our evolution. The parameters are $J = 0.408(3)E_R$, $J' = 0.003(5)E_R$ for configuration I and $J = 0.009(5)E_R$, $J' = 0.446(3)E_R$ for configuration II.

In both cases the ideal evolution has a constant Zak phase. For the first, the two loops traced by $\langle\hat{\boldsymbol{\sigma}}(q)\rangle$ ideally have equal area, but being traced in opposite directions, provide canceling contributions to ϕ_{Z}. Thus we expect $\phi_{\mathrm{Z}} = 0$ throughout the evolution. In the second case, the great circle traced by $\langle\hat{\boldsymbol{\sigma}}(q)\rangle$ ideally always encloses half the surface area of the Bloch sphere, so we expect $\phi_{\mathrm{Z}} = \pi$ throughout. In both cases our observed state shows deviations from the predicted constant value for ϕ_{Z}. We ascribe these fluctuations to imperfect state preparation (most

likely a small amount of residual SS breaking), imperfections in the evolution Hamiltonian (SS breaking and non-complete dimerization), and imperfections in our readout process. Because the oscillation is more complex than the case from Sec. 7.1, and the constant Zak phase predictions rely on details of the evolution rather than q-independence, it is somewhat reasonable that noise and imperfections would yield larger deviations in this case compared to the tunneling oscillation.

Despite the nominally constant Zak phase, both these cases show changing topology quantified by the winding number. In both cases the state periodically returns to the equator and recovers SS every $T/2 = \pi/(2J) \approx 160\ \mu$s. At these times the winding number changes by ± 2 as shown in Fig. 7.2 (c). As before, the gray bands mark the regions within 10% of the times when our theory model predicts SS is recovered, here $nT/2$. This is possible at constant ϕ_{Z} because a jump of ± 2 corresponds to ϕ_{Z} changing by 2π, leaving its value unchanged modulo 2π. For the first case, this results in a transient value of $\nu = 2$, which is not possible for an SSH model eigenstate. While ϕ_{Z} can be heavily affected by noise and imperfections, ν_{exp} is more robust, agreeing with the predictions perfectly when SS is expected, and only deviating at other times when noise in the data is comparable in magnitude to the $\mathbf{e}_x - \mathbf{e}_y$ projected measurements. While our experimental data show some time dependence in their Zak phases, ϕ_{Z} stayed within π of its initial value, confirming that the changing winding number is due to the modulo 2π jump rather than the spurious changes in ϕ_{Z}.

The $\nu = 2$ state is particularly interesting, because the system approaches an eigenstate of the extended SSH model with dominant next-nearest neighbor tunneling [108]

$$\hat{H} = \sum_j \Big[-\left(J' \left| j \uparrow \right\rangle\!\left\langle j \downarrow \right| + J \left| j+1 \uparrow \right\rangle\!\left\langle j \downarrow \right| + J_2 \left| j+2 \uparrow \right\rangle\!\left\langle j \downarrow \right| \right) + \text{H.c.} \Big]. \tag{7.2}$$

The corresponding momentum space Hamiltonian is

$$\hat{H}_q = -\Big(J' + J\cos(\pi q/k_R) + J_2\cos(2\pi q/k_R)\Big)\hat{\sigma}_x - \Big(J\sin(\pi q/k_R) + J_2\sin(2\pi q/k_R)\Big)\hat{\sigma}_y, \tag{7.3}$$

emphasizing the connection between the J_2 term and the possibility of $\nu = 2$. Higher winding numbers also appear in generalized SSH models with a higher dimensional internal state space [109, 110]. Note that Eq. 7.2 is a fine tuned model because it only includes longer range tunneling terms that preserve sublattice symmetry, excluding terms like $|j+1\uparrow\rangle\langle j\uparrow|$, which we would generally expect to arise in lattices where longer range tunneling is allowed. Additionally the $\nu = 2$ case requires $J_2 > J$, which is not typical for lattices realized in real space, although it is possible in synthetic dimension realizations of the SSH model in frequency or momentum space [110–113]. These are substantial barriers to realizing equilibrium $\nu = 2$ states, highlighting how our approach allows the preparation of exotic states. Our approach used unitary evolution under a relatively simple Hamiltonian to dynamically prepare the eigenstates of an experimentally inaccessible model. We speculate that this general framework—dynamical symmetry breaking and recovery—could be used to prepare otherwise inaccessible states of interacting systems.

7.4 TRS Breaking with Tunneling Phase Models

It is possible for the Zak phase to change in time when both the initial state and the evolution Hamiltonian respect SS but not TRS. This scenario was proposed in Ref. [107] using models where the TRS breaking comes from complex tunneling matrix elements with initial states like the ones we studied in Sec. 7.3. In this case the changing Zak phase results from the dynamically

broken SS. We can realize a closely related scenario by starting with eigenstates of the RM model with complex valued tunneling matrix elements and evolving under the phase-free SSH Hamiltonian.

To study this evolution, we prepare a state with $\langle\hat{\boldsymbol{\sigma}}(q)\rangle = \mathbf{e}_y$, an eigenstate of the SSH Hamiltonian with $J = 0, J' = J_0 e^{\pm i\pi/2}$, observing its evolution under a partially dimerized version of our real valued Hamiltonian with $J'/J \approx 5$. We prepared the initial state using a partial tunneling oscillation under a configuration II SSH Hamiltonian as described in Sec. 7.2, starting from $|\downarrow\rangle$ and evolving for $T/4$. Fig. 7.3 (a) shows the measured pseudospin populations for this evolution, while (b) shows the Bloch sphere representation of the state at $t = 400\mu$s along with the fitted theory prediction (SSH model with $J = 0.0362(7)E_R, J' = 0.1696(5)E_R$). Because the system for this evolution is not fully dimerized, there is not a single tunneling period across the band, leading us to present the data in real units rather than tunneling periods. The Zak phase for the evolving state, shown in (c), starts at 0 and increases to $\approx \pi/6$, allowed for by dynamically broken SS. As suggested by the trace in (b) the winding number for this evolution does not change from its initial value of 0.

At evolution for times past the final time in Fig. 7.3, our experimental result deviates further from the model. We suspect that this may correspond with the onset of dephasing from fluctuations in our control fields or atomic interactions. An estimate of the effective chemical potential gives a timescale for the interaction of 2 ms [91]. The timescale for this experiment was twice as long as those described in the previous section, explaining the increased role played by dephasing physics. This longer timescale was necessary because the lattice parameters used to achieve $J \sim J'$ produced slower tunneling rates as a result of a lower values of Ω_{RF}.

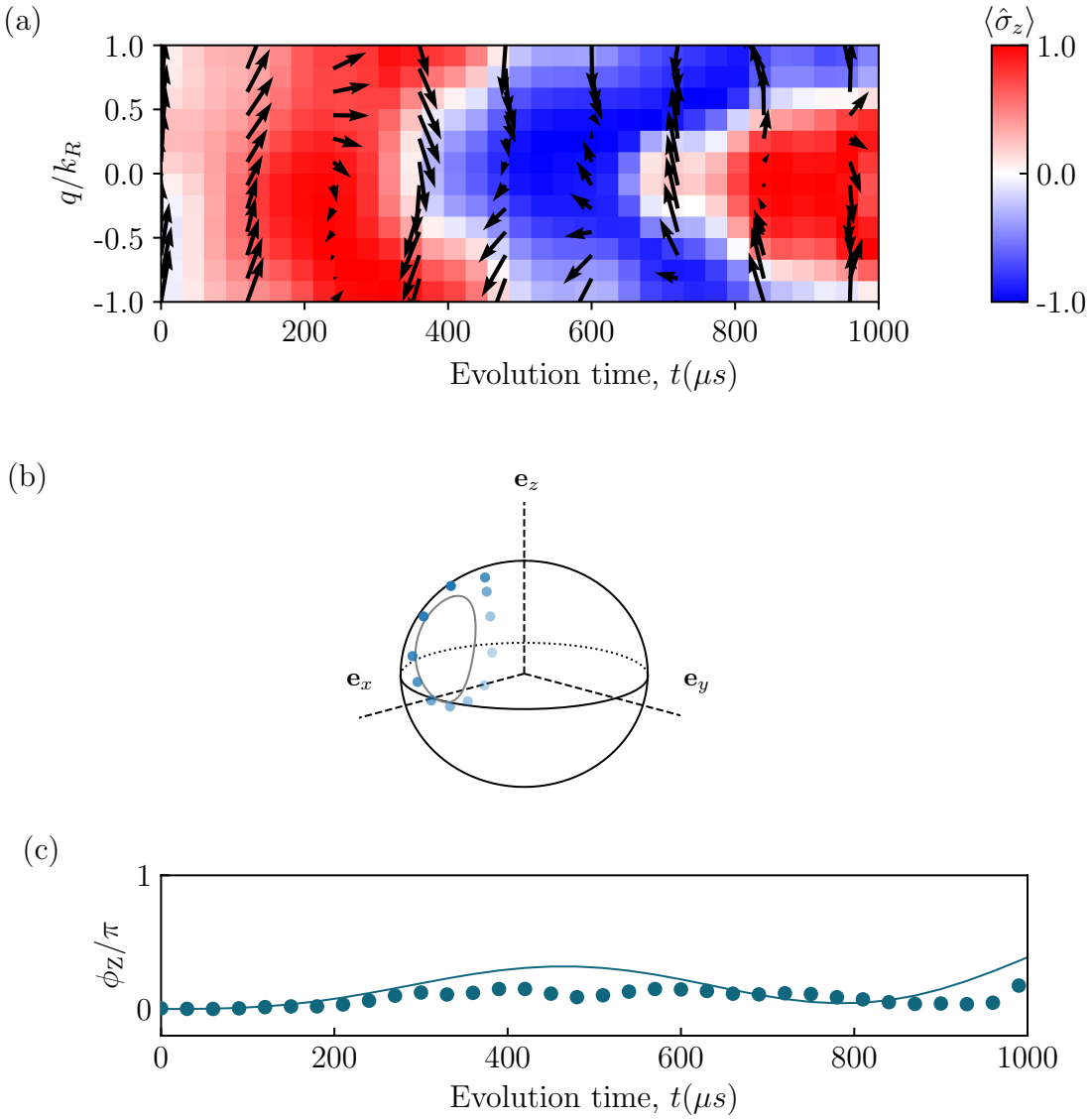

Figure 7.3: Pseudospin state for tunneling starting from a $\hat{\sigma}_y$ eigenstate in a partially dimerized lattice. (a) Full state reconstruction over the oscillation. Color shows $\langle\hat{\sigma}_z(q)\rangle$ while black arrows show $(\langle\hat{\sigma}_x(q)\rangle, \langle\hat{\sigma}_y(q)\rangle)$. (b) States represented as a trajectory on the Bloch sphere for $t = 400\mu$s. The solid curve corresponds to theory generated from a fit to the SSH model. (c) Corresponding Zak phase over the evolution. Points correspond to data and the solid curve corresponds to theory. The time evolving Zak phase corresponds to dynamically broken SS.

Initial state	TRS	PHS	CS	Symmetry class	Configuration
Large Δ RM eigenstate	$+$	$+^*$	1^*	AI (BDI*)	II (Trivial)
Large Δ RM eigenstate	$+$	$+^*$	1^*	AI (BDI*)	I (Topological)
$\phi = \pi/2$ SSH	$+^*$	$+^*$	1	AIII (BDI*)	II (Trivial**)
Trivial SSH eigenstate	$+$	$+$	1	BDI	I (Topological)
Topological SSH eigenstate	$+$	$+$	1	BDI	II (Trivial)

Initial state	Configuration	Result
Large Δ RM eigenstate	II (Trivial)	ϕ_{Z} constant
Large Δ RM eigenstate	I (Topological)	ϕ_{Z} smoothly evolves
$\phi = \pi/2$ SSH	II (Trivial**)	ϕ_{Z} smoothly evolves
Trivial SSH eigenstate	I (Topological)	ϕ_{Z} constant; ν jumps from 0 to 2
Topological SSH eigenstate	II (Trivial)	ϕ_{Z} constant; ν jumps from $+1$ to -1

Table 7.1: Summary of experiments in this chapter organized by initial state and configuration of evolution Hamiltonian. * indicates that a symmetry is present in the initial state but it is different from that of the evolution Hamiltonian (phase-free SSH model). ** means the evolution Hamiltonian was not fully dimerized for the case studied; the stated dimerization corresponds to the larger tunneling strength.

7.5 Summary

In this chapter, we presented paradigmatic examples of how explicit and dynamically induced symmetry breaking can result in changing topology in 1D out-of equilibrium systems. We focused on limited cases, especially fully dimerized lattices as they strikingly show what changes are possible. We included several interesting cases characterized by dynamically induced symmetry breaking. Despite this, we were not able to directly realize one of the key results of Ref [107], a time varying Zak phase due to dynamically broken sublattice symmetry for a class AIII system with no explicit symmetry breaking. This is possible in an SSH-like model with additional couplings and complex hopping amplitudes. Our result from Sec. 7.4 is qualitatively similar but involves explicit breaking of TRS and PHS.

Table 7.1 summarizes the different initial states that we studied, based on their symmetry properties and the configuration for the evolution Hamiltonian, describing how ϕ_Z and ν evolve in time for each case.

One of the most exciting results from the chapter is the $\nu = 2$ state we observed in Sec. 7.3. Because the state exhibits topology beyond what is found in equilibrium states of the simple SSH model, our approach provides an interesting route to creating states with nontrivial topology. The topological out-of-equilibrium states are relatively short lived, so it remains to be seen how the state could be used in future extension of this work. It also remains to be seen how this approach could be used in more general settings, such as systems with higher spatial dimension or interparticle interactions. We hope our work opens the door to study a wide range of possible topological states.

Chapter 8: Topological Dirac Floquet System

In this chapter we describe an experiment using Floquet engineering and our bipartite lattice system to produce a system with a near-perfect Dirac Floquet spectrum with (pseudo)spin-momentum locked linear bands. We measure the displacement over multiple Floquet periods to confirm the predicted drift velocity at $q = 0$ for each pseudospin state, showing pseudospin-momentum locking for the system. We show the dependence of the system on fine-tuned timing by studying the band gap that opens as the system becomes mistimed. The system is described by a topological Floquet winding number of the form introduced in Sec. 5.5.2, which we measure by applying the crystal momentum-resolved pseudospin tomography from the last two chapters to measure the Floquet micromotion of the system across the BZ. Finally we show displacement measurements at finite q, which are consistent with the predicted linear bands, though our measurements do not provide quantitative proof. Most of the results presented in this chapter are published in Ref. [91].

8.1 Floquet Theory

As we introduced in Sec. 5.5.2, particles experiencing a time-periodic potential are naturally described in terms of Floquet modes, directly analogous to the Bloch bands describing particles in spatially periodic potentials. We write the Floquet modes $|\psi_\nu(t)\rangle = \exp\{(-i\epsilon_\nu t/\hbar)\}|\upsilon_\nu(t)\rangle$,

where $|\upsilon_\nu(t)\rangle = |\upsilon_\nu(t+T)\rangle$ has the time periodicity of the Hamiltonian and ϵ_ν is the quasienergy of the Floquet mode, defined modulo $2\pi\hbar/T$. Just as the edges of the first BZ are connected, forming a circle, the quasienergy points $\pm\pi\hbar/T$ are equivalent. Thus the parameter space of a 1D Floquet lattice can be thought of as a 2D torus with coordinates q and t. The dynamics of Floquet systems, when observed stroboscopically (once per period T), are described by a time-independent Floquet Hamiltonian $\hat{H}^{\mathrm{F}}$ with eigenvalues ϵ_ν.

8.1.1 Floquet Engineering

Floquet theory can be used as a general tool to understand periodically driven quantum systems, allowing us to replace evolution under the full time-dependent Hamiltonian with evolution generated by $\hat{H}^{\mathrm{F}}$ as long as we restrict ourselves to stroboscopic observations. Floquet engineering extends this concept to create system with desired exotic or tunable properties. The art and science of Floquet engineering lies in designing the drive to give a particular desired $\hat{H}^{\mathrm{F}}$.

Floquet engineering has been applied to a wide range of systems, from topological insulators [84] to graphene and spintronic systems [114]. Physicists working with ultracold atoms have deployed Floquet engineering to study topological band structures and artificial gauge fields [115, 116].

8.1.2 Calculating Floquet Band Structure

We can calculate the Floquet Hamiltonian and eigenstates (i.e. the Floquet band structure) for a modulated lattice system directly from the time varying Hamiltonian $\hat{H}(t)$. Reviewing Sec. 5.5.2, the time-evolution operator for a full Floquet period is given by the time ordered

exponential

$$\hat{U}(t_0, t_0 + T) = \mathcal{T} \exp\left[\int_{t_0}^{t_0+T} -\frac{i}{\hbar}\hat{H}(t')dt'\right]. \tag{8.1}$$

The specific result depends on the choice of initial time t_0, meaning the stroboscopic behavior depends on the choice of observation time within each period. Numerically, the time evolution operator $\hat{U}$ can be calculated by treating $\hat{H}(t)$ as constant within an interval δt, to give the unitary evolution operator from t to $t+\delta t$, then taking the matrix product of the the time-ordered unitaries for each δt interval.

With $\hat{U}(t_0, t_0 + T)$ in hand, the effective Floquet Hamiltonian can be calculated from

$$\hat{H}^{\mathrm{F}}_{t_0} = i\hbar \log\Big(\hat{U}(t_0, t_0 + T)\Big). \tag{8.2}$$

The Floquet eigenstates and quasienergies are the eigenvectors and eigenvalues of $\hat{H}^{\mathrm{F}}$. For simplicity we take $t_0 = 0$ in our following analysis, meaning the stroboscopic evolution is defined for the state at the start of each period.

8.2 Floquet Engineering Dirac Bands

Next we consider the Floquet eigenstates of a periodically modulated bipartite lattice, where switching between SSH configurations allows constant group velocity motion, with the direction determined by the initial pseudospin state. This protocol closely follows Ref. [53], which formulated the problem with spin-1/2 particles, meaning that rather than alternating between SSH configurations, their protocol alternated between spin dependent tunneling and spin rotations.

In our Floquet "switching" protocol the lattice periodically alternates between configuration I ($J' \approx 0$, $J = J_0$) and configuration II ($J' = J_0$, $J \approx 0$), with period T. The first portion ("half period") of the cycle allows intercell tunneling with $|j+1,\downarrow\rangle \leftrightarrow |j,\uparrow\rangle$, while the second portion allows intracell tunneling with $|j,\downarrow\rangle \leftrightarrow |j,\uparrow\rangle$. The system is perfectly tuned for $J_0 T = \pi$: each half period implements a π-pulse, resulting in full transfer of probability amplitude between neighboring sites. This leads to a displacement of the lattice constant a with each Floquet period, with the direction depending on the initial site occupied ($|j,\uparrow\rangle \rightarrow |j+1,\uparrow\rangle$; $|j,\downarrow\rangle \rightarrow |j-1,\downarrow\rangle$). This intuitive description is based on spatially localized wavepackets, but the same displacement holds for (pseudospin-polarized) crystal momentum eigenstates, with the displacement per cycle being independent of q. Thus the Floquet eigenstates of the system have (pseudo)spin-momentum locked motion with constant velocity $v = \pm a/T$, under stroboscopic observation. The system is described by a 1D Floquet Dirac Hamiltonian

$$\hat{H}^{\mathrm{F}}(q) = qv\hat{\sigma}_z, \tag{8.3}$$

corresponding to massless relativistic particles (the gapless dispersion corresponds to the zero mass case). The spin polarized dispersion relation is shown in Fig. 8.1 for the pure SSH case (a) and a numerical simulation of our bipartite Raman lattice system (b).

Deviation from perfect tuning (exact π-pulses) results in gaps in the quasienergy spectrum, either at $q = 0$ or at the edge of the BZ. Under perfect tuning the system has a (Floquet) pseudospin rotation symmetry, which allows the Floquet eigenstates to separate into decoupled $|\uparrow\rangle$ and $|\downarrow\rangle$ sectors, guaranteeing the bands do not hybridize where they cross at $q = 0$. From Fig. 8.1 we can see that the band for each sector winds around the Floquet-BZ once with q, corresponding

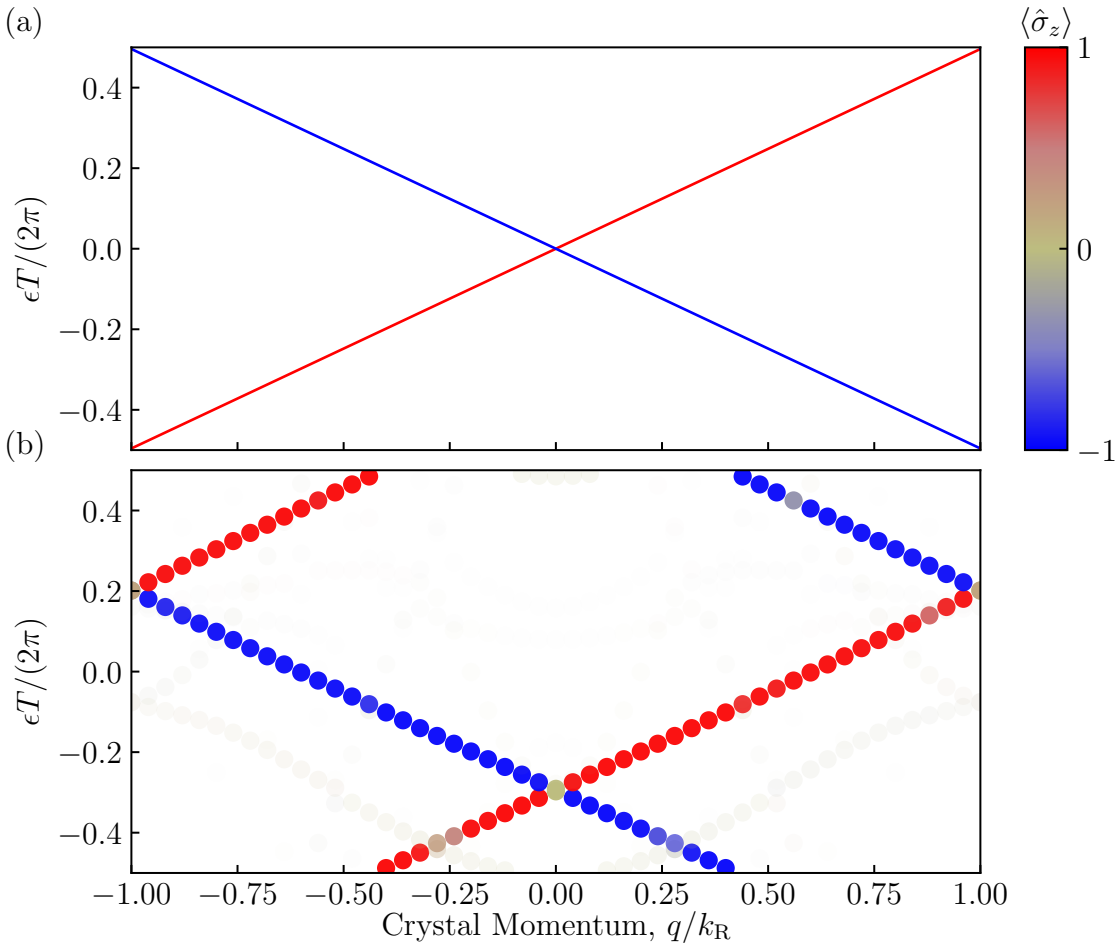

Figure 8.1: Floquet band structure for switching protocol. (a) Idealized two band (SSH) model with complete dimerization. (b) Full numerical simulation of RF+Raman lattice. The full model matches the idealized version very well (up to an overall offset) except at $q = 0$, where slight deviations from perfect timing cause the spin momentum locked bands to hybridize.

to Floquet winding numbers of $\nu_\sigma = \pm 1$ for the $|\uparrow\downarrow\rangle$ sectors as described in Sec. 5.5.2.

$$\nu_\sigma = \frac{1}{2\pi}\int_{\mathrm{BZ}} \frac{d\varepsilon_\sigma(q)}{dq} T dq \qquad \text{(5.29, revisited)}$$

For each initial pseudospin, different crystal momentum states start and end each driving period at the same point on the Bloch sphere (the $|\uparrow\downarrow\rangle$ poles), but evolve q-dependently within the Floquet period. This q-dependent micromotion also reveals the the Floquet winding number for each band, as we will see in Sec. 8.3.

8.2.1 Modulation Implementation

We implement the Floquet driving protocol by changing ϕ_{RF} to switch between lattice configurations every half modulation period. In order to minimize additional excitations to higher bands with each switch, we slowly ramp Ω_{RF} around these switching times, modulating the RF mixer voltage with a tapered cosine waveform, inspired by the Tukey window function, with edge fraction of $\alpha = 30\%$. From 0 to τ the taper function is defined

$$V(t) = O + A \begin{cases} 1/2\cos\left(2\pi t/(\tau\alpha)\right) & ,t < \tau\alpha/2 \\ 1 & ,\tau\alpha/2 \leq t \leq \tau - \tau\alpha/2 \\ 1/2\left(1 - \cos\left(2\pi t/(\tau\alpha) + 2\pi/\alpha\right)\right) & ,t > \tau - \tau\alpha/2, \end{cases} \tag{8.4}$$

where O is an offset and A is the peak value. The function gently ramps from O to $O + A$ with a cosine profile over $\tau\alpha/2$, holds its peak value of $O + A$ for $\tau - \alpha$, then ramps back to O over the next $\tau\alpha/2$ using a a cosine profile.

We create a waveform by periodically repeating the function, changing ϕ_{RF} to alternate between configuration I and configuration II, so that the period is $T = 2\tau$. We generalize the waveform to alternate between different "half" periods τ_I and τ_{II}, allowing the system to spend a different time in each lattice configuration, with total period $T = \tau_I + \tau_{II}$. The true value of Ω_{RF} is modified by the nonlinearity of the mixer, but can safely be thought of as approximately the commanded waveform. We chose the ramping parameters so that the change between configurations would be abrupt with respect to the timescale of the lower band doublet, but slow with respect to the timescales associated with higher band excitations.

Ideally we would simply ramp the RF mixer voltage through 0 with a "bipolar" waveform, taking advantage of the π phase flip in the RF signal when the mixer voltage changes sign, to give the desired value of ϕ_{RF}. In Sec. 6.5 we noted small asymmetry in the tunneling periods for the SSH configurations as well as small deviations from the expected RF phase. Because the calibrated phase values differ by $\approx 1.03\pi$ for configuration I and configuration II instead of exactly π, we correct the phase via the `Novatech` DDS channel at the configuration switching times. This limits our modulation timing to fastest update interval allowed by the `Novatech` channels ($150\ \mu$s), but this is faster than the tunneling timescales in our system, so it did not present a major obstacle. We also compensate for the asymmetry in natural tunneling period for the two configurations be spending proportionally more time in configuration I.

8.2.2 Floquet Pulsing Experiments

To test our experimental control, we let the system evolve under a modulated lattice starting from an initial state of $k = 0$, analogous to our lattice pulsing in Sec. 6.1.2. In anticipation of our

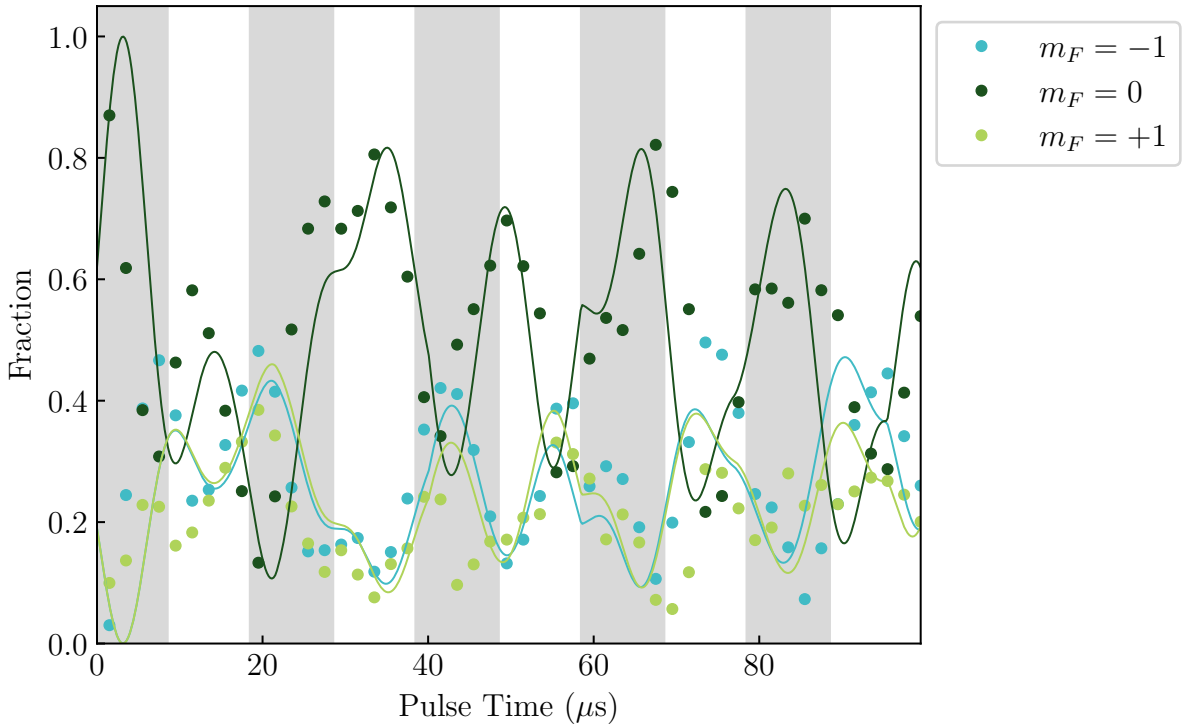

Figure 8.2: Floquet pulsing experiment. The Hamiltonian is modulated by changing ϕ_{RF} by π every 20 μs (shown with gray boxes). To simplify the evolution, we sum the population in different k states, showing the internal state summed over k. The theory curves are a fit to ϕ_{RF} with $\Omega_+ = 12.7E_R, \Omega_- = 5.7E_R, \Omega_{\text{RF}} = 4.5E_R$, yielding $\phi_{\text{RF}} = -0.01\pi$.

configuration switching protocol, we change the RF phase by π periodically every $T_{\text{Fq}}/2$.

Fig. 8.2 shows the results of a pulse experiment with $T_{\text{Fq}} = 40$ μs. We used an approximately calibrated value to control the RF phase, leading to $\phi_{\text{RF}} \approx 0$, which in turn results in the $|m_F = -1\rangle$ and $|m_F = +1\rangle$ populations being approximately equal. This is different from the evolution shown in Fig. 6.5 where we did not calibrate the phase, leading to an arbitrary value of ϕ_{RF}. The evolution is quantitatively similar to what we observed when pulsing the static lattice, though in this case we see discontinuities in the slope of the fit at multiples of $T_{\text{Fq}}/2$, when ϕ_{RF} changes abruptly, most prominently at 60 μs.

8.2.3 Observing Linear Drift in the Floquet System

We apply the drift velocity method introduced in Sec. 6.5 to measure motion under our Floquet driving protocol. This allows us to characterize motion associated with the Floquet band states at $q = 0$. Because the Floquet eigenstates are nearly pseudospin polarized, we prepare them in the same way we prepared pseudospin eigenstates for tunneling oscillations in Secs. 6.5 and 7.2, by adiabatically loading a highly unbalanced lattice. Following this, we abruptly switch the phase to its value for configuration I and begin our Floquet waveform for Ω_{RF}. Fig. 8.3 (a) shows the resulting lattice parameters over the protocol derived from a fit of the SSH model to the full lattice band structure. We measure the state throughout the protocol, allowing us to reconstruct the pseudospin evolution and displacement as in Sec. 6.5.

Fig. 8.3 shows the displacement and pseudospin evolution associated with initial $|q = 0, \uparrow\rangle$ (positive slope) and $|q = 0, \downarrow\rangle$ (negative slope) states. Linear fits to the displacement datasets yield slopes of $\pm 0.89(4)a/T$ and $\pm 0.86(2)a/T$, respectively. This is slightly differ from the drift velocity of a/T predicted by the modulated SSH model, i.e., one unit cell per cycle. Based on numerical studies of the band structure, we conclude that the deviation is due to the nonzero value of both J and J' around the configuration-switching times, allowing unwanted tunneling, and the deviations between our lattice system and the SSH model. Despite this, our numerics show that the group velocity averaged over the BZ has magnitude a/T for both bands, as implied by the (nearly) linear bands in Fig. 8.1 (b).

As seen in Fig. 8.3 (a) either J or J' dominates during the appropriate portion of the cycle. The ratio of the desired tunneling strength to the undesired is $\approx 1\%$, although both rates reach a significant (equal) value during the configuration switching times. This is in reasonable agree-

ment with the results in Ch. 7, where the ratio of tunneling strengths in maximally dimerized configurations was between 1% and 3%, based on a direct fit to the experimental data.

In principle, we could use filled band data to parallelize the linear drift measurement across different q values, using the technique introduced in previous chapters, In practice the signal-to-noise ratio for each q would be too low when measuring displacement using this approach.

8.2.4 Single-Configuration Modulation

As an added to test to characterize our drive, and to confirm the importance of our configuration switching protocol, we implement a single configuration protocol including the same modulation of the RF amplitude without changing ϕ_{RF} to switch the lattice configuration. The resulting time dependent lattice parameters are shown in Fig. 8.4 (a). Motion of a the initial state $|q = 0, \downarrow\rangle$ is shown in Fig. 8.4 (b) along with $\langle\hat{\sigma}_z\rangle$ for the time evolving pseudospin state. The displacement oscillates periodically, similarly to the simple tunneling case discussed in Sec 6.9, although the contribution of higher bands is reduced, due to the smooth ramping of Ω_{RF}. The pseudospin evolution shows similar behavior to the configuration-switching protocol, oscillating with approximately the switching period, as probability amplitude tunnels between neighboring subsites. This emphasizes why we need to measure the average displacement to identify the drift velocity associated with the linear dispersion of our configuration-switching protocol.

For this modulation scheme, the Floquet dispersion (Fig. 8.4 (c)) has a point at $q = 0$ where the bands meet with quadratic curvature, analogous to the spectrum of bilayer graphene [117]. In contrast to the linear dispersion case, we did not load a Floquet eigenstate (or an approximate eigenstate) for the single-configuration protocol, so our observations do not correspond directly

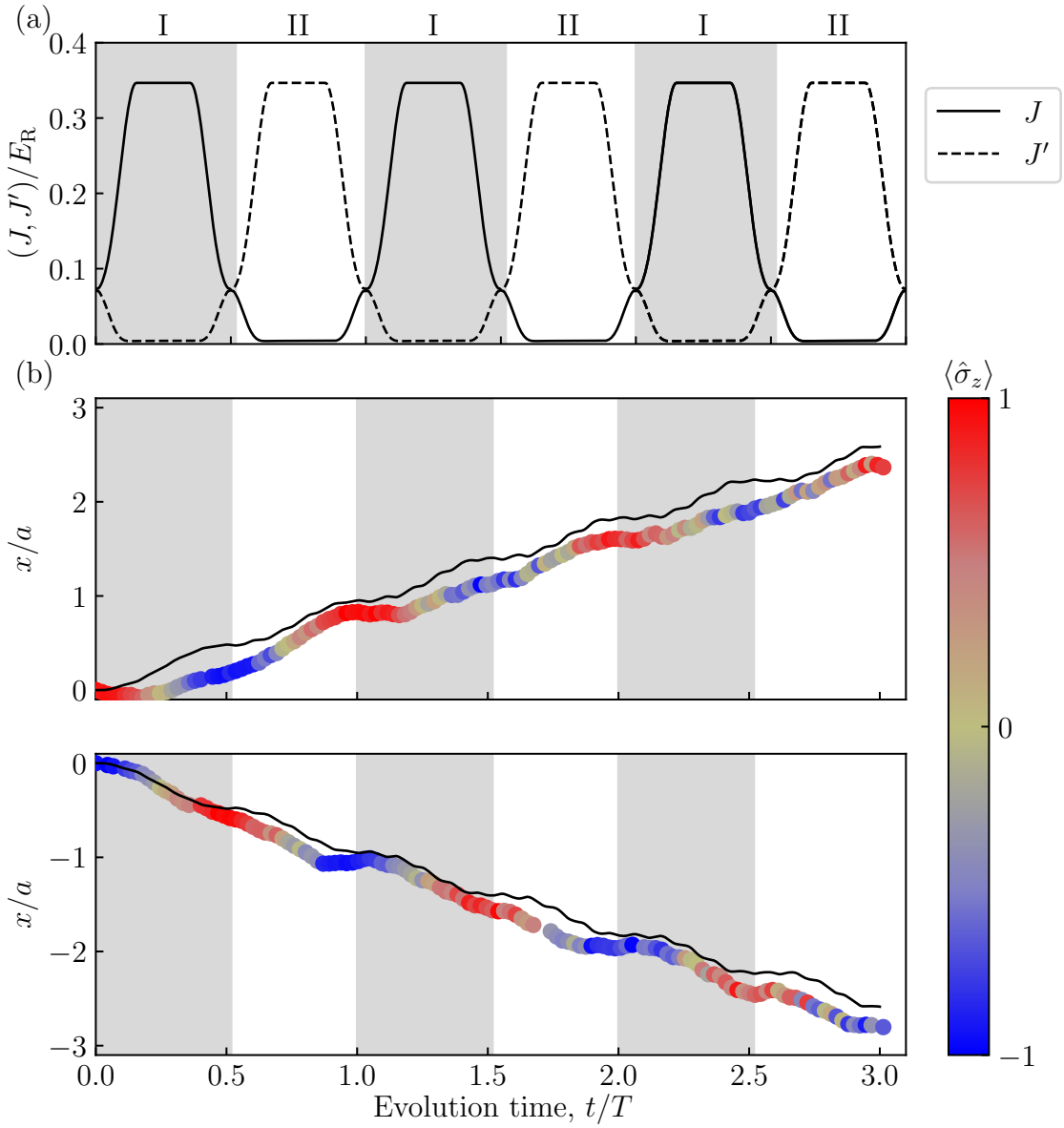

Figure 8.3: Observation of linear drift velocity under tuned Floquet driving. (a) Lattice parameters during Floquet modulation. (b) Displacement and pseudospin evolution for $|q = 0, \uparrow\rangle$ and $|q = 0, \downarrow\rangle$ initial states. Gray boxes indicate times when the lattice is in SSH configuration I while white corresponds to configuration II.

to the states plotted in Fig. 8.4 (c), and the observed lack of drift does not directly imply flat bands.

8.2.5 Evolution under Different Drive

As we discussed earlier, the linear bands of our system are a consequence of perfectly timed Floquet modulation. When the modulation deviates from this perfect timing, gaps open in the Floquet spectrum. To probe this behavior, we modify the timing to have modulation period $T = T_0 + \delta T$, where T_0 is the period for perfect timing. In our specific implementation we changed the timing by reducing the time spent in configuration II while keeping the duration of the configuration I portion constant. This results in a gap of size $\approx 2J_0|\delta T|/T_0$ opening at $q = 0$. The new bands correspond to a Dirac dispersion with finite mass.

Our pure pseudospin, $q = 0$ initial states are no longer eigenstates of the mistuned Floquet Hamiltonian; instead they are an equal superposition of the band states above and below the gap. The time evolution of our initial state under the mistuned Floquet system results from quantum interference of these eigenstates, producing periodic motion. This phenomenon underlies zitterbewegung [118–120], first identified in the context of the Dirac equation.

Fig. 8.5 shows this time evolution for one specific timing. From the pseudospin evolution (Fig. 8.5 (a)) we can see that the tunneling dynamics retain their natural timescale, but the system configuration switches before the atoms have completed a tunneling π-pulse. The displacement (Fig. 8.5 (b)) shows oscillations corresponding to zitterbewegung at a third emergent timescale (slower than the modulation timescale or the natural tunneling timescale). The frequency of the oscillation of the displacement corresponds to the frequency of the gap in the Floquet band

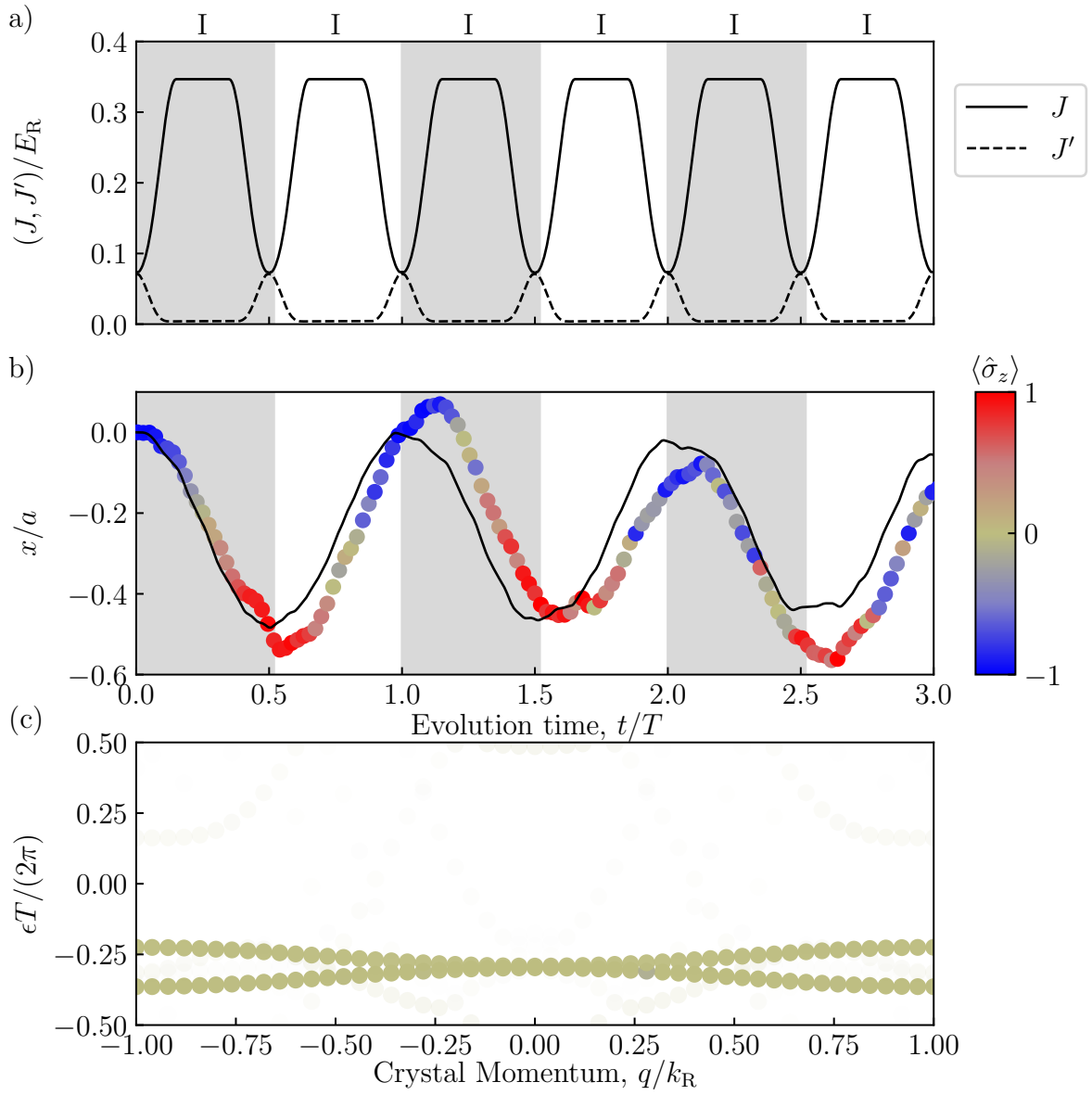

Figure 8.4: Observation of periodic motion under single-configuration Floquet driving. (a) Control timing. (b) Observed displacement and magnetization. Gray boxes are shown in analogy with the configuration switching protocol. (c) Calculated Floquet band structure for single-configuration protocol.

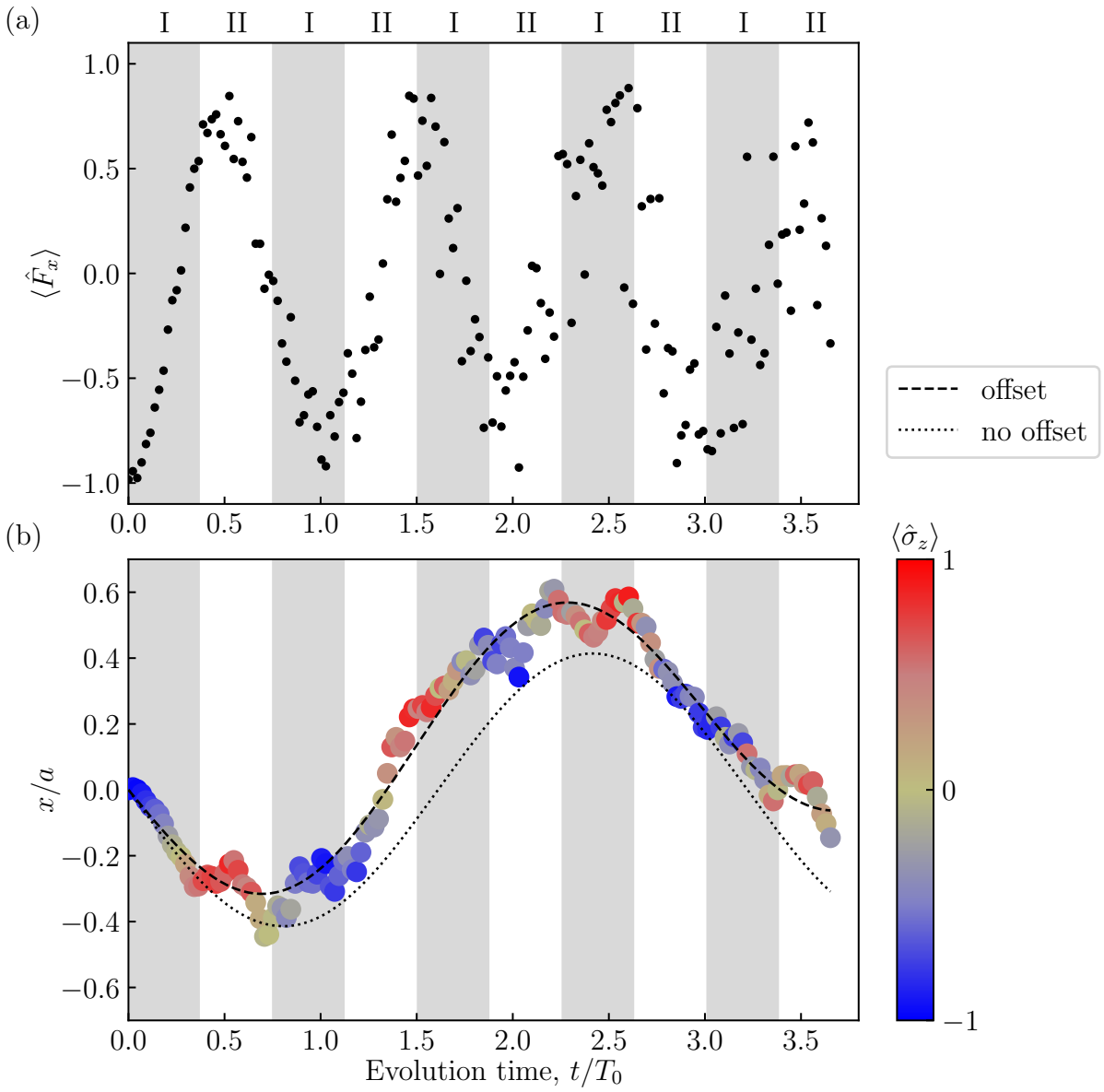

Figure 8.5: Observation of oscillatory motion under mistuned Floquet driving. (a) Oscillating magnetization. The oscillation, corresponding to motion between lattice sites, follows the natural tunneling period T_0 despite the mistimed configuration switching (gray boxes). (b) Oscillating displacement. The displacement oscillates with frequency related to the Floquet band gap. The dashed curves show fits to the displacement with and without a linear offset parameter.

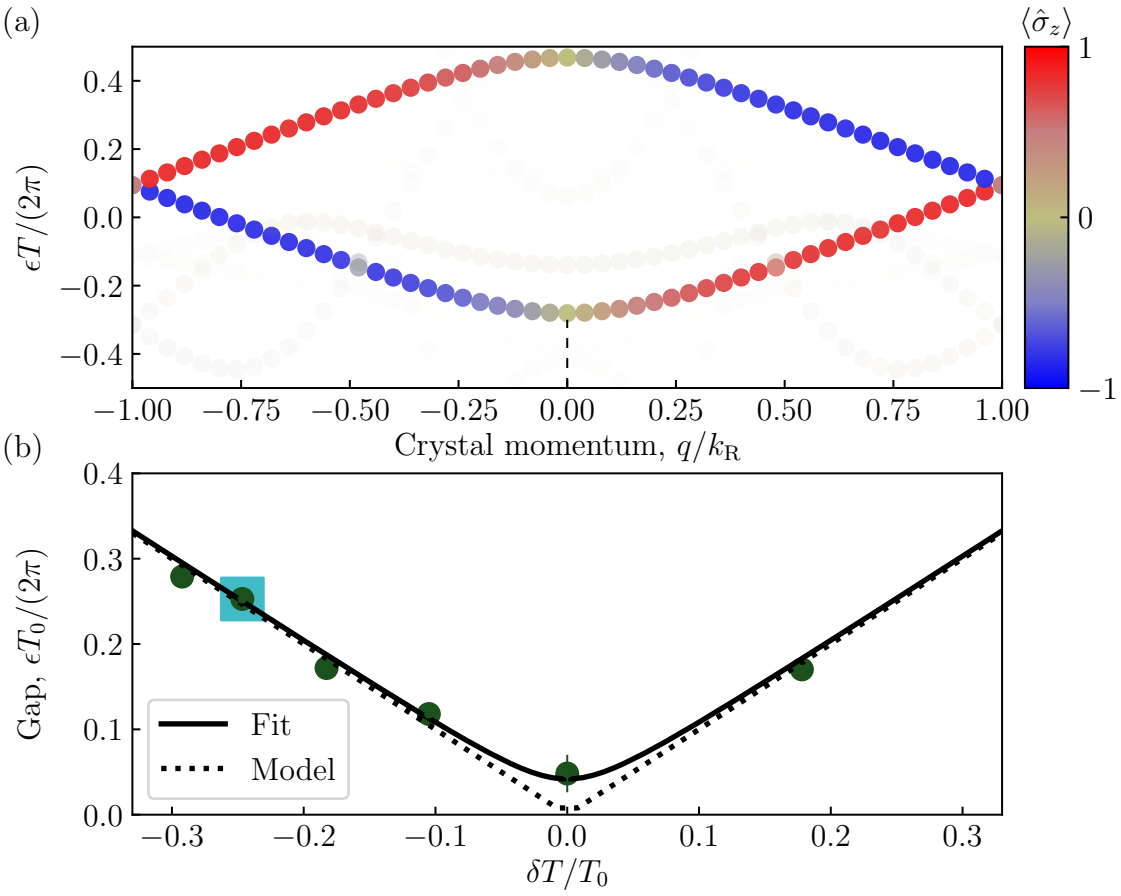

Figure 8.6: Floquet band gap dependence on drive mistiming. (a) Floquet band structure for the parameters of Fig. 8.5. The quasienergy gap at $q = 0$ is indicated by a dashed line. Note that in this case the band gap crosses the edge of the Floquet BZ. (b) Floquet band gap for a range of mistiming values including theory and data. The highlighted point corresponds to the mistiming case from (a) and Fig. 8.5.

structure. Fig. 8.5 (b) includes two sinusoidal fits to the displacement; one is a simple sinusoid, while the other includes a linear offset. The linear offset is needed to fit the data satisfactorily. This is likely due to slight bias in our imaging, resulting in a bias of measured momentum, in turn giving a linear offset to the displacement.

The Floquet band structure for this mistimed case is shown in Fig. 8.6 (a). We extract the gap frequency from measured oscillatory displacement for a range of δT values, shown in Fig. 8.6 (b). A simple model gives a linear dependence of the gap size on $\delta T/T_0$ (dashed curve).

Our data more closely match the hyperbolic fit (solid curve). This indicates that our $\delta T = 0$ case (nominally perfect timing) included some imperfections, bounded above by $0.05(1)(2\pi/T_0)$.

8.3 Measuring Floquet Topology

Next we turn to understanding the topological origin of our Floquet system under perfect timing. The topological Floquet winding number ν_σ, defined in terms of the Floquet band structure for each band $\sigma = \uparrow, \downarrow$, can also be found from the pseudospin micromotion across the BZ. This description of ν_σ is equivalent to the topological invariant characterizing adiabatic charge pumping discussed in Sec. 5.5.1:

$$\nu_\sigma = \frac{1}{2\pi} \int_{BZ} \int_0^T \mathcal{F}(t, q) dq dt. \qquad \text{(Eq. 5.26, revisited)}$$

The Floquet winding number for the $\uparrow$ and $\downarrow$ sectors can be found by integrating the Berry curvature defined in q, t space, which we find from the measured pseudospin-resolved micromotion over one Floquet period under ideal modulation timing. As in Ch. 7 the experiments described in this section use filled band initial states to measure time evolution across the BZ.

Fig. 8.7 shows the reconstructed states for an $|\uparrow\rangle$ initial state, across the BZ over one modulation period, along with the calculated q, t Berry curvature for multiple cases. Panel (a) shows the micromotion for the $|\uparrow\rangle$ band. Experiment (right) agrees closely with numerical calculation (left). The pseudospin data are filtered and normalized as we discussed in Ch. 6 and Ch. 7, with Gaussian root mean squared widths $\Delta t = 10$ μs and $\Delta q = k_R/6$, reducing any contributions from higher band excitations or loss of contrast caused by the filter or imperfection in our measurements. Panel (b) shows the Berry curvature for three cases: the switching protocol for the

$|\uparrow\rangle$ and $|\downarrow\rangle$ bands, and the single-configuration protocol for a $|\uparrow\rangle$ initial state. Note that the latter case is not a Floquet eigenstate. Instead it corresponds to an equivalent initial state to our measurements for the switching protocol. The measured data give winding numbers $\nu_\uparrow = 0.991(5)$ and $\nu_\downarrow = -0.998(4)$ for the initial $|\uparrow\rangle$ or $|\downarrow\rangle$ states; very close to the ideal values of ± 1 and in very good agreement with values of 0.9994, and -0.9995 for our numerical simulations, determined using equivalent analysis. In contrast for the single-configuration case, shown in the bottom panel, our data yield 0.01 (2), compared to 0.0019 from simulation, underscoring the lack of particle transport under that protocol. We use the technique introduced in Sec. 5.4.3 from Ref. [76] because our data are sampled at discrete points in parameter space. The slight deviation from integer values arises because the evolution is not perfectly periodic, even for our numerical simulation.

The integral giving $\nu_{\uparrow\downarrow}$ for the bands in our system is equivalent to the integral we introduced in Sec. 5.5.1 to characterize the quantized displacement in topological charge pumping. Due to this similarity our system can be thought of as a pair of *diabatic* topological charge pumps, with pumping in opposite directions for the two initial pseudospin states.

The topological underpinning of our system closely resembles that of TRS-invariant 2D $\mathbb{Z}_2$ topological insulators for the special case where $\hat{S}_z$ is conserved [58]. For this case the states decouple into $|\uparrow\rangle$ and $|\downarrow\rangle$ sectors each with an associated Chern number c_σ. In terms of the sector Chern numbers, the overall $\mathbb{Z}_2$ invariant is defined

$$n_2 = (c_\uparrow - c_\downarrow)/2 \mod 2. \tag{8.5}$$

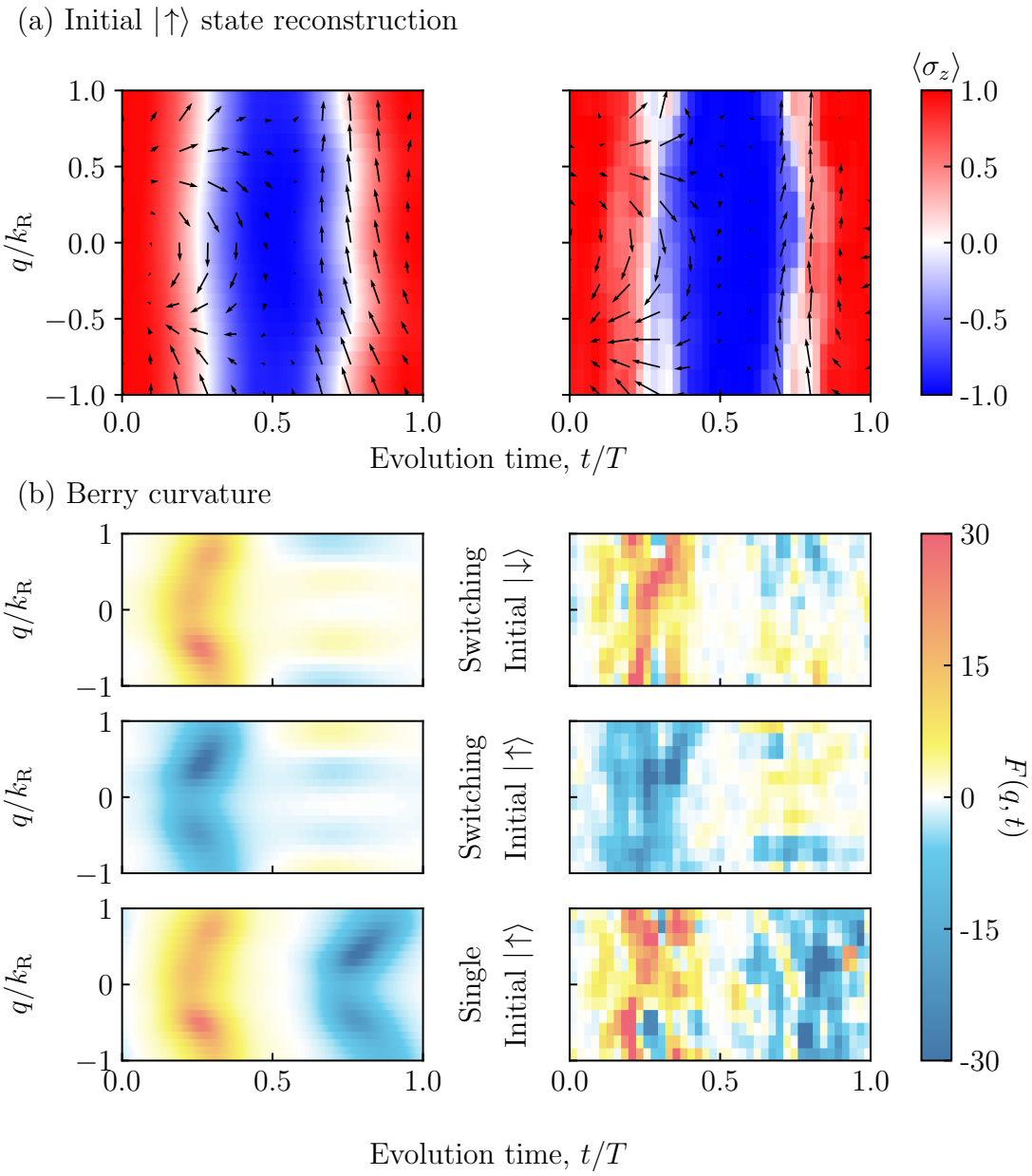

Figure 8.7: Pseudospin resolved micromotion and Berry curvature used to calculate the topological Floquet winding number. (a) State reconstruction (left: theory, right: filtered and normalized experimental data) for a single period of the ideal switching protocol for the $|\uparrow\rangle$ band. The color plot shows $\hat{\sigma}_z$ while the arrows show $\hat{\sigma}_x$ and $\hat{\sigma}_y$. (b) Berry curvature for three different cases: the switching protocol for the $|\uparrow\rangle$ and $|\downarrow\rangle$ bands, and the single-configuration protocol for a $|\uparrow\rangle$ initial state.

8.4 Dispersion Away from $q = 0$

We also present data describing the dispersion of the system found by measuring the drift velocity at finite crystal momentum. We achieve this by applying a kick to the BEC by moving one of our dipole trap beams after loading the lattice, in a similar manner to our dephasing technique, but over a short duration to avoid the spread in q. For the data in this section we use a kick duration of $5\ \mathrm{ms}$ with the strength controlled by the magnitude of the dipole beam movement.

We calculate the displacement as before, but take into account the nonzero crystal momentum. Revising Eq. 6.12 to account for the nonzero value of q gives

$$\langle p \rangle = \sum_n \hbar(2nk_R + q) |\langle k = q + n(2k_R)|\psi\rangle|^2. \tag{8.6}$$

This reveals a weaknesses of the method: the result depends highly on the calibrated value of q, corresponding to how much momentum is imparted by the kick. We determine q after the kick by observing the average displacement of the momentum orders in ToF as a fraction of the BZ size, giving the value of q in units of k_R. We find this method only works well for relatively small kicks up to around 10% of BZ, because larger kicks resulted in spreading of the ToF distribution.

Our results for the displacement during our Floquet driving for a range of kick strengths are shown in Fig. 8.8, starting from the $|q, \downarrow\rangle$ initial state. Based on theory, we expect the displacement to show the same slope in all cases, with any deviation corresponding to slight curvature of the Floquet bands in Fig 8.1. The displacement is consistent between the data by $\approx 40\%$, showing the qualitative behavior we expect but not providing quantitative confirmation of the q-

independent drift velocity. The deviation between the slope for different q values does not seem to follow a trend, suggesting it is likely caused by measurement issues rather than underlying physics beyond our model.

One possible explanation of this discrepancy is the non-uniformity of our probe imaging field. Unfortunately our probe has spatial intensity structure on the scale of k_R in our ToF distribution, leading to possible bias in the atom counting. We overcome this for the $q = 0$ case by aligning the pattern so that the $+2k_R$ and $-2k_R$ peaks, which provide the bulk of the signal for our drift velocity measurements, receive nearly equivalent illumination for $q = 0$, but this is not the case for finite q. It is also possible that the timing of the Floquet modulation was not tuned as to perfect timing as well as the data presented in Sec. 8.2.3.

Stronger kicks produce results where the average slope differed from the $q = 0$ value by significantly more than the data reported here. This is likely due to the distorted shape resulting in an incorrect calibration value for q.

8.5 Conclusion

In this chapter we demonstrated a 1D linearly dispersing system based on nontrivial Floquet topology. The exquisite control and measurability of our ultracold atom system allowed us to tune our system to the topological configuration and measure the underlying topological Floquet winding number. The linear dispersion of our system, along with the ability to open a tunable band gap suggests future application in quantum simulating relativistic massless and massive particles described by the Dirac equation. It is possible we could combine the periodic modulation developed in this chapter with the dimerization experiments discussed in Sec. 7.3 to

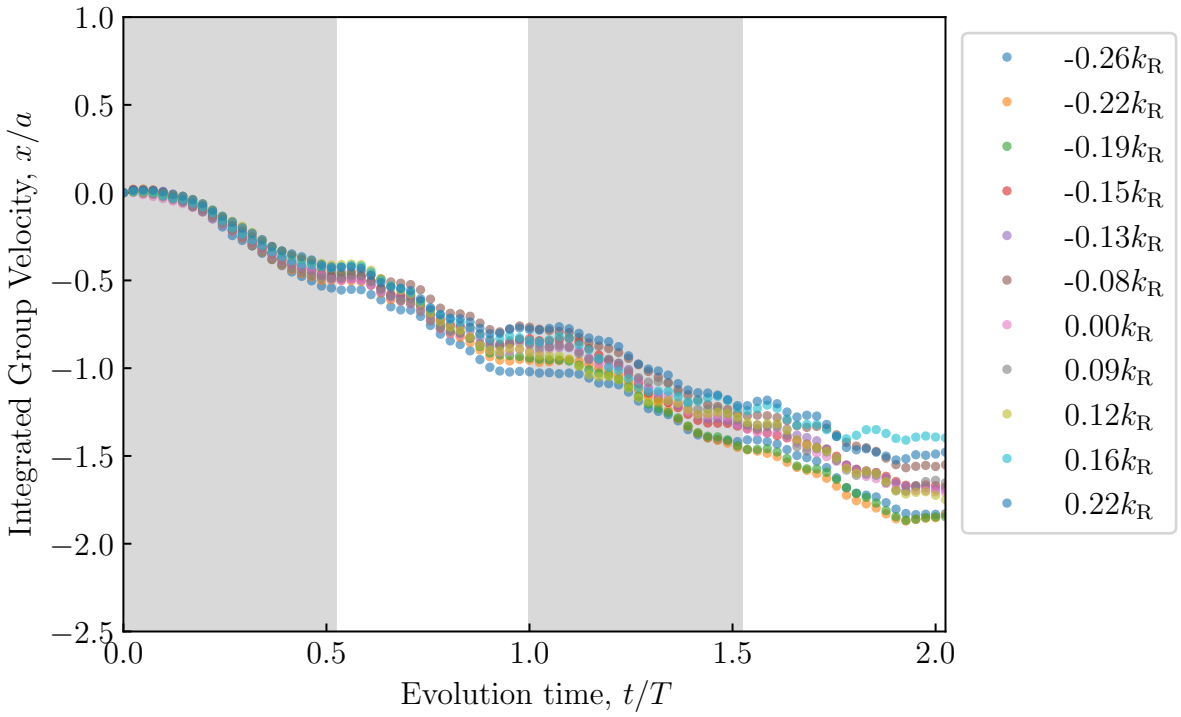

Figure 8.8: Displacement at finite q over two Floquet periods.

create states with higher (static) winding number ($|\nu| > 2$). Our result from Sec. 7.3 essentially used a single tunneling π-pulse to create a state with an effective bond between $\uparrow$ and $\downarrow$ subsites separated by one unit cell, giving $\nu = 2$. Applying another tunneling π-pulse under the opposite configuration, as in our Floquet modulation protocol, would move the effective bond to be $\uparrow$ and $\downarrow$ subsites separated by two unit cells, corresponding to a model with $\nu = 3$, and so on.

Although the experiment was successful, the required fine-tuned timing was onerous, limiting the applicability of this type of Floquet engineering. This presents an interesting direction for future work: can this type of system be generalized to be more robust? The fragility of our system to imperfect timing leads to a general question of robustness. The system is robust against perturbations to the Floquet Hamiltonian that preserve the spin rotation symmetry. This is rather limited because such terms result from time-dependent perturbations in the lab frame, and in gen-

Dataset	Ω_{RF}/E_R	Ω_+/E_R	Ω_-/E_R
Fig. 8.3	4.371 (7)*	12.7 (2)	5.71 (4)
Figs. 8.5, 8.6	4.371 (7)*	13.12 (2)	5.3 (3)
Fig. 8.7	4.371 (7)*	12.71 (2)	5.7 (1)
Fig. 8.8	4.371 (7)*	13.2 (1)	5.3 (3)

Table 8.1: Calibrated lattice parameters used throughout the chapter. *Calibrated value for configuration I.

eral static perturbations in the lab frame lead to symmetry breaking in the Floquet frame. Despite this limitation, we note the connection between our Floquet symmetry protection and dynamical decoupling [121] where systems becomes immune to particular types of time-varying noise.

Table 8.1 includes the calibrated parameters for the experiments used throughout this chapter. While the details of the lattice parameters are important in determining the microscopic details of our experiment, the key physics can be understood in terms of the effective tunneling period and modulation period, hence our choice to express time and crystal momentum in dimensionless units. Because we commanded positive and negative voltages to the RF mixer during configurations I and II, they can have slightly different coupling strengths (although we tried very hard to make them equal). The presented values are from the positive mixer voltage corresponding to configuration I.

Chapter 9: Conclusion and Outlook

9.1 Conclusion

The main thrust of this thesis was to explore new ways topology can manifest itself in quantum systems. We achieved this by quantum simulating the dynamics of 1D bipartite lattice systems, measuring changing topology during out-of-equilibrium evolution, as well as space-time topology defined by the dynamics of a periodically modulated Floquet system. In both cases we were able to directly reconstruct to relevant topological invariants using our crystal momentum-resolved pseudospin quantum state tomography.

In Ch. 6 we introduced our Raman-RF bipartite lattice implementation, demonstrating our ability to reconstruct crystal momentum-resolved sublattice populations, as well as our quantum state tomography technique to reconstruct the full pseudospin state, and our ability to measure motion and displacement from the time-resolved momentum distribution. We demonstrated the utility of these control and measurement techniques by measuring the Zak phase in static lattice configurations as well as the displacement during a tunneling oscillation between sublattice sites. In both cases our results were in very good agreement with theory. These demonstrations emphasize the level of control we have over the lattice system as well as our ability to make detailed measurements, showing two key features of a good quantum simulation platform.

In Ch. 7 we presented studies of out-of-equilibrium evolution of atoms in our bipartite

lattice system. We observed changing topology quantified by the Zak phase and winding number, categorizing evolution scenarios by the presence or absence of symmetries in the initial state and evolution Hamiltonian. We observed explicit as well as dynamically induced symmetry breaking, seeing qualitative agreement with theory including states where the winding number jumps by 2 compared to the starting equilibrium state, resulting in topology not present in equilibrium states of our lattice.

In Ch. 8 we presented a topological Floquet system based on time-modulating our bipartite lattice. This system has pseudospin-momentum locked linear Floquet bands, making it analogous to a massless particle described by the Dirac equation. The system's linear bands are connected to a topological Floquet winding number related to the micromotion; we measured this topological invariant as well as the drift velocity for both bands, finding very good agreement with theory. Although the system required precise tuning, this experiment marks the ability of Floquet engineering to produce exotic band structures, including features not possible in static systems.

9.2 Outlook

The results presented here are a springboard for future studies of topological physics with ultracold atoms or other systems. Our pseudospin measurement technique should be applicable to a range of topological models, so we hope our techniques can be applied to other physics problems. Future work on the RbK apparatus will likely center on improved imaging and projection systems, allowing future work to extend our studies to disordered systems. The addition of time-dependent noise, coupling to auxiliary states, or weak measurement could also extend our results to noisy or open quantum systems.

Our experiments used weakly interacting bosons in 1D. The interactions were in fact so insignificant that non-interacting models yielded very good agreement in most of the cases we studied. As a result, these experiments do not address the promise of quantum simulation to study computationally difficult quantum models. Instead our experiments represent a stepping stone towards more complex quantum simulation efforts and a proof of concept for the experimental techniques we used. We hope future experiments will take inspiration form our work to study quantum dynamics in interacting topological models.

One future goal of quantum simulation experiments is studying computationally difficult models, addressing problems that are difficult or intractable using classical computers [3]. Many physics models can be studied using quantum Monte Carlo methods on classical computers; models that have a sign problem are not suited to this approach [122] and thus present potential opportunities for quantum simulation of classically hard problems. Such problems often involve interacting systems of Fermions or spins, but topological models with bosons can also be limited by the sign problem [123]. For example, both the fermionic and bosonic versions of the Laughlin state associated with the fractional quantum Hall effect [124] suffer from sign problems [123] making them both potential targets for future ultracold atom quantum simulation efforts.

Other atomic physics systems such as Rydberg atoms [125] or trapped atomic ions [126] show promising progress toward novel quantum simulation because their strong interaction can potentially be used to simulate correlated quantum matter. Within the realm of ultracold neutral atoms, degenerate Fermi gases [4] provide a complimentary set of physical systems for quantum simulation and quantum gas microscopes [127] provide potential to measure the microscopic details of quantum simulated systems. It remains to be seen how these tools could be used to extend our study of topology in dynamical quantum systems.

Appendix A: RF Source Design

In this appendix, we present a DC powered device to drive oscillatory (AC) magnetic fields in the megahertz regime. In order to drive reactive loads over a wide frequency range, our device has a low output impedance and is not impedance matched to a 50 Ω transmission line. Although our prototype suffers from reliability and ringing issues, it produced AC fields with peak-peak amplitudes as large as 80 μT at $f = 1$ MHz at a distance of 4.0 cm from the load coil. Our prototype operated up to 5 MHz, but future devices based on our design could operate at higher frequencies. The design uses four transistors in an H-bridge (full bridge) configuration. Our implementation used gallium nitride field effect transistors (GaN FETs), taking advantage of their fast switching speed and low on-state resistance. The design has the potential to produce strong couplings between the internal quantum states of ultracold atoms and could also be used in nuclear magnetic resonance (NMR) experiments.

A.1 Introduction

Radio frequency (RF) magnetic fields can drive transitions between different internal quantum states of electrons, atoms, molecules, and other quantum systems. Such techniques are widely used in quantum physics experiments, including NMR, quantum control, and even during forced evaporative cooling in magnetic traps, an important step in the rapid production of atomic

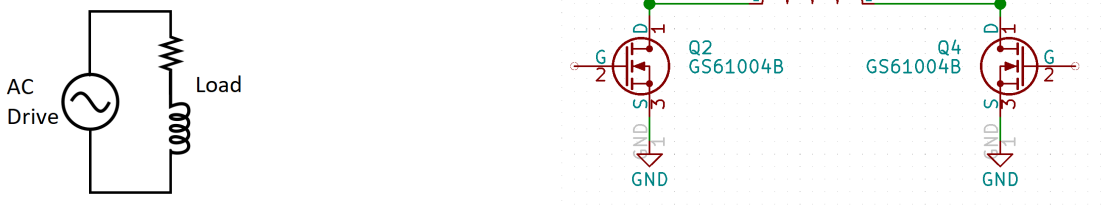

(a) The basic model of a load driven by an AC voltage source.

(b) The basic schematic of an H-bridge. V_{In} is provided by an external DC power supply.

Figure A.1: In our design the AC voltage drive for our coils is provided by an H-bridge. During operation, current flows from the input power supply through one of the two 'high-side' switches, through the load, then through the complimentary 'low-side' switch to ground.

Bose–Einstein condensates [128]. These fields are often generated by passing an oscillatory (AC) current through a wire coil, as shown in Fig. A.1 (a). The required AC drive is typically generated by an RF amplifier impedance matched to a 50 Ω coaxial transmission line. When driving an inductively dominated coil, this approach requires a tuned impedance matching network for the load, which trades off efficiency for broadband operation. In contrast our design does not rely on resonant elements, and allows for broadband performance without tuning. Our design is a potential alternative to RF amplifiers for applications from $\approx$ 10 kHz to 5 MHz.

Our design is based on an H-bridge (full bridge), which consists of four switches as shown in Fig. A.1 (b). The switches are synchronized so that current flows through the load element in opposite directions during complimentary parts of the cycle. Even in the ideal case, our device produces a magnetic field containing many harmonics, which may not be suitable for all applications. Any field effect transistor capable of high frequency switching could be used to implement our design. We implemented a version based on gallium nitride field effect transistors (GaNFETs), motivated by their high maximum switching frequency.

A.2 Operating Principle

The H-bridge circuit in our design ideally outputs a square wave alternating between $+V_{\text{in}}$ and $-V_{\text{in}}$, where V_{in} is the voltage of the DC input power supply. The output has frequency f and phase ϕ set by a digital square wave input. The design is similar to a resonant full bridge DC-AC converter (inverter) without resonant elements. The load element in our design is a coil that acts as a load with lumped inductance L and series resistance R.

Our maximum operating frequency of 5 MHz corresponds to a vacuum wavelength of $\lambda = c/f \approx 60$ m, putting any reasonably sized coil safely within the lumped element limit. Our design also requires that the transmission lines connecting the device to its load be short enough to be considered lumped elements. In this case the transmission lines add a series inductance and resistance to the load. Since all our components and transmission lines can be considered lumped elements, we do not need to operate in an impedance matched configuration. We are primarily interested in the inductive near-field magnetic field produced by a load coil, which is proportional to the current driven by our device. The output impedance of our device is low, allowing for maximum voltage transfer rather than maximum power transfer. This configuration is desirable for driving an inductive load, where the current is limited by the voltage delivered.

Similar circuits based on metal oxide field effect transistors (MOSFETs) have been used to generate RF pulse sequences for use in NMR experiments, with [129] or without resonant elements [130, 131].

A.2.1 Performance

The load is characterized by its LR time constant $\tau = L/R$. The performance of the device is particularly simple in two limits: a high frequency limit ($\tau \gg 1/f$) where the load resistance is negligible compared to the inductive impedance and a low frequency limit ($\tau \ll 1/f$) where the inductive impedance is negligible compared to load resistance.

In the inductively limited case the load current will increase linearly at a rate of V_{in}/L over each half period, forming a periodic triangle wave. Therefore the maximum current will be

$$I_{\text{max,ind}} = \frac{1}{4f}\frac{V_{\text{in}}}{L}. \tag{A.1}$$

In the resistive limit, the load current quickly reaches a maximum value of

$$I_{\text{max,res}} = \frac{V_{\text{in}}}{R}, \tag{A.2}$$

making a square wave pattern.

In general the load current will increase or decrease as one minus a decaying exponential over each half period, depending on the sign of the square wave output voltage. The current waveform is given by

$$I(t) = \pm\left(\frac{V_{\text{in}}}{R} - \left(I_{\text{max}} + \frac{V_{\text{in}}}{R}\right)e^{-t/\tau}\right), \tag{A.3}$$

where t denotes the time after the last voltage switch and the $+(-)$ sign applies when the output voltage is $+(-)V_{\text{in}}$. As in the limiting cases, the waveform reaches its peak value after one-half

period at $t = T/2$. The peak current is

$$I_{\max} = \frac{V_{\text{in}}}{R} \tanh\left(\frac{1}{4f\tau}\right). \tag{A.4}$$

Configurations representative of these three regimes are shown in Fig. A.2. The conditions for the two limiting cases as well as the general result are summarized in Table A.1.

The maximum current is always proportional to the input voltage, so we can control the amplitude of the load current by setting V_{in}. In principle this allows for the creation of a waveform where the amplitude changes with time. The rate of change in amplitude is limited by the response time of the DC power supply.

Limit	Condition	Timescale	Maximum Current
Inductive	$fL \gg R$	$\tau \gg 1/f$	$V_{\text{in}}/(4fL)$
Restive	$R \gg fL$	$1/f \gg \tau$	V_{in}/R
General	None	All	$(V_{\text{in}}/R)\tanh(1/4f\tau)$

Table A.1: Comparison of the two limiting cases of operation where the load is dominated by resistance or inductance, as well as the general expression.

In all cases, we are primarily concerned with the amplitude of the first harmonic component (i.e. the fundamental component, or the carrier) of the Fourier decomposition of the current. This is the desired component of the waveform, while higher frequency components are "side products" of the design. When f is close to resonance with an atomic transition, higher frequency components will have negligible physical impact (as long as there are no other transitions resonant with higher harmonics), so the effective AC field will be equivalent to the fundamental component of the Fourier decomposition. Our approach is similar one used with non-resonant circuits in NMR, in which the nuclear spins can be treated as band-pass filter that rejects frequencies far

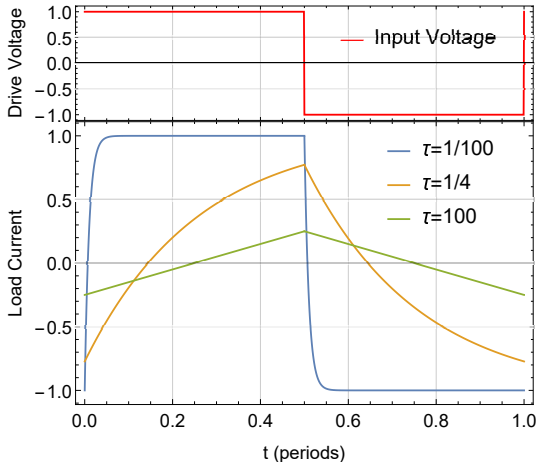

Figure A.2: The output voltage waveform for our circuit (red) and the resulting load current in three regimes: inductively dominated load (small τ), restively dominated load (large τ), and intermediate.

from resonance [130].

We quantify the theoretical performance of our device by calculating the Fourier series decomposition for its current waveform, which is proportional to the magnetic field waveform in the lumped element limit. Our Fourier series convention is described in Sec. A.6. In general the Fourier decomposition of the current for our ideal device only includes odd multiples of the fundamental frequency, as can be seen in the well known limiting cases of the triangle wave and square wave, where the amplitude of the n^{th} Fourier component is zero for even n and for odd n decreases as $1/n$ for the square wave case or $1/n^2$ for the triangle wave case [132]. The relative amplitude of the different Fourier components for three representative cases is shown in Fig. A.3. In all three cases the fundamental frequency component has a significantly larger amplitude than all other components. The second most significant Fourier component has amplitude around 33% of the fundamental in the small τ (resistive) limit and under 20% of the fundamental component in the other cases. The relative amplitude of the higher harmonics decreases as the load enters the inductively dominated (large τ) limit.

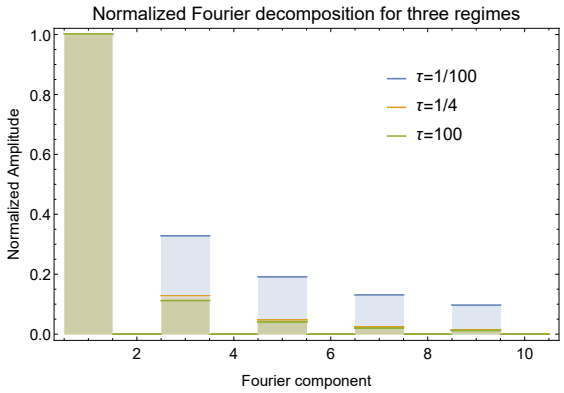

(a) Magnitude of Fourier components normalized by fundamental component for three different cases.

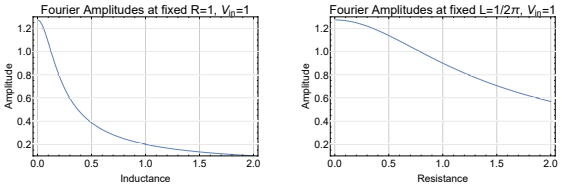

(b) Comparison of fundamental Fourier component amplitude with changing R and L.

Figure A.3: (a) The magnitude of each component in the Fourier decomposition of the current waveform, normalized in the three cases of operation shown in Fig. A.2. The cases are an inductively dominated load, where the load current is approximately a triangle wave, a resistively dominated load, where the current is approximately a square wave, and an intermediate case where the load has significant resistance and inductance. (b) The amplitude of the fundamental Fourier component as a function of L with fixed $R = 1$ and as a function of R with fixed $L = 1/2\pi$ ($|Z_L| = 1$).

The impedance for our ideal load is [133]

$$\begin{aligned} Z &= Z_R + Z_L \\ &= R + i(2\pi f), \end{aligned} \tag{A.5}$$

with magnitude

$$|Z| = \sqrt{(2\pi f L)^2 + R^2}. \tag{A.6}$$

The amplitude of the fundamental Fourier component is determined by the total load impedance $|Z|$—varying L or R while holding $|Z|$ constant does not change the amplitude. The carrier amplitude decreases inversely with $|Z|$. Fig. A.3 (b) shows how the amplitude of the fundamental component changes with variable R and L while the other parameter is held fixed.

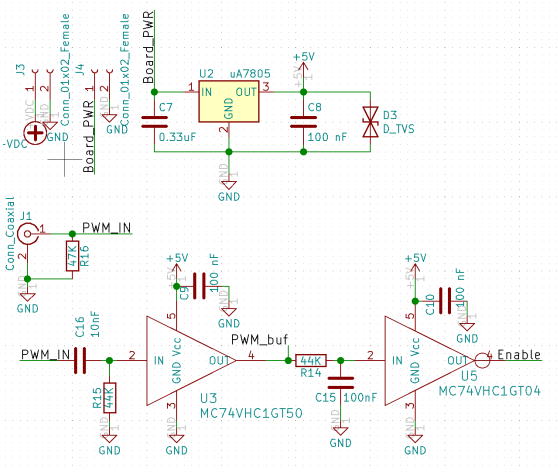

(a) The input and signal buffering stages for our prototype circuit.

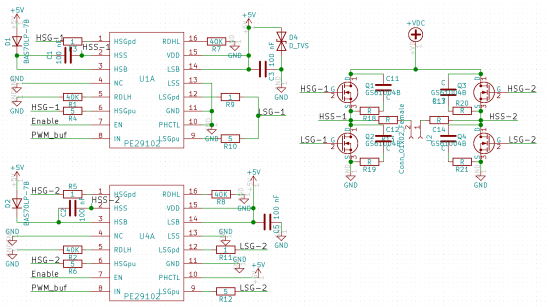

(b) The gate driver and H-bridge portion of our circuit. The upper and lower PE29102 differ only in the nets connected to their respective phase control pins, and the inclusion of a TVS diode, which helps protect both gate drivers.

Figure A.4: The schematic of our prototype design. In this iteration the power for the board (the digital buffers and gate drivers) is supplied by a separate input from the main coil power. Earlier prototypes had one set of power inputs, with board power provided by the main coil power supply, controlled by a linear regulator.

A.3 Prototype

We implemented the design with a prototype circuit using GS61004b FETs from GaN Systems [134] for the four main switches. The GanFETs are rated for a drain-source voltage of 100 V and a drain current of 45 A. Their on state resistance is rated at 5 mΩ. The GaNFET gates are driven by a pair of PE29102 half-bridge gate driver integrated circuits from pSemi [135]. The relative phase of the gate drive waveforms is set by the phase control pin of each PE29102. Setting the two gate drivers to be one half cycle out of phase allows the FETs to operate as an H-bridge. At the rated source current of 2 A, the PE29102 can supply the specified maximum gate charge of 6.2 nC for each FET in 3.1 ns. With a rated current sink capability of 4 A, the drivers can discharge the gates in half the charging time. The PE29102 supports switching frequencies

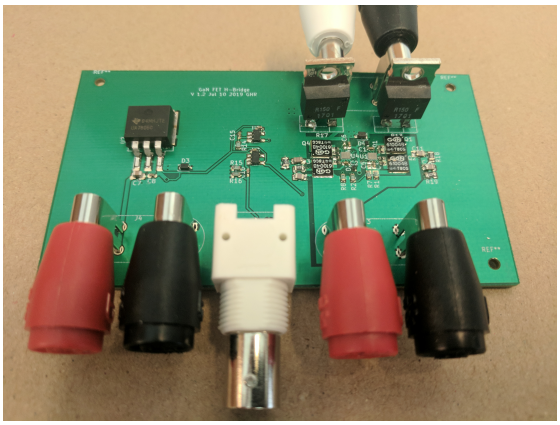

Figure A.5: The prototype GaN FET based H-bridge PCB. The two forward facing banana connectors connect to DC supplies that power the board and the main coils, while the rear banana connectors connect the prototype to the coils. We also worked with smaller prototype boards powered by a single DC supply.

up to 40 MHz and includes a tunable deadtime to prevent cross conduction. [1] We tuned our deadtime to be 4 ns based on the parameters provided in the PE29102 datasheet. The PE29102 gate drivers are used with an external bootstrap diode and 100 nF capacitor that acts as a reservoir of charge when the driver energizes the 'high-side' gates.

Our design also includes an interlock circuit that enables the gate drivers when there is an input signal, and disables them when there is no input. The interlock consists of a non-inverting digital buffer that shifts the HIGH level of the input transistor-transistor logic (TTL) signal to 5 V, an RC low pass filter, and an inverting digital buffer capable of level shifting the filtered signal from 1.65 V to 5 V. The inverting, level-shifting buffer outputs 0 V when the device receives an input signal, and 5 V when there is no input. This signal is sent to the $\overline{\text{EN}}$ pin of each PE29102 gate driver. Our full circuit schematic is shown in Fig. A.4.

Our prototype consists of a two-layer printed circuit broad (PCB) fabricated on 1 oz. copper, shown Fig. A.5. The control signal is sent to the board through a BNC connector, while

[1] Cross conduction ("shoot through") refers to current passing through a complementary pair of FETs during the switching portion of the cycle.

the main and board power cables attach via banana connectors. The load coil is also attached by banana connectors. We were able to use this prototype to test its performance, but experienced several failures of components after moderate use, including the gate drivers, GaNFETs, and buffers in the the interlock system.

When testing an early prototype, we increased the input voltage over 20 V, resulting in some of the GaNFETs releasing a small amount of smoke and becoming discolored. The device stopped working after this. Although this input voltage is well within the specific drain sink voltage range for our GaNFETs, we believe this configuration results in spikes on the 5 V power rail. Since this rail powers the gate drivers, its level determines the voltage delivered to the FET gates during the ON portion of the cycle. GaNFETs are very sensitive to gate-source voltages above 7 V, and we believe transient gate voltages resulted in board failure at input voltages above 20 V.

We decided to use a secondary power supply for the on board electronics and include transient voltage suppression diodes in order to reduce the fluctuations on the 5 V power rail. We did see a reduction in transients on the 5 V rail, but the prototype based on this design ultimately failed due to gate driver issues. We recommend that future implementations of the design make use of a four-layer PCB to enhance ground plane connectivity and shield components from electromagnetic pickup.

A.4 Testing and Performance

We tested our prototype with a load coil mounted a distance of $z = 4.0\ \mathrm{cm}$ from a smaller test coil. This configuration represents one half of our design configuration, which includes two

coils separated by $8.0\,\mathrm{cm}$, so that the field at our desired location would be double the field produced by one coil.

We determined the AC magnetic field at the test location by measuring the voltage that develops across the test coil due to the changing magnetic flux it experiences. From Faraday's law we can infer $V_\mathrm{t} = -\dot{\Phi}_\mathrm{t}$ [136]. Φ_t can be found from the time integral of V_t up to an offset, which we set so that the Φ_t waveform has averages to zero. We can find the spatially averaged magnetic field by dividing Φ_t by the pickup coil area.

The performance of our prototype is primarily characterized by the Fourier amplitude of the magnetic field waveform at the fundamental frequency f. The amplitudes of higher frequency components characterize undesirable side products of our device.

Fig. A.6 shows a simple example of our analysis for data at a carrier frequency of $f = 1.0$ MHz taken with an $n = 2$ turn coil and a series load resistance of 0.66 Ω (consisting of two resistors with 0.33 Ω). High frequency noise in the measured coil voltage waveform is suppressed by the integration, so the $B(t)$ waveform closely resembles the ideal case discussed in Sec. A.2.1. The relative size of the different Fourier components closely resembles the ideal case shown in Fig. A.3. Even multiples of f have much smaller amplitude than odd ones, and the relative amplitudes of the odd components falls off as nearly $1/n^2$, the theoretical scaling for a triangle wave.

We compared the inferred current waveform to the voltage drop measured across one of the load resistors. We converted the load current to an on axis magnetic field by dividing by the load resistance and multiplying by an expression from magnetostatics.

$$B(z) = \frac{\mu_0 R^2 I}{2(z^2 + R^2)^{3/2}} \tag{A.7}$$

This yielded the waveform shown in Fig. A.6b. This approach introduces extra noise owing to EMF pickup from the leads used to measure the voltage drop. Aside from the high frequency noise, the resistive measurement agrees qualitatively with our inductive approach, though the amplitude is approximately 70% of the inductive measurement. One potential explanation for this moderate discrepancy is the connection wires used in the inductive measurement increasing the effective pickup coil area.

Since the performance of our design should improve with reduced overall impedance, we switched to a single turn coil with minimal load resistance (measured to be 0.10 Ω) for further testing. We took data in this configuration at frequencies from 1.0 MHz to 5.0 MHz with input voltages from 6.0 to 14.0 V. Fig A.7 (a) shows the inferred magnetic field for 1.0 MHz at 14.0 V along with three truncated Fourier decompositions. This waveform shows that the prototype suffered from significant ringing (undesirable high frequency noise). This ringing should be inconsequential for our proposed atomic physics applications, since it is far from resonance with any transition, but it may make the devices less attractive for other applications, and may contribute to reliability issues.

We compare the carrier amplitudes across our range of test parameters in Fig. A.7 (b). As expected, the carrier amplitude decreases monotonically with frequency and increases with input voltage. For an ideal device driving a purely inductive load, the amplitude should decrease linearly with frequency and increase linearly with voltage. We see minor deviations from this prediction, but the general trend is reflected in our data. We were, however, surprised to find that the carrier amplitude for the magnetic field in this configuration was significantly smaller in this configuration than in our higher impedance configuration, with our highest amplitude case ($f = 1.0\text{MHz}$, $V_{\text{In}} = 14.0$ V) having roughly one fifth the amplitude of the previous case. This

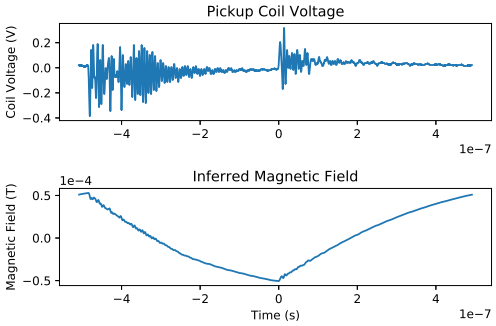

(a) Pickup coil voltage waveform and inferred magnetic field at z=4.0 cm, found by dividing the integrated voltage by pickup coil area.

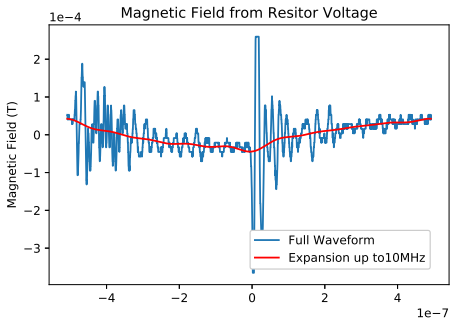

(b) Magnetic field at z=4.0 cm extrapolated from load resistor measurement, including truncated Fourier expansion.

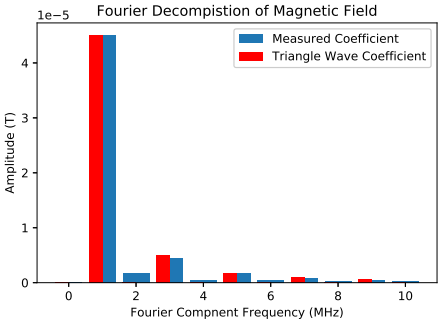

(c) Fourier components of the inferred magnetic field waveform based on our inductive measurement (blue) and Fourier amplitudes of a triangle wave with the same carrier amplitude (red).

Figure A.6: Performance at $f = 1.0$ MHz, $V_{\text{In}} = 15.0$ V, including a series resistance of 0.66 Ω with the coil load. (a) and (b) compare two measurements of the same magnetic field; (a) is based on inductive pickup, while (b) is based on measurements of the voltage drop across a sense resistor.

suggests that our prototype performs better with a moderate impedance load.

Fig. A.7 (c) shows the Fourier amplitudes for a fundamental frequency of 1.0 MHz and 5.0 MHz. In both cases there are secondary spikes around 35 MHz and 90 MHz, and the amplitudes of those frequency components are similar in the two cases, but for a 1 MHz carrier, the fundamental frequency is the largest peak, while in the 5 MHz case the carrier is smaller than the secondary peak at 35 MHz. This indicates that ringing amplitude does not depend strongly on the carrier frequency, and contributes a larger portion to the signal when operating at higher frequencies. We note with some surprise that even multiples of the carrier frequency feature strongly in our measured signal, in contrast to the ideal theoretical case shown in Fig. A.3 and our measurements with a higher impedance load in Fig. A.6.

We can tell from the partial Fourier decomposition shown in Fig. A.7 (a) that components with frequency below 20 MHz determine the general shape of the waveform, while the peak around 35 MHz accounts for the persistent ringing. The high frequency ringing present mainly near the switching points corresponds to the broad peak around 90 MHz.

The qualitative differences between the data in Figs.A.6 and A.7 indicate that using a higher impedance load with some load resistance might reduce ringing and provide better performance.

A.5 Conclusion

Our design is a potential broadband alternative to commercial RF amplifiers for atomic physics experiments; however, a more robust implementation will be required for the design to be useful in a laboratory setting. The design is well suited to situations where a large coupling strength is required, and the coupling strength is constant for a long duration or changes slowly.

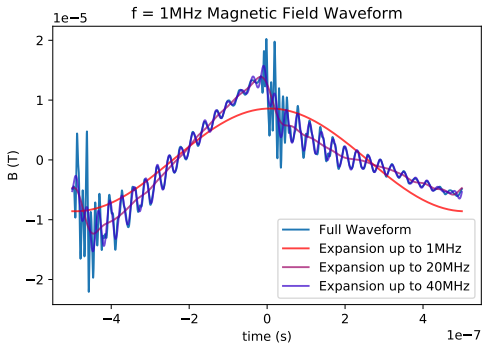

(a) Fourier decomposition of inferred magnetic field waveform at $f = 1.0$ MHz and $V_{\text{In}} = 14.0$ V.

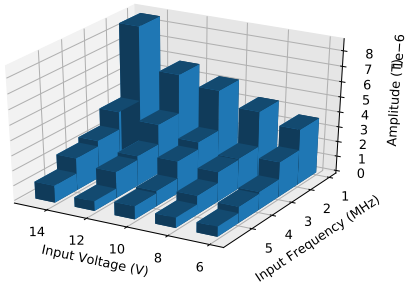

(b) Amplitude of the carrier Fourier component of the inferred magnetic field across our range of tested values.

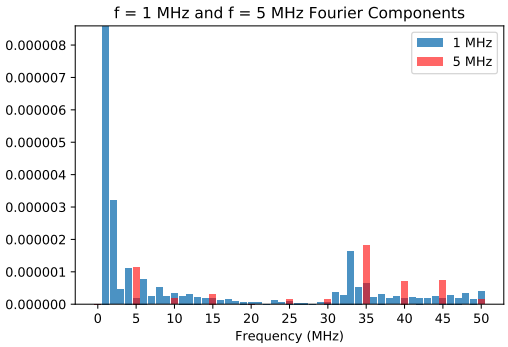

(c) Fourier Amplitudes for the inferred magnetic field from DC to 100 MHz for input frequencies of $f = 1.0$ MHz and 5.0 MHz.

Figure A.7: Performance with negligible load resistance and a single loop coil across a range of frequencies and input voltages. (a) Measured pickup coil voltage and average magnetic field from an inductive measurement at $f = 1.0$ MHz. The blue waveform is the integral of our measured pickup coil voltage, while the red and purple waveforms are Fourier decompositions including only a finite number of terms. (b) Carrier Fourier amplitudes at f = 1.0 MHz through 5.0 MHz at all tested input voltages. (c) Fourier amplitudes at f = 1.0 MHz and 5.0 MHz up to 100 MHz. The values shown are for an input voltage of 14V and reflect the qualitative shape of the Fourier components for lower input voltages.

This makes the design attractive for producing a field for RF "dressing," a technique that can be used to reduce negative the effects of low frequency environmental noise [137]. The design could also be modified for use in NMR experiments.

We designed the device to drive a single coil, with the intention for a pair of devices to drive two coils separated by several cm. Using two devices allows the coils to be operated in a Helmholtz configuration (producing a spatially homogeneous field) or anti-Helmholtz configuration (producing a spatially inhomogeneous field) depending on the relative phase of the two devices. Additionally using a separate device for each coil allows for cable length to be minimized, reducing the effective load inductance. Should larger coupling strengths be required, new implementations of the design could in principle allow for input voltages up to 100 V.

A.6 Fourier Coefficients

We quantify the different frequency components waveform with period $T = 1/f_0$ using complex Fourier coefficients [132]. For a time domain function $f(t)$ the coefficients are defined

$$c_n = \frac{1}{T}\int_{-T/2}^{T/2} dt f(t) \exp\left(-i\frac{2\pi n}{T}t\right), \tag{A.8}$$

so that the time domain function is given by

$$f(t) = \sum_{n=-\infty}^{\infty} c_n \exp\left(+i\frac{2\pi n}{T}t\right). \tag{A.9}$$

The c_n coefficients map to the $\cos$ and $\sin$ coefficients (a_n and b_n) as

$$\begin{aligned} c_0 = &\quad a_0 \\ c_n = &\quad \tfrac{1}{2}(a_n + ib_n) : n > 0 \\ c_n = &\quad \tfrac{1}{2}(a_n - ib_n) : n < 0. \end{aligned} \tag{A.10}$$

Conversely,

$$\begin{aligned} a_n &= c_n + c_{-n} \\ b_n &= i(c_{-n} - c_n). \end{aligned} \tag{A.11}$$

The phase of c_n determine the relative phases of the different frequency components of $f(t)$. We are interested in total amplitude at a give frequency; this is given by

$$\begin{aligned} \sqrt{a_n^2 + b_n^2} &= \sqrt{(c_n + c_{-n})^2 - (c_n - c_{-n})^2} \\ &= \sqrt{(2\,\mathrm{Re}(c_n))^2 - (2i\,\mathrm{Im}(c_n))^2} \\ &= 2|c_n|. \end{aligned} \tag{A.12}$$

In our intended use case, performance is determined by the Fourier amplitude at the carrier frequency. Note that the peak-to-peak amplitude for a given frequency component is twice the Fourier amplitude of Eq. A.12.

Appendix B: Imaging systems

In this appendix, we describe the design and construction of a new custom imaging objective for the RbK experiment. We begin by introducing the basic operating principles of imaging systems and how to quantify their performance. Next, we describe the design of our custom objective. Finally, we conclude with the performance of prototypes based on our design.

B.1 Imaging Basics

An imaging system is a set of optics that collects light from points in the object plane and focus them to points in the image plane. We can use a ray optics picture to understand many aspects of imaging systems. Each point in the object plane can be thought of as emitting a set of rays in all directions. Of those rays, a subset will be able to propagate through our imaging system and will be focused by the optics to converge at a point in the image plane. The ray at the center of each bundle is called the chief ray, while the rays at the edge (i.e the rays with the largest angle from the chief ray that can propagate through the imaging system) are called marginal rays.

Only a finite set of points emit rays that can travel through the imaging system at all; these points define the field of view. The field stop is whatever aperture in the system limits the field of view (i.e. the surface the blocks chief rays outside the field of view from propagating through the system). In contrast, the aperture stop is the aperture in the system that limits the marginal rays.

B.1.1 Keplerian telescope

A common modality of image forming systems is the Keplerian telescope, consisting of two positive focal length lenses separated by a distance of $f_1 + f_2$. This setup can act both as a microscope, taking diverging rays from an object plane and focusing them to an image plane, or as a telescope, taking in parallel rays (corresponding to an infinite distance object) and outputting parallel rays. These two configurations are shown in Fig. B.1. When acting as a microscope the first lens is place a distance f_1 from the object plane, and the image plane is located a distance f_2 from the second lens.

The magnification of a Keplerian imaging system is $m = -f_2/f_1$, with the minus sign corresponding to the inverted image produced by the system. In a similar way to magnification of an image, a Keplerian telescope can be used to expand or compress a laser beam.

We call the first element in a Keplerian imaging system the objective lens (or just objective). For the simplest case the objective is a single lens; it may also be multiple lenses forming a compound objective. The second lens in the system is called the tube lens (equivalently this lens is called the eye lens in a telescope [138]). The tube lens can also be a compound lens system, although it is commonly a single lens. This is because in a microscope configuration, the tube lens is on the low numerical aperture (NA) side of the imaging system (as seen in the shallow cone angle on the right side of Fig. B.1 (b)) and thus its optical performance is typically not a limiting factor. Typically commercially available achromatic doublets are used in this roll because of their flexibility, good optical performance, and simplicity to implement.

We can use multiple imaging systems in series; in this case the second imaging system is called an optical relay, which uses the image formed by the primary imaging system as its object.

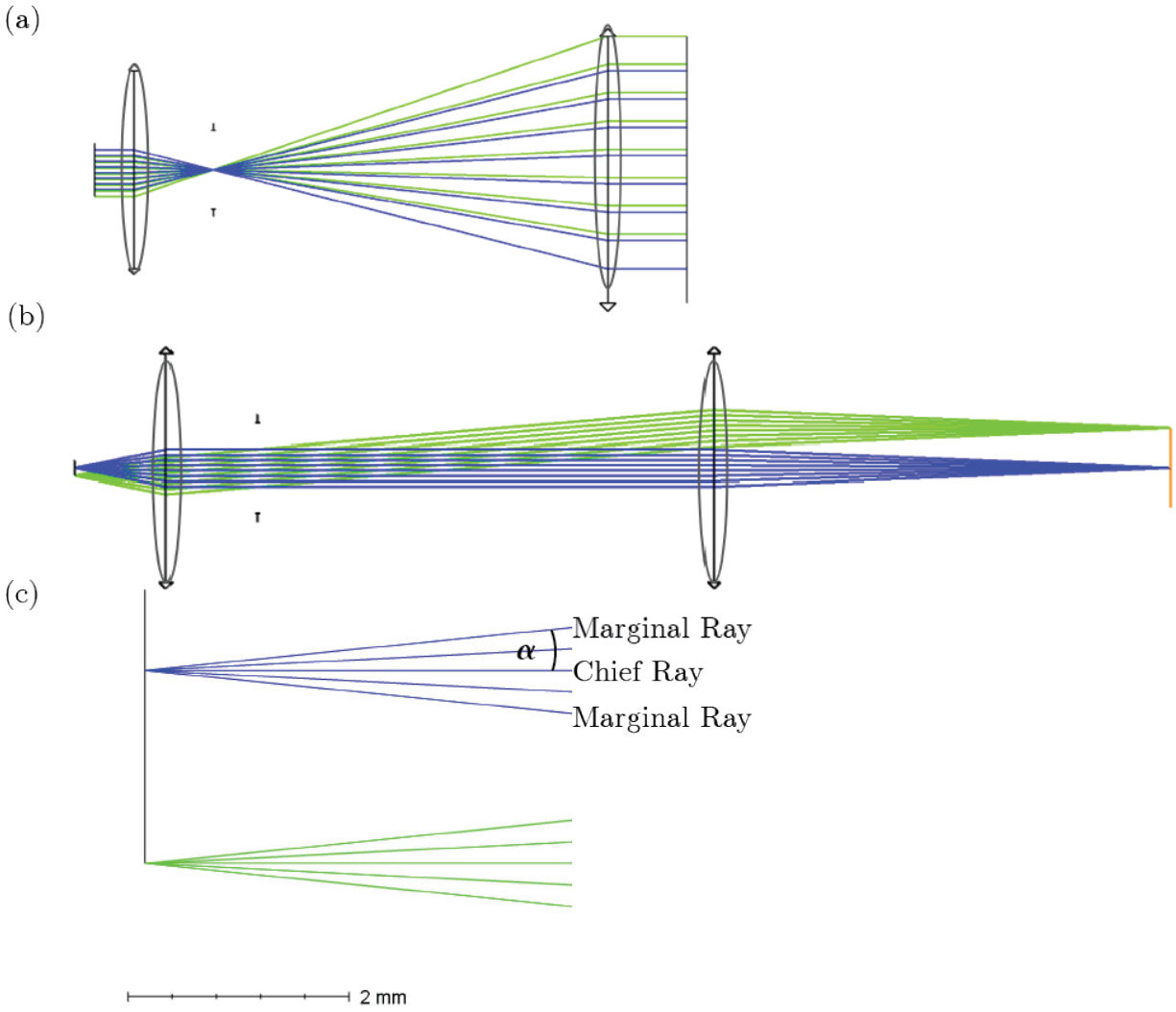

Figure B.1: Schematic of Keplerian telescope operating as a telescope (a) and microscope (b) along with ray labels (c). The telescope configuration corresponds to an object at infinite distance while the microscope corresponds to a finite object distance. In both cases the lenses have a $1/5$ focal length ratio giving a magnification of $m = -5$.

We will elaborate on optical relays in Sec. B.1.5

B.1.2 Numerical aperture and resolution

All imaging systems accept rays at a finite set of angles, leading to a finite resolution. This is connected to the wave nature of light, so the best possible optical performance for a given acceptance angle is called the diffraction limit. We call the angle between the chief ray and the marginal ray α and use it to define the numerical aperture

$$\mathrm{NA} = \sin\alpha, \tag{B.1}$$

where we have assumed the imaging medium has index of refraction of $n = 1$. Fig B.1 (c) shows the chief and marginal rays along with the angle α for $\mathrm{NA} = 0.25$. The NA corresponds to how much light—the total illumination as well as what angular components—from a small region of object space is allowed through the imaging system [138]. A system with $|m| > 1$ will have a wider cone angle in the object plane compared to the image plane, meaning the object space NA, $\mathrm{NA_O}$ is larger than the image space NA, $\mathrm{NA_I}$ by a factor of $|m|$. This means that the optical performance required for the tube lens is typically less demanding than the objective lens in a microscope, as we introduced in the previous section.

To model an ideal imaging system, we start with the electric field distribution associated with the object. We will assume the object is illuminated with monochromatic light of wavelength λ. It is useful to think about image formation in terms of the transverse distribution of the optical field and intensity. Fourier components of the object field with transverse spatial frequency less

than

$$k_{\mathrm{NA}} = \mathrm{NA}\frac{2\pi}{\lambda} \tag{B.2}$$

will be able to pass though the imaging system. All field components with higher spatial frequency will be blocked by the aperture stop, resulting a truncated field. To model the resulting image, we take the inverse Fourier transform of the field, giving the distribution at the image plane, then take its magnitude squared to find the image intensity:

$$I(\mathbf{x}) = |FT\left(\mathbf{E}(\mathbf{k})\right)|^2. \tag{B.3}$$

As we will explore in the next section, the resulting image has finite resolution, quantified by the NA of the system.

B.1.3 Performance

It is illuminating to consider how a finite NA imaging system modifies light from a point source (i.e. an object having infinitesimal x-space size and infinite k-space size). For a diffraction limited system, the resulting pattern is an Airy disk, with size determined by the NA of the system.[1] This defines the point spread function (PSF), which describes an imaging system's response to a point source. Along with the PSF, which quantifies performance in real space, imaging performance is captured by the optical transfer function (OTF), which describes how the system transmits different Fourier components of the image pattern. The OTF is defined as the Fourier transform of the PSF. The modulus of the OTF, or the modulation transfer function (MTF)

[1]The Airy pattern results from a circular aperture in 2D. Note that if the calculation is done in 1D the result is a sinc^2 function which is qualitatively similar but quantitatively different from the Airy pattern.

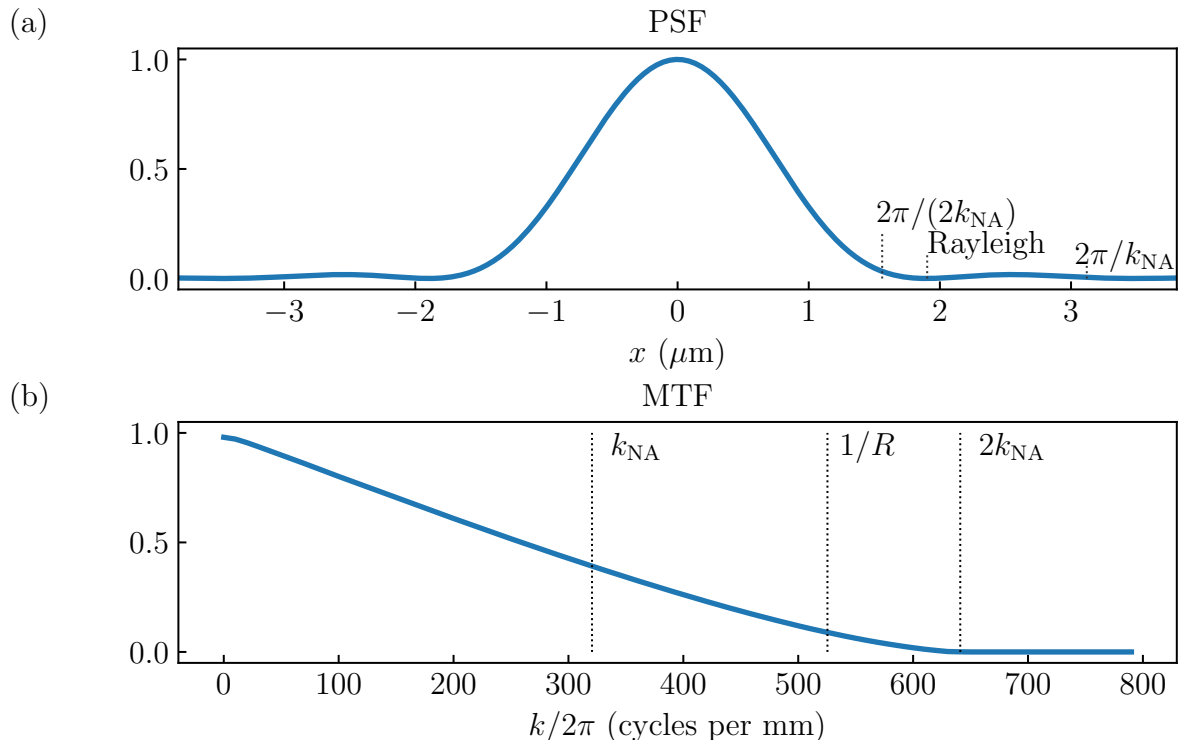

Figure B.2: Point spread function and corresponding MTF for an ideal imaging system with NA=0.25. Dotted lines give the lengths and wavevectors associated with the Abbe resolution, the Rayleigh criterion, and the spatial cutoff frequency.

describes how different spatial frequency components will be attenuated by the imaging forming process. The lowest spatial frequency that is nonzero for the MTF is the cutoff frequency, which for an ideal imaging system is $2k_{\mathrm{NA}}$. Fig. B.2 shows the PSF (Airy disk) and MTF for an ideal imaging system with $\mathrm{NA} = 0.25$ using imaging light with $\lambda = 780$ nm, generated using the truncation and Fourier transform method discussed in the context of Eq. B.3.

The most commonly used quantifier for the resolution of an imaging system is the Rayleigh criterion, which is based on the image space size of a diffraction limited spot. Specifically the resolution is $R = 0.61\lambda/\mathrm{NA}$, corresponding to the distance to the first minimum of the Airy disk. If we assume two point sources produce an image consisting of two overlapping Airy disks, we find we can easily resolve the points as separate if they are separated by at least R.

A competing, though less popular definition is the Sparrow criterion: we can just barely tell the difference between two overlapping points and a single point if they are separated by at least $0.5\lambda/\mathrm{NA} = 2\pi/(2k_{\mathrm{NA}})$ [138].

Considering the Fourier space representation of spatial features of the object leads to the Abbe resolution criterion. By considering a spatial feature with a particular wavevector as a diffraction grating, we find that for on-axis illumination, the smallest features that are allowed through the system have $k = \mathrm{NA}/\lambda$. Generalizing to oblique illumination can allow higher wavevector components through, up to $k = 2\mathrm{NA}/\lambda$ [139]. The on-axis limit corresponds to the case we will discuss in the context of coherent illumination in Sec. B.1.4, while the oblique illumination case gives a resolution corresponding to the OTF cutoff frequency and the Sparrow criterion.

The cutoff frequency, defined based on Fourier space analysis, corresponds to the length scale of the Sparrow criterion and a slightly smaller length than the Rayleigh criterion, as shown in Fig. B.2. Based on the coordinate space definition of the Rayleigh criterion, this means that images produced by a diffraction limited imaging system will have subtle features on a length scale below what is easily discernible.

As we have seen, even ideal imaging systems have finite resolution controlled by the numerical aperture of the system; with the exception of super resolution techniques [140], all optical systems are subject to the diffraction limit. Other effects, in particular optical aberrations can further limit the optical performance of a real-world imaging system. To quantify this loss of performance, we use the Strehl ratio, which compares the height of the PSF for an imaging system to that of an ideal system. This can be thought of as quantifying how much aberrations spread out the imaging-forming light beyond a diffraction-limited spot. The Strehl ratio can also

be calculated by comparing the area under the MTF to the area for an ideal imaging system [138].

B.1.4 Coherent and Incoherent Illumination

In the previous section, we considered the spatial frequency components from an infinitesimal (pinhole) source, and found that spatial frequency components up to $2k_{\mathrm{NA}}$ appeared in the image. This corresponds to the resolution cutoff for 'incoherent' imaging, where the image is formed by interference between different transverse frequency components of the scattered field, with maximum transverse frequency k_{NA}, so that the maximum frequency in the interference pattern is $2k_{\mathrm{NA}}$. In contrast in the 'coherent' imaging modality, the image is predominately formed by interference between a strong 'probe' field and the scattered field. As with incoherent imaging, the scattered fields have maximum transverse frequency k_{NA}, but because the image is formed by interference between these fields and the spatially uniform ($k = 0$) probe field, the maximum spatial frequency component in the image is k_{NA}. Because our absorption imaging uses a probe field, it is coherent imaging, and the resolution limit corresponding to k_{NA} applies.

This physics is equally applicable to describe imaging and projection, for example of digital micromirror device (DMD) patterns. In Fig. B.3 we consider light reflected by a random subset of DMD pixels, propagating through an ideal imaging system. (a) shows the resulting image after passing through an ideal imaging system with $\mathrm{NA} = 0.25$. (b)-(d) describe the spatial Fourier components of the resulting image. We find that the image contains a 'DC' peak at k=0, a strong plateau bounded by k_{NA} corresponding to the coherent imaging component, and a much weaker component at higher k corresponding to incoherent image formation. For practical purposes the dominant part of the projected image can be assumed to have a spatial resolution

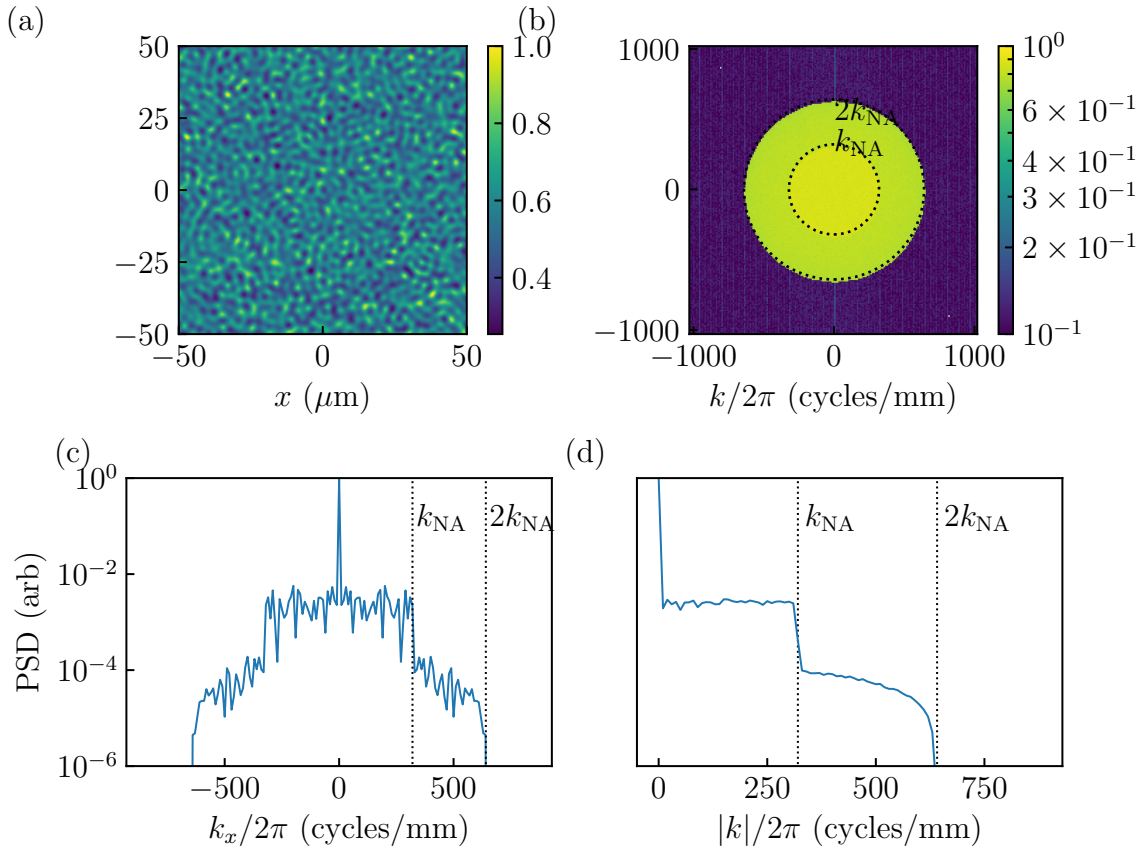

Figure B.3: Fourier analysis of imaging or projection of a random pattern. (a) Coordinate space image after propagating through a system with $\mathrm{NA} = 0.25$. (b) 2D Fourier space decomposition of image. (c) 1D cross-section of power spectral density. (d) Radial average of power spectral density. The resulting image/projection includes Fourier components up to $2k_{\mathrm{NA}}$, but the dominant contribution comes from components below k_{NA}.

limit corresponding to k_{NA}; components with finer spatial features are approximately two orders of magnitude weaker.

B.1.5 Optical relays

A second imaging system can be added in series with the primary to change the magnification or extend the system. In this configuration, the object for the secondary 'relay' system is the image formed by the primary system. The total magnification is the product of the magnification for the two systems $M = m_{\mathrm{obj}} m_{\mathrm{relay}}$. This makes relay systems an attractive option to achieve a high magnification with limited size. Additionally when using a Keplerian relay with a Keplerian primary imaging system, the net magnification will be positive, corresponding to a non-inverted image.

Because ray cone size is different at different part of the imaging system, the effective numerical aperture is different at different parts of the relay. For a Keplerian imaging system with an object space space $\mathrm{NA}_{O,p}$, the image space will have $\mathrm{NA}_{I,p} = \mathrm{NA}_{O,p}/|m|$. Since a relay takes the intermediate image formed by the primary imaging system as its object, the final image space NA will be further modified to $\mathrm{NA}_{\mathrm{I,r}} = \mathrm{NA}_{\mathrm{O,p}}/(|m_{\mathrm{p}}||m_{\mathrm{r}}|)$. When using a relay for magnification, this means the optical performance requirement of the relay optics are lower than the requirements for the primary optics.

B.2 Imaging Objective Design

Next, we move from the basics of imaging systems to describe our imaging system design. The starting point for our imaging objective is the well known design of Alt [141], which uses four

singlet lenses and achieves diffraction limited performance while compensating for the presence of a vacuum window. Bennie et. al. extended this approach, creating a similar design using only commercially available singlet lenses [142]. Our choice of imaging solutions is limited by a relatively long working distance (30. mm from the object plane to the window, and at minimum 39 mm from the object plane to the first lens of the objective) and the presence of our vacuum window (9 mm fused silica). This marks an advantage of cell based ultracold atom experiments which are often compatible with commercial objectives with shorter working distances.

Our goal was to achieve diffraction-limited performance at the highest NA possible, while using off-the-shelf optical components. Our criterion for desired performance was a Strehl ratio greater than 3/4 over a field of view of at least $100\mu\mathrm{m}$. To this end we used a commercially available imaging aspheric lens [Edmund Optics #12-448]. We used this lens as an element in the general form of the Alt/Bennie objective, then optimized the performance, using Zemax OpticStudio to change the surfaces and spacing of the remaining three lenses. Because of the high design NA (up to 0.5) our largest design challenge was spherical aberration from the flat window as well as any spherical lenses we included in the design. Following this optimization, we went through a a process of stock lens matching, finding suitable catalog lenses to replace the optimized lenses in our optical design. We proceeded in cycles of optimization and stock matching until all the lenses in the design were comically available, and the performance met our goal.

We produced two prototype designs in this way. In the first, we matched the aberrations of a compound objective to a compound tube lens, using four lenses total. The cross section and technical description for this design are shown in Fig. B.4. In the second we designed a corrected compound objective consisting of four lenses that could be used with any tube lens (Fig. B.5).

(a)

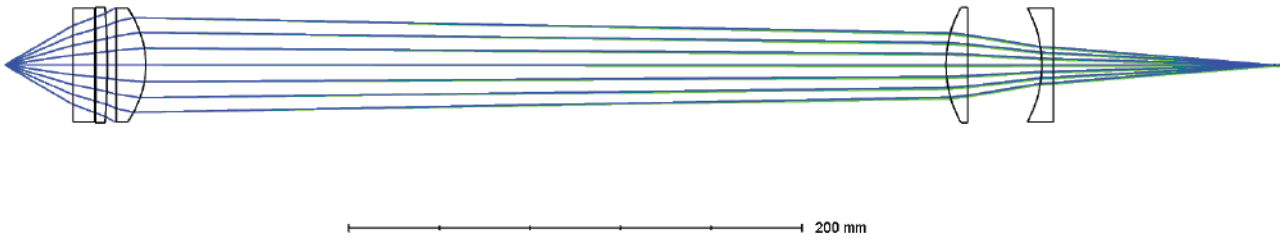

(b)

	Surface Type		Comment	Radius	Thickness	Material	Coating	Clear Semi-Dia	Chip Zone	Mech Semi-Dia	Conic	TCE x 1E-6	2nd Order Ter	4th Order Ter	6th Order Ter	8th Order Ter	10th Order Te
0	OBJECT	Standard		Infinity	30.000			0.100	0.000	0.100	0.000	0.000					
1	(aper)	Standard		Infinity	9.530	F_SILICA		25.000 U	0.000	25.000	0.000	-					
2	(aper)	Standard		Infinity	0.500			25.000 U	0.000	25.000	0.000	0.000					
3	(aper)	Standard	LE4822	-1580.240	5.000	F_SILICA		25.400 U	0.000	25.400	0.000	-					
4	(aper)	Standard		-356.690	4.047			25.400 U	0.000	25.400	0.000	0.000					
5	STOP (aper)	Standard	12-448	Infinity	13.058	N-SF6		22.500 U	2.500	25.000	0.000	-					
6	(aper)	Even Asphere		-40.259	352.809			22.500 U	2.500	25.000	-0.770	0.000	-0.000	-1.479E-07	7.468E-11	5.681E-14	-1.783E-17
7	(aper)	Standard	LA1050	51.500	9.690	N-BK7		25.400 U	0.000	25.400	0.000	-					
8	(aper)	Standard		Infinity	32.611			25.400 U	0.000	25.400	0.000	0.000					
9	(aper)	Standard	45-036	-51.680	5.000	N-BK7		24.500 U	0.500	25.000	0.000	-					
10	(aper)	Standard		Infinity	97.665			24.500 U	0.500	25.000	0.000	0.000					

Figure B.4: Prototype acting as a complete imaging system.

The second approach is greatly preferred since it groups the system into individual elements, with the aberrations corrected within each element. Furthermore it allows the magnification to be changed by replacing the tube lens with any appropriately performing optic, where the first would require a careful redesign to give optimal performance.

Figs. B.6 and B.7 show the PSF, obtained by measuring the image produced from a $1\mu\mathrm{m}$ pinhole, for our two prototypes. For the first case (design Fig. B.4 and results Fig. B.6) the primary objective has a magnification of $m_p = 4.5$ (obtained from Zemax simulations); we combined with with a relay having $m_r = 5$ for a total magnification of 22.5. For the second (design Fig. B.5 and results Fig. B.7) we used a tube lens with $f = 500\mathrm{mm}$ for a primary magnification of $m_p = 9.6$ and a relay with $m_r = 10$ so that the total magnification was 96.

In both cases the observed system performance approximately corresponds to an NA of around 0.2, much less than the design NA of 0.45, although the limiting aperture in our system would be compatible with NA up to 0.45. We suspect that the deviation is due to uncorrected

(a)

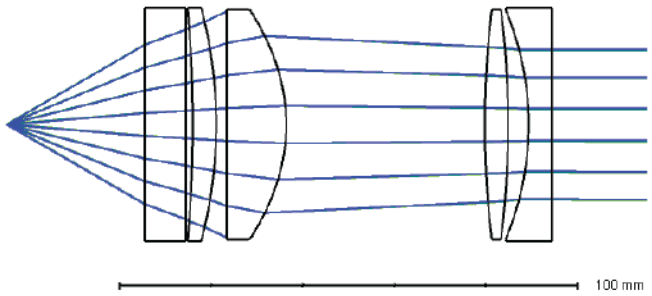

(b)

	Surface Type		Comment	Radius	Thickness	Material	Coating	Clear Semi-Dia	Chip Zone	Mech Semi-Dia	Conic	TCE x 1E-6	2nd Order Ter	4th Order Ter	6th Order Ter	8th Order Ter	10th Order Te
0	OBJECT	Standard		Infinity	30.000			0.100	0.000	0.100	0.000	0.000					
1		Standard		Infinity	9.042	F_SILICA		17.361	0.000	25.400 U	0.000	-					
2		Standard		Infinity	1.532			20.664	0.000	25.400	0.000	0.000					
3	(aper)	Standard	LE1985-B	-279.120	5.100	N-BK7		25.400 U	0.000	25.400	0.000	-					
4	(aper)	Standard	LE1985-B	-100.080	2.213			25.400 U	0.000	25.400	0.000	0.000					
5	(aper)	Standard		Infinity	13.058	N-SF6		22.500 U	2.500	25.000	0.000	-					
6	STOP (aper)	Even Asphere		-40.259	43.396			22.500 U	2.500	25.000	-0.770	0.000	-0.000	-1.479E-07	7.468E-11	5.681E-14	-1.783E-17
7	(aper)	Standard	45908INK	205.860	5.050	N-BK7		24.500 U	0.500	25.000	0.000	-					
8	(aper)	Standard		-205.860	4.500			24.500 U	0.500	25.000	0.000	0.000					
9	(aper)	Standard	45-038	-64.600	5.000	N-BK7		24.500 U	0.500	25.400	0.000	-					
10	(aper)	Standard		Infinity	300.000			25.400 U	0.000	25.400	0.000	0.000					

Figure B.5: Prototype acting as an infinity corrected objective.

spherical aberration. This could be caused by deviations in the lens spacing of our prototype compared to the design, or by deviations in the optics from their specified parameters. The rays from parts of the aperture beyond the cone angle given by $\mathrm{NA} = 0.2$ are not focused at the focal plane and thus show up as background in the measured PSF. The radial averaging and fitting in Figs. B.6 and B.7 was done after a background subtraction, where the background was approximately 20% of the peak brightness, including contributions from noise, stray light as well as aberrated components of the image.

B.2.1 Measuring the vacuum window thickness

The optimal lens placement in our design depends strongly on the thickness of our vacuum window. Our specification for the window had a tolerance of 0.25 mm (approximately 3%) which is too large for the optical performance we want. Based on this, we decided to measure the window thickness using reflected laser light, using the specified index of refraction and measuring

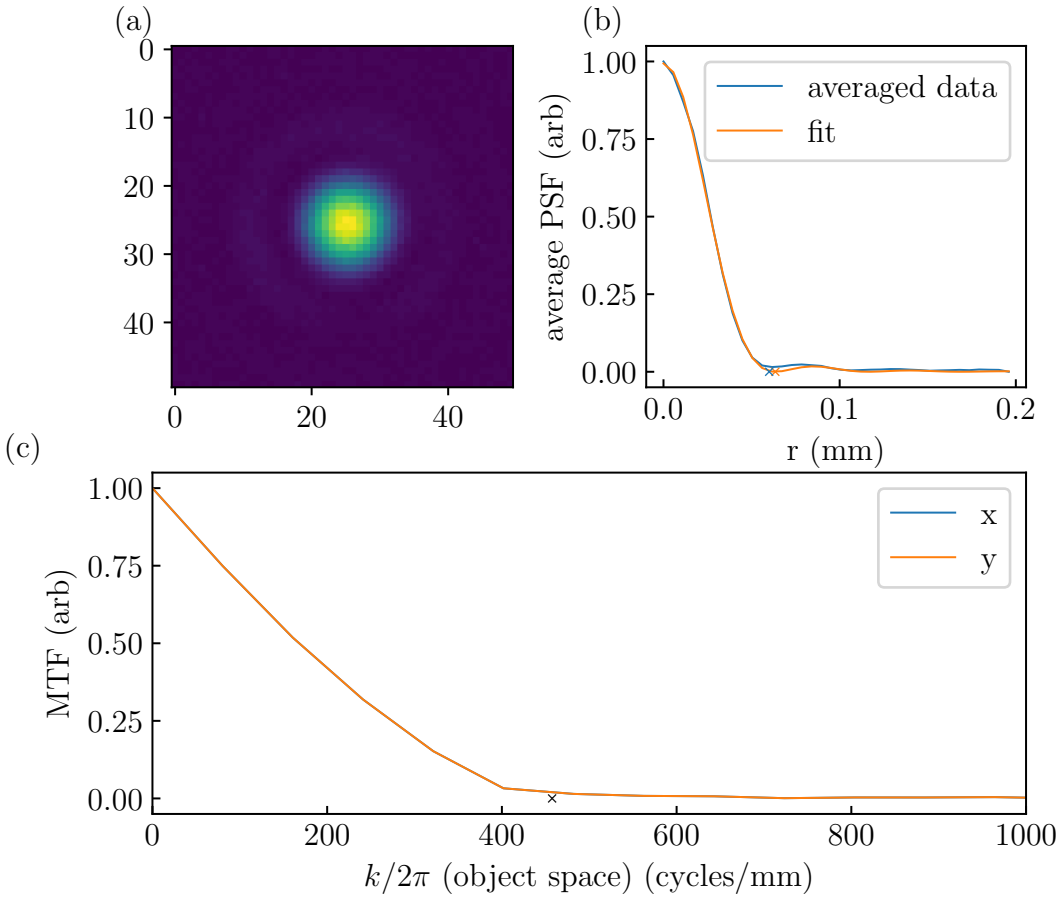

Figure B.6: Measured PSF for imaging system prototype for design in Fig. B.4. Because of an additional optical relay the total magnification was $M = 22.5$. (a) 2D image. (b) Radially averaged image and fit to the ideal PSF, given by an Airy disk. (c) Cross sections of the 2D Fourier transform, corresponding to the MTF. The "x" marks the location of the cutoff frequency corresponding to the first 0 in the PSF.

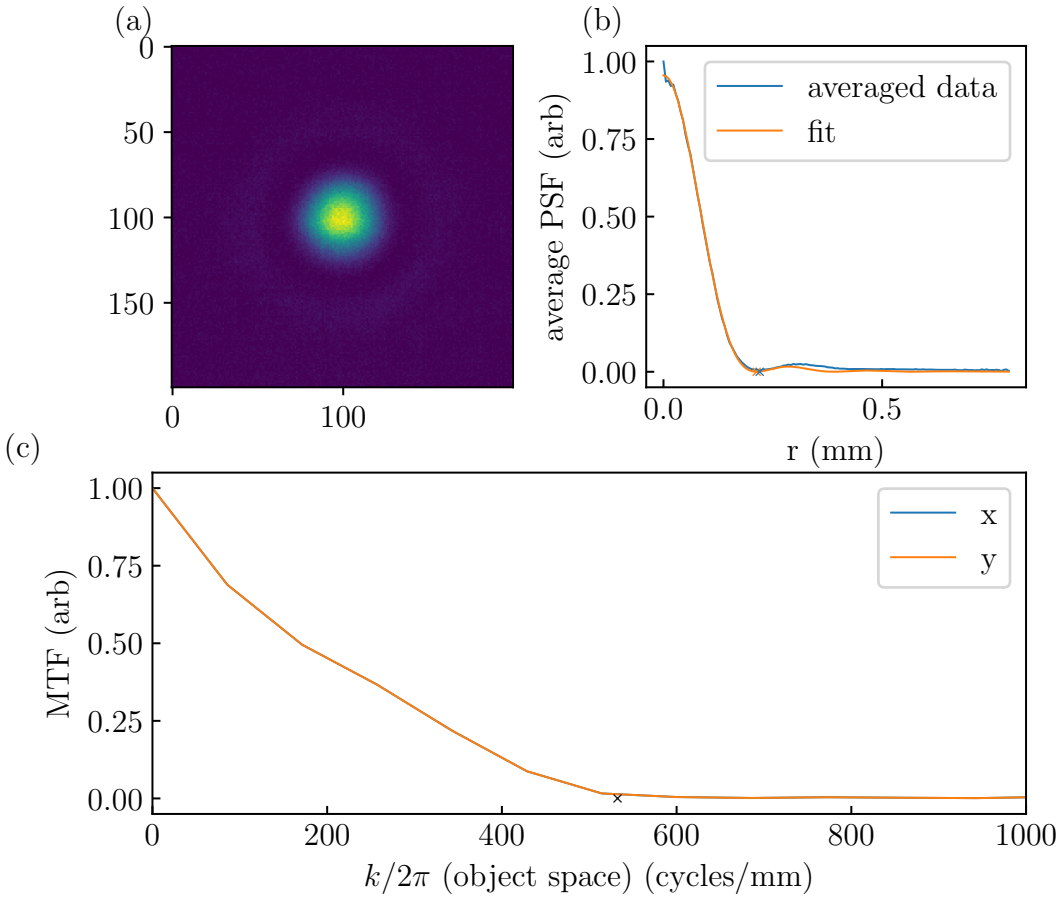

Figure B.7: Measured PSF for imaging system prototype for the infinity corrected design in Fig. B.5. Because of an additional optical relay the total magnification was $M = 96$. (a) 2D image. (b) Radially averaged image and fit to the ideal PSF, given by an Airy disk. (c) Cross sections of the 2D Fourier transform, corresponding to the MTF. The "x" marks the location of the cutoff frequency corresponding to the first 0 in the PSF.

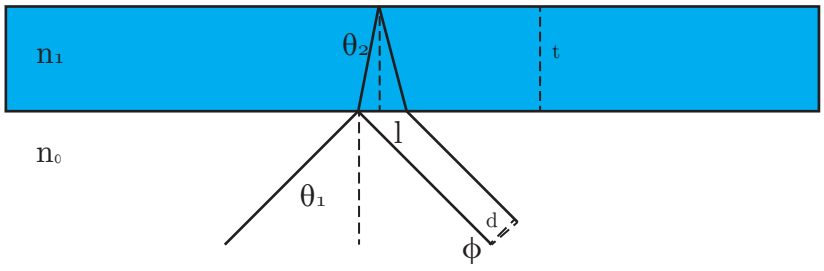

Figure B.8: Window thickness measurement geometry.

the separation between two reflected spots to infer the thickness. Fig. B.8 shows the geometry and the measured quantities: θ_1 and m. By fixing the angle of the CCD screen to θ_1, we set the relative screen angle ϕ to zero, so that the measured spacing equals d. Deviation between the camera angle and θ_1 is quantified by ϕ, which ideally would be 0, but is a potentially large source of systematic error. θ_2 can be obtained from θ_1 using Snell's law and tabulated values for n for air and fused silica $n_0 = 1.00029$, $n_1 = 1.4607$ [143].

$$\theta_2 = \sin^{-1}\left(\sin(\theta_1)\frac{n_0}{n_1}\right) \tag{B.4}$$

The thickness can be obtained from the measured quantities via

$$l = d\sec\theta_1, \tag{B.5}$$

$$t = \frac{l}{2}\cot\theta_2. \tag{B.6}$$

To perform the measurement, we used a 532 nm laser and a fiber collimator mounted to a rotational stage acting as a makeshift goniometer, set so that the beam left at an angle of 45.0 degrees relative to the window (θ_1). We chose this so that we could set the angle of the camera

to 45 degrees using a level (no goniometer was available to mount the camera.) Our measured value of $d = 7.1(2)\mathrm{mm}$ corresponds to a thickness of $9.0(3)\mathrm{mm}$, agreeing with the specified value of $9.0\mathrm{mm}$. The uncertainty in the calculated value is not an improvement over the specified tolerance, so this method may require better equipment to deliver a precision result.

Appendix C: Creating solitons with controllable and near-zero velocity in Bose–Einstein condensates

Editors' Suggestion | Featured in Physics

Creating solitons with controllable and near-zero velocity in Bose-Einstein condensates

A. R. Fritsch, Mingwu Lu, G. H. Reid, A. M. Piñeiro, and I. B. Spielman*

Joint Quantum Institute, National Institute of Standards and Technology, and University of Maryland, Gaithersburg, Maryland 20899, USA

(Received 29 January 2020; accepted 14 April 2020; published 20 May 2020)

Established techniques for deterministically creating dark solitons in repulsively interacting atomic Bose-Einstein condensates (BECs) can only access a narrow range of soliton velocities. Because velocity affects the stability of individual solitons and the properties of soliton-soliton interactions, this technical limitation has hindered experimental progress. Here we create dark solitons in highly anisotropic cigar-shaped BECs with arbitrary position and velocity by simultaneously engineering the amplitude and phase of the condensate wave function, improving upon previous techniques which explicitly manipulated only the condensate phase. The single dark soliton solution present in true one-dimensional (1D) systems corresponds to the kink soliton in anisotropic three-dimensional systems and is joined by a host of additional dark solitons, including vortex ring and solitonic vortex solutions. We readily create dark solitons with speeds from zero to half the sound speed. The observed soliton oscillation frequency suggests that we imprinted solitonic vortices, which for our cigar-shaped system are the only stable solitons expected for these velocities. Our numerical simulations of 1D BECs show this technique to be equally effective for creating kink solitons when they are stable. We demonstrate the utility of this technique by deterministically colliding dark solitons with domain walls in two-component spinor BECs.

DOI: 10.1103/PhysRevA.101.053629

Localized excitations such as vortices and kink solitons in atomic Bose-Einstein condensates (BECs) have attracted much attention. Solitons are long-lived shape-preserving solitary waves typically stabilized by a balance between linear and nonlinear effects [1–5]. Experiments with dark solitons in repulsively interacting systems first identified different regimes of stability for solitons [6–8] before exploring effects including soliton interactions [9] and diffusion [10]. For all their success, these experiments could deterministically produce solitons within only a narrow range of velocities. Inspired by Ref. [11], we demonstrate a straightforward technique for creating dark solitons that provides full control over their position and velocity.

The propagation velocity of dark solitons in quasi-one-dimensional (1D) systems determines many of their properties; indeed, their maximum speed is bounded by the local speed of sound c in their host BEC. A pair of colliding dark solitons will, long after the collision, have unchanged shape and velocity, with the effect of interaction being only in a displacement in their asymptotic trajectories [12]. For sufficiently small relative velocities the collision can be viewed as if the two solitons reflect from each other like equal-mass hard spheres [13], giving the same asymptotic velocity and shapes as if they had passed through each other. This is sometimes referred to as a "noninteracting" collision.

A dark soliton manifests as a moving density depletion in a BEC (we call a stationary density depletion a "black soliton"), whose width increases with velocity and whose depth decreases with velocity. Across a soliton, the underlying BEC wave function has a phase difference that determines its velocity. In anisotropic three-dimensional (3D) systems such as ours, this overall longitudinal phase drop can be accompanied by transverse structure, leading to a host of distinct dark solitons. The single dark soliton solution present in true 1D systems, for which a transverse structure is absent, corresponds to the kink soliton in anisotropic 3D systems. The solitonic vortex is another example of a solitonic excitation present in 3D systems; although its velocity-dependent longitudinal phase drop and density profile are qualitatively similar to those of kink solitons, as a vortex, it also has a phase singularity where the density vanishes. In three-dimensional traps, kink solitons are stable only for a range of velocities that depend on the trap geometry [1]. In regimes where kink solitons are unstable, solitonic vortices are stable. For our system, the kink soliton is predicted to be unstable except for velocities very close to c, and for almost all parameters, the solitonic vortex is predicted to be the only stable solitonic excitation [14].

There is no single and universally agreed upon definition of a solitonic vortex in the literature. One definition hinges on the fact that a vortex in a channel whose transverse size is much smaller than its length and has the same asymptotic phase profile as a soliton in the longitudinal direction [15]. While the other definition notes that when the transverse harmonic oscillator length becomes comparable to the healing length, the vortex density profile is reminiscent of a kink soliton [16]. In this paper we remain agnostic about the choice of definition, but our experiment corresponds to the first definition.

The established technique for producing dark solitons simply consists of laser-imprinting a longitudinal phase difference onto the BEC wave function. A soliton at rest typically has a density profile width of about 0.5 μm, while its phase profile is a step function. Imaging systems used to optically imprint the phase change typically have resolution limits of 1.5 μm or more. Furthermore, the established technique does

*ian.spielman@nist.gov; http://ultracold.jqi.umd.edu

not reduce the density in a controllable way at the soliton position. Instead, the optical dipole force resulting from intensity change at the soliton position changes the density in a way that is not generally consistent with the imprinted phase difference. All these features give poor overlap with the desired soliton wave function [6,7,10]. As a result, these experiments have only successfully produced solitons moving at a substantial fraction of the sound velocity. We overcome this limit by simultaneously engineering the BEC density and phase. This control allows us to improve the spatial mode-matching between the applied potential and the desired soliton wave function. This allows us to create solitons with speed ranging from zero to half the velocity of sound.

This manuscript is organized as follows: First, we summarize the essential properties of dark solitons in repulsively interacting 1D BECs, which still captures the essential physics for dark solitons in anisotropic 3D systems; second, we describe our experimental methods for imprinting and detecting solitons; third, we demonstrate our protocol and explore its range of applicability; and lastly, we exhibit the utility of this approach by colliding a dark soliton with a domain wall in a two-component spinor BEC.

I. DARK SOLITONS IN REPULSIVE BECS

Bose-Einstein condensates well below their transition temperatures, i.e., with negligible thermal fraction, are well described by the Gross-Pitaevskii equation (GPE). Solitons are exact solutions of the one-dimensional GPE [17,18],

$$i\hbar\frac{\partial}{\partial t}\Psi(z,t)=\left[-\frac{\hbar^2}{2m}\frac{\partial^2}{\partial z^2}+U(z)+g_{1D}|\Psi(z,t)|^2\right]\Psi(z,t), \tag{1}$$

for particles of mass m, which approximately describes highly anisotropic systems where transverse motion is frozen out by strong confinement, leaving behind only longitudinal dynamics. For harmonic transverse confinement with transverse trapping frequencies ω_x and ω_y, the 1D interaction constant is $g_{1D}=2\hbar a(\omega_x\omega_y)^{1/2}$, where a is the 3D s-wave scattering length. In the GPE, $\Psi(z,t)$ is interpreted as the condensate wave function whose magnitude gives the local 1D atomic density $n(z,t)=|\Psi(z,t)|^2$. An infinite homogeneous system is characterized by the chemical potential $\mu=g_{1D}n$ and has low-energy phonon excitations with speed of sound $c=\sqrt{g_{1D}n/m}$ [19].

A dark soliton appears as a moving depletion in the background BEC; for an infinite and homogeneous system a dark soliton with velocity v is exactly described by

$$\Psi_s(z,t)=\sqrt{n}\left\{i\frac{v}{c}+\sqrt{1-\frac{v^2}{c^2}}\times\tanh\left[\sqrt{1-\frac{v^2}{c^2}}\frac{(z-vt)}{\xi}\right]\right\}\exp\left(-\frac{i\mu t}{\hbar}\right). \tag{2}$$

The healing length $\xi=\hbar/mc$ is the typical minimum length scale on which the condensate wave function can appreciably change. This soliton solution can be characterized by ϕ, the change in the condensate phase across the soliton. The soliton velocity, characteristic density profile width w_s, and depth n_s are all derived from the phase via

$$\frac{v}{c}=\cos\frac{\phi}{2}, \tag{3a}$$

$$\frac{w_s}{\xi}=\csc\frac{\phi}{2}=\frac{1}{\sqrt{1-v^2/c^2}}, \tag{3b}$$

$$\frac{n_s}{n}=\sin^2\frac{\phi}{2}=1-\frac{v^2}{c^2}. \tag{3c}$$

The phase change across a stationary black soliton, i.e., with zero central density, is therefore π. This result further shows that as the soliton velocity approaches that of sound, its wave function smoothly connects to the ground-state wave function.

Like most experiments with solitons, ours takes place in a highly elongated system with $\omega_z\ll\omega_{x,y}$, but with $\omega_{x,y}<\mu/\hbar$, requiring the 3D GPE for a proper description. The 3D GPE supports many solitonic solutions [14], from kink solitons—the analog to dark solitons in 1D—to vortex rings and solitonic vortices. Reference [1] showed that with sufficient transverse confinement, kink solitons can be unconditionally stable in anisotropic 3D systems; however, our system is in a regime where only rapidly moving kink solitons with $v/c\gtrsim 0.9$ are stable.

The most common method to create solitons writes the phase drop ϕ associated with the soliton wave function onto initially homogeneous BECs. In practice, this phase is imprinted by briefly applying an external potential $V(z)$, for example, a step function, that changes the wave-function phase by $\phi=V(z)t_p/\hbar$, where t_p is the duration of the applied pulse. Typically, $V(z)$ is generated by a far-detuned laser, and t_p should be shorter than $t_c=\hbar/\mu$, the time it takes an excitation moving at the speed of sound to traverse a single healing length, so the density remains unchanged over the pulse duration. Ideally, the imprinted phase would determine the initial soliton velocity; however, the phase imprinting system always has a finite resolution limiting the lowest possible soliton velocity. In our experiment $c\sim 2\,\mathrm{mm/s}$ giving $\xi\sim 0.4\,\mu\mathrm{m}$, so that a slowly moving soliton with velocity $0.1c$ will have a width $w_s\sim 0.4\,\mu\mathrm{m}$, which is much smaller than our resolution of $2.8\,\mu\mathrm{m}$.[1] This rightly suggests that a BEC following such a phase imprinting process will differ significantly from the desired soliton wave function.

Our improved method overcomes this limitation by first depleting the density at the desired soliton location with two important outcomes: (1) the imprinted phase profile can better match that of a soliton because decreasing the density locally increases the healing length, thereby increasing the soliton width w_s; and (2) the density depletion is better mode matched to the density depletion at a soliton's center.

[1]Defined as the distance between the central peak and the first minimum of the Airy disk.

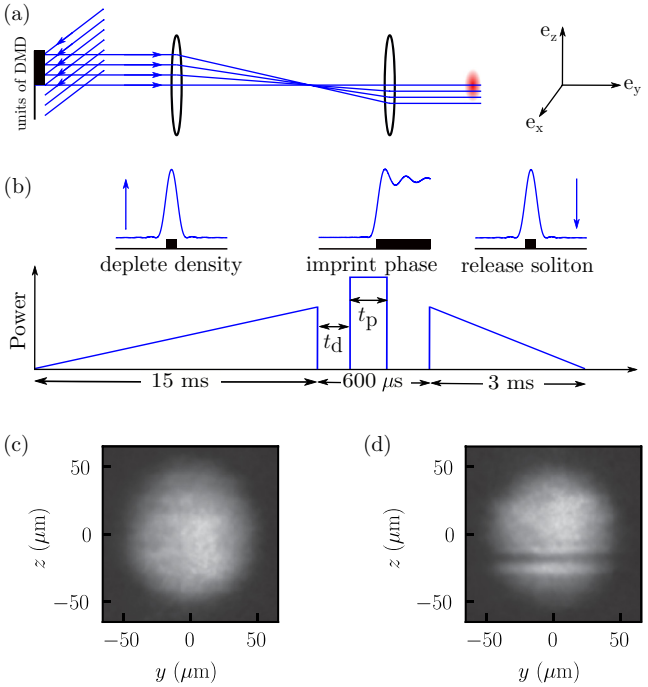

FIG. 1. Experimental concept. (a) Far-detuned laser light illuminates the surface of a DMD, which is programmed to reflect the light with the desired pattern. The DMD patterns are demagnified and imaged onto the atoms, which are represented as the red cloud. The trap laser beams are not shown in this figure. (b) Time sequence used to create solitons with the DMD pattern. The laser power during each phase of the experiment (vertical axis) was controlled using an acousto-optic modulator. The insets depict the potential resulting from the DMD patterns, accounting for the 2.8 μm (see footnote 1) resolution of our imaging system (because of the finite aperture, but neglecting any aberrations). (c) Absorption image of a typical BEC after TOF without solitons. (d) A BEC created with similar experimental conditions including a soliton.

II. EXPERIMENTAL SYSTEM

Our experiments begin with ^{87}Rb BECs having $N = 2.4(2) \times 10^5$ atoms[2] in the $|f = 1, m_f = 0\rangle$ internal state in a time-averaged crossed optical dipole trap of wavelength $\lambda = 1064$ nm. One of the beams is rastered along $\mathbf{e}_z$, with maximum displacement of about one waist, painting an elongated trap with frequencies $(\omega_x, \omega_y, \omega_z) = 2\pi \times [94.5(6), 153(1), 9.1(1)]$ Hz. The measured (see below) longitudinal Thomas-Fermi (TF) radius of our BEC is $R^z_{\rm TF} = 55(1)\,\mu$m, and the chemical potential is $\mu = h \times 1.1(1)$ kHz. We create arbitrary repulsive potentials $V(z)$ using far blue-detuned laser light of wavelength $\lambda = 777.6$ nm, spatially patterned by a digital micromirror device (DMD, Texas Instruments DLP LightCrafter Module, DLP3000).[3] The light reflected by the DMD is imaged onto the atoms (the DMD surface is focused at the BEC) using an imaging system that demagnifies ($\times 12$) the pattern as schematically shown in Fig. 1(a). There we illustrate the situation where the DMD is programmed to reflect half of the laser profile.

We engineer the local BEC density with a dimplelike potential created by programming the DMD to reflect the light in a stripe which, after demagnification, is about 270 μm wide along $\mathbf{e}_y$ and 1.8 μm along $\mathbf{e}_z$, as shown in the first inset to Fig. 1(b), including the impact of finite resolution. We ramp the optical potential from zero to $h \times 0.78(4)$ kHz in 15 ms, reducing the local atomic density by about 70%. Next, the light is extinguished for $t_d = 100\,\mu$s, while the DMD is updated[4] to display a step function, illuminating the BEC to one side of the dimple. The step potential is applied for a time t_p up to 170 μs, which, for our potential of magnitude $V = h \times 5.5(3)$ kHz, results in an accumulated relative phase up to $1.9(1)\,\pi$. To avoid abrupt changes in the BEC density after phase imprinting, we reapply the dimple potential and ramp its magnitude to zero in 3 ms. The times to ramp the dimple up and down were chosen to be slow enough to be reasonably adiabatic and fast enough so that the soliton does not propagate very far during the ramp down. For comparison we create solitons without density engineering by applying the same time sequence with the dimple potential set to zero.

After a variable evolution time, the dipole trap potential is removed, allowing the BEC to expand for a 15 ms time of flight (TOF), after which time the BEC is imaged using standard absorption imaging [20]. A typical image of a TOF-expanded BEC with no soliton imprinted is shown in Fig. 1(c); each dark soliton appears as a local dip in the density as in Fig. 1(d). Note that because of the trap geometry, the cloud in the $\mathbf{e}_y$ direction expands faster than in $\mathbf{e}_z$, such that the two directions have similar sizes at this particular expansion time. Because the BEC expands so slowly in the $\mathbf{e}_z$ direction, our analysis of the TOF images assumes that the z positions in TOF correspond to the z positions in trap at the time of release.

We experimentally calibrate the phase imprinting and density engineering potential by adiabatically loading the BEC into the steplike potential usually used for phase imprinting described above. From the time-of-flight images and the Castin-Dum scaling theory of BEC expansion [21] we determine the difference in the mean-field energy, i.e., the local chemical potential $\mu(z)$ between the two sides of the steplike potential. This calibrates the step potential. For more

[2]All uncertainties herein reflect the uncorrelated combination of single-sigma statistical and systematic uncertainties.

[3]Certain commercial equipment, instruments, or materials are identified in this paper in order to specify the experimental procedure adequately. Such identification is not intended to imply recommendation or endorsement by the National Institute of Standards and Technology, nor is it intended to imply that the materials or equipment identified are necessarily the best available for the purpose.

[4]This DMD can refresh every 250 μs, which includes about 150 μs of signal and/or electronics delay and about 100 μs for the mechanical response of the mirrors. Therefore, we command the DMD to change 150 μs before extinguishing the dimple light, and we wait another 100 μs while the mirrors change mechanically before applying the phase imprinting light. We leave the phase imprinting light on for the desired time. We anticipate reapplying the dimple by commanding the DMD to change to the dimple configuration at an appropriate time sufficiently long before reapplying the dimple light. The light is turned on/off in much less than 1 μs using an acousto-optic modulator.

details and discussion about the approximation involved, see Appendix A.

We measure the sound velocity in the BEC by intentionally inducing density perturbations in the condensate launched by abruptly turning on the dimple potential at the trap center, creating a pair of density waves traveling in opposite directions at the speed of sound [22]. We associate the average speed of these waves with a 1D speed of sound, giving $c = 1.65(5)\,\mathrm{mm/s}$, which is related to the 3D speed of sound by $c = c_{3D}/\sqrt{2}$, as is appropriate for highly elongated 3D BECs such as ours [19]. This speed is consistent with the 3D speed of sound derived from the chemical potential $c_{3D} = 2.2(1)\,\mathrm{mm/s}$, which would imply $c = 1.58(7)\,\mathrm{mm/s}$.

Even our improved protocol does not result in the perfect soliton wave function, resulting in undesired excitations that manifest as density modulations propagating at the speed of sound. These reach the extremes of the BEC and dissipate in less than 100 ms. We therefore take our earliest data 150 ms after phase imprinting to obtain a clean background for tracking solitons.

III. RESULTS

Here we compare the standard phase imprinting protocol with our improved protocol for creating solitons. Figure 2 illustrates our main result: (a) the standard protocol can only create solitons with a velocity so large that they have an oscillation amplitude comparable to the Thomas-Fermi radius; (b) the improved protocol can create solitons with no discernible motion, i.e., black solitons. In this section, we quantitatively compare the ability of these two techniques to create solitons on demand.

We first turn to a more detailed discussion of the data presented in Fig. 2, for which the phase imprinted was $\phi = 1.8(1)\,\pi$. Both (a) and (b) include 1D cross-sectional slices of our BEC after TOF as a function of time, illustrating the representative density profiles from which we obtain the soliton position by fitting the dip to a Gaussian function. These positions, for three repetitions of the experiment, are displayed by the semitransparent symbols in the accompanying panel and follow approximately sinusoidal trajectories. This raw data shows key differences between solitons created via these two protocols: the shallower solitons created using the standard protocol oscillate with larger amplitude, implying a higher peak velocity. This is consistent with our expectations that more rapidly moving solitons are associated with a shallower density depletion.

In Fig. 2, when fewer than three symbols are displayed, no soliton was observed in one or more of the trials at that time. Our data therefore indicates that fast solitons, created using the standard protocol, have shorter lifetimes than the stationary solitons. We suspect that this results in part from friction dissipation mechanisms, leading to a more rapid destabilization of fast-moving solitons similar to those discussed in Refs. [10,23,24]. In the latter two references, diffusion and damping resulted from the interaction with a dilute background of impurities. In the present case, the computation of the collision integral would result from the reflection of phonons rather than impurities.

For harmonically trapped 1D BECs, solitons follow sinusoidal trajectories described by $z(t) = A\sin(\omega_s t + \phi)$, with

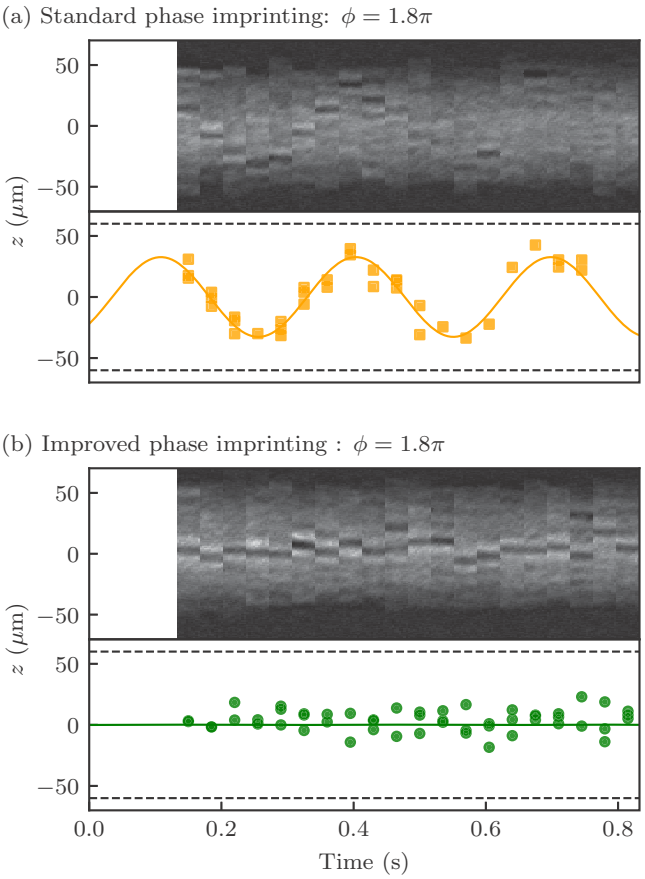

FIG. 2. Oscillation of dark solitons created using a $1.8(1)\,\pi$ phase imprint showing: (a) the standard protocol and (b) the improved protocol. In both cases, the top panel plots 1D longitudinal slices taken through our TOF-expanded BECs as a function of soliton evolution time for a single realization of the experiment at each time. The bottom panels plot the resulting soliton positions (symbols), with three realizations of the experiment for each time. The curve in (a) is a sinusoidal fit to the data described in the main text. Because the data in (b) reveals a stationary soliton, we used the procedure described in Appendix C to plot a sinusoidal oscillation with amplitude $A = 0.19\,\mu$m and $\omega_s = 2\pi \times 3.0\,$Hz. Dashed lines represent the edges of our BECs.

predicted oscillation frequency $\omega_{sol} = \omega_z/\sqrt{2}$, which is also valid for kink solitons in 3D. The factor of $\sqrt{2}$ is often described in terms of the ratio between the "inertial" and "physical" (or "bare") masses of a dark soliton, $\eta = m_{in}/m_{ph}$, $\omega_{sol} = \omega_z/\sqrt{\eta}$, with $\eta_k = 2$ for a kink soliton. The bare mass is related to the number of missing particles, and the inertial mass is related to the response to an external force. We measure an oscillation frequency of $\omega_s = 2\pi \times 3.0(1)\,$Hz. This differs significantly from the expected $\omega_z/\sqrt{2} = 2\pi \times 6.4(1)\,$Hz for a kink soliton. Therefore, we consider the possibility that we are observing a solitonic vortex. The mass ratio for solitonic vortices exhibiting small-amplitude oscillations depends on the chemical potential and transverse trapping frequency $\omega_\perp$ [14], which for our case gives $\eta_{sv} \approx 9$. For $\eta_{sv} \approx 9$ the computed oscillation frequency is $\omega_s \approx 2\pi \times 3\,$Hz, consistent with the observed frequency. Because our transverse frequencies are unequal, it is not *a priori* clear how to average

TABLE I. Transverse trapping frequencies $\omega_\perp$ and typical averages and the associated solitonic vortex mass ratio.

Expression	$\omega_\perp$ Value	$\eta_{sv} \approx$
ω_x	$2\pi \times 94.5(6)$ Hz	13
$\sqrt{\omega_x \omega_y}$	$2\pi \times 120.2(5)$ Hz	9
$(\omega_x + \omega_y)/2$	$2\pi \times 123.8(6)$ Hz	9
ω_y	$2\pi \times 153(1)$ Hz	7

them, or if averaging is suitable at all. Table I displays the transverse trapping frequencies and possible averages; we find both the geometric and arithmetic averages to be consistent with the observed soliton oscillation frequency.

Figure 3(a) plots the TOF soliton oscillation amplitude, obtained from a sinusoidal fit (except for imprinting time 160 μs, where we used the procedure described in Appendix C), as a function of the imprinting phase, and compares our experimental data (filled symbols) to results of 1D GPE simulations (solid curves, see Appendix B), which we expect to provide only qualitative guidance for solitonic vortices. This figure shows that the standard protocol (orange) creates solitons within a very narrow window of amplitudes, all comparable to R_{TF}, while the improved protocol (green) can tune the oscillation amplitude from this large value through zero. We observe experimentally that visible solitons are not created for phase imprints below about π, while above 2π, multiple solitons are created. Figure 3 therefore focuses on phase imprinting within this interval. The velocities, extracted from the sinusoidal fits and normalized by our measured sound velocity, are plotted in Fig. 3(b). This data shows that when standard phase imprinting is used (orange squares), solitons can only be created with velocities around $0.4c$, which is consistent with previous works [9,25]. In contrast, when the improved method is used (green circles) we acquire almost full control over the soliton velocity, including the ability to generate nearly stationary solitons. In this case, the oscillation amplitude is $A_I = 0(2)\,\mu$m, resulting in a peak velocity of $0.00(4)c$, which corresponds to a stationary soliton within our experimental uncertainty (see Appendix C).

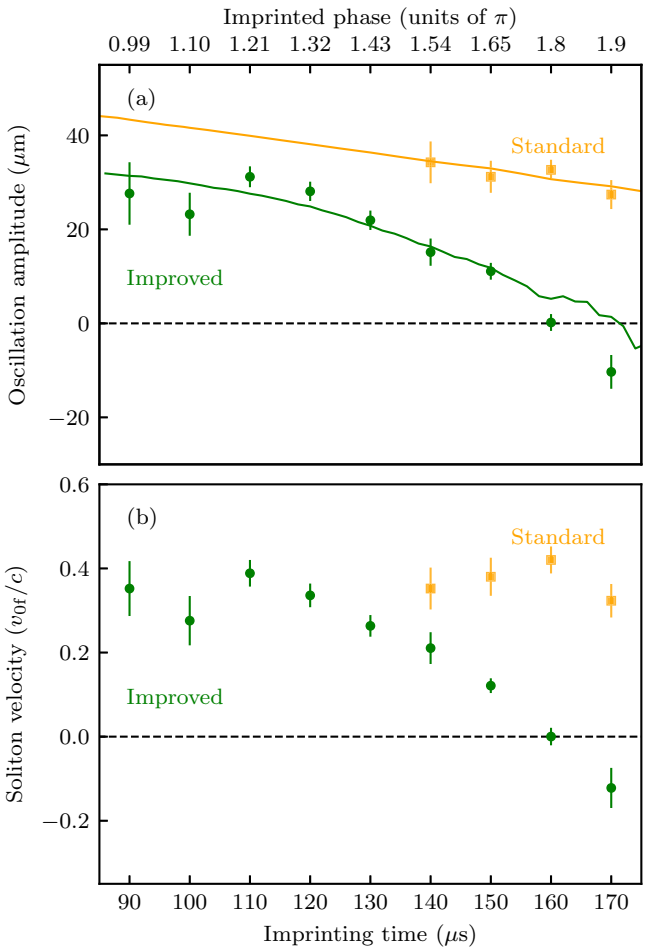

FIG. 3. Soliton oscillation amplitude (a) and velocity (b) for different imprinted phases. The imprinted phase (top axis) is related to the imprinting time (bottom axis) by our calibration of the DMD potential. Solid curves show the results of numerical simulations, and filled symbols are experimental data for the standard (orange) and improved (green) protocols.

IV. SOLITON–DOMAIN WALL COLLISIONS

We conclude with an application of our technique, deterministically colliding a dark soliton with a domain wall formed at the interface between the spin components of an immiscible binary BEC. The latter can be seen as a solitonic excitation in the sense that it is localized and long-lived magnetic excitation in a two-component BEC. The addition of the spin degree of freedom enriches the physics of solitons, both introducing new localized solitonic objects as well as altering the physics of dark solitons. For example, dark-bright solitons—a dark soliton in one component whose core is filled with the other component—have been created and collided [9]. This is also similar to earlier experiments creating vortices in spinor BECs in which the vortex core was filled with atoms in a different internal state [26].

To create a domain wall, we apply a radio frequency π pulse to our $|f = 1, m_f = 0\rangle$ BEC, putting each atom into an equal superposition of $|f = 1, m_f = +1\rangle$ and $|f = 1, m_f = -1\rangle$. The small, negative spin-dependent scattering length a_2 in ^{87}Rb, with $a_2/a \approx -0.005$ makes this binary mixture immiscible [27–29], leading to the formation of stable domain walls with size given by the spin-healing length $\xi_s = \xi\sqrt{|a/a_2|} \approx 5\,\mu$m. The BEC is held for 2 s in the presence of a small magnetic field gradient to initialize a domain wall between the two spin states.[5] After the soliton creation and a chosen propagation time, we perform spin-sensitive imaging by applying a magnetic field gradient ($\approx$0.6 mT cm^{-1}) during

[5]The gradient is not strictly necessary to initiate the domain wall, but the addition of gradient along the longitudinal direction of the BEC decreases the time for the system to reach equilibrium. We adiabatically apply a bias of the order of 10^{-4} T along the longitudinal direction, which due to imperfection in the alignment is enough to produce the gradient necessary to deterministically create the domain wall.

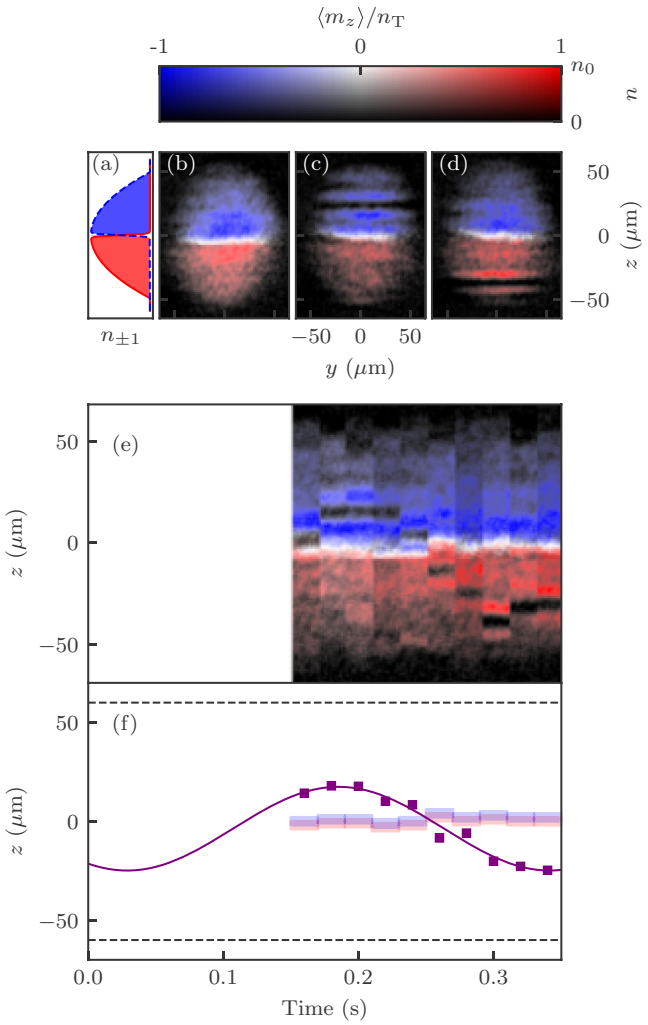

FIG. 4. Soliton crossing a domain wall. (a) Domain wall formed by atoms in different spin states. Absorption images of two-component BECs: (b) without a soliton present, (c) with a soliton in the $|f = 1, m_f = -1\rangle$ component, and (d) with a soliton in the $|f = 1, m_f = +1\rangle$ component. (e) Cross-sectional images resolving the domain wall and the soliton motion. (f) Extracted soliton and domain position averaged over three repetitions of the experiment.

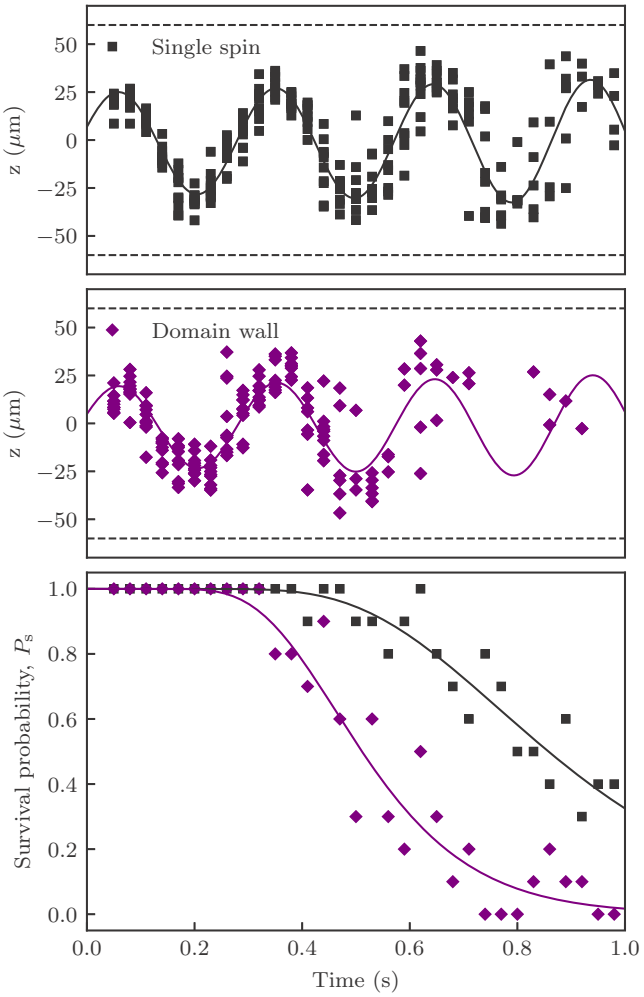

FIG. 5. Solitons oscillating in condensates including a domain wall. Position of solitons oscillating in a single-spin condensate (top) and a condensate with a domain wall present (center). For each time there are ten realization of the same experiment, and fewer points indicate that no soliton was observed in one or more realization. Solid curves are fits to $e^{\gamma} \sin(\omega t + \phi)$, where γ accounts for the possibility that soliton decay is associated with change in the oscillation amplitude (if these were kink solitons and if the decay mechanism were to involve reduction in the soliton depth, this would increase the soliton velocity and hence its oscillation amplitude). Dashed lines represent the edges of our BECs. The survival probability obtained from these ten realizations is shown in the bottom panel. Solid curves are the fit to the survival probability function.

TOF so that atoms in different magnetic states separate before absorption imaging. Figure 4(a) we plot the theoretical expected local density $n_{\pm 1}(\mathbf{r})$ of each spin component in a ground-state BEC containing a domain wall, where $n_{+1}(\mathbf{r})$ is displayed in red and $n_{-1}(\mathbf{r})$ is displayed in blue. In Fig. 4(b) we plot the magnetization $m_z(\mathbf{r}) \equiv n_{+1}(\mathbf{r}) - n_{-1}(\mathbf{r})$ of such a system after TOF in a color scale normalized by the total density $n_T(\mathbf{r}) \equiv n_{+1}(\mathbf{r}) + n_{-1}(\mathbf{r})$.

We create solitons on one side of the domain wall by offsetting the optical potential, patterned by the DMD, from the BEC center. Typical absorption images with solitons on either side of the domain wall are shown in Figs. 4(c) and 4(d). In Fig. 4(e) we show a sequence of normalized magnetization slices at different times as the solitons cross the domain wall. Figure 4(f) shows the soliton position averaged over three different experimental realizations. From these images we can see that the soliton oscillates as in Fig. 2 and is transmitted through the domain wall with no perceptible reflection or change in its trajectory, suggesting that the submicrometer scale soliton travels undistorted through the much thicker domain wall.

Figure 5 shows that the mean soliton trajectory is essentially indistinguishable without (top) and with (middle) the domain wall present, even after multiples passages through the domain wall. Although the mean trajectories are indistinguishable, the fate of solitons differs greatly between these two cases. The bottom panel shows that successive soliton–domain wall collisions reduce the soliton's survival

probability. In the presence of the domain wall (purple diamonds), the soliton survival probability decays to only 10% after ≈0.7 s, which is much lower than the survival probability for solitons created in single-component BECs (black squares), which is about 70% for the same time.

Our data shows that solitons are able to cross the domain wall at least two times with a high probability of survival, suggesting that the effects of the passage accumulate, contributing to subsequent decay. We fit (Fig. 5 bottom panel) the survival probability to the cumulative log-normal distribution,

$$P_s(t) = 1 - \frac{1}{2}\,\mathrm{erfc}\left[-\frac{\ln(t/\tau)}{\sqrt{2}\sigma}\right], \tag{4}$$

which describes systems where the probability of decay at time t depends on an accumulation of disrupting events. The constant τ is the characteristic time when P_s falls to $1/2$ and σ is the distribution width. In the presence of a domain wall, $\tau_{dw} = 0.51(1)\,\mathrm{s}$ is significantly smaller than for the single-spin case $\tau = 0.86(2)\,\mathrm{s}$. In both cases the BEC is prepared with the same trap geometry and at a similar temperature so the thermodynamic and transverse instabilities [1] should contribute in the same way. One possible dissipation mechanism involves the transfer of energy from the soliton to the domain wall, with each interaction incrementally destabilizing the soliton. Furthermore, the lifetime difference might be explained by a small thermally driven contamination of the majority spin with the minority spin in both domains, as investigated in Refs. [10,24].

Studies with different soliton velocities, soliton sizes, and domain-wall thicknesses might find a regime where solitons are reflected rather than transmitted when they impact a domain wall.

V. OUTLOOK AND DISCUSSION

We implemented an improved method to create dark solitons in BECs with controlled velocity and arbitrary position, combining standard phase imprinting with density engineering. The observed soliton oscillation frequency along with the theoretical stability diagram for kink solitons [1,14] suggests that we created solitonic vortices; however, our direct experimental evidence is not able to resolve the expected vortex structure [30]. Our numerical simulations in 1D (which is valid with greater transverse frequency or lower chemical potential) show that this technique generates well-controlled kink solitons.

We demonstrated the utility of the improved method by studying solitons incident on a domain wall and found that solitons pass through the domain wall and have increased decay probability after crossing the domain wall a few times. Even in 1D, collisions between solitons and magnetic domain walls have received little attention, but we expect that they have much in common with soliton-soliton collisions. When, as in our experiment, the magnetic domain wall is large in comparison with the soliton, we would expect the soliton—an excitation residing in density and phase—to "adiabatically" follow the slowly changing magnetization. This suggests that the collision will leave the soliton's shape unchanged, but because atoms displaced by the soliton are of opposite spin after the soliton has traversed the domain wall, we expect the domain wall to shift by roughly the healing length in a direction opposite to the soliton propagation direction. This is similar to a "noninteracting" collision.

When the soliton and domain wall become comparable in size, the soliton can no longer be thought of as a pointlike particle and a number of outcomes are possible, ranging from noninteracting to beam-splitter-like, to perfect reflection. Further studies are needed to fully understand soliton behavior in the presence of a domain wall.

Our capability for creating solitons with tunable velocities, including stationary solitons, enables the study of many phenomena, including dissipative dynamics [23,24], soliton stability and decay in different trap geometries [1,14], and soliton-soliton collisions in both the "reflection" and "transmission" regimes [13,25]. Furthermore, high-resolution nondestructive imaging techniques could be used to track the *in situ* soliton position and better understand their behavior [31]. Lastly, our technique could be used to study the predicted velocity-dependent spin structure of solitons in spin-orbit coupled BECs [32].

ACKNOWLEDGMENTS

This work was partially supported by the AFOSR's Quantum Matter MURI, the NIST, and the NSF through the PFC@JQI (Award No. 1430094). A.M.P. acknowledges support from the Louis Stokes Alliances for Minority Participation (LSAMP) Bridge to the Doctorate Program at the University of Maryland, College Park, under Grant No. 1612736. We are grateful for insights from a very detailed reading of our manuscript by W. D. Phillips and M. Zhao.

APPENDIX A: CALIBRATING POTENTIALS

Our time-of-flight images give a 2D ($y - z$) column density distribution having been integrated along x. We separately integrate along z the density distributions on either side of the step, giving us two distributions along y. We fit these two distributions to find the two TF radii. We apply the Castin-Dum procedure as if the two sides were separately expanded from our 3D harmonic trap, ignoring the steplike potential. We believe this procedure is justified because the confinement, and hence the expansion, is much stronger in the transverse x, y directions than in the longitudinal z direction. From the in-trap TF radii we extract the chemical potential for each side of the step. In the spirit of the local density approximation we identify the difference between these two chemical potentials as the difference of the local chemical potential on either side of the step. According to the Thomas-Fermi approximation, this is the height of the external step potentials.

APPENDIX B: NUMERICAL SIMULATIONS

We simulate the standard and improved phase imprinting methods using a 1D GPE assuming a transverse profile of the inverted-parabola Thomas-Fermi form, with width given by the local chemical potential. This approach correctly produces the 3D collective mode frequencies when the transverse dynamics are fast, allowing the transverse wave function to adiabatically follow the "chemical potential" derived from

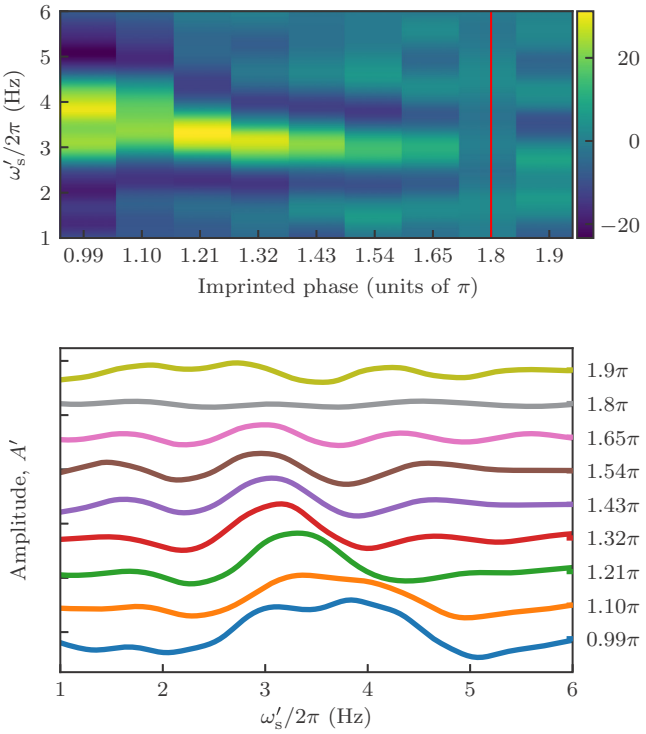

FIG. 6. Spectral analysis for solitons created using our improved protocol. Top panel shows in a color scale the amplitude for each frequency ω_s' vs the imprinted phase. Vertical red line is placed at the imprinted phase that creates stationary solitons. Bottom panel shows the individual plots with a vertical displacement to avoid overlapping the curves.

the time-changing 1D density. This gives the 1D GPE-like equation

$$i\hbar\frac{\partial}{\partial t}\Psi(z,t)=\left[-\frac{\hbar^2}{2m}\frac{\partial^2}{\partial z^2}+U(z)+g'_{1D}|\Psi(z,t)|\right]\Psi(z,t), \tag{B1}$$

where $g'_{1D}=2\hbar(a\omega_x\omega_y)^{1/2}$, and is related to the usual $g_{1D}=a^{1/2}g'_{1D}$.

The time evolution of the GPE is performed through the split-step Fourier method [33] in steps of 0.2 μs, and the ground state is found using imaginary time propagation. We simulate 2.6×10^5 ^{87}Rb atoms, which for our trap frequencies leads to a chemical potential of $\mu=h\times1.1$ kHz and $R_{TF}=56.4\,\mu$m. The grid ranges from -70 to 70 μm in steps of $\Delta z=0.025\,\mu$m.

We account for the finite resolution of the lens system by using potentials with smoothed edges, generated by removing Fourier components above the maximum optical resolution. The patterns used to engineer the density and step potential to imprint the phase are shown in Fig. 1, along with the resolution-limited intensity profile. We allow the simulated BEC to expand in TOF for 15 ms after the soliton oscillation time while quenching the interaction strength to model the rapid Castin-Dum transverse expansion in this 1D simulation. We analyze numerical results in the same way as we analyze the experimental data.

The results for the numerical simulations shown in Fig. 3 were obtained using a step potential of magnitude $V_t=h\times5.5$ kHz and a dimple $V_{dt}=h\times0.78$ kHz. Both potentials have the same magnitude used in the experiment. We attribute the small difference between numerical and experimental data to our numerical 1D simulation not fully describing the dynamics in our 3D system.

APPENDIX C: DISTINGUISHING BETWEEN SLOWLY MOVING AND STATIONARY SOLITONS

Our experimentally observed soliton positions have uncorrelated shot-to-shot noise on the scale of a few micrometers. Because most of our solitons oscillate with amplitude much larger than this noise, it generally contributes minimal uncertainty to our fits. This is not the case for our nearly stationary solitons.

Solitons created with nonzero velocity have a characteristic oscillation frequency. In contrast, solitons created at rest do not oscillate but still are susceptible to displacements due to shot-to-shot variation, and a fitting procedure with frequency as a free parameter will misidentify stationary solitons as moving solitons with frequency set by the noise spectrum. To distinguish between these cases we implemented a Fourier spectral analysis. Because our signal undergoes only about three oscillations in our time window of duration T, the $\delta\omega=2\pi/T$ transform limit makes conventional Fourier methods inapplicable.

For our spectral analysis, we fit the soliton dynamics to $z(t)=A'\sin(\omega_s't+\phi)$, with the frequency held constant at ω_s' for each fit. The fit-amplitude A' provides the spectral weight for that frequency; we then repeat the fitting procedure for different values of ω_s', ranging from $\omega_s'=2\pi\times1.0$ to $2\pi\times6.0$ Hz to obtain spectrograms.

Figure 6 shows the results of this technique, applied to solitons produced using our improved method. The top panel shows the amplitude in a color scale, while the bottom panel depicts the data for different applied phases displaced vertically to avoid overlapping the curves.

This figure clearly reveals the oscillation frequency at around $2\pi\times3$ Hz for all but the smallest oscillation, where no motion is resolvable above the noise. For the phase imprint of 1.8π there is no distinguishable feature at the expected oscillation frequency. From the fit we obtain $A'=0(2)\,\mu$m at $\omega_s'=2\pi\times3$ Hz. This is the argument underlying our statement that we have created dark solitons with no discernible motion within our experimental uncertainties.

[1] A. Muryshev, G. V. Shlyapnikov, W. Ertmer, K. Sengstock, and M. Lewenstein, Dynamics of Dark Solitons in Elongated Bose-Einstein Condensates, Phys. Rev. Lett. **89**, 110401 (2002).

[2] V. A. Brazhnyi, V. V. Konotop, and V. Kuzmiak, Dynamics of matter solitons in weakly modulated optical lattices, Phys. Rev. A **70**, 043604 (2004).

[3] Y. V. Kartashov and V. V. Konotop, Solitons in Bose-Einstein Condensates with Helicoidal Spin-Orbit Coupling, Phys. Rev. Lett. **118**, 190401 (2017).

[4] G. Juzeliūnas, J. Ruseckas, P. Öhberg, and M. Fleischhauer, Formation of solitons in atomic Bose-Einstein condensates by dark-state adiabatic passage, Lith. J. Phys. **47**, 351 (2007).

[5] P. B. Wigley, L. M. Starkey, S. S. Szigeti, M. Jasperse, J. J. Hope, L. D. Turner, and R. P. Anderson, Precise wave-function engineering with magnetic resonance, Phys. Rev. A **96**, 013612 (2017).

[6] S. Burger, K. Bongs, S. Dettmer, W. Ertmer, K. Sengstock, A. Sanpera, G. V. Shlyapnikov, and M. Lewenstein, Dark Solitons in Bose-Einstein Condensates, Phys. Rev. Lett. **83**, 5198 (1999).

[7] J. Denschlag, J. E. Simsarian, D. L. Feder, C. W. Clark, L. A. Collins, J. Cubizolles, L. Deng, E. W. Hagley, K. Helmerson, W. P. Reinhardt, S. L. Rolston, B. I. Schneider, and W. D. Phillips, Generating solitons by phase engineering of a Bose-Einstein condensate, Science **287**, 97 (2000).

[8] B. P. Anderson, P. C. Haljan, C. A. Regal, D. L. Feder, L. A. Collins, C. W. Clark, and E. A. Cornell, Watching Dark Solitons Decay into Vortex Rings in a Bose-Einstein Condensate, Phys. Rev. Lett. **86**, 2926 (2001).

[9] C. Becker, S. Stellmer, P. Soltan-Panahi, S. Dörscher, M. Baumert, E.-M. Richter, J. Kronjäger, K. Bongs, and K. Sengstock, Oscillations and interactions of dark and dark-bright solitons in Bose-Einstein condensates, Nat. Phys. **4**, 496 (2008).

[10] L. M. Aycock, H. M. Hurst, D. K. Efimkin, D. Genkina, H.-I. Lu, V. M. Galitski, and I. B. Spielman, Brownian motion of solitons in a Bose–Einstein condensate, Proc. Natl. Acad. Sci. **114**, 2503 (2017).

[11] L. D. Carr, J. Brand, S. Burger, and A. Sanpera, Dark-soliton creation in Bose-Einstein condensates, Phys. Rev. A **63**, 051601(R) (2001).

[12] D. J. Frantzeskakis, Dark solitons in atomic Bose–Einstein condensates: From theory to experiments, J. Phys. A: Math. Theor. **43**, 213001 (2010).

[13] A. Weller, J. P. Ronzheimer, C. Gross, J. Esteve, M. K. Oberthaler, D. J. Frantzeskakis, G. Theocharis, and P. G. Kevrekidis, Experimental Observation of Oscillating and Interacting Matter Wave Dark Solitons, Phys. Rev. Lett. **101**, 130401 (2008).

[14] A. M. Mateo and J. Brand, Stability and dispersion relations of three-dimensional solitary waves in trapped Bose-Einstein condensates, New J. Phys. **17**, 125013 (2015).

[15] M. J. H. Ku, W. Ji, B. Mukherjee, E. Guardado-Sanchez, L. W. Cheuk, T. Yefsah, and M. W. Zwierlein, Motion of a Solitonic Vortex in the BEC-BCS Crossover, Phys. Rev. Lett. **113**, 065301 (2014).

[16] J. Brand and W. P. Reinhardt, Generating ring currents, solitons and svortices by stirring a Bose-Einstein condensate in a toroidal trap, J. Phys. B: At., Mol. Opt. Phys. **34**, L113 (2001).

[17] Y. S. Kivshar, T. J. Alexander, and S. K. Turitsyn, Nonlinear modes of a macroscopic quantum oscillator, Phys. Lett. A **278**, 225 (2001).

[18] C. Barenghi and N. G. Parker, A Primer on Quantum Fluids, *Springer Briefs in Physics* (Springer, New York, 2016).

[19] E. Zaremba, Sound propagation in a cylindrical Bose-condensed gas, Phys. Rev. A **57**, 518 (1998).

[20] W. Ketterle, D. S. Durfee, and D. M. Stamper-Kurn, Making, probing and understanding Bose-Einstein condensates, in *Bose-Einstein Condensation in Atomic Gases*, edited by M. Inguscio, S. Stringari, and C. E. Wieman, Proceedings of the International School of Physics "Enrico Fermi," Course CXL (IOS Press, Amsterdam, 1999), pp. 67–176.

[21] Y. Castin and R. Dum, Bose-Einstein Condensates in Time Dependent Traps, Phys. Rev. Lett. **77**, 5315 (1996).

[22] M. R. Andrews, D. M. Kurn, H.-J. Miesner, D. S. Durfee, C. G. Townsend, S. Inouye, and W. Ketterle, Propagation of Sound in a Bose-Einstein Condensate, Phys. Rev. Lett. **79**, 553 (1997).

[23] D. K. Efimkin, J. Hofmann, and V. Galitski, Non-Markovian Quantum Friction of Bright Solitons in Superfluids, Phys. Rev. Lett. **116**, 225301 (2016).

[24] H. M. Hurst, D. K. Efimkin, I. B. Spielman, and V. Galitski, Kinetic theory of dark solitons with tunable friction, Phys. Rev. A **95**, 053604 (2017).

[25] S. Stellmer, C. Becker, P. Soltan-Panahi, E.-M. Richter, S. Dörscher, M. Baumert, J. Kronjäger, K. Bongs, and K. Sengstock, Collisions of Dark Solitons in Elongated Bose-Einstein Condensates, Phys. Rev. Lett. **101**, 120406 (2008).

[26] M. R. Matthews, B. P. Anderson, P. C. Haljan, D. S. Hall, C. E. Wieman, and E. A. Cornell, Vortices in a Bose-Einstein Condensate, Phys. Rev. Lett. **83**, 2498 (1999).

[27] T.-L. Ho, Spinor Bose Condensates in Optical Traps, Phys. Rev. Lett. **81**, 742 (1998).

[28] A. Widera, F. Gerbier, S. Fölling, T. Gericke, O. Mandel, and I. Bloch, Precision measurement of spin-dependent interaction strengths for spin-1 and spin-2 ^{87}Rb atoms, New J. Phys. **8**, 152 (2006).

[29] D. L. Campbell, R. M. Price, A. Putra, A. Valdés-Curiel, D. Trypogeorgos, and I. B. Spielman, Magnetic phases of spin-1 spin-orbit-coupled Bose gases, Nat. Commun. **7**, 10897 (2016).

[30] S. Donadello, S. Serafini, M. Tylutki, L. P. Pitaevskii, F. Dalfovo, G. Lamporesi, and G. Ferrari, Observation of Solitonic Vortices in Bose-Einstein Condensates, Phys. Rev. Lett. **113**, 065302 (2014).

[31] D. V. Freilich, D. M. Bianchi, A. M. Kaufman, T. K. Langin, and D. S. Hall, Real-time dynamics of single vortex lines and vortex dipoles in a Bose-Einstein condensate, Science **329**, 1182 (2010).

[32] D. Ma and C. Jia, Soliton oscillation driven by spin-orbit coupling in spinor condensates, Phys. Rev. A **100**, 023629 (2019).

[33] J. Javanainen and J. Ruostekoski, Symbolic calculation in development of algorithms: Split-step methods for the Gross–Pitaevskii equation, J. Phys. A: Math. Gen. **39**, L179 (2006).

Bibliography

[1] Daniel A Steck. Rubidium 87 d line data. 2001. Available online at http://steck.us/alkalidata (revision 2.2.2, 9 July 2021).

[2] Richard P Feynman. Simulating physics with computers. In *Feynman and computation*, pages 133–153. CRC Press, 2018.

[3] Ehud Altman, Kenneth R Brown, Giuseppe Carleo, Lincoln D Carr, Eugene Demler, Cheng Chin, Brian DeMarco, Sophia E Economou, Mark A Eriksson, Kai-Mei C Fu, et al. Quantum simulators: Architectures and opportunities. *PRX Quantum*, 2(1):017003, 2021.

[4] Immanuel Bloch, Jean Dalibard, and Sylvain Nascimbene. Quantum simulations with ultracold quantum gases. *Nature Physics*, 8(4):267–276, 2012.

[5] Daniel Kleppner. A short history of atomic physics in the twentieth century. *Reviews of Modern Physics*, 71(2):S78, 1999.

[6] Davide Castelvecchi. The Stern–Gerlach experiment at 100. *Nature Reviews Physics*, 4(3):140–142, 2022.

[7] Jonathan P Dowling and Gerard J Milburn. Quantum technology: the second quantum revolution. *Philosophical Transactions of the Royal Society of London. Series A: Mathematical, Physical and Engineering Sciences*, 361(1809):1655–1674, 2003.

[8] William D Phillips. Nobel lecture: Laser cooling and trapping of neutral atoms. *Reviews of Modern Physics*, 70(3):721, 1998.

[9] JR Ensher, Deborah S Jin, MR Matthews, CE Wieman, and Eric A Cornell. Bose–Einstein condensation in a dilute gas: Measurement of energy and ground-state occupation. *Physical Review Letters*, 77(25):4984, 1996.

[10] Cl C Bradley, CA Sackett, JJ Tollett, and Randall G Hulet. Evidence of bose-einstein condensation in an atomic gas with attractive interactions. *Physical Review Letters*, 75(9):1687, 1995.

[11] Kendall B Davis, M-O Mewes, Michael R Andrews, Nicolaas J van Druten, Dallin S Durfee, DM Kurn, and Wolfgang Ketterle. Bose-einstein condensation in a gas of sodium atoms. *Physical Review Letters*, 75(22):3969, 1995.

[12] David J Thouless, Mahito Kohmoto, M Peter Nightingale, and Marcel den Nijs. Quantized Hall conductance in a two-dimensional periodic potential. *Physical Review Letters*, 49(6):405, 1982.

[13] M Zahid Hasan and Charles L Kane. Colloquium: topological insulators. *Reviews of modern physics*, 82(4):3045, 2010.

[14] János K Asbóth, László Oroszlány, and András Pályi. A short course on topological insulators. *Lecture notes in physics*, 919:166, 2016.

[15] AR Fritsch, Mingwu Lu, GH Reid, AM Piñeiro, and IB Spielman. Creating solitons with controllable and near-zero velocity in bose-einstein condensates. *Physical Review A*, 101(5):053629, 2020.

[16] Christopher J Foot. *Atomic physics*, volume 7. OUP Oxford, 2004.

[17] Ennio Arimondo, M Inguscio, and P Violino. Experimental determinations of the hyperfine structure in the alkali atoms. *Reviews of Modern Physics*, 49(1):31, 1977.

[18] Gregory Breit and I I Rabi. Measurement of nuclear spin. *Physical Review*, 38(11):2082, 1931.

[19] Daniel A Steck. Quantum and atom optics. 2007. Available online at http://steck.us/teaching (revision 0.13.15, 28 July 2022).

[20] DM Brink and CV Sukumar. Majorana spin-flip transitions in a magnetic trap. *Physical Review A*, 74(3):035401, 2006.

[21] Isidor Isaac Rabi. Space quantization in a gyrating magnetic field. *Physical Review*, 51(8):652, 1937.

[22] Rudolf Grimm, Matthias Weidemüller, and Yurii B Ovchinnikov. Optical dipole traps for neutral atoms. In *Advances in atomic, molecular, and optical physics*, volume 42, pages 95–170. Elsevier, 2000.

[23] Nathan Goldman, G Juzeliūnas, Patrik Öhberg, and Ian B Spielman. Light-induced gauge fields for ultracold atoms. *Reports on Progress in Physics*, 77(12):126401, 2014.

[24] Harold J Metcalf and Peter Van der Straten. Laser cooling and trapping of neutral atoms. *The Optics Encyclopedia: Basic Foundations and Practical Applications*, 2007.

[25] Jun John Sakurai and Jim Napolitano. Modern quantum mechanics, revised edition, 2017.

[26] W Ketterle, DS Durfee, and DM Stamper-Kurn. Making, probing and understanding Bose–Einstein condensates. In *Bose–Einstein Condensation in Atomic Gases*, pages 67–176. IOS Press, 1999.

[27] Anand Ramanathan, Sérgio R Muniz, Kevin C Wright, Russell P Anderson, William D Phillips, Kristian Helmerson, and Gretchen K Campbell. Partial-transfer absorption imaging: A versatile technique for optimal imaging of ultracold gases. *Review of Scientific Instruments*, 83(8):083119, 2012.

[28] I Shvarchuck, CH Buggle, DS Petrov, K Dieckmann, M Zielonkowski, M Kemmann, TG Tiecke, W Von Klitzing, GV Shlyapnikov, and JTM Walraven. Bose–Einstein condensation into nonequilibrium states studied by condensate focusing. *Physical Review Letters*, 89(27):270404, 2002.

[29] A H van Amerongen, J J P van Es, P Wicke, K V Kheruntsyan, and N J van Druten. Yang-yang thermodynamics on an atom chip. *Physical Review Letters*, 100(9):090402, 2008.

[30] AH van Amerongen et al. One-dimensional Bose gas on an atom chip. *Annales de Physique*, 33(3):1–94, 2008.

[31] Walther Gerlach and Otto Stern. Der experimentelle nachweis der richtungsquantelung im magnetfeld. *Zeitschrift für Physik*, 9(1):349–352, 1922.

[32] Markus Greiner, Olaf Mandel, Theodor W Hänsch, and Immanuel Bloch. Collapse and revival of the matter wave field of a bose–einstein condensate. *Nature*, 419(6902):51–54, 2002.

[33] Karina Jimenez-Garcia. *Artificial gauge fields for ultracold neutral atoms*. PhD thesis, University of Maryland, College Park, 2013.

[34] Lauren Moise Aycock. *Topological excitations in an atomic Bose gas & sexual harassment reported by undergraduate physicists*. PhD thesis, Cornell University, 2017.

[35] Dina Genkina. *Measuring Topology of BECs in a Synthetic Dimensions Lattice*. PhD thesis, University of Maryland, College Park, 2019.

[36] Wolfgang Pauli. The connection between spin and statistics. *Physical Review*, 58(8):716, 1940.

[37] Stephen J Blundell and Katherine M Blundell. *Concepts in thermal physics*. Oxford University Press on Demand, 2010.

[38] Michel Le Bellac, Fabrice Mortessagne, G George Batrouni, and George Batrouni. *Equilibrium and non-equilibrium statistical thermodynamics*. Cambridge University Press, 2004.

[39] Franco Dalfovo, Stefano Giorgini, Lev P Pitaevskii, and Sandro Stringari. Theory of Bose–Einstein condensation in trapped gases. *Reviews of modern physics*, 71(3):463, 1999.

[40] Harold J Metcalf and Peter van der Straten. Laser cooling and trapping of atoms. *JOSA B*, 20(5):887–908, 2003.

[41] SC Bell, M Junker, M Jasperse, LD Turner, Y-J Lin, IB Spielman, and Robert E Scholten. A slow atom source using a collimated effusive oven and a single-layer variable pitch coil zeeman slower. *Review of Scientific Instruments*, 81(1):013105, 2010.

[42] Wolfgang Ketterle and NJ Van Druten. Evaporative cooling of trapped atoms. In *Advances in atomic, molecular, and optical physics*, volume 37, pages 181–236. Elsevier, 1996.

[43] Y-J Lin, Abigail R Perry, Robert L Compton, Ian B Spielman, and James V Porto. Rapid production of ^{87}Rb Bose–Einstein condensates in a combined magnetic and optical potential. *Physical Review A*, 79(6):063631, 2009.

[44] Philip Thomas Starkey, Christopher James Billington, Shaun Phillip Johnstone, Martijn Jasperse, K Helmerson, Lincoln David Turner, and Russell Paul Anderson. A scripted control system for autonomous hardware-timed experiments. *Review of Scientific Instruments*, 84(8):085111, 2013.

[45] Daryl W Preston. Doppler-free saturated absorption: Laser spectroscopy. *American Journal of Physics*, 64(11):1432–1436, 1996.

[46] Rüdiger Paschotta. Gaussian beams. *Encyclopedia of Laser Physics and Technology*, 2011.

[47] G Gauthier, I Lenton, N McKay Parry, M Baker, MJ Davis, H Rubinsztein-Dunlop, and TW Neely. Direct imaging of a digital-micromirror device for configurable microscopic optical potentials. *Optica*, 3(10):1136–1143, 2016.

[48] Neil W Ashcroft and N David Mermin. *Solid state physics*. Cengage Learning, 2022.

[49] M J Rice and E J Mele. Elementary excitations of a linearly conjugated diatomic polymer. *Physical Review Letters*, 49(19):1455, 1982.

[50] H-I Lu, Max Schemmer, Lauren M Aycock, Dina Genkina, Seiji Sugawa, and Ian B Spielman. Geometrical pumping with a Bose-Einstein condensate. *Physical Review Letters*, 116(20):200402, 2016.

[51] W P Su, J R Schrieffer, and Ao J Heeger. Solitons in polyacetylene. *Physical Review Letters*, 42(25):1698, 1979.

[52] Michael A Nielsen and Isaac Chuang. Quantum computation and quantum information, 2002.

[53] Jan Carl Budich, Ying Hu, and Peter Zoller. Helical floquet channels in 1d lattices. *Physical Review Letters*, 118(10):105302, 2017.

[54] Xiao-Gang Wen. Topological orders and edge excitations in fractional quantum Hall states. *Advances in Physics*, 44(5):405–473, 1995.

[55] Lev Landau. The theory of phase transitions. *Nature*, 138(3498):840–841, 1936.

[56] Mikio Nakahara. *Geometry, topology and physics*. CRC press, 2018.

[57] Eric W Weisstein. Gaussian curvature. *https://mathworld. wolfram. com/*, 2008.

[58] C L Kane. *Topological Insulators: Chapter 1. Topological Band Theory and the Z2 Invariant*, volume 6. Elsevier Inc. Chapters, 2013.

[59] J Weis and K Von Klitzing. Metrology and microscopic picture of the integer quantum hall effect. *Philosophical Transactions of the Royal Society A: Mathematical, Physical and Engineering Sciences*, 369(1953):3954–3974, 2011.

[60] Mengyun He, Huimin Sun, and Qing Lin He. Topological insulator: Spintronics and quantum computations. *Frontiers of Physics*, 14(4):1–16, 2019.

[61] Klaus v Klitzing, Gerhard Dorda, and Michael Pepper. New method for high-accuracy determination of the fine-structure constant based on quantized hall resistance. *Physical Review Letters*, 45(6):494, 1980.

[62] Bertrand I Halperin. Quantized hall conductance, current-carrying edge states, and the existence of extended states in a two-dimensional disordered potential. *Physical Review B*, 25(4):2185, 1982.

[63] Alexei Kitaev. Periodic table for topological insulators and superconductors. In *AIP conference proceedings*, volume 1134, pages 22–30. American Institute of Physics, 2009.

[64] Andreas P Schnyder, Shinsei Ryu, Akira Furusaki, and Andreas WW Ludwig. Classification of topological insulators and superconductors. 1134(1):10–21, 2009.

[65] Ching-Kai Chiu, J C Y Teo, Andreas P. Schnyder, and Shinsei Ryu. Classification of topological quantum matter with symmetries. *Reviews of Modern Physics*, 88:035005, Aug 2016.

[66] Michael Victor Berry. Quantal phase factors accompanying adiabatic changes. *Proceedings of the Royal Society of London. A. Mathematical and Physical Sciences*, 392(1802):45–57, 1984.

[67] Michael Berry. The geometric phase. *Scientific American*, 259(6):46–55, 1988.

[68] Konstantin Yu Bliokh. Geometrical optics of beams with vortices: Berry phase and orbital angular momentum hall effect. *Physical Review Letters*, 97(4):043901, 2006.

[69] Julio C Gutiérrez-Vega. Pancharatnam–Berry phase of optical systems. *Optics letters*, 36(7):1143–1145, 2011.

[70] J Zak. Berry's phase for energy bands in solids. *Physical Review Letters*, 62(23):2747, 1989.

[71] RD King-Smith and David Vanderbilt. Theory of polarization of crystalline solids. *Physical Review B*, 47(3):1651, 1993.

[72] Raffaele Resta and David Vanderbilt. Theory of polarization: a modern approach. In *Physics of Ferroelectrics*, pages 31–68. Springer, 2007.

[73] N R Cooper, J Dalibard, and I B Spielman. Topological bands for ultracold atoms. *Reviews of modern physics*, 91(1):015005, 2019.

[74] Marcos Atala, Monika Aidelsburger, Julio T Barreiro, Dmitry Abanin, Takuya Kitagawa, Eugene Demler, and Immanuel Bloch. Direct measurement of the Zak phase in topological bloch bands. *Nature Physics*, 9(12):795–800, 2013.

[75] Barry Simon. Holonomy, the quantum adiabatic theorem, and Berry's phase. *Physical Review Letters*, 51(24):2167, 1983.

[76] Takahiro Fukui, Yasuhiro Hatsugai, and Hiroshi Suzuki. Chern numbers in discretized Brillouin zone: efficient method of computing (spin) Hall conductances. *Journal of the Physical Society of Japan*, 74(6):1674–1677, 2005.

[77] Roberta Citro and Monika Aidelsburger. Thouless pumping and topology. *arXiv preprint arXiv:2210.02050*, 2022.

[78] Shuta Nakajima, Takafumi Tomita, Shintaro Taie, Tomohiro Ichinose, Hideki Ozawa, Lei Wang, Matthias Troyer, and Yoshiro Takahashi. Topological Thouless pumping of ultracold fermions. *Nature Physics*, 12(4):296–300, 2016.

[79] Michael Lohse, Christian Schweizer, Oded Zilberberg, Monika Aidelsburger, and Immanuel Bloch. A Thouless quantum pump with ultracold bosonic atoms in an optical superlattice. *Nature Physics*, 12(4):350–354, 2016.

[80] Joaquín Minguzzi, Zijie Zhu, Kilian Sandholzer, Anne-Sophie Walter, Konrad Viebahn, and Tilman Esslinger. Topological pumping in a floquet-bloch band. *Physical Review Letters*, 129(5):053201, 2022.

[81] KJM Schouten and V Cheianov. Rapid-cycle thouless pumping in a one-dimensional optical lattice. *Physical Review A*, 104(6):063315, 2021.

[82] Savvas Malikis and Vadim Cheianov. An ideal rapid-cycle thouless pump. *SciPost Physics*, 12(6):203, 2022.

[83] T Kitagawa, E Berg, M Rudner, and E Demler. Topological characterization of periodically driven quantum systems. *Physical Review B*, 82(23):235114, 2010.

[84] Netanel Lindner, Gil Refael, and Victor Galitski. Floquet topological insulator in semiconductor quantum wells. *Nature*, 7(6):490–495, 2011.

[85] F Nur Ünal, André Eckardt, and Robert-Jan Slager. Hopf characterization of two-dimensional floquet topological insulators. *Physical Review Research*, 1(2):022003, 2019.

[86] Sebabrata Mukherjee, Alexander Spracklen, Manuel Valiente, Erika Andersson, Patrik Öhberg, Nathan Goldman, and Robert R Thomson. Experimental observation of anomalous topological edge modes in a slowly driven photonic lattice. *Nature communications*, 8(1):1–7, 2017.

[87] Lukas J Maczewsky, Julia M Zeuner, Stefan Nolte, and Alexander Szameit. Observation of photonic anomalous floquet topological insulators. *Nature communications*, 8(1):1–7, 2017.

[88] Karen Wintersperger, Christoph Braun, F Nur Ünal, André Eckardt, Marco Di Liberto, Nathan Goldman, Immanuel Bloch, and Monika Aidelsburger. Realization of an anomalous floquet topological system with ultracold atoms. *Nature Physics*, 16(10):1058–1063, 2020.

[89] F Nur Ünal, Babak Seradjeh, and André Eckardt. How to directly measure floquet topological invariants in optical lattices. *Physical Review Letters*, 122(25):253601, 2019.

[90] G H Reid, Mingwu Lu, A R Fritsch, A M Piñeiro, and I B Spielman. Dynamically induced symmetry breaking and out-of-equilibrium topology in a 1d quantum system. *Physical Review Letters*, 129(12):123202, 2022.

[91] Mingwu Lu, G. H. Reid, A. R. Fritsch, A. M. Piñeiro, and I. B. Spielman. Floquet engineering topological Dirac bands. *Physical Review Letters*, 129:040402, Jul 2022.

[92] Karina Jimenez-Garcia, Lindsay J LeBlanc, Ross A Williams, Matthew C Beeler, Abigail R Perry, and Ian B Spielman. Peierls substitution in an engineered lattice potential. *Physical Review Letters*, 108(22):225303, 2012.

[93] Bindiya Arora, MS Safronova, and Charles W Clark. Tune-out wavelengths of alkali-metal atoms and their applications. *Physical Review A*, 84(4):043401, 2011.

[94] G Juzeliūnas and I B Spielman. Flux lattices reformulated. *New Journal of Physics*, 14(12):123022, 2012.

[95] Sarthak Subhankar, Yang Wang, Tsz-Chun Tsui, SL Rolston, and James V Porto. Nanoscale atomic density microscopy. *Physical Review X*, 9(2):021002, 2019.

[96] Jennifer Sebby-Strabley, Ben L Brown, M Anderlini, Patricia J Lee, William D Phillips, James V Porto, and Philip R Johnson. Preparing and probing atomic number states with an atom interferometer. *Physical Review Letters*, 98(20):200405, 2007.

[97] Simon Fölling, Stefan Trotzky, Patrick Cheinet, Michael Feld, Robert Saers, Artur Widera, Torben Müller, and Immanuel Bloch. Direct observation of second-order atom tunnelling. *Nature*, 448(7157):1029–1032, 2007.

[98] Joseph B Altepeter, Daniel FV James, and Paul G Kwiat. Quantum state tomography. In *Quantum State Estimation*, pages 113–145. Springer, 2004.

[99] Philipp Hauke, Maciej Lewenstein, and André Eckardt. Tomography of band insulators from quench dynamics. *Physical Review Letters*, 113(4):045303, 2014.

[100] Tracy Li, Lucia Duca, Martin Reitter, Fabian Grusdt, Eugene Demler, Manuel Endres, Monika Schleier-Smith, Immanuel Bloch, and Ulrich Schneider. Bloch state tomography using Wilson lines. *Science*, 352(6289):1094–1097, 2016.

[101] Nick Fläschner, BS Rem, M Tarnowski, D Vogel, D-S Lühmann, K Sengstock, and Christof Weitenberg. Experimental reconstruction of the Berry curvature in a Floquet Bloch band. *Science*, 352(6289):1091–1094, 2016.

[102] N Fläschner, D Vogel, M Tarnowski, BS Rem, D-S Lühmann, Markus Heyl, JC Budich, L Mathey, K Sengstock, and C Weitenberg. Observation of dynamical vortices after quenches in a system with topology. *Nature Physics*, 14(3):265–268, 2018.

[103] A M Piñeiro, D Genkina, Mingwu Lu, and I B Spielman. Sauter–Schwinger effect with a quantum gas. *New Journal of Physics*, 21(8):083035, 2019.

[104] Sebastian Diehl, Enrique Rico, Mikhail A Baranov, and Peter Zoller. Topology by dissipation in atomic quantum wires. *Nature Physics*, 7(12):971–977, 2011.

[105] Y-J. Lin, R. L. Compton, K Jimenez-Garcia, W. D. Phillips, J. V. Porto, and I. B. Spielman. A synthetic electric force acting on neutral atoms. *Nature Physics*, 7(7):531–534, March 2011.

[106] B K Stuhl, H-I Lu, L M Aycock, D Genkina, and I B Spielman. Visualizing edge states with an atomic Bose gas in the quantum Hall regime. *Science*, 349(6255):1514–1518, 2015.

[107] Max McGinley and Nigel R Cooper. Topology of one-dimensional quantum systems out of equilibrium. *Physical Review Letters*, 121(9):090401, 2018.

[108] Hsiu-Chuan Hsu and Tsung-Wei Chen. Topological Anderson insulating phases in the long-range Su-Schrieffer-Heeger model. *Physical Review B*, 102(20):205425, 2020.

[109] Lei Xiao, Xingze Qiu, Kunkun Wang, Zhihao Bian, Xiang Zhan, Hideaki Obuse, Barry C Sanders, Wei Yi, and Peng Xue. Higher winding number in a nonunitary photonic quantum walk. *Physical Review A*, 98(6):063847, 2018.

[110] Dizhou Xie, Wei Gou, Teng Xiao, Bryce Gadway, and Bo Yan. Topological characterizations of an extended Su–Schrieffer–Heeger model. *npj Quantum Information*, 5(1):1–5, 2019.

[111] Eric J Meier, Fangzhao Alex An, and Bryce Gadway. Observation of the topological soliton state in the su–schrieffer–heeger model. *Nature communications*, 7(1):1–6, 2016.

[112] Avik Dutt, Momchil Minkov, Ian AD Williamson, and Shanhui Fan. Higher-order topological insulators in synthetic dimensions. *Light: Science & Applications*, 9(1):1–9, 2020.

[113] Dmytro Dubyna, Jamal Busnaina, Zheng Shi, Jimmy Shih-Chun Hung, Ibrahim Nsanzineza, and Christopher Wilson. Simulation of the Su–Schrieffer–Heeger model using a superconducting parametric cavity. *Bulletin of the American Physical Society*, 2022.

[114] Takashi Oka and Sota Kitamura. Floquet engineering of quantum materials. *Annual Reviews of Condensed Matter*, 10:387–408, 2019.

[115] Christof Weitenberg and Juliette Simonet. Tailoring quantum gases by Floquet engineering. *Nature Physics*, 17(12):1342–1348, 2021.

[116] Christian Schweizer, Fabian Grusdt, Moritz Berngruber, Luca Barbiero, Eugene Demler, Nathan Goldman, Immanuel Bloch, and Monika Aidelsburger. Floquet approach to $\mathbb{Z}_2$ lattice gauge theories with ultracold atoms in optical lattices. *Nature*, 15(11):1168–1173, 2019.

[117] Yuanbo Zhang, Tsung-Ta Tang, Caglar Girit, Zhao Hao, Michael C. Martin, Alex Zettl, Michael F. Crommie, Y. Ron Shen, and Feng Wang. Direct observation of a widely tunable bandgap in bilayer graphene. *Nature*, 459(7248):820–823, 2009.

[118] Erwin Schrödinger. *Über die kräftefreie Bewegung in der relativistischen Quantenmechanik*. 1930.

[119] AO Barut and AJ Bracken. Zitterbewegung and the internal geometry of the electron. *Physical Review D*, 23(10):2454, 1981.

[120] Lindsay J LeBlanc, M C Beeler, Karina Jimenez-Garcia, Abigail R Perry, Seiji Sugawa, R A Williams, and Ian B Spielman. Direct observation of zitterbewegung in a Bose–Einstein condensate. *New Journal of Physics*, 15(7):073011, 2013.

[121] F. F. Fanchini, J. E. M. Hornos, and R. d. J. Napolitano. Continuously decoupling single-qubit operations from a perturbing thermal bath of scalar bosons. *Physical Review A*, 75:022329, Feb 2007.

[122] Matthias Troyer and Uwe-Jens Wiese. Computational complexity and fundamental limitations to fermionic quantum monte carlo simulations. *Physical Review Letters*, 94(17):170201, 2005.

[123] Omri Golan, Adam Smith, and Zohar Ringel. Intrinsic sign problem in fermionic and bosonic chiral topological matter. *Physical Review Research*, 2(4):043032, 2020.

[124] Horst L Stormer, Daniel C Tsui, and Arthur C Gossard. The fractional quantum hall effect. *Reviews of Modern Physics*, 71(2):S298, 1999.

[125] Hendrik Weimer, Markus Müller, Igor Lesanovsky, Peter Zoller, and Hans Peter Büchler. A rydberg quantum simulator. *Nature Physics*, 6(5):382–388, 2010.

[126] Rainer Blatt and Christian F Roos. Quantum simulations with trapped ions. *Nature Physics*, 8(4):277–284, 2012.

[127] Florian Schäfer, Takeshi Fukuhara, Seiji Sugawa, Yosuke Takasu, and Yoshiro Takahashi. Tools for quantum simulation with ultracold atoms in optical lattices. *Nature Reviews Physics*, 2(8):411–425, 2020.

[128] Kendall B. Davis, Marc-Oliver Mewes, Michael A. Joffe, Michael R. Andrews, and Wolfgang Ketterle. Evaporative cooling of sodium atoms. *Physical Review Letters*, 74:5202–5205, Jun 1995.

[129] J Zhen, R Dykstra, C Eccles, G Gouws, and S Obruchkov. A compact class d rf power amplifier for mobile nuclear magnetic resonance systems. *Review of Scientific Instruments*, 88(7):074704, 2017.

[130] Timothy Hopper, Soumyajit Mandal, David Cory, Martin Hürlimann, and Yi-Qiao Song. Low-frequency nmr with a non-resonant circuit. *Journal of Magnetic Resonance*, 210(1):69–74, 2011.

[131] S Mandal, S Utsuzawa, DG Cory, M Hürlimann, M Poitzsch, and Y-Q Song. An ultra-broadband low-frequency magnetic resonance system. *Journal of Magnetic Resonance*, 242:113–125, 2014.

[132] Eric W Weisstein. Fourier series. *from MathWorld–A Wolfram Web Resource. http://mathworld.wolfram.com/FourierSeries.html*, 2004.

[133] Paul Horowitz and Winfield Hill. *The art of electronics*. Cambridge Univ. Press, 1989.

[134] GaN Systems. *100V Enhancement Mode GaN Transistor*, 2018.

[135] pSemi. *UltraCMOS® High-speed FET Driver, 40 MHz*, 2018.

[136] John David Jackson. *Classical Electrodynamics*. John Wiley & Sons, 1999.

[137] D Trypogeorgos, A Valdés-Curiel, N Lundblad, and I. B. Spielman. Synthetic clock transitions via continuous dynamical decoupling. *Physical Review A*, 97(1):013407, 2018.

[138] Warren J Smith. *Modern optical engineering: the design of optical systems*. McGraw-Hill Education, 2008.

[139] Geoffrey De Villiers and E Roy Pike. *The limits of resolution*. CRC press, 2016.

[140] Eric Betzig and Jay K Trautman. Near-field optics: microscopy, spectroscopy, and surface modification beyond the diffraction limit. *Science*, 257(5067):189–195, 1992.

[141] Wolfgang Alt. An objective lens for efficient fluorescence detection of single atoms. *Optik*, 113(3):142–144, 2002.

[142] Lisa Marie Bennie, Philip Thomas Starkey, Martijn Jasperse, Christopher James Billington, Russell Paul Anderson, and Lincoln David Turner. A versatile high resolution objective for imaging quantum gases. *Optics express*, 21(7):9011–9016, 2013.

[143] Ian H Malitson. Interspecimen comparison of the refractive index of fused silica. *Josa*, 55(10):1205–1209, 1965.